technische universität
dortmund

Dissertation

Theory and Applications of Wide Field Surface Plasmon Resonance Microscopy for Discrete Particles Detection

submitted in partial fulfillment of the
requirement for the degree of

Dr. rer. nat.

to the Faculty of Physics of the TU
Dortmund University, Germany

by

Qais Mohammad Turki Al Bataineh, M.Sc.

Dortmund, 2024

Accepted by the Faculty of Physics of the TU Dortmund University, Germany.

Day of the oral examination: 24.02.2025

Examination board:

PD Dr. Joachim Franzke

Prof. Dr. Manfred Bayer

Prof. Dr. Kevin Kröninger

PD Dr. Jörg Bünemann

ABSTRACT

Detecting and characterizing nano-objects with low concentrations, such as biological particles, is a substantial challenge in analytical science. The wide-field surface plasmon resonance microscopy (WF-SPRM) can detect individual nano-objects in solutions and gas media bound to the sensor surface. Therefore, WF-SPRM can detect low nano-object concentrations because the image contains several square millimeters. In this work, the fundamental parameters for building highly sensitive WF-SPRM were optimized. The effective medium model of the SPR sensor treated the molecules bound on the sensor surface as an effective medium with an effective refractive index and thickness. However, WF-SPRM can detect individual nano-objects in solutions and gas media. Therefore, we derived a discrete particle model of SPR to describe the SPR sensor of discrete particle detection. Theoretical, numerical, and experimental analyses of the SPR detection principle were performed by considering discrete particle detection. The calculated single and double nanoparticle intensity profiles from the discrete particle model are in accordance with experimental data.

Additionally, the influence on the SPR sensitivity of coating the gold/silver layer with a dielectric layer with varying refractive index is also studied. Different polyelectrolyte brushes, like polyacrylic acid, polyacrylic acid-polyethylene oxide, and polyacrylic acid/iodine, are used to validate the enhancement of the SPR sensitivity. Validation experiments are performed using polystyrene and silica nanoparticles of varying sizes. The SPR discrete particle model is introduced to describe the detection principle for discrete particles. Theoretical, numerical, and experimental analyses were conducted, and the calculated intensity profiles of single and double nanoparticles from the discrete particle model were compared to the experimental profiles.

Finally, the surface plasmon coupling behavior between the localized surface plasmons (LSPs) of different shapes and sizes of metal nanostructures and the propagating surface plasmons (PSPs) of the metal surface is investigated by employing experimental, simulation, and theoretical approaches. First, the coupling behavior of the gold layer of WF-SPRM with single-, two-, and multiple-gold nanoparticles (AuNPs) with different AuNPs sizes is investigated using theoretical, simulation, and experimental approaches. After that, different shapes of AgNSs, including sphere, triangle plate, and hexagonal plate, are synthesized using a one-step solvothermal reduction method. The surface plasmon coupling behavior between the LSPs of different shapes of AgNSs and the PSPs of the Ag surface is investigated using wide-field surface plasmon resonance microscopy (WF-SPRM), finite element method, and derived method based on scattering theory.

ZUSAMMENFASSUNG

Das Erkennen und Charakterisieren von Nano-Objekten mit niedrigen Konzentrationen, wie beispielsweise biologischen Partikeln, stellt eine erhebliche Herausforderung in der analytischen Wissenschaft dar. Die Weitfeld-Oberflächenplasmonenresonanz-Mikroskopie (WF-SPRM) kann einzelne Nano-Objekte in Lösungen und Gasmedien, die an die Sensoroberfläche gebunden sind, detektieren. Daher kann WF-SPRM niedrige Konzentrationen von Nano-Objekten nachweisen, da das Bild mehrere Quadratmillimeter umfasst. In dieser Arbeit wurden die grundlegenden Parameter für den Bau einer hochsensitiven WF-SPRM optimiert. Das effektive Medium-Modell des SPR-Sensors behandelte die an die Sensoroberfläche gebundenen Moleküle als ein effektives Medium mit einem effektiven Brechungsindex und einer effektiven Dicke. Allerdings kann WF-SPRM einzelne Nano-Objekte in Lösungen und Gasmedien detektieren. Daher haben wir ein diskretes Partikelmodell der SPR abgeleitet, um den SPR-Sensor für die Detektion diskreter Partikel zu beschreiben. Theoretische, numerische und experimentelle Analysen des SPR-Detektionsprinzips wurden unter Berücksichtigung der Detektion diskreter Partikel durchgeführt. Die berechneten Intensitätsprofile von Einzel- und Doppel-Nanopartikeln aus dem diskreten Partikelmodell stimmen mit experimentellen Daten überein.

Zusätzlich wurde der Einfluss auf die SPR-Sensitivität durch Beschichtung der Gold/Silber-Schicht mit einer dielektrischen Schicht mit variierendem Brechungsindex untersucht. Verschiedene Polyelektrolyt-Bürsten, wie Polyacrylsäure, Polyacrylsäure-Polyethylenoxid und Polyacrylsäure/Iod, wurden verwendet, um die Verbesserung der SPR-Sensitivität zu validieren. Validierungsexperimente wurden mit Polystyrol- und Silica-Nanopartikeln unterschiedlicher Größen durchgeführt. Das diskrete Partikelmodell der SPR wurde eingeführt, um das Detektionsprinzip für diskrete Partikel zu beschreiben. Theoretische, numerische und experimentelle Analysen wurden durchgeführt, und die berechneten Intensitätsprofile von Einzel- und Doppel-Nanopartikeln aus dem diskreten Partikelmodell wurden mit den experimentellen Profilen verglichen.

Abschließend wird das Oberflächenplasmon-Kopplungsverhalten zwischen den lokalisierten Oberflächenplasmonen (LSPs) von Metall-Nanostrukturen unterschiedlicher Formen und Größen und den propagierenden Oberflächenplasmonen (PSPs) der Metalloberfläche durch experimentelle, Simulations- und theoretische Ansätze untersucht. Zunächst wird das Kopplungsverhalten der Goldschicht der WF-SPRM mit einzelnen, zwei und mehreren Goldnanopartikeln (AuNPs) unterschiedlicher AuNP-Größen unter Verwendung theoretischer, Simulations- und experimenteller Ansätze untersucht. Danach werden verschiedene Formen von AgNSs, einschließlich Kugel, Dreieckplatte und Hexagonplatte, durch eine einstufige solvothermale Reduktionsmethode synthetisiert. Das Oberflächenplasmon-Kopplungsverhalten zwischen den LSPs unterschiedlicher Formen von AgNSs und den PSPs der Ag-Oberfläche wird unter Verwendung der Weitfeld-Oberflächenplasmonenresonanz-Mikroskopie (WF-SPRM), der Finite-Elemente-Methode und einer abgeleiteten Methode basierend auf der Streutheorie untersucht.

TABLE OF CONTENTS

PUBLICATIONS

Peer-reviewed journal articles

This thesis is based on the following publications of the author. The publications are listed in ascending chronological order.

1. **Qais M. Al-Bataineh**, Victoria Shpacovitch, Diyar Sadiq, Ahmad Telfah, and Roland Hergenröder, *Surface Plasmon Resonance Sensitivity Enhancement Based on Protonated Polyaniline Films Doped by Aluminium Nitrate*. Biosensors 2022, 12(12), 1122. https://doi.org/10.3390/bios12121122. (Al-Bataineh et al., 2022)

   (IF[i]: 5.7, Sc. Per.[ii]: 78%, Q1)

2. **Qais M. Al-Bataineh**, Ahmad D. Telfah, Victoria Shpacovitch, Carlos J. Tavares, and Roland Hergenröder, *Switchable Polyacrylic Acid Polyelectrolyte Brushes for Surface Plasmon Resonance Applications*. Sensors 2023 23(9), 4283. https://doi.org/10.3390/s23094283. (Al-Bataineh et al., 2023a)

   (IF: 3.**9,** Sc. Per.: 87%, Q1)

3. **Qais M. Al-Bataineh**, Ahmad D. Telfah, Carlos J. Tavares, Roland Hergenröder, *Surface plasmon coupling between wide-field SPR microscopy and gold nanoparticles*. Scientific Reports 13.1 (2023): 22405. https://doi.org/10.1038/s41598-023-49583-3. (Al-Bataineh et al., 2023b)

   (IF: 4.6**,** Sc. Per.: 92%, Q1)

4. **Qais M. Al-Bataineh**, Ahmad D. Telfah, Carlos J. Tavares, Roland Hergenröder, *Modeling and analysis of discrete particle detection in wide-field surface plasmon resonance microscopy*. Sensors and Actuators: A. Physical 370 **(**2024**):** 115266**.** https://doi.org/10.1016/j.sna.2024.115266**.** (Al-Bataineh et al., 2024a)

   (IF: 4.6, Sc. Per.: 90%, Q1)

5. **Qais M. Al-Bataineh**, Ahmad D. Telfah, Carlos J. Tavares, Roland Hergenröder, *Wide-field surface plasmon resonance microscope based on polyethylene oxide/polyacrylic acid brushes*. Applied Surface Science 649 (2024): 159189. https://doi.org/10.1016/j.apsusc.2023.159189. (Al-Bataineh et al., 2024b)

   (IF: 6.7, Sc. Per.: 95%, Q1)

6. **Qais M. Al-Bataineh**, Gaith Rjoub, Ahmad D. Telfah, Ahmad A. Ahmad, Carlos J. Tavares, Roland Hergenröder, *Developing surface plasmon resonance imaging for discrete particle detection based on a silver layer coated with polyacrylic acid/iodine polyelectrolyte brushes*. Applied Surface Science 682 (2024): 161755. https://doi.org/10.1016/j.apsusc.2024.161755 (Al-Bataineh et al., 2024c)

   (IF: **6.7,** Sc. Per.: 95%, Q1)

7. **Qais M. Al-Bataineh**, Ihsan Aljarrah, Ahmad A. Ahmad, Gaith Rjoub, Ahmad D. Telfah, Roland Hergenröder, *Surface Plasmon Coupling Between Different Shapes of Silver Nanostructures and Wide Field SPR Microscopy*. Submitted to Journal of Materials Science. (Al-Bataineh et al., 2024d)

   (IF: **4.0,** Sc. Per.: 86%, Q1)

[i] IF: Impact Factor
[ii] Sc.Per: Scopus percentile

The work presented in the PhD project has been presented at the following international conferences:

1. **Qais M. Al-Bataineh**, Ahmad D. Telfah, Victoria Shpacovitch, Roland Hergenröder. *Switchable Polyacrylic Acid Polyelectrolyte Brushes as a Functional Biosensor Surface*. Al-Zaytoonah International Pharmaceutical Conference 2022 (ZIPC2022), Amman, Jordan, 18-20 October 2022.

   (Poster)

2. **Qais M. Al-Bataineh**, Ahmad D. Telfah, Roland Hergenröder. *Wide-field surface plasmon resonance microscopy for discrete particle detection*. International Conference on Advanced Materials - ICAM 2023. Irbid, Jordan 22-24 May 2023.

   (Poster)

3. **Qais M. Al-Bataineh**. *Shape Memory Polyelectrolyte Brushes Based on Mixed PEO/PAA Toward Virus Detection Applications*. International Conference on Advanced Materials - ICAM 2023. Irbid, Jordan 22-24 May 2023.

   (Presentation)

4. **Qais M. Al-Bataineh,** Ahmad D. Telfah, Roland Hergenröder. *Wide-field surface plasmon resonance microscopy for discrete particle detection*. International Conference for the Science and Pharmacy (MSPC2). Mutah University, Karak, Jordan 25-27 October 2023.

   (Poster)

STATEMENT OF ORIGINAL AUTHORSHIP

The work contained in this thesis has not been previously submitted to meet requirements for an award at this or any other higher education institution. To the best of my knowledge and belief, the thesis contains no material previously published or written by another person except where due reference is made.

DEDICATION

To my great dad

The man who supports and encourages me, confident in my abilities, which made my life so special.

To my lovely mam

For the warm feelings, prayers, and support that made my life so unique.

To my tender wife

For the support and warm feelings, which help me in my academic career.

To my family and friends

For the support, assistant, dialogues, and help when even I need them.

To my advisors

I dedicate this work to my advisors, Dr. Roland Hergenröder and PD Dr. Joachim Franzke. They were always positive and trusted me to do this work.

To my teachers

I extend my thanks and regards to Dr. Ahmad Telfah and Prof. Ahmad Al Omari for their kindness, guidance, and support during the research. They never hid their encouragement and support for me through the years of my studies. I learned from them how to be a cooperative and independent researcher.

I am grateful to all.

Qais M. Al Bataineh

ACKNOWLEDGMENT

All praise is due to Allah, sobhanh wa ta'ala, for giving me patience and passion, as well as for aiding me in completing this work.

First and foremost, I would like to express my sincere thanks to my advisors, Dr. Roland Hergenröder and PD Dr. Joachim Franzke, for giving me the opportunity to pursue a PhD, and for their support and encouragement throughout my study. Additionally, I would like to thank my committee members for their suggestions and valuable comments.

My sincere appreciation is extended to Dr. Ahmad Telfah for helping and guiding me throughout my study. Thank you for your trust and confidence in my capability to advance my PhD and in my ability to succeed in my work. Without his suggestions, guidance, and supervision, I wouldn't have been able to accomplish my work.

I am very fortunate to have the ability to work closely with Prof. Carlos Tavares, and I really appreciate his unlimited support and thoughtfulness during my work.

My sincere appreciation is extended to Prof. Ahmad Al-Omari, Dr. Lubabah Migdadi, Ahmad Al-Bahti, Ihsan Aljarrah, Ahmad Migdadi, Mahmoud Telfah, and Lina Alakhras for helping and guiding me throughout the laboratory work. Without their help, I couldn't have finished this work.

This work would not have been without the inspiration, support, and love of my father, my mother, and my family.

My sincere appreciation is extended to my wife "Areen Bani-Salameh". Areen is not only a wife but also a colleague, a partner, a supporter, and a friend with unconditional love, trust, faith, and care.

I am grateful to everyone who contributed either directly or indirectly to my work to achieve my goal.

With my appreciation and thanks.

Qais Al Bataineh

"Of course. I was an ordinary person who studied hard. There are no miracle people. It just happens. They got interested in this and learned all this stuff."

–Richard P. Feynman

CHAPTER 1

1. INTRODUCTION

1.1. Research Motivation

Recently, different classes of biosensors have been developed for biological particle detection, drug detection, and medical diagnosis (Mehrotra, 2016), including optical sensors (Ma et al., 2021; Ma et al., 2020; Zhang et al., 2020), electrochemical sensors (Cui et al., 2019; M. Wang et al., 2022), and electrical impedance sensors (Burinaru et al., 2022; Cisneros et al., 2022). In general, biosensors contain four main components: analyte, recognition, transducer, and signal processing, i.e., analyte represents the chemical components that are measured and described, recognition is a bio-receptor that sensitive to analyte recognition, transducer turns the bio-recognition event to measured signals, while the signal processor prepares the deduced signal for display (Singh et al., 2020). In particular, optical sensors are considered the most sensitive sensors, which can be divided into different types, such as surface plasmon resonances, ring resonators, interferometers, etc. (Fan et al., 2008). However, detecting and characterizing nano-objects with low concentrations, such as biological particles, is a substantial challenge in analytical science (Scherbahn et al., 2016).

In nanophotonics, plasmonics is a novel idea that combines the characteristics of electronics and photonics by confining light energy to a surface plasmon, which is a nanometer-scale oscillating field of free electrons (Khan et al., 2023). Because metal can support surface plasmon polariton (SPP) modes, which are electromagnetic waves connected to the collective oscillations of free electrons in the metal, metals are essential to plasmonics (Alzoubi et al., 2023). Surface plasmons (SPs) are collective electronic excitations at the interface of dielectrics and metals. Although there is a wide range of plasmonic metal nanostructures, two types of plasmonic modes can be used to distinguish them: propagating surface plasmons (PSPs) and localized surface plasmons (LSPs), which are highly sensitive to changes in the immediate

environment. Unlike PSPs, which use plasmon propagation along metallic surfaces, LSPs are localized to individual nanoparticles (Rycenga et al., 2011). The localized surface plasmon resonance depends on numerous parameters, including metal shape, metal size, crystallization, and the dielectric environment (Gaur et al., 2021). In theory, each one of these variables can be changed to customize the plasmon's characteristics for a range of uses. In particular, it is interesting to manufacture metal nanoparticles under controlled conditions with varying shapes since this makes it possible to adjust their properties more versatilely in numerous cases (Yang et al., 2007).

On the other hand, propagating surface plasmon polaritons (SPPs) are induced by the interactions between the *p*-polarized light and free-conduction electrons at the interface of dielectric and metal (Barnes et al., 2003; Otto, 1968). These SPPs are attractive for different label-free techniques in advanced nanostructure detection applications (Masson, 2017; Xue et al., 2019a), including metal nanoparticles (Xue et al., 2019b; Yang et al., 2019; Yano et al., 2022), biomolecules (Bellassai et al., 2019; Shpacovitch et al., 2018; Srivastava et al., 2020), and gases (Usman et al., 2019b).

Due to their various features, such as label-free detection, high sensitivity, high reproducibility, real-time measurements, and low cost, surface plasmon resonance (SPR) sensors have recently earned growing attention among all optical biosensors to investigate the interactions of the nano-objects bounding to the sensor surface (Masson, 2017; Xue et al., 2019a). The SPR sensor was designed based on an attractive phenomenon called surface plasmon polariton (SPP), representing the optically excited SPR in thin metal films. The collective electronic excitation originates from a resonant interaction between the incident photons and the free electrons in the metal films. The electrons in the metal film oscillate at a plasma frequency (ω_p) against a static background of positive charged metal ions. At resonance, the angular frequency of the incident electromagnetic wave corresponds to ω_p. In addition, for a thin metal film between two dielectric media, the plasma resonance at a frequency (ω_{sp}) is modified compared to the phenomenon in the bulk metal, single metal-dielectric interface, or small metal particles embedded within a dielectric media (Oliveira et al., 2015). The resonant interaction of the surface-confined plasmons with light in metal films generates the surface plasmon polaritons.

Conventional SPR sensor is based on monochromatic light shining the metal thin film through a prism since illuminated metal film at a specific angle leads to exciting electrons on the metal surface, which generates an electric field (Nguyen et al., 2015; Wang et al., 2019). However, bounding the nano-object to the metal surface increases the refractive index of the system and consequently changes the incident angle. The incident angle change is measured for a real-time response curve (Nguyen et al., 2015). In addition, SPR sensors measure a wide

range of binding interactions, such as protein adsorption, ligand-receptor binding, and hybridization of RNA and DNA (Singh et al., 2020).

Detecting and exploring low concentrations of chemical and biological particles remains challenging (Fan et al., 2008; Scherbahn et al., 2016). Here, the wave properties of the surface plasmon polaritons are used in real-time imaging of discrete particles based on wide-field surface plasmon resonance microscopy (WF-SPRM) (Lenssen et al., 2018; Zybin, 2010). WF-SPRM is a real-time detection method of single particles in solutions bound to the sensor surface using the classical Kretschmann's configuration (Kretschmann, 1996). WF-SPRM thus allows for the detection of low concentrations of nano-objects.

In this technique, a *p*-polarized laser beam illuminates a metal layer through a glass prism, and the reflected light is imaged onto a CCD camera, enabling high-resolution imaging of the binding events (Figure 1.1a). At a certain angle of incidence, the resonance angle, the incident *p*-polarized light generates evanescent surface plasmon waves (SPWs) along the metal/analyte interface, reducing the reflectance beam intensity. After the particle is bound to the metal surface, the evanescent field of the SPWs is disturbed due to scattering with a particle (Yu et al., 2014). Localized variations in reflectivity caused by the deformation of the SPWs' evanescent field result in a bright spot in the image that is surrounded by concentric surface plasmon waves (Figure 1.1b) (Nizamov et al., 2022; Shpacovitch et al., 2018). Many factors affect the surface plasmons, such as light wavelengths, metal layer thickness and properties, prism properties, and the surrounding dielectric medium properties (Steiner, 2004).

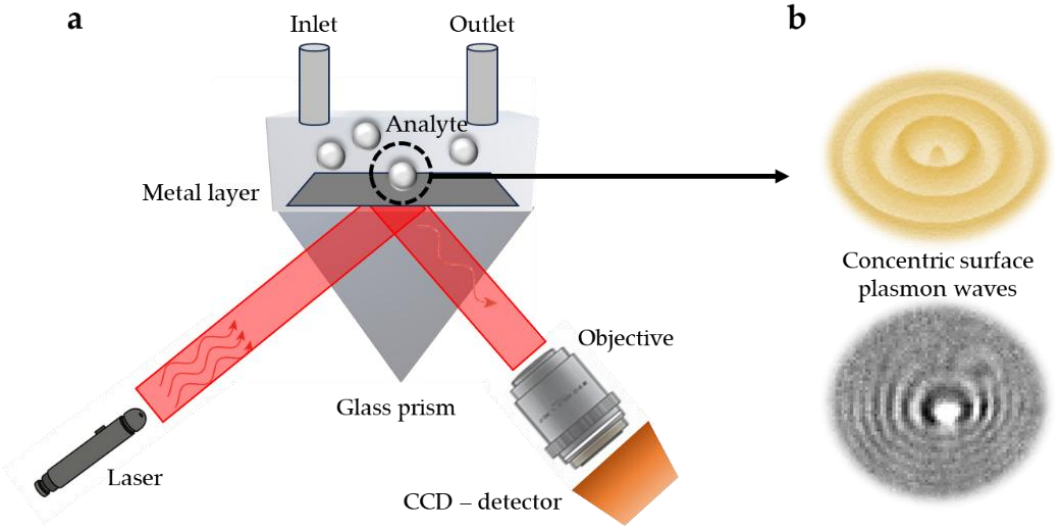

Figure 1.1: (a) Schematic diagram of Kretschmann's configuration based on glass prism, Ag-layer with an analyte for sensing particles. **(b)** Diagram for generated SPR concentric wave as a result of the particle acting on the metal's surface.

This thesis is dedicated to the development of a high-sensitive wide-field surface plasmon resonance microscope by optimizing the fundamental parameters that influence the imaging performance. Additionally, the influence of coating the gold/silver layer with a dielectric layer with varying refractive index on the SPR sensitivity is studied. Polyaniline as a conjugated polymer along with different polyelectrolyte brushes, like polyacrylic acid (PAA), polyethylene oxide/ polyacrylic acid (PEO/PAA), and polyacrylic acid/iodine (PAA/I_2), are used to validate the enhancement of the SPR sensitivity. Validation experiments are performed using polystyrene and silica nanoparticles of varying sizes. The SPR discrete particle model is introduced to describe the detection principle for discrete particles. Theoretical, numerical, and experimental analyses were conducted, and the calculated intensity profiles of single and double nanoparticles from the discrete particle model were compared to the experimental profiles. Finally, the surface plasmon coupling behavior between the localized surface plasmons (LSPs) of different shapes and sizes of metal nanostructures and the propagating surface plasmons (PSPs) of the metal surface is investigated by employing experimental, simulation, and theoretical approaches.

1.2. Literature Review

The first commercial non-imaging surface plasmon resonance (SPR) instrument was introduced in 1990. After that, systems for dedicated applications have been introduced by various manufacturers as complements to all-purpose research instrumentation. The impact of SPR biosensors on biomolecular interaction studies is growing continuously (McDonnell, 2001). Over the last three decades, this research field has grown significantly, as exhibited in Figure 1.2.

Many attempts have been made to develop a WF-SPRM for real-time detection of single nanoparticles on thin metal films based on the SPR phenomenon. In 2007, B. Huang et al. designed an SPR microscope using a high numerical aperture objective to investigate the high-resolution information about surfaces (Huang et al., 2007). In the same year, N. Ly et al. presented a surface plasmon resonance imaging method for label-free and real-time imaging of proteins in micro/nanofluidic channels (Ly et al., 2007). After that, D. Boecker et al. presented a SPR imaging method with charge-coupled device detection for biotin detection (Boecker et al., 2008). A. Peterson et al. presented the real-time SPR imaging method to monitor cellular modifications to the extracellular matrix in real-time (Peterson et al., 2009). L. Wang et al. demonstrated label-free imaging, detection, and size measurements of single viral particles with a surface plasmon resonance imaging technique (Wang et al., 2010).

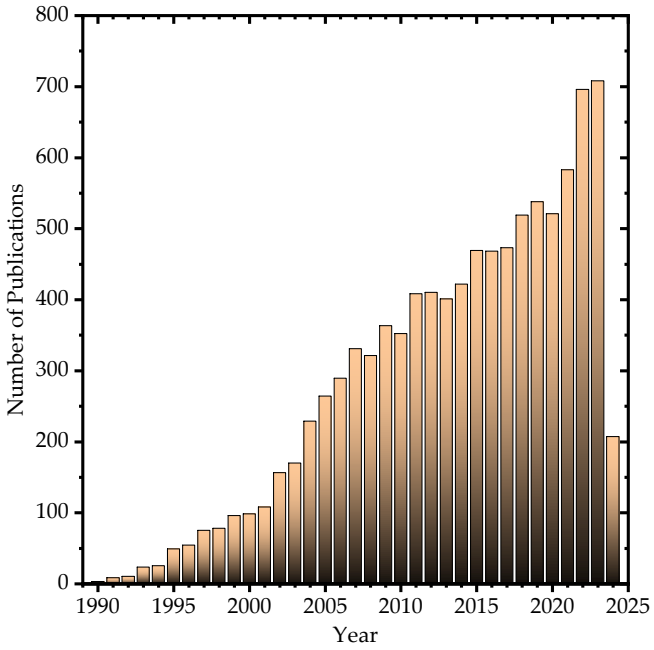

Figure 1.2: Number of publications with the keyword "Surface Plasmon Resonance Biosensor" between 1990 and 2024. The data was retrieved in April 2024 from Scupos.

In 2010, A. Zybin et al. proposed a method based on WF-SPRM to record the real-time detection of single virus-like particles with a size of about 100 nm (Zybin et al., 2010). After that, E. Gurevich et al. presented a new analytical method for concentration measurements using WF-SPRM based on counting single nanoparticles bounded to a functional sensor surface (Gurevich et al., 2011). V. Shpacovitch et al. have used WF-SPRM to visualize the binding events between round-shaped viruses (inactivated influenza A virus) and virus-like particles (human immunodeficiency virus (HIV)-based virus-like particles) to the functionalized sensor surface. They concluded that the WF-SPRM is an efficient research tool for quantifying and characterizing biological submicrometer objects (Shpacovitch et al., 2015). In addition, V. Shpacovitch et al. have used WF-SPRM to perform real-time detection of the label-free microvesicles to the sensor surface functionalized by protein A/G and anti-target antibody (Shpacovitch et al., 2017). A. Zybin et al. proposed a simple model to describe the signal formation in WF-SPRM of the interaction between the nanoobjects and metal surfaces. In addition, they concluded that the thickness of a gold layer plays an essential role in WF-SPRM sensitivity (Zybin et al., 2017). G. Ma et al. developed an optical imaging technology based on WF-SPRM to quantify the size, mobility, and charge of single proteins simultaneously and to monitor protein-ligand interactions and associated conformation changes in proteins (Ma et al., 2020). S. Dai et al. developed an SPR holographic microscopy to achieve the functionality of real-time mapping of the cell-substrate adhesion gap and its evolution in situ (Dai et al., 2021).

Moreover, various research studies have been conducted to enhance the sensitivity of SPR sensing devices by using multiple detection methods (Shalabney et al., 2011). Film materials coated on the gold layer, such as polyelectrolytes, conductive polymers, graphene, and transition metal dichalcogenides, have been used to enhance the SPR sensitivity (Omar et al., 2020; Park et al., 2021; Viti et al., 2017) due to their interesting optical and chemical properties (Agarwal et al., 2018; Politano et al., 2016; Politano et al., 2017).

F. Usman et al. used the PANI/chitosan composite as a coating layer on the gold surface to enhance the SPR sensitivity for low-concentration detection of acetone vapor. They concluded that coating the gold layer with PANI/chitosan composite enhances the sensor device's sensitivity (Usman et al., 2019a). In addition, for ultra-low concentration detection, signal amplification tags are used to improve the sensitivity for SPR detection. Gold nanoparticles (AuNPs) are the most effective tags for detection enhancement due to their unique optical properties in addition to their high physical and chemical stability (Yang et al., 2019).

1.3. Contributions

This work (in the form of a cumulative thesis) is devoted to developing a high-sensitive wide-field surface plasmon resonance microscope by optimizing the fundamental parameters and introducing a dielectric layer above the metal surface, which influences imaging performance. Additionally, the SPR discrete particle model is introduced to describe the detection principle for discrete particles. Finally, the surface plasmon coupling between the localized surface plasmons of metal nanostructures and propagating surface plasmons of the metal surface is also presented. It is postulated that such approaches are still highly unexplored in this application area and hold promise for further advances in single-particle detection. Its main contributions involve the development of:

1. **A discrete particle model for particle detection in wide-field surface plasmon resonance microscope.** An effective medium model describes the SPR sensor principle by treating molecules bound on the sensor surface as an effective medium with an effective refractive index and thickness. On the other hand, the discrete particle model is introduced to describe the detection principle for discrete particles. Theoretical, numerical, and experimental analyses are conducted to describe the experimental data of single and double nanoparticle detection. The proposed model is compared with experimental data to validate its accuracy and applicability.

   (Al-Bataineh et al., 2024a)

2. **Improving the sensitivity of WF-SPRM: Conductive Polymer**. In an attempt to enhance the detection sensitivity of WF-SPRM, conductive polymer nanocomposite film, or more specifically, polyaniline/aluminum nitrate nanocomposite film, is deposited on the gold layer due to its interesting optical and chemical properties (Usman et al., 2019c). The sensitivity of the WF-SPRM-based gold layer coated with polyaniline/aluminum nitrate nanocomposite film was investigated using a theoretical approach as well as experimental measurements.

   (Al-Bataineh et al., 2022)

3. **Improving the sensitivity of WF-SPRM: Polyelectrolyte brushes**. Various studies have been conducted to enhance the sensitivity and selectivity of the SPR sensors using polyelectrolyte brushes (Ferrand-Drake del Castillo et al., 2019). In our work, polyacrylic acid (PAA), polyethylene oxide/ polyacrylic acid (PEO/PAA), and polyacrylic acid/iodine (PAA/I_2) are designed to improve the sensitivity of the WF-SPRM. The sensitivity of the WF-SPRM-based gold/silver layer coated different types of polyelectrolyte brushes was investigated using a theoretical approach as well as experimental measurements.

   (Al-Bataineh et al., 2023a); (Al-Bataineh et al., 2024b); (Al-Bataineh et al., 2024c)

4. **Surface plasmon coupling between LSPs and PSPs**. The surface plasmon coupling behavior between the localized surface plasmons (LSPs) of different shapes and sizes of metal nanostructures and the propagating surface plasmons (PSPs) of the metal surface is investigated by employing experimental, simulation, and theoretical approaches. First, the coupling behavior of the gold layer of WF-SPRM with single-, two-, and multiple-gold nanoparticles (AuNPs) with different AuNPs sizes is investigated. After that, different shapes of AgNSs, including sphere, triangle plate, and hexagonal plate, are synthesized using a one-step solvothermal reduction method. The surface plasmon coupling behavior between the LSPs of different shapes of AgNSs and the PSPs of the Ag surface is investigated using wide-field surface plasmon resonance microscopy (WF-SPRM), finite element method, and derived method based on scattering theory.

   (Al-Bataineh et al., 2023b); (Al-Bataineh et al., 2024d)

CHAPTER 2

2. WIDE-FIELD SURFACE PLASMON RESONANCE MICROSCOPE

2.1. Preface

The area of surface plasmon resonance nano-optics has developed to the point where it is now possible to construct metallic nanostructures with specific optical properties. From a physical point of view, surface plasmons are surface electromagnetic waves that travel parallel to the metal/dielectric interface. Since the surface plasmon waves are on the metal/dielectric interface, these oscillations are extremely sensitive to any change in this boundary, such as molecule adsorption to the metal surface. First, the more widely used and well-understood planar surface plasmon resonance theory, which finds application in biomolecular contact sensing will be covered.

A wide-field surface plasmon resonance microscope (WF-SPRM), based on Kretschmann's configuration, employs the surface plasmon resonance phenomenon to detect individual biological and non-biological nanoparticles in solution. WF-SPRM allows the detection, sizing, and quantification of biological nanoparticles, such as viruses, virus-like particles, and extracellular vesicles. The focus will be on the fundamental parameters influencing the imaging performance of WF-SPRM to enhance biosensing sensitivity. Validation experiments are performed using polystyrene/silica nanoparticles of varying sizes and nanoparticles made from different materials. The influence of coating the gold layer with a dielectric layer with varying refractive index on the SPR sensitivity is also studied.

2.2. Surface Plasmon Theory

2.2.1. The Evanescent Wave

In WF-SPRM, the resultant plasmons on the dielectric-metal and metal-dielectric interfaces produce an electric field that penetrates the dielectric medium, which is called the evanescent wave because the wave amplitude decreases exponentially with increasing distance from the interface (Nagata et al., 2000). It is appropriate to give a mathematical explanation of the evanescent wave, which is essential to the idea of surface plasmon resonance (SPR) sensing, before going into more detail about surface plasmons. Since the evanescent field is a consequence of the phenomena of total internal reflection, we can start from here.

Consider the refraction of an electromagnetic wave at an interface between two media (1 and 2) with refractive indices (n_1 and n_2), respectively (Figure 2.1). The direction of the wavevector ($\vec{k}$) is parallel to the wave propagation, and its magnitude is given by (Schasfoort, 2017),

$$k = \sqrt{k_x^2 + k_y^2 + k_z^2} = n\frac{2\pi}{\lambda} = n\frac{\omega}{c} \tag{2.1}$$

where: λ and c are the wavelength and propagation velocity in vacuum, respectively (Raether, 2006). Our problem becomes effectively two-dimensional when we can choose the direction of the light beam so that $k_z = 0$. Snell's law is given by,

$$n_1 \sin\alpha = n_2 \sin\beta \tag{2.2}$$

or, equivalently,

$$k_{x_1} = k_{x_2} \equiv k_x \tag{2.3}$$

Using equations (2.1) and (2.2), the component of the wavevector k_y perpendicular to the interface is given by,

$$k_{y_2}^2 = n_1^2\left(\frac{2\pi}{\lambda}\right)^2\left(\frac{n_2^2}{n_1^2} - \sin^2\alpha\right) \tag{2.4}$$

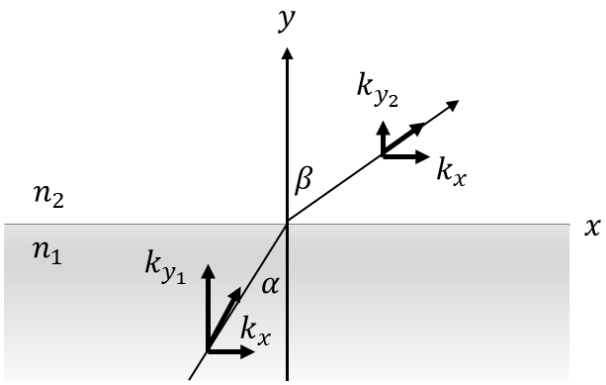

Figure 2.1: Refraction of light at an incident angle α at an interface of two media with different refractive indices.

Assuming that $n_1 > n_2$, which is the case when the light comes from the prism into the water. From equation (2.2), it can be seen that $\sin\alpha = n_2/n_1$, so in total internal reflection, the right part of equation (2.4) is negative and, consequently, k_y is purely imaginary. In medium 2, there is a traveling wave parallel, so in the x-direction to the interface is given by,

$$E_2 = E_0 e^{-\kappa_{y_2} y} \exp(i\omega t - ik_x x) \tag{2.5}$$

where: E_0 is the amplitude of the electric field, and ω is the angular frequency. Here, the amplitude of the electric field decays exponentially along the y-direction with a characteristic distance of $1/\kappa_{y_2} \equiv 1/ik_{y_2}$. The electric field in medium 2 represents the evanescent field, which is decaying from the surface.

2.2.2. Surface Plasmon Dispersion

Here, only *p*-polarized light interacting with an interface is discussed since the interaction between *p*-polarized light and metal film generates the propagating surface plasmon waves. For any interface between two media, the complex reflection coefficient r_p for *p*-polarized incident light electric field is described by Fresnel's equation,

$$r_p = \frac{E_i}{E_r} = |r_p| e^{i\varphi} = \left|\frac{\tan(\alpha-\beta)}{\tan(\alpha+\beta)}\right| e^{i\varphi} \tag{2.6}$$

where: E_i and E_r are the incident and reflected electric fields, respectively. Additionally, a phase change φ of the reflected field relative to the incident field occurs depending on the refractive indices of the materials. The reflectance is given by,

$$R_p = |r_p|^2 \tag{2.7}$$

Now, two special cases exist:

- If $\alpha + \beta = \pi/2$, then the denominator of equation (2.6) becomes very large, and R_p becomes zero. This case describes the Brewster angle, where there is no reflection of *p*-polarized light.
- If $\alpha - \beta = \pi/2$, the R_p becomes infinite; there is a finite E_r for a very small E_i. This case corresponds to resonance.

From the second case, one can deduce the dispersion relation, where $\cos\alpha = -\sin\beta$ and $\tan\alpha = k_{1x}/k_{1y} = -n_2/n_1$. For the components of the wavevector $\vec{k} = (k_x, k_y)$, we can write,

$$k_x^2 = k_1^2 - k_{y_1}^2 = k_1^2 - k_x^2 \frac{\varepsilon_1}{\varepsilon_2} \tag{2.8}$$

$$k_x = \frac{\omega}{c}\sqrt{\frac{\varepsilon_1\varepsilon_2}{\varepsilon_1+\varepsilon_2}} \tag{2.9}$$

$$k_{y_i} = \frac{\omega}{c}\sqrt{\frac{\varepsilon_i^2}{\varepsilon_1+\varepsilon_2}} \tag{2.10}$$

where: ε_1 and ε_2 are the dielectric constants of materials 1 and 2, respectively. Equations (2.9) and (2.10) represent SPR dispersion equations for the interface between two half-infinite

media. Now, consider that medium 2 is a metal, which implies that the low refractive index medium (in our case, water) becomes medium 3. Medium 2 contains a large number of free electrons, and the consequence is that at an angular frequency $\omega < \omega_p$, its dielectric constant ε_2 will be negative (Reitz, 2009),

$$\varepsilon_2(\omega) = 1 - \frac{\omega_p^2}{\omega^2} \tag{2.11}$$

$$\omega_p = \sqrt{\frac{4\pi n_e e^2}{m_e}} \tag{2.12}$$

where: ω_p is the plasma frequency, n_e is the free electron density, e and m_e are the electron charge and mass, respectively. This implies that $\omega < \omega_p$, no electromagnetic field can propagate in a metal. More specifically, provided that $\varepsilon_2 > -\varepsilon_1$, the interface that k_{y_i} is imaginary, whereas k_x remains real. Thus, an electromagnetic wave exists, propagating strictly along the interface, with evanescent tails extending into both sides of the interface.

2.3. Conventional Surface Plasmon Resonance Sensor

The SPR phenomenon is a coherent oscillation of the free electrons at the metal/dielectric interface, where the yielded quanta from the oscillations are called surface plasmons (Q. Wang et al., 2022). WF-SPRM was designed based on a Kretschmann configuration for a thin metal layer (Figure 2.2a). The light will reflect when polarized light illuminates the metal film through the glass prism. By changing the incident light angle, the reflected light intensity reaches a minimum, which is called the resonance angle (Figure 2.2b, black line). The edge of total internal reflection (θ_c) is a significant parameter to validate correct sample alignment. At the resonance angle, the reflectivity reaches the minimum, which means surface plasmons excitation, inducing surface plasmon resonance, where the *p*-polarized light interacts with the free electron of a metal film, resulting in free electron oscillations (Peterson et al., 2014). The resonance angle depends on the optical refractive indices of the media on both sides of the metal. Therefore, the SPR angle is suitable for providing information on the particle bounding at the sensing surface; changing the refractive index when the detected particles bounded to the sensing surface leads to a shift in the resonance angle (Figure 2.2b, blue line). In addition, the SPR sensing device can monitor the change in the resonance angle as a time function, which allows for studying the interaction kinetics in real-time. The single interaction curve between the bound particle and the metal surface contains four main events: baseline, particle association, steady state, and particle dissociation (Figure 2.2c) (Rich et al., 2003).

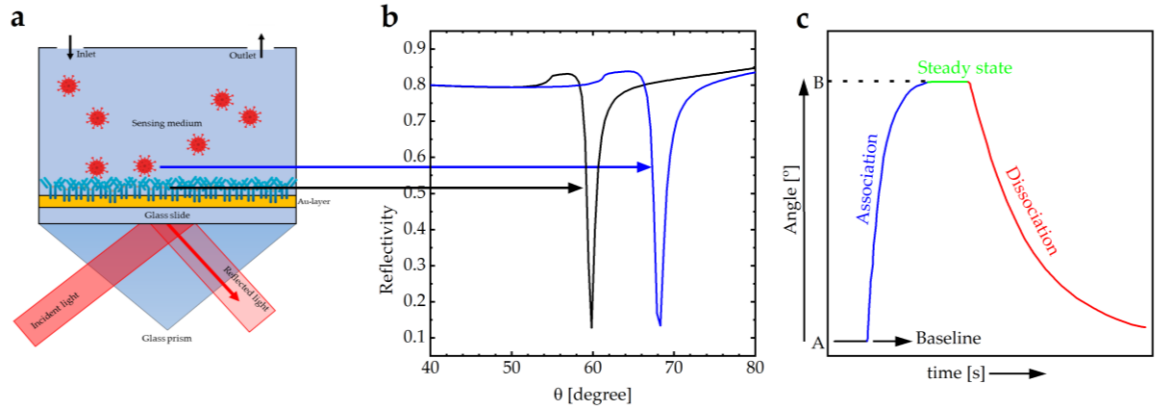

Figure 2.2: (a) 2D illustration of the SPR sensor, **(b)** corresponding SPR reflectivity curve for Kretschmann's configuration, and **(c)** The resonance angle changes as a function of time.

2.4. Mathematical Effective Medium Model

The effective medium model of the SPR sensor treats the adsorbed molecules on the sensor surface as an effective medium with an effective refractive index and thickness (Figure 2.3a). When light penetrates the metal layer along the z-axis, *p*-polarized SPR waves are generated at the metal/dielectric media interface. The SPR phenomenon is described using Maxwell's equations as follows:

$$E_i(\vec{r},t) = (E_{ix}, 0, E_{iz})\left[e^{-|Z|k_{iz}} e^{i(xk_{ix}-\omega t)}\right] \tag{2.13}$$

$$H_i(\vec{r},t) = (0, H_{iy}, 0)\left[e^{-|Z|k_{iz}} e^{i(xk_{ix}-\omega t)}\right] \tag{2.14}$$

where: ω is the frequency, E is the electric field vector, H is the magnetic field vector, k_{iz} and k_{ix} are the z and x wave vector components. Applying the continuity conditions,

$$k_{iz} = \sqrt{\varepsilon_i \left(\frac{\omega}{c}\right)^2 - k_{ix}^2} \tag{2.15}$$

and,

$$\frac{k_{z1}}{\varepsilon_m} H_{1y} + \frac{k_{z2}}{\varepsilon_d} H_{2y} = 0 \tag{2.16}$$

$$H_{1y} - H_{2y} = 0 \tag{2.17}$$

When the determinant is equal to zero,

$$k_{z1}\varepsilon_d + k_{z2}\varepsilon_m = 0 \tag{2.18}$$

At $k_{x1} = k_{x2} = k_x$, the expression becomes:

$$k_x = \frac{\omega}{c}\sqrt{\frac{\varepsilon_m \varepsilon_d}{\varepsilon_m + \varepsilon_d}} \tag{2.19}$$

Equation (2.19) represents the SPW vector $k_x = k_{sp}$, illustrating the surface plasmon generation. ε_m and ε_d are the dielectric constants of the metal and dielectric layers. The

transfer matrix method is used to investigate the reflectivity curve of the N-layer Kretschmann configuration model as follows (Maurya et al., 2015),

$$\begin{pmatrix} U_1 \\ V_1 \end{pmatrix} = M \begin{pmatrix} U_{N-1} \\ V_{N-1} \end{pmatrix} \tag{2.20}$$

where: (U_1, V_1) and (U_{N-1}, V_{N-1}) are the boundary terms of the 1st and Nth layers of electromagnetic fields. Equation (2.21) represents the characteristic matrix (Maurya et al., 2015),

$$\prod_{K=2}^{N-1} M_k = \begin{pmatrix} M_{11} & M_{12} \\ M_{21} & M_{22} \end{pmatrix} \tag{2.21}$$

where:

$$M_k = \begin{pmatrix} \cos\beta_k & -\frac{i\sin\beta_k}{q_k} \\ -iq_k\sin\beta_k & \cos\beta_k \end{pmatrix} \tag{2.22}$$

$$q_k = \frac{\sqrt{\varepsilon_k - n_1^2\sin\theta_1^2}}{\varepsilon_k} \tag{2.23}$$

$$\beta_k = \frac{2\pi d_k}{\lambda}\left(\sqrt{\varepsilon_k - n_1^2\sin\theta_1^2}\right) \tag{2.24}$$

where: d_k is the thickness of the k_{th}-layer, θ_1 and λ are the incident angle and wavelength of the incident light. Subsequently, the complex reflection coefficient (r_p) is given by,

$$r_p = \left[(M_{11} + M_{12}q_5)q_1 - \frac{(M_{21}+M_{22}q_5)}{(M_{11}+M_{12}q_5)q_1} + (M_{21} + M_{22}q_5)\right] \tag{2.25}$$

The reflectivity (R_p) is obtained by,

$$R_p = |r_p|^2 \tag{2.26}$$

When the polarized light illuminates the Au layer through the glass prism, the light reflection varies by changing the incident angle until it reaches the minimum at the resonance angle (θ_R). Employing WINSPALL software, the resonance angle for prism/Au layer (50 nm)/water is ~59.5° (Figure 2.3b, black line). The reflectivity reaches the minimum at θ_R, indicating surface plasmon excitation when the *p*-polarized light interacts with the free electron of a metal film, resulting in free electron oscillations (Peterson et al., 2014). Assuming a molecular layer of PS (10 nm) deposited on the Au layer, the resonance angle increases to about 60.2° due to a variation in the refractive index of the media above the Au layer (Figure 2.3b, blue line). According to the effective medium model, the change in the reflectivity (ΔR) is related to the resonance angle shift ($\Delta\theta$) by (Jung et al., 1998; Shumaker-Parry et al., 2004),

$$\Delta R(\theta) = -\frac{dR(\theta)}{d\theta}\Delta\theta \tag{2.27}$$

where: $dR(\theta)/d\theta$ is the slope of the reflectivity as a function of angle shift (Figure 2.3c).

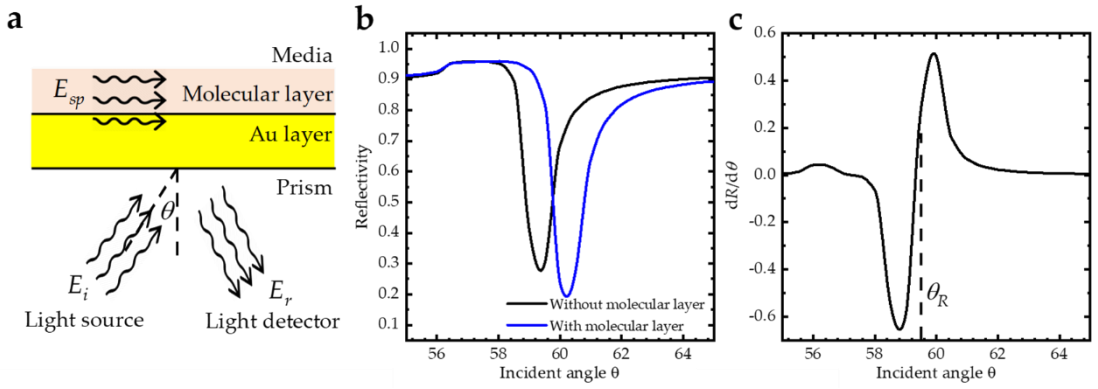

Figure 2.3: The effective medium model of the SPR sensor. **(a)** Schematic diagram of the effective medium model showing the setup. **(b)** SPR reflectivity curves, with the black line representing the curve without a 10 nm thick polystyrene film and the blue line representing the curve with this film, were calculated using Fresnel's equations. **(c)** The slope of the reflectivity curve indicates the sensitivity.

2.5. WF-SPRM Instrument

This section focuses on optimizing the key parameters for constructing a high-efficiency WF-SPRM system. Initially, red to near-infrared (NIR) light (wavelength range: 600-800 nm) was validated for generating a strong SPR signal. The red light efficiently excites maximum surface plasmon polaritons (SPPs) due to the strong coupling between photons in this wavelength range and the surface electrons of the gold layer under momentum matching. This coupling pulls electrons along the gold surface, producing the SPR effect (Novotny et al., 2012). Hence, selecting an SPR microscope with a laser wavelength within the 600-800 nm range is ideal for gold and silver layers, as it provides a smaller SPR angle and greater SPR signal and sensitivity compared to other wavelength ranges (Halpern et al., 2014). Figure 2.4 presents the schematic diagram of the home-built WF-SPRM experimental setup based on Kretschmann's configuration (Kretschmann, 1971). The red-light laser diode HL6750MG (Thorlabs GmbH, Germany) with a 685 nm wavelength illuminates the gold layer through a glass prism (SF10, n=1.725, Eksma Optics, Lithuania) with four polished sides measuring $20.0 \times 25.0 \times 16.3$ mm^3, with an angle of $56° \pm 5°$ at a fixed incidence angle (Figure 2.5). The choice was made for a glass prism with a high refractive index (n=1.725) to enable a larger internal incident angle and consequently allow the incident light to reach the critical angle for total internal reflection at the prism-metal interface (Rothenhäusler et al., 1988). An objective lens (Canon Compact-Macro Lens EF 50 mm 1:2.5) coupled to a video camera equipped with a CMOS chip (MT9P031) featuring a resolution of 5 Mp and a pixel size of 2.2×2.2 μm^2 is used for imaging the gold surface. The high numerical aperture (NA) objective ($NA > 1.4$) effectively couples the illumination and imaging optics (Huang et al., 2007).

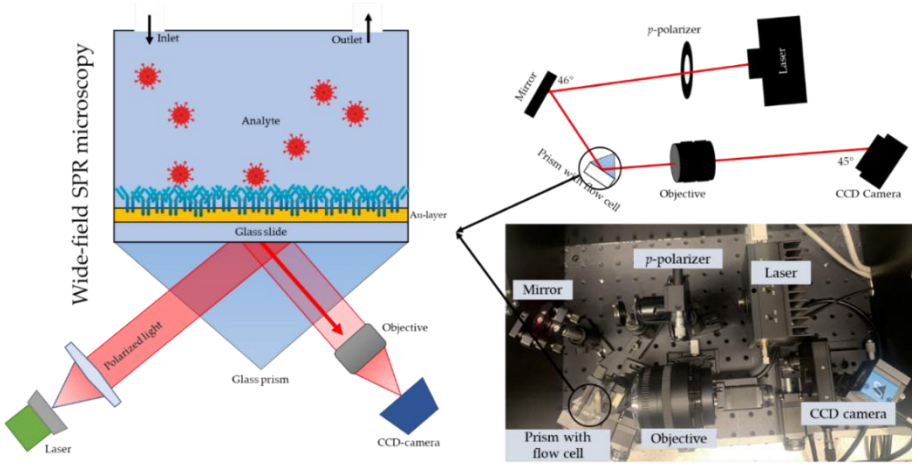

Figure 2.4: Schematic diagram of the experimental design of WF-SPRM based on Kretschmann's configuration.

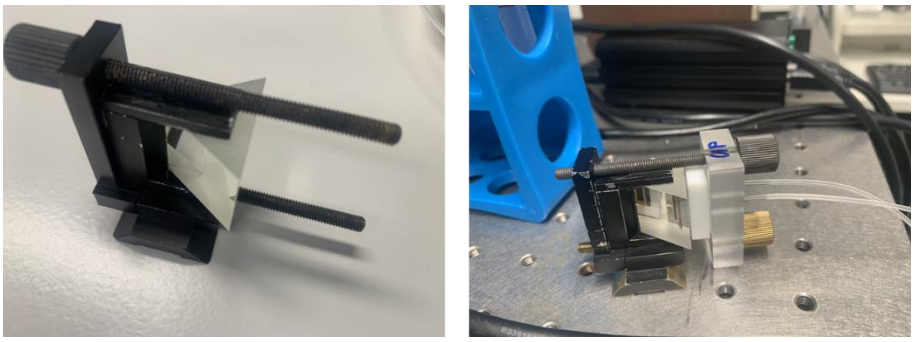

Figure 2.5: SF10 Glass prism.

2.6. Metal-Sensor Substrate Preparation

Before depositing the gold layer onto the glass substrate, it is essential to apply a titanium interlayer (Ti) to enhance the adhesion between the gold/silver and the glass surface. The stable titanium layer should have a minimum thickness of approximately 3-5 nm. Therefore, a Ti layer with a thickness of 5 nm and a complex refractive index of ($n = 2.6112 + 0.1532\, i$) is considered in the calculations (Johnson et al., 1974).

Kretschmann's configuration of the prism-Ti(5 nm)-Au/Ag(various thicknesses from 20 to 60 nm) system is simulated to optimize the thickness for strong SPP excitation (Figure 2.6). In this section, the minimum reflectivity ($R_{\min}$) is considered to optimize the thickness of the gold and silver layers. For the gold-sensor substrate, glass substrates were coated with a titanium layer (5 nm)/ gold layer (45 nm) (Innolume), which is accepted with A. Zybin et al. study (Zybin et al., 2017). On the other hand, for silver-sensor substrate, glass substrates were coated with a titanium layer (3 nm)/ silver layer (50 nm) (Platypus technologies).

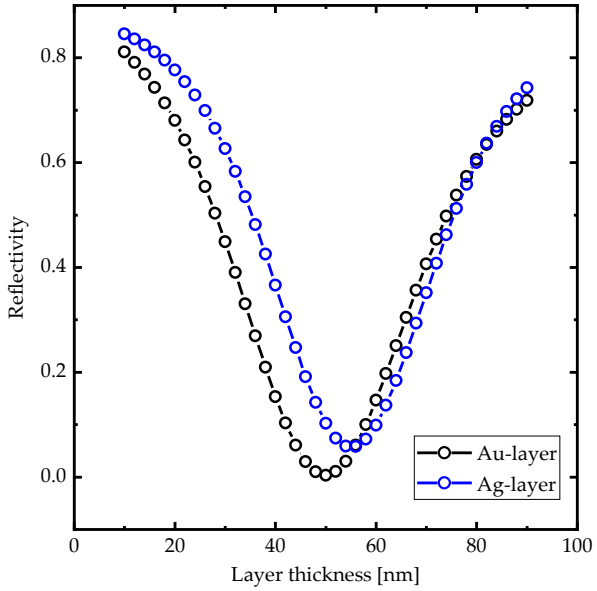

Figure 2.6: Calculated response of R_{min} of the SPR curves as an Au- and Ag layers thickness.

Accordingly, SF10 polished glass slides with a refractive index matching the glass prism ($n = 1.725$) were procured from Helma Optics (Germany). Subsequently, these glass slides were coated with a titanium adhesive layer, measuring 5 nm in thickness, followed by a 41-45 nm gold layer ($n = 0.15, k = 4.91$) using a magnetron-sputtering technique (Innolume, Dortmund, Germany). On the other hand, SF10 polished glass slides were coated with a titanium adhesive layer, measuring 3 nm in thickness, followed by a 50 nm silver layer ($n = 0.05, k = 3.90$) (Platypus technologies).

The sensor substrates were cut into small plates to fit the sizes of the flow cell (Figure 2.7a). The cutting process was performed using a diamond cutter and a designed steel plate (Figure 2.7b, c). These plates have a size of 13 × 9 mm. A careful cleaning procedure was performed before employing the gold/silver-sensor substrates in SPR imaging. A meticulous cleaning procedure was performed before employing the gold-sensor substrate in SPR imaging. The substrate is immersed in a piranha solution for 5 minutes. The piranha solution is prepared by slowly adding 30 mL of sulfuric acid (Sigma-Aldrich) to 10 mL of hydrogen peroxide (VWR chemicals) at 4 °C due to the exothermic nature of the reaction. Subsequently, the gold-sensor substrates are thoroughly rinsed with distilled water and absolute ethanol (99.85%) to eliminate any residual piranha solution and then dried using argon gas.

Following the cleaning process, the gold-sensor substrate is precisely positioned on the base of the glass prism using RI matching immersion liquid (2 µL, Cargille Laboratories via VWR, $n = 1.725$) to ensure there is no air gap between the gold-sensor substrate and the prism (Figure 2.7d). To prevent liquid leakages, a polydimethylsiloxane (PDMS, Sigma-Aldrich) gasket is placed between the gold-sensor substrate and the Teflon flow cell (Figure 2.7e).

Subsequently, the 0.51 mm thick Teflon flow cell with an average flow rate of 300 µL/minute is securely sealed to the gold-sensor substrate (Figure 2.7f). Additionally, the flow rate is directed from down to up to avoid any formation of liquid bubbles.

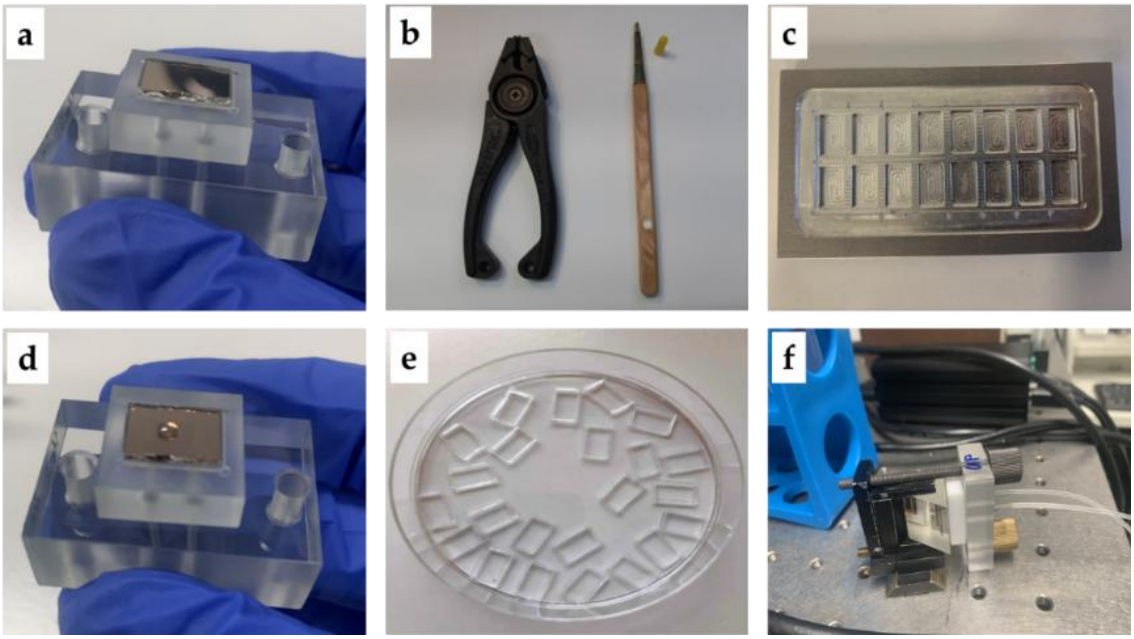

Figure 2.7: Gold-sensor substrate preparation **(a)** fitted gold-sensor substrate to the sizes of the flow cell, **(b)** diamond cutter, **(c)** wafer cleaving pliers, **(d)** using RI matching immersion liquid, **(e)** PDMS gaskets, and **(f)** the final gold-sensors substrate connected to glass prism and flow cell.

2.7. Experimental Procedure

Polystyrene nanoparticles (PSNPs) and silica nanoparticles (SilicaNPs) are employed as the primary examples for WF-SPRM measurements. The nanoparticles have an average diameter between 100-400 nm. In this chapter, polystyrene nanoparticles (PSNPs) with an average diameter of 200 nm and a refractive index of $n = 1.59$ are employed as the primary example (Figure 2.8). To improve the adsorption of PSNPs and SilicaNPs to the sensor surface, an aluminum hydroxide chloride layer is deposited on the gold substrate by applying 150 µL of the solution and allowing it to sit for 10-30 minutes at room temperature. Subsequently, the gold substrate is washed with distilled water and dried using argon gas. Additionally, biological nanoparticles can be immobilized on the sensor surface by coating it with corresponding antibodies. To prepare the nanoparticles stock solution, 0.1 g of nanoparticles are mixed with 0.3% sodium chloride in 1.0 L of filtered distilled water at room temperature for 2 hours. Before introducing the nanoparticle stock solution into the sensor cell, a sodium chloride buffer solution (NaCl, 0.3%) passes through the cell for 1-2 minutes. Subsequently, the nanoparticle stock solution is injected into the sensor cell. Under optimal ionic strength

conditions, experiments at flow rates in the range of 60−673 µL/min for silicaNPs and PSNPs were performed (Kuzmichev et al., 2018).

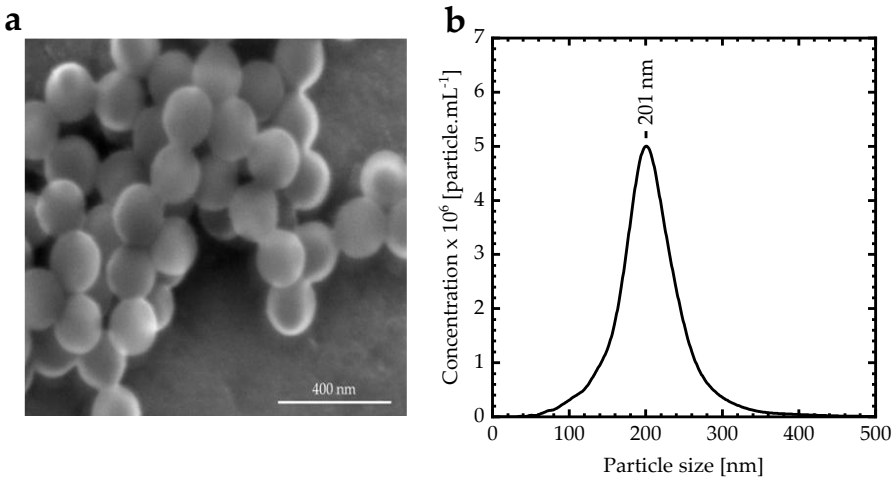

Figure 2.8: Polystyrene nanoparticles (PSNPs) characterizations **(a)** SEM micrograph and **(b)** Nanoparticle tracking analysis.

2.8. WF-SPRM Data Analysis

The data analysis in WF-SPRM is based on observing the perturbation in the propagation conditions of surface plasmons caused by nano-objects adsorption. WF-SPRM allows visualization of optical patterns resulting from the scattering of surface plasmon waves. When a particle binds to the sensor surface, it disturbs the evanescent field of the surface plasmon wave, leading to local changes in reflectivity, manifesting as a spot in the image (Yu et al., 2014). ImageJ software is employed to determine the detection signal associated with the nanoparticle binding event (Rasband, 1997-2018). The image processing passes through four stages using Image J software (Rasband, 1997-2018): a raw image, removing background, generated particle candidates, and finally, particle analysis, including time dependence of particle detection to observe the binding events (Figure 2.9) (Libuschewski, 2017; Siedhoff, 2016). The signal intensity increases suddenly at the center of the binding event. The intensity of the scattering waves surrounding the particle is gradually decreasing from the centre outwards (Figure 2.9d).

After the particle is bound to the metal surface, the evanescent field of the SPWs is disturbed due to scattering with a particle (Yu et al., 2014). Localized variations in reflectivity caused by the deformation of the SPWs' evanescent field result in a bright spot in the image that is surrounded by concentric surface plasmon waves, as discussed in (Valle et al., 1997) (Figure 2.9d). The WF-SPRM data is collected as a matrix of pixel intensity at successive time points, allowing for analysis of the time-dependent relative intensity before and after particle binding on the sensor surface (Figure 2.9d). The intensity shows low values before PSNPs

bind to the sensor surface. However, at approximately 36 seconds, the local intensity increases, indicating the moment when PSNPs are bound to the surface.

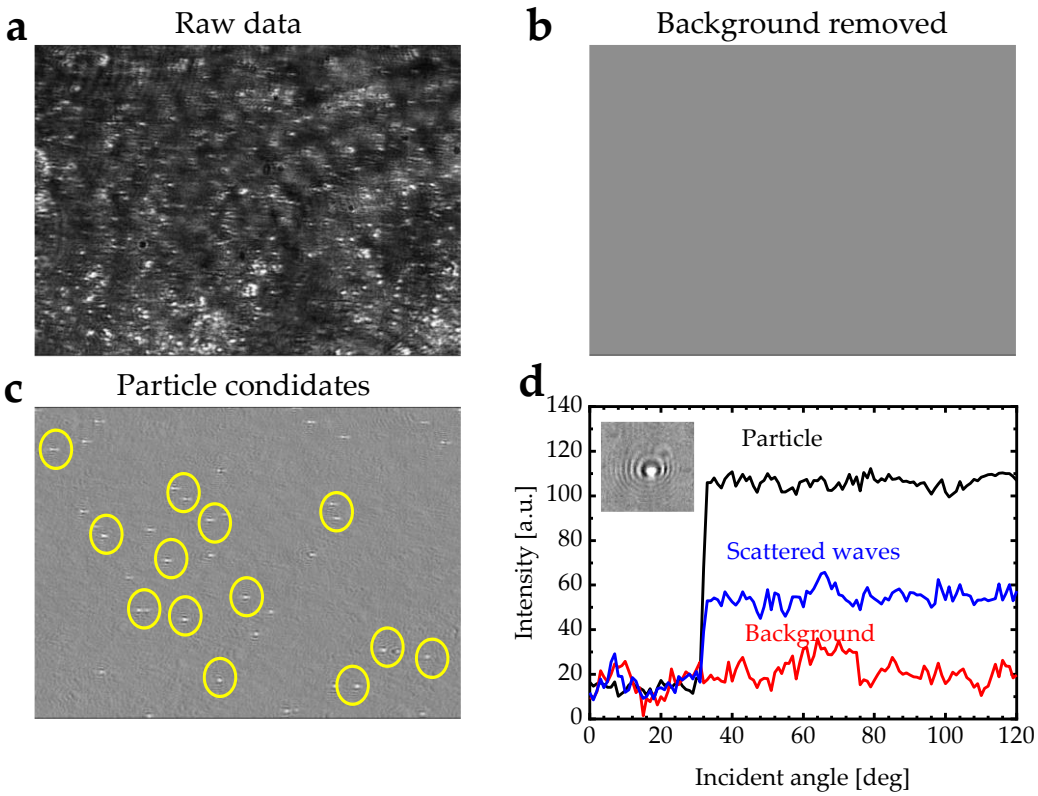

Figure 2.9: The image processing passes through four stages: **(a)** a raw image, **(b)** removing background, **(c)** generating particle candidates, and **(d)** and finally, particle analysis; particle analysis includes time dependence of particle detection.

2.9. WF-SPRM Results: Silver versus Gold

The WF-SPRM measurements for silicaNP with different sizes, 100, 200, and 300 nm, detected by Au and Ag layers were performed at the same conditions, including laser wavelength and resonance angle optimization to compare the SPR sensitivity of Au and Ag layers. The time dependence of the local intensity of silicaNP with different sizes, 100, 200, and 300 nm, detected by Au and Ag layers, was measured three times, and the average value is illustrated in Figure 2.10a. The magnitude of the intensity step is proportional to the size of the detected particles. Additionally, the intensity step magnitude of silicaNP detected by the Ag layer is higher than the silicaNP detected by the Au layer.

The WF-SPRM experimental results show that two parameters affect the signal intensity, the first being the metal sensor surface type. The signal intensity of the 100 silicaNP detected by the Au layer is about 79 a.u., whereas the signal intensity of 100 silicaNP detected by the Ag layer is about 226 a.u. (Figure 2.10b). This can be attributed to the changing in overlap

between the adsorbed particle and the evanescent field. In addition, the second parameter is the optical particle size, where the signal intensity of silicaNP detected by the Au layer increases from about 79 a.u. to about 204 a.u. as silicaNP size increases from 100 to 300 nm. On the other hand, the signal intensity of silicaNP detected by the Ag layer increases from about 226 a.u. to about 373 a.u. as silicaNP size increases from 100 to 300 nm. The signal intensity for silicaNP detected by Au and Ag layers can be fitted by a straight line between 100 and 300 nm, indicating the fundamental difference between the Mie scattering, which would result in a quadratic intensity dependence and the signal-generating method.

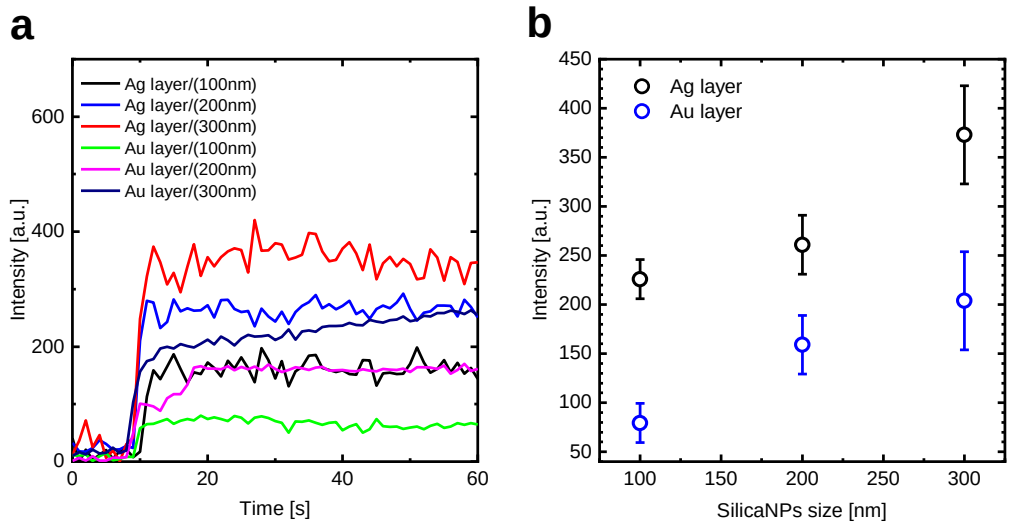

Figure 2.10: WF-SPRM results: silver versus gold. (a) The time dependence of the local intensity of silicaNP with different sizes, 100, 200, and 300 nm, was detected by Au and Ag layers. **(b)** Experimental intensity of detected silicaNP by Au and Ag layer as a function of silicaNP size.

2.10. Coating metal layer with a dielectric layer

Coating the metal layer with a dielectric layer is a highly effective modification to enhance the sensitivity of the SPR sensor (Menegazzo et al., 2011; Yılmaz et al., 2017). In this section, the refractive index, extinction coefficient, and thickness of the dielectric layer are optimized to achieve improved sensitivity. Initially, the sensitivity enhancement resulting from the metal coating with a dielectric layer is explained (Mudgal et al., 2020). The propagation constant (β_{ev}) can characterize the propagation of evanescent waves and given by Equation (2.28) (Anower et al., 2021),

$$\beta_{ev} = \frac{2\pi}{\lambda_{light}} n_{prism} \sin\theta \tag{2.28}$$

Here, n_{prism} and θ represent the refractive index of the prism and the incident light angle at the metal surface, respectively, and λ_{light} is the light wavelength. Additionally, the

propagating constant of the surface plasmon wave for the SPR sensor with a single metal layer and sensing medium is given by Equation (2.29) (Anower et al., 2021),

$$\beta_{SPW} = \frac{2\pi}{\lambda_{light}} \sqrt{\frac{n_{metal}^2 n_{sm}^2}{n_{metal}^2 + n_{sm}^2}} \tag{2.29}$$

Here, n_{metal} and n_{sm} represent the refractive indices for metal and sensing medium, respectively. Equations (2.28) and (2.29) can be connected to get the resonance SPR angle as,

$$\theta_{SPR} = \sin^{-1}\left(\frac{1}{n_{prism}} \sqrt{\frac{n_{metal}^2 n_{sm}^2}{n_{metal}^2 + n_{sm}^2}}\right) \tag{2.30}$$

In addition, by coating the metal surface with a dielectric layer of refractive index ($n_{dielectric}$) in the SPR sensor changes the SPR angle equation to (Akib et al., 2021),

$$\theta_{SPR} = \sin^{-1}\left(\frac{1}{n_{prism}} \sqrt{\frac{n_{metal}^2 n_{dielectric}^2 n_{sm}^2}{n_{metal}^2 + n_{dielectric}^2 + n_{sm}^2}}\right) \tag{2.31}$$

The sensitivity of SPR sensors (S) is calculated by $S = \Delta\theta/\Delta n$, where: $\Delta\theta$ is the SPR angle shift, and Δn is the refractive index change. As seen in Equation (2.31), the effect of the increasing effective refractive index on the SPR angle shift can be analyzed. As shown in Figure 2.11a, increasing the refractive index value of the dielectric layer increases the SPR angle. The linear fit of the SPR angle shifts as a function of refractive index changes, representing the sensitivity of the SPR sensor (Figure 2.11b). The sensitivity and detection accuracy (DA = 1/LW), with LW is the linewidth of the reflectivity curve, of the SPR sensor of the prism-Ti-gold system is 119.5 deg.RIU^{-1} and 0.70 deg.$^{-1}$, respectively. Coating the gold layer with a dielectric layer with a refractive index lower than 1.8 decreases the sensitivity and DA. However, increasing the refractive index above 1.8 significantly increases the SPR sensor sensitivity (Figure 2.11). In contrast, the detection accuracy decreases continuously with increasing refractive index of the dielectric layer due to the concomitant increase in the line width of the SPR signal.

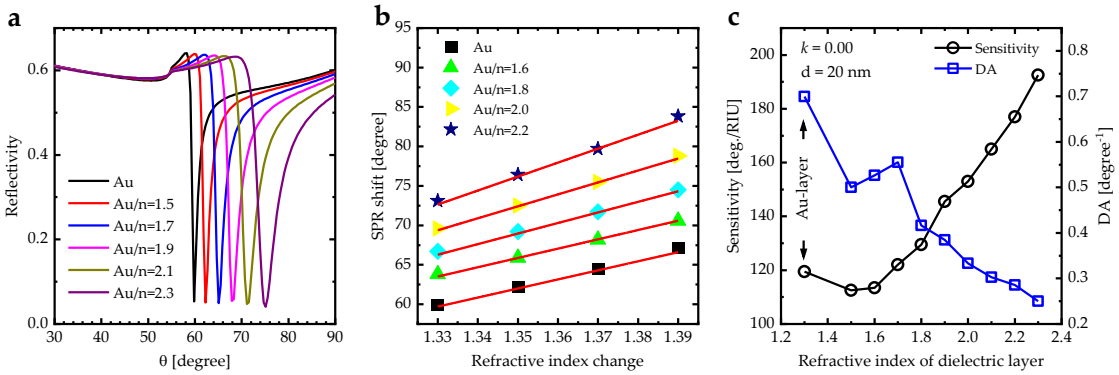

Figure 2.11: (a) SPR reflectivity curve for Kretschmann's configuration of the prism-Ti-gold-dielectric system for selected refractive indices of a dielectric layer, **(b)** SPR angle shift versus the refractive index change of selected refractive indices of a dielectric layer, and **(c)** Sensitivity and DA variation as a function of refractive indices of a dielectric layer of prism-Ti-gold- dielectric system.

The effect of extinction coefficient and thickness variation is also studied to optimize the dielectric layer coated with the Au-layer to get higher sensitivity (Figure 2.12). The sensitivity does not depend on the extinction coefficient value. However, an increase in the extinction coefficient value of the dielectric layer decreases the detection accuracy (Figure 2.12a). Therefore, it is concluded that the lower extinction coefficient with a higher refractive index of the dielectric layer is considered a target for coating the Au-layer to get higher sensitivity with an acceptable detection accuracy of SPR sensors. In addition, to achieve high sensitivity with an acceptable detection accuracy for SPR sensors, the thickness of the dielectric layer should be in the range of 15-20 nm (Figure 2.12b).

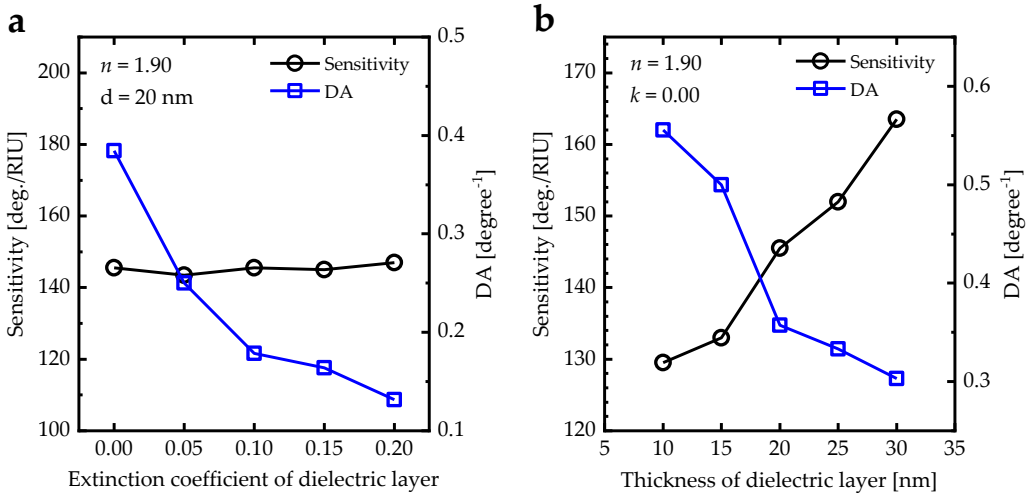

Figure 2.12: Sensitivity and DA variation as a function of **(a)** extinction coefficient and **(b)** thickness of a dielectric layer of prism-Ti-gold- dielectric system.

Subsequently, PSNPs were employed as an example for real-time measurements in two systems: prism/Ti(5 nm)/Au(45 nm) and prism/Ti(5 nm)/Au(45 nm)/dielectric($n = 1.9, k = 0.01, 20\ nm$). The signal-to-noise ratio (S/N) and the linewidth in the line profile plot for three individually bound PSNPs to the surface are calculated to investigate the efficiency of the SPR sensor (Figure 2.13). The signal-to-noise ratio of the prism/Ti(5 nm)/Au(45 nm)/dielectric($n = 1.9, k = 0.01, 20$ nm) system is 265, which outperformed that of the prism/Ti(5 nm)/Au(45 nm) system (S/N = 150), thereby confirming our theoretical findings.

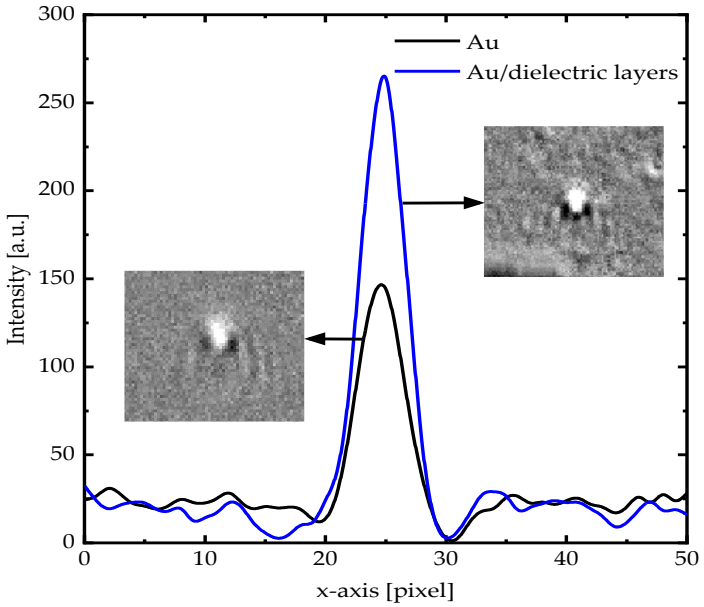

Figure 2.13: Line profile plot of PSNPs detected by Au layer and Au/n=1.9 layers.

2.11. Characterizations of Dielectric Layers

Before we proceed to the following chapters, the characterization techniques for the dielectric layers are presented to understand the importance of each technique. The chemical structure and composition of the conductive polymer composite, as well as the polyelectrolyte brushes, are investigated using Fourier transform infrared spectroscopy, nuclear magnetic resonance spectroscopy, and X-ray photoelectron spectroscopy. For instance, these spectroscopic techniques are used to investigate the binding between the polymer and the fillers, as well as investigate the binding between the polyelectrolyte brushes and the gold through the thiolated group. Additionally, the morphological structure of the dielectric layers is examined using a scanning electron microscope and atomic force microscope. For instance, the switchable process between collapsed form and stretched form of polyelectrolyte brushes is investigated using an atomic force microscope.

Based on the discussion in the previous section, Coating the metal layer with a high refractive index dielectric layer yields high SPR sensor sensitivity. Therefore, the refractive index of the dielectric layer is investigated by analyzing the transmittance and reflectance spectra that are measured using UV-Vis spectroscopy.

2.11.1. Fourier transform infrared spectroscopy (FTIR)

Infrared (IR) spectroscopy is one of the most well-known and widely used spectroscopic methods due to its usefulness in determining and identifying compounds' structures. It is used to determine functional groups in molecules. The chemical properties of the synthesized

films were investigated by studying the vibrational bands obtained from FTIR spectrometers (Bruker VERTEX 80/80v Vacuum FTIR Spectrometers) in the spectral range of 4000-400 cm^{-1} at ambient conditions.

2.11.2. Nuclear magnetic resonance spectroscopy (NMR)

Nuclear magnetic resonance (NMR) spectroscopy is a spectroscopic technique used to study molecular structure by examining the interaction of an oscillating radio-frequency electromagnetic field with nuclei in an external magnetic field. An NMR spectrum can provide detailed information about molecular structure and dynamics, information that is difficult to obtain by any other method. The chemical properties of the synthesized films were investigated using ^{1}H NMR measurements (600.13 MHz, Bruker AVANCE III NMR spectrometer). ^{1}H NMR measurements were conducted at 600.13 MHz using A 5 mm high-resolution multi-channel and broadband (5 mm BBO model) equipped with Z-gradient.

2.11.3. X-ray photoelectron spectroscopy (XPS)

X-ray photoelectron spectroscopy (XPS) is a surface-sensitive quantitative spectroscopic technique based on the photoelectric effect that can identify the elements within a material, their chemical state, and the overall electronic structure and density of the electronic states in the material. The near ambient pressure X-ray photoelectron spectroscopy (NAP-XPS) measurements were performed at pressures of 1 mbar and room temperature.

2.11.4. X-ray diffraction (XRD)

X-ray diffraction (XRD) is a characterization technique used to investigate and quantify the crystalline nature of materials based on the X-ray diffraction from the atom planes within the materials. Powder X-ray diffraction (XRD) is a universal characterization technique for thin films and nanomaterials (Debye et al., 1916). Powder XRD analysis provides essential information about the crystal structure of the nanomaterials, such as phase identification, degree of crystallinity, crystallite size, microstructure, mechanical properties, morphology, and sample purity. The crystal structure of the films was investigated using powder X-ray diffraction (XRD, Malvern Panalytical Ltd.) by $CuK\alpha_1$ ray ($\lambda = 0.1540598$ nm) in angles range of 10°-70° with a step of 0.02°.

2.11.5. Scanning electron microscope (SEM)

The SEM is a tool for creating images of the otherwise invisible worlds of micro-space (1 micrometer = 10^{-6}m) and nano-space (1 nanometer = 10^{-9}m). SEMs can magnify an object from about 10 times up to 300,000 times. A scale bar is usually provided on an SEM image. The

scale bar is used to calculate the sizes of features in the image. The film morphology was investigated using a scanning electron microscope (SEM, FEI Quanta FEG 450).

2.11.6. Atomic force microscope (AFM)

The Atomic Force Microscope (AFM) scans a probe across a sample surface. The AFM probe consists of a sharp tip at the end of a flexible cantilever that protrudes from a holder plate called a holder chip. The tip is typically pyramidal or conical in shape and is four to five μm in height with a diameter at the apex of 10 to 20 nm, and is positioned at the end of a cantilever, which is typically 100 to 200 μm long. Either the probe or sample is mounted on a piezoelectric scanner, which can move in the x, y, and z directions, and is used to raster scan the probe across the sample surface to acquire an image in 3 dimensions. The film morphology was investigated using atomic force microscopy (AFM) (SPM SmartSPM™-1000).

2.11.7. Thermogravimetric analysis (TGA)

Thermal analysis measures physical or chemical changes in a material as a function of temperature**.** Thermogravimetric analysis continuously measures the weight of a sample as a function of temperature and time. The thermal stability was measured using thermogravimetric analysis (TGA) (NETZSCH Premier Technologies).

2.11.8. UV-Vis spectroscopy

The optical properties of films are defined as the changes in the light upon interacting with the films. Many factors influence the optical properties of the films, such as surface nature, film thickness, electronic structure, and the interface between the film and substrate and the film and air. Optical properties were investigated by analyzing transmittance and reflectance spectra measured using a UV–Vis spectrophotometer (Hitachi U-3900H) with a total internal sphere. These properties relate to the optical constants, such as refractive index and extinction coefficient.

2.11.9. Four-point probe

The 4-point probe contains four electrodes organized in an equidistant linear array. The electrical conductivity was measured by a 4-point probe (Microworld Inc.) connected with a high-resolution multimeter (Keithley 2450 Sourcemeter) for various temperatures from 298-328 K.

CHAPTER 3

3. WORK PUBLISHED IN THE CUMULATIVE THESIS

This cumulative thesis comprises seven full papers. The author of this thesis is the first author of all papers. The thesis is structured as follows:

3.1. Modeling and Analysis of Discrete Particle Detection

In (Al-Bataineh et al., 2024a), titled "Modeling and analysis of discrete particle detection in wide-field surface plasmon resonance microscopy," we focus firstly on designing the wide-field surface plasmon resonance microscope as well as optimizing the main parameters for building a highly sensitive wide-field surface plasmon resonance microscope, including laser wavelength, prism refractive index, the numerical aperture of the objective, and the gold layer thickness (Figure 3.1a). Additionally, the flow rate of the nanoparticle stock solution is determined through the particle transfer model (Figure 3.1b). After that, the enhancement of the detection measurements, as a result of signal-to-noise optimization, is demonstrated by applying different parameters for SPR detection. Following the measurements of the wide-field surface plasmon resonance microscope, the image processing is described (Figure 3.1c). Finally, the particle analysis, including the time dependence of particle detection, is presented (Figure 3.1d).

An effective medium model describes the surface plasmon resonance (SPR) sensor principle, treating molecules bound on the sensor surface as an effective medium with an effective refractive index and thickness (Figure 3.2a). On the other hand, a discrete particle model of SPR is introduced to describe the detection principle for discrete particles (Figure 3.2b). Theoretical, numerical, and experimental analyses are conducted to describe the intensity profiles of single and double nanoparticles from the discrete particle model. Finally, the influence of coating the gold layer with a dielectric layer on the SPR sensitivity is investigated for varying refractive indices.

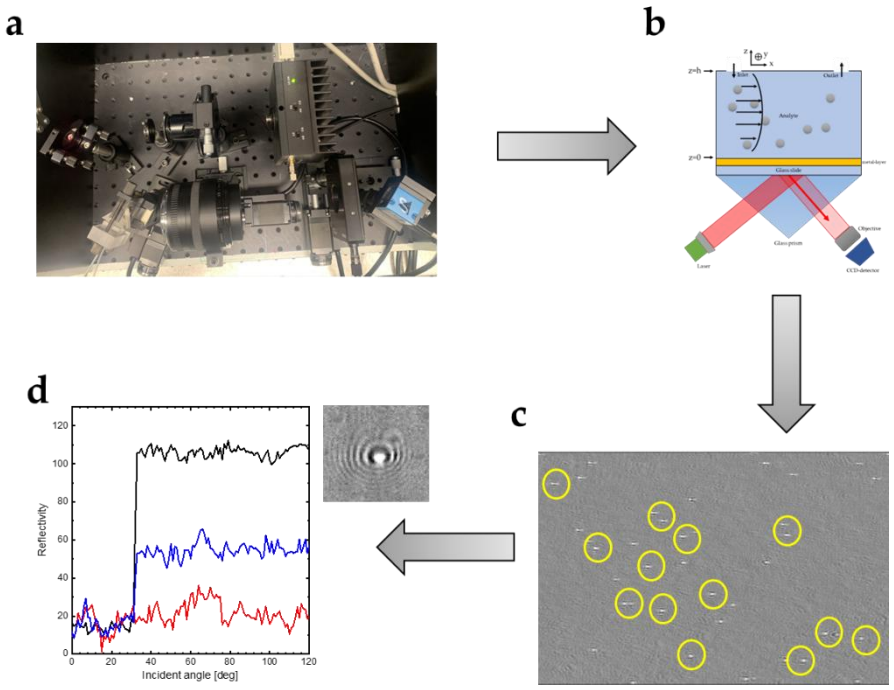

Figure 3.1: (a) The design of the wide-field surface plasmon resonance microscope. **(b)** Particle transfer model. **(c)** The image processing. **(d)** Particle analysis: particle analysis includes time dependence of particle detection.

Many models have been reported to help us understand discrete particle detection in the physics frame. All of these models were derived based on the scattering of the propagating surface plasmon waves by the detecting particle. In their models, some literature used fast Fourier transform imaging to fit the discrete particle detection (Ma et al., 2020; Yu et al., 2014; Yu et al., 2017). On the other hand, some literature used Green's function to fit discrete particle detection (Evlyukhin et al., 2005; Evlyukhin et al., 2015; Novotny et al., 1997).

However, in (Al-Bataineh et al., 2024a), we propose a new method for modeling and analysis of the discrete particle detection of WF-SPRM. Using the finite element method, we analyzed the resultant electric field from the scattering of the propagating surface plasmon waves by the detecting particle. The design and analysis of a proposed model for the SPR sensor are conducted using COMSOL Multiphysics. The calculated conditions of COMSOL Multiphysics are adjusted in the same way as the experimental conditions, with free triangular meshes and element size of 6.09×10^{-5} - 0.03 μm. After that, we fit the experimental data using the derived model based on the resultant electric field. From the fitting process, we can investigate many essential parameters for WF-SPRM measurements, including decaying constant and phase shift.

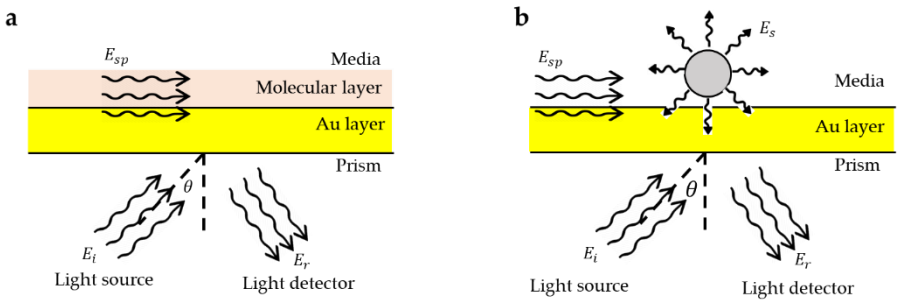

Figure 3.2: (a) An effective medium model of the surface plasmon resonance sensor. **(b)** A discrete particle model of the surface plasmon resonance sensor.

3.2. Improving the Sensitivity of WF-SPRM: Conductive Polymer

As discussed in Section 2.10, coating the metal layer with a dielectric layer is a highly effective modification to enhance the sensitivity of the SPR sensor (Menegazzo et al., 2011; Yılmaz et al., 2017). Many studies have been focused on using polyaniline nanocomposite films to enhance the sensitivity of the SPR sensor. For instance, (Usman et al., 2019c) have reported that the functionalization of the SPR sensor with the PANI/chitosan demonstrates an interesting application of the sensor for detecting a low concentration of acetone vapor. They proved that coating the gold layer with PANI/chitosan enhances the sensitivity of the conventional SPR sensor for acetone vapor. Additionally, in (Al-Bataineh et al., 2023c), we proved theoretically that coating the gold layer with nano-SnO_2/polyaniline composite films enhances the sensitivity of the SPR sensor.

To the best of our knowledge, before (Al-Bataineh et al., 2022), titled "Surface Plasmon Resonance Sensitivity Enhancement Based on Protonated Polyaniline Films Doped by Aluminium Nitrate," there was no attempt to investigate the enhancement of the WF-SPRM sensitivity using conjugated polymer nanocomposite films. In our study, we enhanced the sensitivity of the discrete particle imaging of WF-SPRM by coating the gold layer with polyaniline/aluminum nitrate nanocomposite films. The sensitivity of the WF-SPRM was investigated using a theoretical approach and experimental measurements.

The modeling (simulation) of SPR measurements confirmed that the inclusion of growing concentrations of aluminum nitrate in polyaniline/aluminum nitrate nanocomposite films enhances the sensitivity of the sensor. Additionally, the experimental results confirmed that coating the cold layer with polyaniline/aluminum nitrate nanocomposite film increases the signal-to-noise ratio, which means an increase in sensor sensitivity.

3.3. Improving the Sensitivity of WF-SPRM: Polyelectrolyte Brushes

Polyelectrolyte brushes (PEBs) are charged poly acids or bases grafted to the substrate surface. To the best of our knowledge, before our work, there was no attempt to investigate the enhancement of the WF-SPRM sensitivity using polyelectrolyte brushes.

Coating the metal layer with a dielectric layer is a highly effective modification to enhance the sensitivity of the SPR sensor (Menegazzo et al., 2011; Yılmaz et al., 2017). As mentioned in Section 2.10, coating the metal layer with a dielectric layer with a high refractive index and low extinction coefficient is considered a target for coating the metal layer to get higher sensitivity with an acceptable detection accuracy of SPR sensors. Additionally, several researchers have stated that the proteins bind to PEBs even when they have the same net charge (Ballauff et al., 2006).

Here, we investigate the influence of coating the gold/silver layer with polyelectrolyte brushes with varying refractive indices on the SPR sensitivity (Figure 3.3). Different polyelectrolyte brushes, like polyacrylic acid (PAA), polyethylene oxide - polyacrylic acid (PEO/PAA), and polyacrylic acid/iodine (PAA/I_2), are used to validate the enhancement of the SPR sensitivity. Validation experiments are performed using polystyrene and silica nanoparticles of varying sizes.

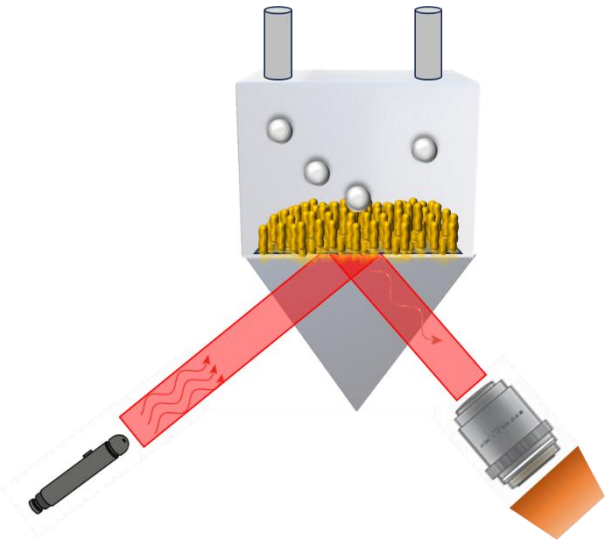

Figure 3.3: Wide-field surface plasmon resonance microscope based on polyelectrolyte brushes.

(Al-Bataineh et al., 2023a), titled "Switchable Polyacrylic Acid Polyelectrolyte Brushes for Surface Plasmon Resonance Applications," presented wide-field surface plasmon resonance microscope sensors based on a gold layer coated with polyacrylic acid polyelectrolyte brushes (PAA PEBs) to enhance the sensitivity of nanoobject detection. Firstly, the switching behavior of the PAA PEBs against changes in the pH values was investigated by analyzing the chemical, morphological, optical, and electrical properties. After that, the sensitivity of the SPR sensing device was investigated using a theoretical approach, as well as experimental measurements. Finally, we concluded that coating an Au-layer with PAA PEBs enhances the sensitivity of the SPR sensing device and improves the spatial resolution of the recorded image.

(Al-Bataineh et al., 2024b), titled "Wide-field surface plasmon resonance microscope based on polyethylene oxide/polyacrylic acid brushes", presented a wide-field surface plasmon resonance microscope (WF-SPRM) based on polyethylene oxide/polyacrylic acid (PEO/PAA) polyelectrolyte brushes (PEBs) for particle detection application. Morphological, chemical, and crystal structural analyses confirm that the PEO/PAA brushes undergo a transition from a collapsed to a stretched state as the solvent pH is increased from 1 to 10. Theoretical and experimental approaches study the sensitivity of WF-SPRM utilizing Au-(PEO/PAA) polyelectrolyte layers. We concluded that coating an Au-layer with PEO/PAA PEBs enhances the sensitivity of the SPR sensing device and improves the spatial resolution of the recorded image. Finally, the discrete particle model is presented to describe the discrete particle detection by WF-SPRM, demonstrating a good agreement between the calculated intensity profile and experimental data.

The silver-based sensor has superior accuracy and a sharp resonance curve, which provides a stronger contrast than the gold sensor (Srivastava et al., 2020). Therefore, in (Al-Bataineh et al., 2024c), titled "Developing surface plasmon resonance imaging for discrete particle detection based on a silver layer coated with polyacrylic acid/iodine polyelectrolyte brushes," we presented a wide-field surface plasmon resonance microscope (WF-SPRM) based on a silver layer coated with polyacrylic acid/iodine (PAA/I_2) polyelectrolyte brushes (PEBs) for particle detection application. The PAA/I_2 PEBs were used as a coating for the Ag layer to overcome silver oxidation and improve the WF-SPRM's sensitivity (Karki et al., 2022; Meradi et al., 2022). Our results provide insight into the enhancement of sensitivity and capabilities of WF-SPRM for discrete particle detection across a range of biomedical applications. Additionally, we present a mathematical model for SPR detection of discrete particles. The proposed model aligned with a curve fitting process to describe the SPR sensing profile for adsorbed particles in discrete particle detection. The calculated intensity profiles for the silicaNP with different sizes by Ag layer and Ag-PAA/I_2 layers describe the experimental profile well, supporting the validity of the model we deduced.

3.4. Surface Plasmon Coupling Between LSPs and PSPs

Finally, the surface plasmon coupling behavior between the localized surface plasmons (LSPs) of different shapes and sizes of metal nanostructures and the propagating surface plasmons (PSPs) of the metal surface is investigated by employing experimental, simulation, and theoretical approaches. To the best of our knowledge, before our work, there was no attempt to investigate the surface plasmon coupling behavior between the localized surface plasmons (LSPs) of the nanostructures and the propagating surface plasmons (PSPs) of the metal surface.

In (Al-Bataineh et al., 2023b), titled "Surface plasmon coupling between wide-field SPR microscopy and gold nanoparticles," the coupling behavior of the wide field surface plasmon microscopy (WF-SPRM) with single-, two-, and multiple-gold nanoparticles (AuNPs) with different AuNPs sizes is investigated using theoretical, simulation, and experimental approaches. A discrete particle model of SPR is used to understand the interaction between an Au-layer and a single AuNP and double AuNPs. Finally, it is demonstrated that plasmonic multiple particle scattering can be represented by an effective media, which is described by Maxwell-Garnet equations.

(Al-Bataineh et al., 2024d), titled "Surface Plasmon Coupling Between Different Shapes of Silver Nanostructures and Wide Field SPR Microscopy" presents the surface plasmon coupling behavior between the LSPs of different shapes of AgNSs, and the PSPs of the Ag surface are investigated using a wide-field surface plasmon resonance microscope, finite element method, and derived method based on scattering theory. The intensity distribution of the binding event between the AgNS and the Ag surface is calculated by fitting a curve to describe the surface plasmon coupling between AgNSs and the Ag layer.

CHAPTER 4

4. DISCUSSION AND CONCLUSIONS

Detecting and exploring nano-objects, especially at low concentrations, including viruses and extracellular vesicles (ECVs), remain challenging in analytical science. SPR sensors have gained significant attention due to their high sensitivity, real-time measurements, label-free detection, reproducibility, and cost-effectiveness. Wide-field surface plasmon resonance microscopy (WF-SPRM) operates based on the principles of SPR using the classical Kretschmann's configuration. However, it offers a distinct detection method and information acquisition, enabling the detection and exploration of individual nano-objects in solutions and gas media bound to the sensor surface. WF-SPRM thus allows for the detection of low concentrations of nano-objects.

A strong SPR signal is generated in the laser wavelength range of 600-800 nm, and to achieve this, a glass prism with a refractive index of 1.725 is selected. A high single numerical aperture objective of 2.5 is used to combine both illumination and imaging optics. The gold and silver thicknesses range of 45 nm and 50 nm were selected, respectively, to achieve higher detection accuracy. Polystyrene nanoparticles with an average size of 200 nm serve as an example for real-time WF-SPRM measurements. The first step in the WF-SPRM data analysis is suppressing image background and noise. This is achieved by frame averaging and normalization to the local light intensity. The averaged signals are then subtracted in each frame, and the time dependence of the difference is plotted. Subsequently, the time-dependent relative intensity before and after the binding of particles to the sensor surface is measured.

The effective mathematical model describes the SPR sensor principle, where molecules bound to the sensor surface are treated as an effective medium with an effective refractive index and thickness. Additionally, a discrete particle model of SPR describes the principles of discrete particle detection. Theoretical, numerical, and experimental analyses of the SPR detection principle are performed, considering discrete particle detection. The calculated

intensity profiles of single nanoparticles and 2-nanoparticles from the discrete particle model agree well with the experimental data.

Coating the metal layer with a dielectric layer is a highly effective modification to enhance the sensitivity of the SPR sensor. Coated the metal layer with dielectric layer with high refractive index and low extinction coefficient is considered a target for coating the metal layer to get higher sensitivity with an acceptable detection accuracy of SPR sensors. The influence of the coating metal sensing surface (gold/silver) with polyaniline/aluminum nitrate (PANI/$Al(NO_3)_3$) nanocomposite film, polyacrylic acid polyelectrolyte brushes (PAA PEBs), polyethylene oxide/polyacrylic acid polyelectrolyte brushes (PEO/PAA PEBs), polyacrylic acid/iodine polyelectrolyte brushes (PAA/I_2 PEBs) on the sensitivity of the WF-SPRM was investigated.

Figure 4.1 illustrates the signal-to-noise ratio of WF-SPRM based on bare Au, Au – PANI/$Al(NO_3)_3$, Au – PAA PEBs, Au – PEO/PAA PEBs, bare Ag, and Ag – PAA/I_2 PEBs. First, the signal-to-noise ratio of WF-SPRM based on the Au layer is 6 ± 1, increasing after coating with PANI/$Al(NO_3)_3$ nanocomposite film to 10 ± 1. In addition, the linewidth of the recorded image decreased from 5 pixels to 4 pixels using the Au – PANI/$Al(NO_3)_3$ layers. After that, PAA PEBs were deposited on an Au layer using a thiol bound (PAA-SH), confirmed by XPS and NMR spectroscopy. The signal-to-noise ratio of WF-SPRM based on the Au layer coated with PAA PEBs to 18. In addition, the linewidth of the recorded image decreased from 6 pixels to 5 pixels using the Au-PAA layers. The sensitivity of the WF-SPRM based on Au-(PEO/PAA PEBs) layers is explored through theoretical and experimental approaches. The signal-to-noise ratio for the Au-(PEO/PAA PEBs) layer increases from 6 ± 1 to 20 ± 1 compared to the Au layer. For now, we can conclude that coating the Au layer with PANI/$Al(NO_3)_3$, PAA PEBs, and PEO/PAA PEBs enhances the sensitivity of the WF-SPRM. The higher refractive index is for PEO/PAA PEBs, which leads to a higher signal-to-noise ratio.

In addition, the signal-to-noise ratio of WF-SPRM based on bare Ag is found to be 8 ± 1, which is higher than the signal-to-noise ratio of WF-SPRM based on bare Au. Coating the Ag layer with PAA/I_2 PEBs increases the signal-to-noise ratio to 25 ± 1. Therefore, we can conclude that WF-SPRM based on Ag-PAA/I_2 PEBs has the highest signal-to-noise ratio compared to other sensing substrate systems. Additionally, the signal intensity of silicaNP detected by the Ag layer increases from about 226 a.u. to about 373 a.u. as silicaNP size increases from 100 to 300 nm. On the other hand, the signal intensity of silicaNP detected by the Ag-PAA/I_2 layers increases from about 454 a.u. to about 820 a.u. as silicaNP size increases from 100 to 300 nm. Finally, we introduced a mathematical model to describe the SPR sensing mechanism based on discrete particles, nanostructures, viruses, or cells. The calculated

intensity profiles for the silicaNP with different sizes by Ag layer and Ag-PAA/I_2 layers describe the experimental profile well, supporting the validity of the model we deduced.

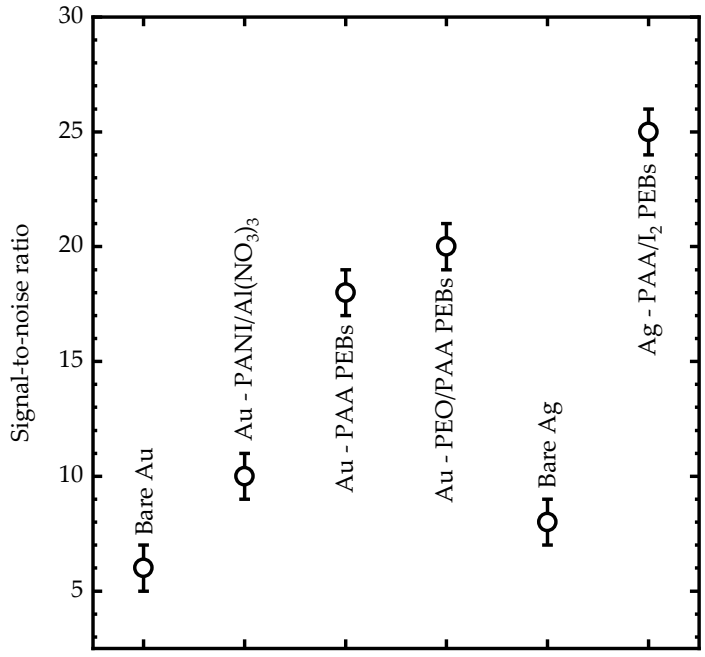

Figure 4.1: Comparison of the signal-to-noise ratio of WF-SPRM based on bare Au, Au – PANI/Al(NO_3)$_3$, Au – PAA PEBs, Au – PEO/PAA PEBs, bare Ag, and Ag – PAA/I_2 PEBs.

The surface plasmon coupling between the localized surface plasmons (LSPs) of metal nanostructures and propagating surface plasmons (PSPs) of the metal layer was investigated. Therefore, the coupling behavior of WF-SPRM with single, double, and multiple gold nanoparticles (AuNPs) of varying sizes was investigated through a combination of theoretical, simulation, and experimental approaches. When AuNPs bind to the Au surface, it disrupts the system's symmetry. Furthermore, plasmon coupling occurs between the AuNPs and the Au surface, leading to the generation of an induced charge in the Au surface, which interacts with AuNPs. The signal intensity of a single AuNP increases from 208 a.u. to 583 a.u. as the particle size increases from 40 nm to 80 nm, indicating that the signal-building mechanism is based on Rayleigh scattering theory. A discrete particle model of SPR is used to understand the interaction between the Au-layer and a single AuNP. The calculated intensity profile of the single AuNP from the discrete particle model aligns with the experimental data. Additionally, the superposition of surface plasmon waves between two AuNPs is studied using the finite element method and experimental data from WF-SPRM. The surface plasmon waves around the two particles result from the superposition of electric fields between these waves. Combining plasmon intensities of two AuNPs with an initial phase difference (φ) as $|a + a|^2$ (or $|2a|^2$) yields a quantum superposition of $|2a|^2 = |a|^2 + |a|^2 + 2|a|^2 \cos\varphi$, resulting in complex and cumulative superposed plasmon intensities.

Finally, the multiple particles near the Au layer are represented as effective media, described by Maxwell-Garnet equations. The sensitivity of 40 nm AuNPs is 50.6 deg./RIU, and this sensitivity increases linearly to 93.5 deg./RIU for the detection of 80 nm AuNPs.

In addition, the surface plasmon coupling behavior between the localized surface plasmons (LSPs) of different shapes of silver nanostructures (AgNSs) and the propagating surface plasmons (PSPs) of the silver surface was investigated by employing experimental, simulation, and theoretical approaches. Different shapes of AgNSs, including sphere, triangle plate, and hexagonal plate, are synthesized using a one-step solvothermal reduction method with an average particle size of 40, 130, and 190 nm, respectively. XRD patterns indicate that all AgNSs exhibit polycrystalline face-centered cubic (fcc) structures with preferred (111) orientation. The LSPs of different AgNSs are investigated using UV-Vis spectroscopy and the finite element method, where the spherical AgNSs exhibit a single Gaussian absorption band at 410 nm. In contrast, the triangle and hexagonal AgNSs exhibit multiple Gaussian absorption bands, representing different modes of plasmon excitation of out-of-plane quadrupole resonance, in-plane dipole, and in-plane quadrupole resonance. Finally, the surface plasmon coupling behavior between the LSPs of different shapes of AgNSs and the PSPs of the Ag surface is investigated using wide-field surface plasmon resonance microscopy (WF-SPRM), finite element method and derived method based on scattering theory. When the AgNSs bound to the Ag surface, the LSPs of the AgNSs are coupled with the PSPs of the Ag surface through near-field coupling, increasing the induced charge of the Ag surface and consequently disrupting the electric field symmetry and interacting with the free electrons of the AgNSs, which increases the electric field between the Ag surface and AgNSs. The intensity distribution of the binding event between the AgNS and the Ag surface is calculated by fitting a curve to describe the surface plasmon coupling between AgNSs and the Ag layer.

CHAPTER 5

5. APPENDIX I: ORIGINAL PAPERS

Section	Paper Title	Contribution
5.1	Original Paper I: Modeling and analysis of discrete particle detection in wide-field surface plasmon resonance microscopy (Al-Bataineh et al., 2024a)	- Development of concept - Development of model - Conduct of experiment - Discussion of results - Co-authoring of manuscript
5.2	Original Paper II: Surface Plasmon Resonance Sensitivity Enhancement Based on Protonated Polyaniline Films Doped by Aluminium Nitrate (Al-Bataineh et al., 2022)	- Development of concept - Conduct of experiment - Discussion of results - Co-authoring of manuscript
5.3	Original Paper III: Switchable Polyacrylic Acid Polyelectrolyte Brushes for Surface Plasmon Resonance Applications (Al-Bataineh et al., 2023a)	- Development of concept - Conduct of experiment - Discussion of results - Co-authoring of manuscript
5.4	Original Paper IV: Wide-field surface plasmon resonance microscope based on polyethylene oxide/polyacrylic acid brushes (Al-Bataineh et al., 2024b)	- Development of concept - Conduct of experiment - Discussion of results - Co-authoring of manuscript
5.5	Original Paper V: Developing surface plasmon resonance imaging for discrete particle detection based on a silver layer coated with polyacrylic acid/iodine polyelectrolyte brushes (Al-Bataineh et al., 2024c)	- Development of concept - Development of model - Conduct of experiment - Discussion of results - Co-authoring of manuscript
5.6	Original Paper VI: Surface plasmon coupling between wide-field SPR microscopy and gold nanoparticles (Al-Bataineh et al., 2023b)	- Development of concept - Development of model - Conduct of experiment - Discussion of results - Co-authoring of manuscript

5.7	Original Paper VII: Surface Plasmon Coupling Between Different Shapes of Silver Nanostructures and Wide Field SPR Microscopy (Al-Bataineh et al., 2024d)	- Development of concept - Development of model - Conduct of experiment - Discussion of results - Co-authoring of manuscript

5.1. Original Paper I: (Al-Bataineh et al., 2024a)

Sensors & Actuators: A. Physical 370 (2024) 115266

Contents lists available at ScienceDirect

Sensors and Actuators: A. Physical

journal homepage: www.journals.elsevier.com/sensors-and-actuators-a-physical

Modeling and analysis of discrete particle detection in wide-field surface plasmon resonance microscopy

Qais M. Al-Bataineh [a,b,*], Ahmad D. Telfah [c,d], Carlos J. Tavares [e], Roland Hergenröder [a,*]

[a] Leibniz-Institut für Analytische Wissenschaften-ISAS-e.V., Dortmund 44139, Germany
[b] Department of Physics, TU Dortmund University, Dortmund 44227, Germany
[c] Department of Physics, University of Nebraska at Omaha, Omaha NE-68182, USA
[d] Nanotechnology Center, The University of Jordan, Amman 11942, Jordan
[e] Physics Centre of Minho and Porto Universities (CF-UM-UP), University of Minho, Guimaraes 4804-533, Portugal

ARTICLE INFO

Keywords:
Surface plasmon resonance (SPR)
Wide-field SPR microscopy (WF-SPRM)
SPR discrete particle model
Nano-object detection

ABSTRACT

Wide-field surface plasmon resonance microscopy (WF-SPRM), based on Kretschmann's configuration, is a powerful technique for detecting nano-objects in solution. In this study, key parameters for building a highly sensitive WF-SPRM are optimized, including laser wavelength, prism refractive index, numerical aperture of the objective, and gold layer thickness. A medium model describes the surface plasmon resonance (SPR) sensor principle, treating molecules bound on the sensor surface as an effective medium with an effective refractive index and thickness. On the other hand, the SPR discrete particle model is introduced to describe the detection principle for discrete particles. Theoretical, numerical, and experimental analyses are conducted, and the calculated intensity profiles of single and double nanoparticles from the discrete particle model describe the experimental profiles well. Furthermore, the influence of coating the gold layer with a dielectric layer on the SPR sensitivity is investigated for varying refractive indices.

1. Introduction

Biosensors are essential analytical tools consisting of four main components: analyte, recognition element, transducer, and signal processing. The analyte represents the target molecules being measured, while the recognition element acts as the bio-receptor that specifically interacts with the analyte. The transducer converts the bio-recognition event into measurable signals, and the signal processor prepares and presents the deduced signals for analysis [1]. The optical sensors, including surface plasmon resonances, ring resonators, and interferometers, are known for their high sensitivity. However, detecting and exploring nano-objects, especially at low concentrations, including viruses and extracellular vesicles (ECVs), remain challenging [2,3]. SPR sensors have gained significant attention due to their high sensitivity, real-time measurements, label-free detection, reproducibility, and cost-effectiveness [4,5]. Conventional SPR sensors use monochromatic light directed onto a gold thin film through a prism, which excites surface plasmon-polaritons and generates an evanescent electric field. Objects near the metal surface cause variations in the refractive index, which can be measured by monitoring the incident angle shift to obtain real-time response curves [6,7].

Wide-field surface plasmon resonance microscopy (WF-SPRM) operates based on the SPR phenomenon using Kretschmann's configuration. However, it offers a distinct detection method and information acquisition, enabling the detection and exploration of discrete nano-objects in solutions bound to the sensor surface. Therefore, WF-SPRM thus allows for the detection of low concentrations of nano-objects. In this technique, a polarized laser beam illuminates a gold layer through a glass prism, and the illuminated region is imaged onto a CCD camera, enabling high-resolution imaging of the binding events. A bright spot appears on the image, indicating the presence of the detected particle bound to the surface [8–14]. A metallic coating is applied to the prism to facilitate attenuated total reflection and support surface plasmon propagation [15].

A traditional medium model describes the principle of the SPR sensor by treating molecules bound to the sensor surface as an effective medium with an effective refractive index and thickness. However, WF-SPRM can detect individual nano-objects in solutions and gases. Therefore, an SPR discrete particle model is introduced to describe the detection principle for discrete particles [16,17].

* Corresponding authors at: Leibniz Institut für Analytische Wissenschaften-ISAS-e.V., Dortmund 44139, Germany.
E-mail addresses: qais.albataineh@tu-dortmund.de (Q.M. Al-Bataineh), roland.hergenroeder@isas.de (R. Hergenröder).

https://doi.org/10.1016/j.sna.2024.115266
Received 11 August 2023; Received in revised form 4 March 2024; Accepted 7 March 2024
Available online 8 March 2024

This study focuses on the fundamental parameters influencing the imaging performance of WF-SPRM to enhance biosensing sensitivity. Key factors such as laser wavelength, prism refractive index, numerical aperture of the objective, and gold layer thickness are investigated. Validation experiments are performed using polystyrene nanoparticles of varying sizes and nanoparticles made from different materials. The influence on the SPR sensitivity of coating the gold layer with a dielectric layer with varying refractive index is also studied. Furthermore, theoretical analyses are conducted to compare using a gold layer with a dielectric coating to that of a plain gold layer in detecting different types of cancer cells. Our findings shed light on the improved sensitivity and capabilities of WF-SPRM in discrete particle detection for various biomedical applications.

2. Experimental section

2.1. WF-SPRM instrument

This section focuses on optimizing the key parameters for constructing a high-efficiency WF-SPRM system. Initially, red to near-infrared (NIR) light (wavelength range: 600–800 nm) was validated for generating a strong SPR signal. The red light efficiently excites maximum surface plasmon polaritons (SPPs) due to the strong coupling between photons in this wavelength range and the surface electrons of the gold layer under momentum matching. This coupling pulls electrons along the gold surface, producing the SPR effect (Supplementary S1) [18]. Hence, selecting an SPR microscope with a laser wavelength within the 600–800 nm range is ideal, as it provides a smaller SPR angle and greater SPR signal and sensitivity [19]. Additionally, the objective's numerical aperture performance is reduced for wavelengths outside their design range [8].

Fig. 1 presents the schematic diagram of the home-built WF-SPRM experimental setup based on Kretschmann's configuration [20]. The red-light laser diode HL6750MG (Thorlabs GmbH, Germany) with a 685 nm wavelength illuminates the gold layer through a glass prism (SF10, n=1.725, Eksma Optics, Lithuania) with four polished sides measuring $20.0 \times 25.0 \times 16.3\ mm^3$, with an angle of $56° \pm 5°$ at a fixed incidence angle (Figure S1). The choice was made for a glass prism with a high refractive index (n=1.725) [21], an objective lens (Canon Compact-Macro Lens EF 50 mm 1:2.5) coupled to a video camera equipped with a CMOS chip (MT9P031) featuring a resolution of 5 Mp and a pixel size of $2.2 \times 2.2\ \mu m^2$, is used for imaging the gold surface. The high numerical aperture (NA) objective ($NA > 1.4$) effectively couples the illumination and imaging optics [22], resulting in a relatively small field of view, approximately $0.1 \times 0.1\ mm^2$ [8].

2.2. Gold-sensor substrate preparation

Before depositing the gold layer onto the glass substrate, it is essential to apply a titanium interlayer (Ti) to enhance the adhesion between the gold and the glass surface. The stable titanium layer should have a minimum thickness of approximately 5 nm. Therefore, a Ti layer with a thickness of 5 nm and a complex refractive index of ($n = 2.6112 + 0.1532i$) is considered in the calculations [23]. Additionally, to achieve higher detection accuracy and sensitivity, the optimal thickness range for the gold layer is in the range of 40–45 nm (Supplementary S2), which aligns with the findings of A. Zybin et al. [14]. Accordingly, SF10 polished glass slides with a refractive index matching the glass prism ($n = 1.725$) were procured from Helma Optics (Germany). Subsequently, these glass slides were coated with a titanium adhesive layer, measuring 5 nm in thickness, followed by a 41–45 nm gold layer ($n = 0.15, k = 4.91$) using a magnetron-sputtering technique (Innolume, Dortmund, Germany). To attain the best sensitivity, the transmittance of the gold-sensor substrate at 685 nm is 4%. A meticulous cleaning procedure was performed before employing the gold-sensor substrate in SPR imaging. The substrate is immersed in a piranha solution for 5 minutes. The piranha solution is prepared by slowly adding 30 mL of sulfuric acid (Sigma-Aldrich) to 10 mL of hydrogen peroxide (VWR chemicals) at 4 °C due to the exothermic nature of the reaction. Subsequently, the gold-sensor substrates are thoroughly rinsed with distilled water and absolute ethanol (99.85%) to eliminate any residual piranha solution and then dried using argon gas. Following the cleaning process, the gold-sensor substrate is precisely positioned on the base of the glass prism using RI matching immersion liquid (2 µL, Cargille Laboratories via VWR, $n = 1.725$) to ensure there is no air gap between the gold-sensor substrate and the prism. To prevent liquid leakages, a polydimethylsiloxane (PDMS, Sigma-Aldrich) gasket is placed between the gold-sensor substrate and the Teflon flow cell. Subsequently, the 0.51 mm thick Teflon flow cell with an average flow rate of 300 µL/minute is securely sealed to the gold-sensor substrate (Figure S5). Additionally, the flow rate is directed from down to up to avoid any formation of liquid bubbles.

2.3. Experimental procedure

Polystyrene nanoparticles (PSNPs) are employed as the primary example for WF-SPRM measurements. The PSNPs have an average diameter of 200 nm and a refractive index of $n = 1.59$ [24]. An

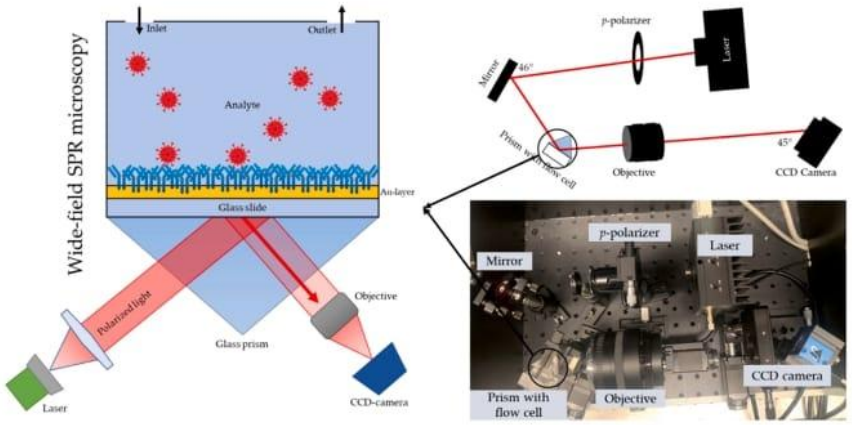

Fig. 1. Schematic diagram of the experimental home-built design of WF-SPRM based on Kretschmann's configuration.

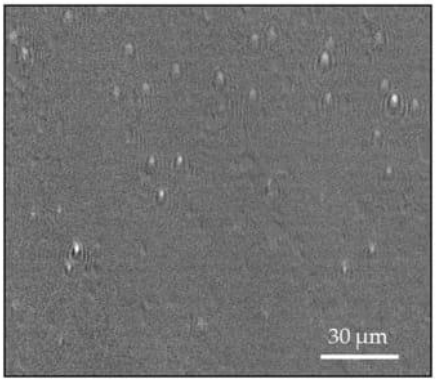

Fig. 2. WF-SPRM image for 200 nm PSNPs. Light spots indicate particle binding to the sensor surface.

aluminum hydroxide chloride layer is deposited on the gold substrate to allow the connection between PSNPs and the sensor surface by applying 150 µL of the solution and allowing it to sit for 10–30 minutes at room temperature. Subsequently, the gold substrate is washed with distilled water and dried using argon gas. To prepare the nanoparticles stock solution, 0.1 g of nanoparticles are mixed with 0.3% sodium chloride in 1.0 L of filtered distilled water at room temperature for 2 hours to achieve a low concentration of nanoparticles. Before introducing the nanoparticle stock solution into the sensor cell, a sodium chloride buffer solution (NaCl, 0.3%) passes through the cell for 1–2 minutes. Subsequently, the nanoparticle stock solution is injected into the sensor cell. After the flow system reaches equilibrium, the prism, along with the mounted flow cell, is rotated until the resonance angle ($4R_{min}$) is attained. Starting from this minimum, the measuring point is adjusted to $4R_{min}$ into the linear region of the reflectivity curve by rotating the angle of incidence counter-clockwise [25].

2.4. WF-SPRM data analysis

The data analysis in WF-SPRM is based on observing the perturbation in the propagation conditions of surface plasmons caused by nano-objects adsorption. WF-SPRM allows visualization of optical patterns resulting from the scattering of surface plasmon waves. When a particle binds to the sensor surface, it disturbs the evanescent field of the surface plasmon wave, leading to local changes in reflectivity, manifesting as a bright spot in the image. ImageJ software is employed to determine the detection signal associated with the nanoparticle binding event [26]. To begin the WF-SPRM data analysis, the image background and noise are suppressed by averaging about 200 frames and subtracting each frame from the background. Following this, the time dependence of the intensity variation is plotted to observe the binding events. An illustrative example of detecting 200 nm polystyrene nanoparticles is presented in Fig. 2 and Fig. 3.

A single particle bound to the sensor surface exhibits an asymmetric shape with concentric surface plasmon waves around it, as discussed in [27,28] (Fig. 3). The WF-SPRM data is collected as a matrix of time points and pixels, allowing for analysis of the time-dependent relative intensity before and after particle binding on the sensor surface (Fig. 3a). The intensity shows low values before PSNPs bind to the sensor surface. However, at approximately 36 seconds, the local intensity increases, indicating the moment when PSNPs are bound to the surface.

2.5. Numerical model

The design and analysis of traditional and proposed models for the SPR sensor are conducted using COMSOL Multiphysics based on the finite element method. A 2D geometry is proposed, consisting of prism/Ti layer (~ 5 nm)/Au layer (~50 nm)/water. For the traditional molecular layer model, a 10 nm thick molecular layer of polystyrene is added, while for the proposed particle detection model, a 200 nm polystyrene nanoparticle at 10 nm above the gold layer is placed. The gold layer is illuminated with a light source at a wavelength of 685 nm incident on the top of the SF11 prism. Free triangular meshes were used in the simulated SPR sensor with the element size of 6.09 $\times 10^{-5}$ - 0.03 µm. Additionally, the incident light angle variates from 20° to 89° with a 0.1° step. The reflectivity curve as a function of the incident angle is calculated, and the resonance angle is determined at the minimum reflectivity.

3. Results and discussion

Firstly, the traditional mathematical medium model is introduced, wherein molecules bound on the sensor surface are considered an effective medium with an effective refractive index and thickness. Since this model describes the SPR sensor principle by treating molecules bound to the sensor surface as an effective medium, the traditional mathematical medium model cannot describe low concentrations of detected particles. Subsequently, a theoretical model incorporating the

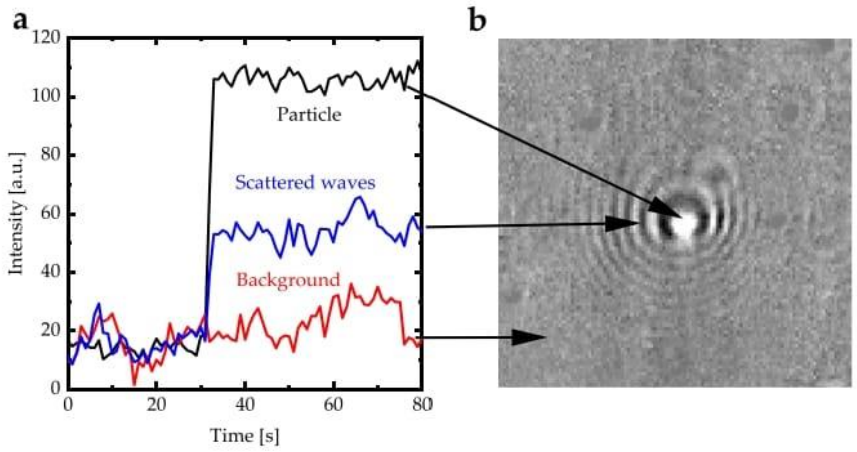

Fig. 3. (a) Temporal evolution of intensity in the central region of the bright spot for PSNPs bound to the Au-layer. (b) Representative processed image depicting polystyrene particles bound to the sensor surface.

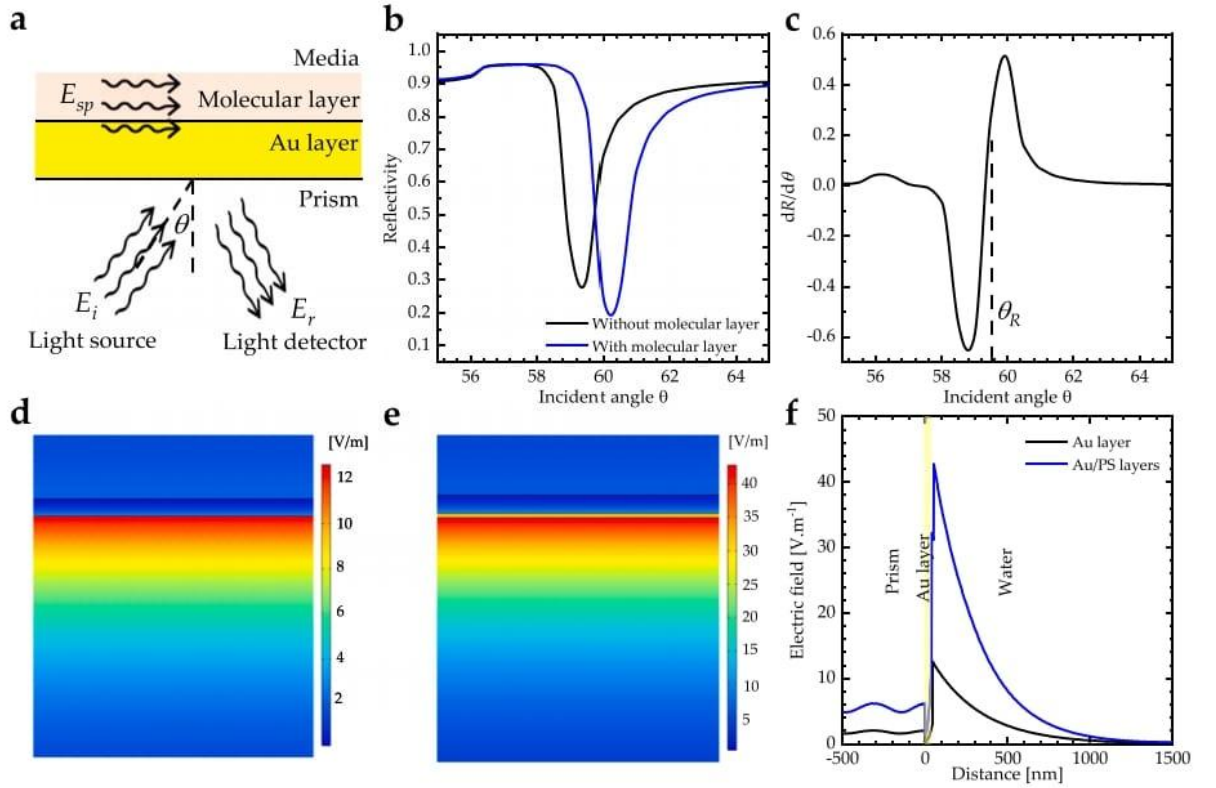

Fig. 4. The traditional medium model of the SPR sensor. (a) Schematic diagram of the traditional medium model showing the setup. (b) SPR reflectivity curves, with the black line representing the curve without a 10 nm thick polystyrene film and the blue line representing the curve with this film, were calculated using Fresnel's equations. (c) The slope of the reflectivity curve indicates the sensitivity. Electric field distributions along the Kretschmann's configuration of the structures, (d) without and (e) with a 10 nm thick polystyrene film at resonance angles. (f) The electric field profile is along the perpendicular direction to the gold layer at the resonance angle.

interaction between discrete particles and the sensor surface (discrete particle theory of SPR), where WF-SPRM can detect individual nano-objects in solutions and gases, is presented. This proposed model is compared with experimental data to validate its accuracy and applicability.

3.1. Traditional mathematical model

The traditional medium model of the SPR sensor treated the detected molecules near the sensor surface as an effective medium with an effective refractive index and thickness (Fig. 4a). When light transmits the Au-layer, *p*-polarized SPR waves are generated at the metal/dielectric media interface. The SPR phenomenon is described using Maxwell's equations in (x, 0, z) as follows:

$$E_i(\vec{r},t) = (E_{ix}, 0, E_{iz})\left[e^{-|Z|k_{iz}} e^{i(xk_{ix}-\omega t)}\right] \quad (1)$$

$$H_i(\vec{r},t) = (0, H_{iy}, 0)\left[e^{-|Z|k_{iz}} e^{i(xk_{ix}-\omega t)}\right] \quad (2)$$

where: ω is the frequency, E is the electric field vector, H is the magnetic field vector, k_{iz} and k_{ix} are the z and x wave vector components. Applying the continuity conditions,

$$k_{iz} = \sqrt{\varepsilon_i\left(\frac{\omega}{c}\right)^2 - k_{ix}^2} \quad (3)$$

and,

$$\frac{k_{z1}}{\varepsilon_m}H_{1y} + \frac{k_{z2}}{\varepsilon_d}H_{2y} = 0 \quad (4)$$

$$H_{1y} - H_{2y} = 0 \quad (5)$$

When the determinant is equal to zero,

$$k_{z1}\varepsilon_d + k_{z2}\varepsilon_m = 0 \quad (6)$$

At $K_{x1} = K_{x2} = K_x$, the expression becomes:

$$K_x = \frac{\omega}{c}\sqrt{\frac{\varepsilon_m\varepsilon_d}{\varepsilon_m + \varepsilon_d}} \quad (7)$$

Eq. (7) represents the SPW vector $K_x = K_{sp}$, illustrating the surface plasmon generation. ε_m and ε_d are the dielectric constants of the metal and dielectric layers. The transfer matrix method is used to investigate the reflectivity curve of the N-layer Kretschmann configuration model as follows [29],

$$\begin{pmatrix} U_1 \\ V_1 \end{pmatrix} = M\begin{pmatrix} U_{N-1} \\ V_{N-1} \end{pmatrix} \quad (8)$$

where: (U_1, V_1) and (U_{N-1}, V_{N-1}) are the borderline terms of the 1st and Nth layers of electromagnetic fields. Eq. 9 represents the characteristic matrix [29],

$$\prod_{K=2}^{N-1} M_K = \begin{pmatrix} M_{11} & M_{12} \\ M_{21} & M_{22} \end{pmatrix} \quad (9)$$

where:

$$M_K = \begin{pmatrix} \cos\beta_k & \frac{i\sin\beta_k}{q_k} \\ -iq_k\sin\beta_k & \cos\beta_k \end{pmatrix} \quad (10)$$

$$q_k = \frac{\sqrt{\varepsilon_k - n_1^2\sin\theta_1^2}}{\varepsilon_k} \quad (11)$$

$$\beta_k = \frac{2\pi d_k}{\lambda}\left(\sqrt{\varepsilon_k - n_1^2\sin\theta_1^2}\right) \quad (12)$$

Where: d_k is the thickness of the k_{th}-layer, θ_k and λ are the incident angle and wavelength of the incident light. Subsequently, the complex reflection coefficient (r_p) is given by,

$$r_p = \left[(M_{11} + M_{12}q_5)q_1 - \frac{(M_{21} + M_{22}q_5)}{(M_{11} + M_{12}q_5)q_1} + (M_{21} + M_{22}q_5)\right] \quad (13)$$

The reflectivity (R_p) is obtained by,

$$R_p = |r_p|^2 \quad (14)$$

When the polarized light illuminates the Au layer through the glass prism, the light reflection varies by changing the incident angle until it reaches the minimum at the resonance angle (θ_R), i.e., for prism/Au layer/water, the resonance angle is ~59.5° (Fig. 4b, black line). The reflectivity reaches the minimum at θ_R, indicating surface plasmon excitation that induces surface plasmon resonance, where the *p*-polarized light interacts with the free electron of a metal film, resulting in free electron oscillations [30]. Assuming a molecular layer of PS (10 nm) deposited on the Au layer, the resonance angle increases to about 60.2° due to a variation in the refractive index of the media above the Au layer (Fig. 4b, blue line). According to the traditional medium model, the change in the reflectivity (ΔR) is related to the resonance angle shift ($\Delta\theta$) by [31,32],

$$\Delta R(\theta) = -\frac{dR(\theta)}{d\theta}\Delta\theta \quad (15)$$

where: $dR(\theta)/d\theta$ is the slope of the reflectivity as a function of angle shift (Fig. 4c). Additionally, Kretschmann's configuration of the structure (prism/Au/water) is simulated using COMSOL Multiphysics to investigate the electric field distribution across the structure at resonance angle, with and without adding a PS layer of 10 nm (Fig. 4d, e, respectively). Due to the maximum surface plasmon excitations, the electric field is enhanced at the metal/analyte interface for the resonance angle (Fig. 4d). Adding a PS layer on the Au layer increases the electric field intensity at the PS/analyte interface (Fig. 4e). The electric field profile at the resonance angle is illustrated in Fig. 4f. A significant rise in the electric field is generated at the gold/analyte interface, and

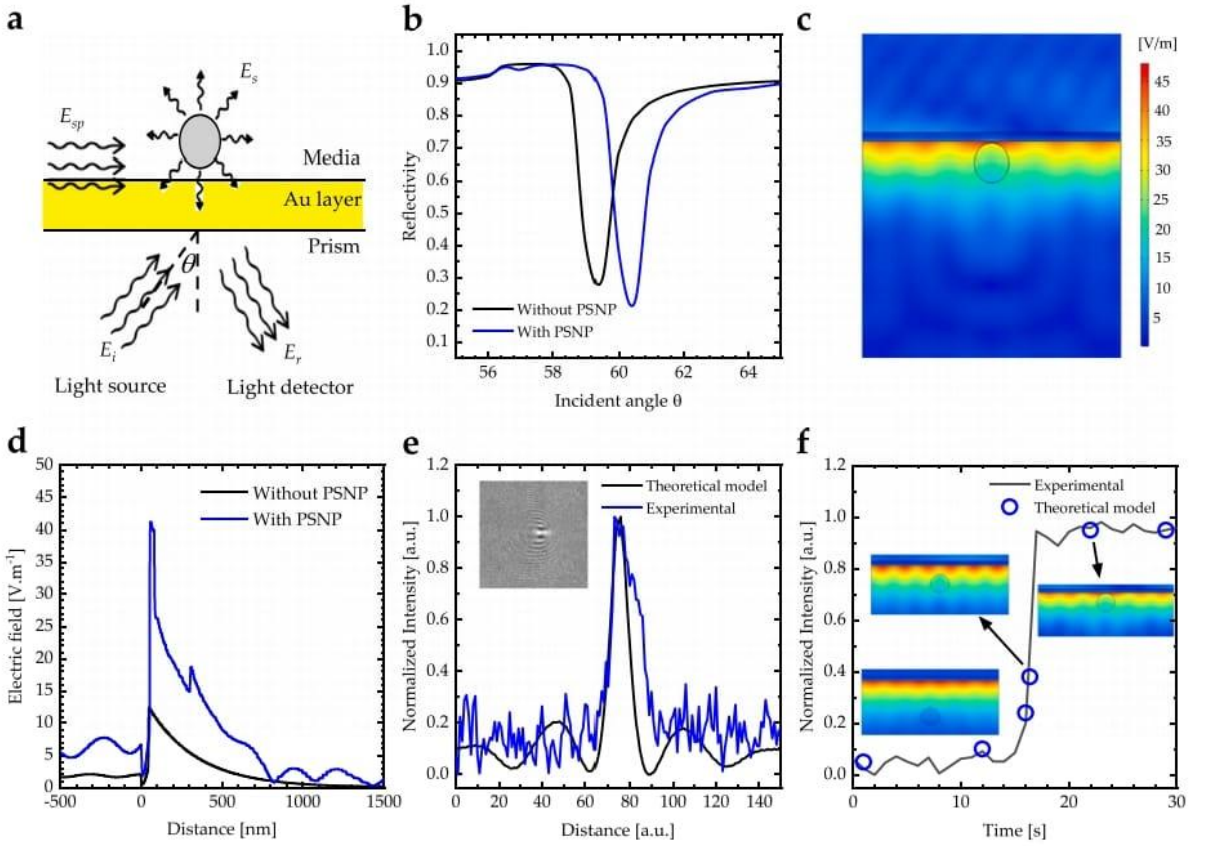

Fig. 5. Discrete particle model of THE SPR sensor. (a) Schematic of the discrete particle model, (b) SPR reflectivity curves without (black line) and with (blue line) PSNP of 200 nm. (c) Electric field distributions along the Kretschmann's configuration of the structure with PSNP of 200 nm. (d) The electric field profile is along the perpendicular direction to the gold layer at resonance angle without/with PSNP of 200 nm. (e) Experimental and calculated intensities vs. distance of PSNP. (f) Time dependence of the intensity in the middle of the bright spot for PSNP bounded to the Au layer compared to calculated intensity for different location distances of PSNP from the Au surface.

the electric field intensity decreases exponentially in the analyte-containing detected biomolecules.

3.2. SPR discrete particle model

WF-SPRM can detect individual nano-objects in solutions and gases. Therefore, an SPR discrete particle model is introduced to describe the detection principle for discrete particles [16,17]. SPR discrete particle model describes the interaction between the surface plasmon polaritons and the detected particle as follows. Fig. 5a illustrates a discrete particle detection using an SPR sensor as well as the electric field generated between the detected particle and the Au-layer. First, the interaction between the incident p-polarized light and the Au-layer is described, where the incident *p*-polarized light is either reflected from the Au-layer (E_r) or transmitted into Au-layer, exciting surface plasmon waves (E_{sp}) [33]. The total electric field is [34–36],

$$E = E_r \sin(\omega t) + E_{sp} \sin(\omega t + \varphi) \tag{16}$$

where: φ is the phase shift. Additionally, the resulting intensity from the detection process in SPR is given by [14],

$$I = c \quad \varepsilon_0 \quad n \quad |E|^2 = c \quad \varepsilon_0 \quad n \quad \left|E_r \sin(\omega t) + E_{sp} \sin(\omega t + \varphi)\right|^2 \tag{17}$$

or,

$$I = \frac{1}{2} c \quad \varepsilon_0 \quad n \left(E_r^2 + E_{sp}^2 + 2E_r E_{sp} \cos\varphi\right) \tag{18}$$

where: ε_0 is the vacuum permittivity. Afterward, the excited surface plasmon waves will scatter from the detected particle with concentric surface plasmon waves around it. Elastic scattering theory describes scattered fields of surface plasmons by a particle as a decaying cylindrical plasmonic wave [28,37,38],

$$E_s(r, r') = E_{sp}^0(r') e^{-\kappa|r-r'|} e^{-ik|r-r'|} \tag{19}$$

where: r' is the particle location, $E_{sp}(r')$ is the surface plasmon field at the particle's location, κ and k are the decaying constant and wavenumber of the SP. Subsequently, according to Born's approximation, the total surface plasmon field (E_{sp}) is [37,39],

$$E_{sp}(r, r') = E_{sp}^0(r) + \alpha E_{sp}^0(r') e^{-\kappa|r-r'|} e^{-ik|r-r'|} = E_{sp}^0(r) + \alpha E_s(r, r') \tag{20}$$

where: α is a scattering coefficient related to the particle's polarizability. $E_{sp}^0(r)$ is the SP field in the absence of the particle. The SPR image contrast of the particle is described by,

$$I(r, r') = \frac{1}{2} c \quad \varepsilon_0 \quad n \left[\left(E_r^2 + \left(E_{sp}^0(r) + \alpha E_s(r, r') \right)^2 + 2E_r \left(E_{sp}^0(r) + \alpha E_s(r, r') \right) \cos\varphi \right) - \left(E_r^2 + E_{sp}^2 + 2E_r E_{sp} \cos\varphi \right) \right] \tag{21}$$

3.3. Single Particle

When a molecule is bound to the Au surface, it destroys the electric field symmetry on the Au surface that results from the SPR phenomenon. Assuming a polystyrene nanoparticle with a diameter of 200 nm located 5 nm above the Au layer, the resonance angle increases to approximately 60.2°, comparable to a molecular layer of polystyrene (Fig. 5b). The electric field distribution across the structure at the resonance angle with the PSNP of 200 nm is shown in Fig. 5c. At the resonance angle, the electric field is enhanced at the metal/analyte interface, breaking the electric field symmetry. The electric field profile at the resonance angle with the presence of the PSNP shows a significant increase in the electric field at the gold/analyte interface. At the same time, it decreases exponentially within the detected particles containing the analyte. Additionally, a small peak appears in the middle of the PSNP, indicating the enhancement of the electric field around it (Fig. 5d). On the other hand, when a particle binds to the sensor surface, it disturbs the evanescent field of the surface plasmon wave, leading to local changes in reflectivity, manifesting as a bright spot in the image. The intensity distribution of the binding event between the molecule and the Au surface can be calculated using Eq. 21. The calculated intensity profile describes the experimental profile well, validating our derived model to describe the discrete particle detection by SPR sensors (Fig. 5e). Additionally, the time dependence of relative intensities during the binding of PSNP to the Au surface illustrates the well-matching between the experimental and calculated data (Fig. 5f). From these results, it can be concluded that the SPR discrete particle model can describe the spatiotemporal interactions of the discrete particle detection using WF-SPRM since the model can describe the intensity profile of the detected particle as well as the time dependence of relative intensities during the binding of the detected particle to the Au surface.

The signal intensity of the detected nanoparticles is influenced by two primary parameters, the first being the nanoparticle size [40]. As depicted in Fig. 6a, the signal intensity of polystyrene nanoparticles (PSNPs) shows a linear increase as the particle diameter ranges from 100 to 400 nm. Furthermore, the linear dependence of signal intensity reaffirms that the images correspond to individual particles rather than agglomerates. The second parameter affecting the signal intensity is the refractive index of the nanoparticles. For instance, gold nanoparticles (AuNPs) with a diameter of 80 nm exhibit higher signal intensity compared to silica nanoparticles (with a refractive index of $n = 1.420$ [30]) and PSNPs (Fig. 6b).

3.4. Two-Particle Interference

When double PSNPs are located in proximity to the Au gold surface, at a distance smaller than the SP propagation length, the SP waves around them interact through constructive and destructive interferences, leading to the breakdown of system symmetry in the electric field (Fig. 7a). The electric field profile at the resonance angle, in the presence of the PSNPs, exhibits a pronounced rise in intensity at the gold/analyte interface, followed by an exponential decrease in the electric field intensity within the analyte-containing detected molecules. Additionally, a small peak appears at the midpoint between the two PSNPs, indicating an enhancement of the electric field in this region (Fig. 7b). The contrast in the surface plasmon resonance (SPR) image of the two PSNPs can be described by the following expression:

$$I(r) = I_1 + I_2 + c \quad \varepsilon_0 \quad n|E_{s1}||E_{s2}|\cos(\varphi_1 - \varphi_2) \tag{22}$$

with, E_{sj} is the scattering electric field of particle j, which is given by,

$$E_{sj} = E_{sp}^0(r_j) e^{-\kappa|r-r_j|} e^{-ik|r-r_j|} \tag{23}$$

$$I_j(r,\dot{r}) = \frac{1}{2}c \quad \varepsilon_0 \quad n\left[\left(E_r^2 + \left(E_{sp}^0(r) + \alpha E_{sj}\right)^2 + 2E_r\left(E_{sp}^0(r) + \alpha E_{sj}\right)\cos\varphi\right) - \left(E_r^2 + E_{sp}^2 + 2E_r E_{sp}\cos\varphi\right)\right] \tag{24}$$

Fig. 7c presents the intensity profile distribution for the experimental case of two PSNPs near the Au surface, compared with the calculated intensity profile. It is evident that the calculated intensity profile described the experimental data well, indicating the validation of our derived model.

3.5. Coating gold layer with a dielectric layer

Coating the gold layer with a dielectric layer is a highly effective modification to enhance the sensitivity of the SPR sensor [41,42]. In this section, the refractive index, extinction coefficient, and thickness of the dielectric layer are optimized to achieve improved sensitivity. Initially, the sensitivity enhancement resulting from the gold coating with a dielectric layer is explained [43]. The propagation constant (β_{ev}) can characterize the propagation of evanescent waves and given by Eq. (25) [44],

$$\beta_{ev} = \frac{2\pi}{\lambda_{light}} n_{prism}\sin\theta \tag{25}$$

Here, n_{prism} and θ represent the refractive index of the prism and the incident light angle at the metal surface, respectively, and λ_{light} is the light wavelength. Additionally, the propagating constant of the surface plasmon wave for the SPR sensor with a single metal layer and sensing medium is given by Eq. (26) [44],

$$\beta_{SPW} = \frac{2\pi}{\lambda_{light}}\sqrt{\frac{n_{metal}^2 n_{sm}^2}{n_{metal}^2 + n_{sm}^2}} \tag{26}$$

Here, n_{metal} and n_{sm} represent the refractive indices for metal and sensing medium, respectively. Eqs. 25 and 26 at resonance can be connected to get the resonance SPR angle as,

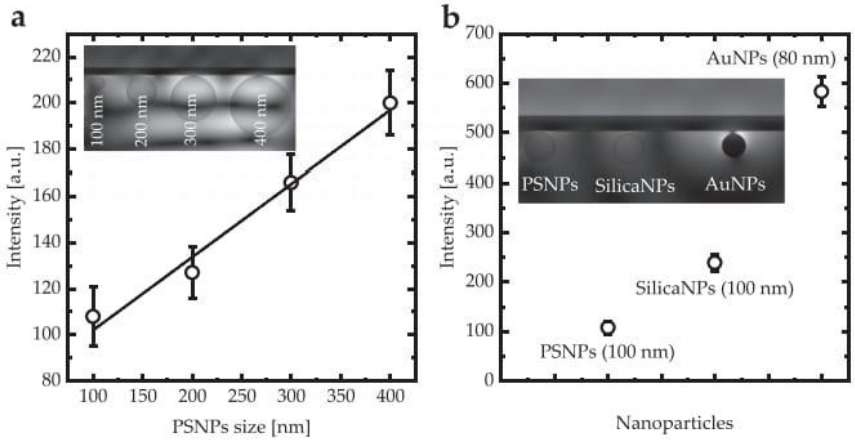

Fig. 6. (a) Response of SPR intensity as a function of a PSNPs size, and (b) Response of SPR intensity for different nanoparticle refractive indices.

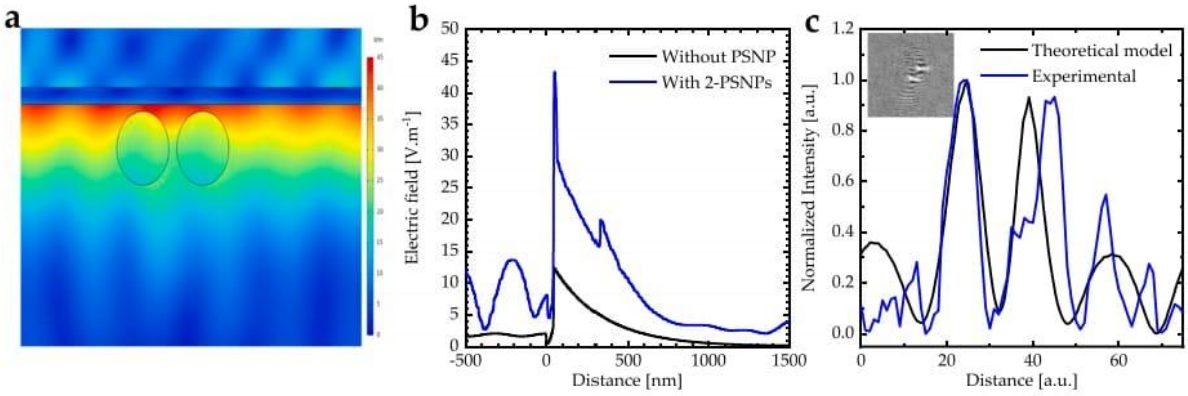

Fig. 7. Two-particle interference model of the SPR sensor. (a) Electric field distributions along the Kretschmann's structure configuration with 2-PSNPs of 200 nm. (b) The electric field profile is along the perpendicular direction to the gold layer at resonance angle without/with 2-PSNPs of 200 nm. (c) Experimental and calculated intensities vs. distance of 2-PSNPs.

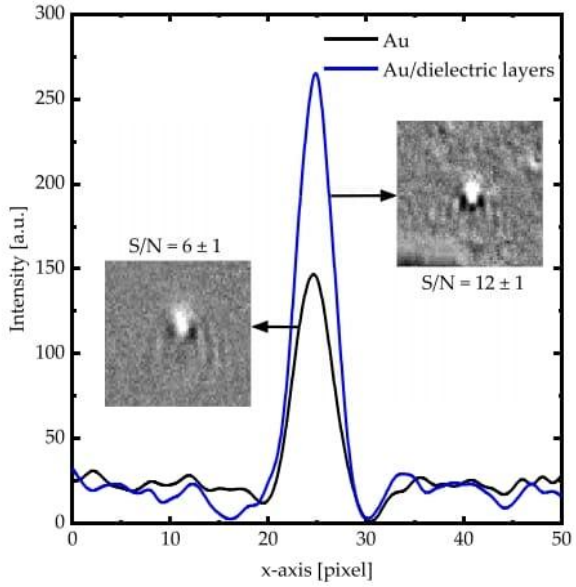

Fig. 8. Line profile plot showing the detection of PSNPs by Au layer and Au/n=1.9 layers.

$$\theta_{SPR} = \sin^{-1}\left(\frac{1}{n_{prism}}\sqrt{\frac{n_{metal}^2 n_{sm}^2}{n_{metal}^2 + n_{sm}^2}}\right) \tag{27}$$

In addition, by coating the metal surface with a dielectric layer of refractive index ($n_{dielectric}$) in the SPR sensor changes the SPR angle equation to [45],

$$\theta_{SPR} = \sin^{-1}\left(\frac{1}{n_{prism}}\sqrt{\frac{n_{metal}^2 n_{dielectric}^2 n_{sm}^2}{n_{metal}^2 + n_{dielectric}^2 + n_{sm}^2}}\right) \tag{28}$$

The sensitivity of SPR sensors (S) is calculated by $S = \Delta\theta/\Delta n$, where: $\Delta\theta$ is the SPR angle shift, and Δn is the refractive index change. As seen in Eq. (28), the SPR angle shift increases with an increase in the effective refractive index of the system. Supplementary S3 demonstrates that coating the gold layer with a dielectric layer having a refractive index above 1.8 significantly increases the sensitivity of the SPR sensor. Furthermore, to achieve high sensitivity with acceptable detection accuracy, the thickness of the dielectric layer should fall within the range of 15–20 nm.

Subsequently, PSNPs were employed as an example for real-time measurements in two systems: prism/Ti(5 nm)/Au(45 nm) and prism/Ti(5 nm)/Au(45 nm)/dielectric($n = 1.9, k = 0.01, 20nm$). The signal-to-noise ratio (S/N) and the linewidth in the line profile plot for three individually bound PSNPs to the surface are calculated to investigate the efficiency of the SPR sensor (Fig. 8). The signal-to-noise ratio (S/N) of the prism/Ti(5 nm)/Au(45 nm)/dielectric($n = 1.9, k = 0.01, 20$nm) system outperformed that of the prism/Ti(5 nm)/Au(45 nm) system, thereby confirming our theoretical findings.

Our previously published research investigated the effect of coating the Au-layer with dielectric layers on the SPR sensitivity. For instance, coating the Au-layer by complex composite films based on polyaniline (PANI) doped hydrochloric acid (HCl) incorporated with aluminum nitrate ($Al(NO_3)_3$) increases the signal-to-noise ratio for PSNP detecting from 3.95 for bare Au-layer to 8.82 [46]. On the other hand, coating the Au-layer with polyacrylic acid polyelectrolyte brushes (PAA PEBs) increases the signal-to-noise ratio for PSNP detection from 6 for bare Au-layer to 18 [47].

4. Conclusions

A strong SPR signal is generated in the laser wavelength range of 600–800 nm, and to achieve this, a glass prism with a refractive index of 1.725 is selected. A high single numerical aperture objective of 2.5 is used to combine both illumination and imaging optics. The gold thickness range of 40–45 nm is selected to achieve a higher detection accuracy. Polystyrene nanoparticles with an average size of 200 nm serve as an example for real-time WF-SPRM measurements. The first step in the WF-SPRM data analysis is to suppress image background and noise. This is achieved by frame averaging and normalization to the local light intensity. The averaged signals are then subtracted in each frame, and the time dependence of the difference is plotted. Subsequently, the time-dependent relative intensity before and after the binding of particles to the sensor surface is measured. It is observed that increasing particle size leads to an increase in signal intensity. Moreover, AuNPs exhibit a higher signal intensity compared to silica nanoparticles and PSNPs. The traditional mathematical model is utilized to describe the SPR sensor principle, where molecules bound to the sensor surface are treated as an effective medium with an effective refractive index and thickness. Additionally, a discrete particle model of SPR describes the principles of discrete particle detection. Theoretical, numerical, and experimental analyses of the SPR detection principle are performed, considering discrete particle detection. The calculated intensity profiles of single nanoparticles and 2-nanoparticles from the discrete particle model agree well with the experimental data. Furthermore, the effect on the SPR sensitivity of coating the gold layer with a dielectric layer of varying refractive indices is investigated. Finally, polystyrene nanoparticles of size 200 nm have recurred as an example for real-time measurements to validate the results and to present the WF-SPRM data analysis method. In conclusion, an optical imaging technology is developed to detect and quantify discrete particles, such as viruses, proteins, and cancer cells, and monitor the time-dependence interactions between the detected particles and gold sensors. It is anticipated that this technology will complement the traditional technologies and enable the detection of low concentration biological and chemical particles.

CRediT authorship contribution statement

Ahmad Telfah: Writing – original draft, Visualization, Validation, Supervision, Resources, Methodology, Investigation, Conceptualization. **Qais Al Bataineh:** Writing – original draft, Visualization, Software, Methodology, Formal analysis, Data curation, Conceptualization. **Roland Hergenröder:** Writing – review & editing, Validation, Supervision, Resources, Project administration, Investigation, Data curation. **Carlos Tavares:** Writing – review & editing, Visualization, Formal analysis.

Declaration of Competing Interest

The authors declare no conflict of interest.

Data availability

Data will be made available on request.

Acknowledgments

The scientific support by the Ministerium für Innovation, Wissenschaft und Forschung des Landes Nordrhein-Westfalen, the Senatsverwaltung für Wirtschaft, Technologie und Forschung des Landes Berlin, and the Bundesministerium für Bildung und Forschung is gratefully acknowledged. C.T. acknowledges the funding from FCT/PIDDAC through the Strategic Funds project reference UIDB/04650/2020–2023.

Appendix A. Supporting information

Supplementary data associated with this article can be found in the online version at doi:10.1016/j.sna.2024.115266.

References

[1] S. Singh, et al., 2D nanomaterial-based surface plasmon resonance sensors for biosensing applications, Micromachines vol. 11 (8) (2020) 779.
[2] X. Fan, I.M. White, S.I. Shopova, H. Zhu, J.D. Suter, Y. Sun, Sensitive optical biosensors for unlabeled targets: a review, Anal. Chim. Acta vol. 620 (1-2) (2008) 8–26.
[3] V. Scherbahn, S. Nizamov, V.M. Mirsky, Plasmonic detection and visualization of directed adsorption of charged single nanoparticles to patterned surfaces, Acta vol. 183 (11) (2016) 2837–2845.
[4] J.-F. Masson, Surface plasmon resonance clinical biosensors for medical diagnostics, ACS Sens. vol. 2 (1) (2017) 16–30.
[5] T. Xue, et al., Ultrasensitive detection of miRNA with an antimonene-based surface plasmon resonance sensor, Nat. Commun. vol. 10 (1) (2019) 1–9.
[6] H.H. Nguyen, J. Park, S. Kang, M. Kim, Surface plasmon resonance: a versatile technique for biosensor applications, Sensors vol. 15 (5) (2015) 10481–10510.
[7] D. Wang, et al., Recent advances in surface plasmon resonance imaging sensors, Sensors vol. 19 (6) (2019) 1266.
[8] S. Nizamov, S.D. Sazdovska, V.M. Mirsky, A review of optical methods for ultrasensitive detection and characterization of nanoparticles in liquid media with a focus on the wide field surface plasmon microscopy, Anal. Chim. Acta (2022) 339633.
[9] I. Sidorenko, et al., Computer assisted detection and quantification of single adsorbing nanoparticles by differential surface plasmon microscopy, Microchim. Acta vol. 183 (1) (2016) 101–109.
[10] S. Nizamov, V. Scherbahn, V.M. Mirsky, Detection and quantification of single engineered nanoparticles in complex samples using template matching in wide-field surface plasmon microscopy, Anal. Chem. vol. 88 (20) (2016) 10206–10214.
[11] V. Shpacovitch, et al., Application of the PAMONO-sensor for quantification of microvesicles and determination of nano-particle size distribution, Sensors vol. 17 (2) (2017) 244.
[12] H.K. Rouf, T. Haque, Performance enhancement of Ag-Au bimetallic surface plasmon resonance biosensor using InP, Prog. Electromagn. Res. M vol. 76 (2018) 31–42.
[13] V. Shpacovitch, R. Hergenroeder, Optical and surface plasmonic approaches to characterize extracellular vesicles. A review, Anal. Chim. Acta vol. 1005 (2018) 1–15.
[14] A. Zybin, V. Shpacovitch, J. Skolnik, R. Hergenröder, Optimal conditions for SPR-imaging of nano-objects, Sens. Actuators B: Chem. vol. 239 (2017) 338–342.
[15] G. Steiner, Surface plasmon resonance imaging, Anal. Bioanal. Chem. vol. 379 (3) (2004) 328–331.
[16] Q.M. Al-Bataineh, A.D. Telfah, C.J. Tavares, R. Hergenröder, Surface plasmon coupling between wide-field SPR microscopy and gold nanoparticles, Sci. Rep. vol. 13 (1) (2023) 22405.
[17] Q.M. Al-Bataineh, A.D. Telfah, C.J. Tavares, R. Hergenröder, Wide-field surface plasmon resonance microscope based on polyethylene oxide/polyacrylic acid brushes, Appl. Surf. Sci. vol. 649 (2024) 159189.
[18] L. Novotny, B. Hecht, Principles of nano-optics, Cambridge university press, 2012.
[19] A.R. Halpern, J.B. Wood, Y. Wang, R.M. Corn, Single-nanoparticle near-infrared surface plasmon resonance microscopy for real-time measurements of DNA hybridization adsorption, ACS nano vol. 8 (1) (2014) 1022–1030.
[20] E. Kretschmann, The determination of optical constants of metals by excitation of surface plasmons (Die Bestimmung optischer Konstanten von Metallen durch Anregung von Oberflächenplasmaschwingungen), Z. Phys. vol. 241 (1971) 313–324.
[21] B. Rothenhäusler, W. Knoll, Surface–plasmon microscopy, Nature vol. 332 (6165) (1988) 615–617.
[22] B. Huang, F. Yu, R.N. Zare, Surface plasmon resonance imaging using a high numerical aperture microscope objective, Anal. Chem. vol. 79 (7) (2007) 2979–2983.
[23] P. Johnson, R. Christy, Optical constants of transition metals: Ti, v, cr, mn, fe, co, ni, and pd, Phys. Rev. B vol. 9 (12) (1974) 5056.
[24] H.-J. Schnorrenberg, M. Hengstebeck, K. Schlinkmeier, The attenuation of a coherent field by scattering, Opt. Commun. vol. 117 (5-6) (1995) 532–540.
[25] A. Zybin, C. Grunwald, V.M. Mirsky, J. Kuhlmann, O.S. Wolfbeis, K. Niemax, Double-wavelength technique for surface plasmon resonance measurements: basic concept and applications for single sensors and two-dimensional sensor arrays, Anal. Chem. vol. 77 (8) (2005) 2393–2399.
[26] W.S. Rasband. ImageJ. National Institutes of Health. https://imagej.nih.gov/ij/.
[27] P. Valle, E. Ortiz, J. Saiz, Near field by subwavelength particles on metallic substrates with cylindrical surface plasmon excitation, Opt. Commun. vol. 137 (4-6) (1997) 334–342.
[28] B. Hecht, H. Bielefeldt, L. Novotny, Y. Inouye, D. Pohl, Local excitation, scattering, and interference of surface plasmons, Phys. Rev. Lett. vol. 77 (9) (1996) 1889.
[29] J. Maurya, Y. Prajapati, V. Singh, J. Saini, R. Tripathi, Performance of graphene–MoS 2 based surface plasmon resonance sensor using silicon layer, Opt. Quantum Electron. vol. 47 (11) (2015) 3599–3611.
[30] A.W. Peterson, M. Halter, A. Tona, A.L. Plant, High resolution surface plasmon resonance imaging for single cells, BMC Cell Biol. vol. 15 (1) (2014) 1–14.
[31] L.S. Jung, C.T. Campbell, T.M. Chinowsky, M.N. Mar, S.S. Yee, Quantitative interpretation of the response of surface plasmon resonance sensors to adsorbed films, Langmuir vol. 14 (19) (1998) 5636–5648.
[32] J.S. Shumaker-Parry, C.T. Campbell, Quantitative methods for spatially resolved adsorption/desorption measurements in real time by surface plasmon resonance microscopy, Anal. Chem. vol. 76 (4) (2004) 907–917.
[33] H. Yu, X. Shan, S. Wang, H. Chen, N. Tao, Molecular scale origin of surface plasmon resonance biosensors, Anal. Chem. vol. 86 (18) (2014) 8992–8997.
[34] H. Raether, Surface plasmons on gratings, Surf. plasmons Smooth Rough. Surf. gratings (1988) 91–116.
[35] T. Leskova, A. Maradudin, W. Zierau, Surface plasmon polariton propagation near an index step, Opt. Commun. vol. 249 (1-3) (2005) 23–35.
[36] S.-H. Cao, W.-P. Cai, Q. Liu, Y.-Q. Li, Surface plasmon–coupled emission: what can directional fluorescence bring to the analytical sciences? Annu. Rev. Anal. Chem. vol. 5 (2012) 317–336.
[37] S.I. Bozhevolnyi, V. Coello, Elastic scattering of surface plasmon polaritons: modeling and experiment, Phys. Rev. B vol. 58 (16) (1998) 10899.
[38] A. Shchegrov, I. Novikov, A. Maradudin, Scattering of surface plasmon polaritons by a circularly symmetric surface defect, Phys. Rev. Lett. vol. 78 (22) (1997) 4269.
[39] S.I. Bozhevolnyi, Localization phenomena in elastic surface-polariton scattering caused by surface roughness, Phys. Rev. B vol. 54 (11) (1996) 8177.
[40] V. Shpacovitch, et al., Application of surface plasmon resonance imaging technique for the detection of single spherical biological submicrometer particles, Anal. Biochem. vol. 486 (2015) 62–69.
[41] N. Menegazzo, B. Herbert, S. Banerji, K.S. Booksh, Discourse on the utilization of polyaniline coatings for surface plasmon resonance sensing of ammonia vapor, Talanta vol. 85 (3) (2011) 1369–1375.
[42] E. Yılmaz, E. Özgür, N. Bereli, D. Türkmen, A. Denizli, Plastic antibody based surface plasmon resonance nanosensors for selective atrazine detection, Mater. Sci. Eng.: C. vol. 73 (2017) 603–610.
[43] N. Mudgal, M.K. Falaswal, T. Ismail, I. Fahim, M. Tiwari, G. Singh, Study of approaches to implement the prism-based surface plasmon resonance sensors. Optical and Wireless Technologies, Springer, 2020, pp. 353–362.
[44] M.S. Anower, M.M. Rahman, M.S. Rahman, Hybrid heterostructures for SPR biosensor, Biosens. -Curr. Nov. Strateg. Biosens. (2021) 8.
[45] T.B.A. Akib, et al., Design and numerical analysis of a graphene-coated SPR biosensor for rapid detection of the novel coronavirus, Sensors vol. 21 (10) (2021) 3491.
[46] Q.M. Al-Bataineh, V. Shpacovitch, D. Sadiq, A. Telfah, R. Hergenröder, Surface plasmon resonance sensitivity enhancement based on protonated polyaniline films doped by aluminum nitrate, Biosensors vol. 12 (12) (2022) 1122.
[47] Q.M. Al-Bataineh, A.D. Telfah, V. Shpacovitch, C.J. Tavares, R. Hergenröder, Switchable polyacrylic acid polyelectrolyte brushes for surface plasmon resonance applications, Sensors vol. 23 (9) (2023) 4283.

Qais Al Bataineh is a physicist with excellent scientific research background and practical experiences in developing methods and investigating nanotechnology and thin films, including metals, metal oxides, metal sulfides, metal nitrides, polymers, conductive polymers, and nanocomposites, as well as their actual applications. Moreover, I focus on novel materials, methods, and techniques that have not been invented or implemented before because I believe in revolutionary research steps where the results can significantly enrich the research fields. For instance, I have derived many mathematical models, including optical bandgap energy, electrical conductivity within the percolation phenomenon, and ionic-electronic coupling. I have participated in more than 80 published research papers until now. My research in nanotechnology and thin films offered me a chance to work in the field of optical coating, antireflection coating, UV-shielding, hydrophobic and hydrophilic surfaces, optoelectronic and electronic devices, catalytic degradation, water splitting, solar energy storage materials, UV-photodetector, antimicrobial nanostructures, anticancer nanostructures, anti-corrosion coating, and biosensors. Through working in my research career, I have learned many analysis methods in characterization techniques, including chemical characterizations (using Fourier transform infrared spectroscopy (FTIR), nuclear magnetic resonance spectroscopy (NMR), X-ray photoelectron spectroscopy (XPS)), crystal characterizations (using X-ray diffraction (XRD)), morphological characterizations (using scanning electron microscope (SEM), atomic force microscope (AFM), and water contact angle measurements), thermal characterizations (using thermogravimetric analysis (TGA) and Differential scanning calorimetry (DSC)), optical characterizations (using UV-Vis spectroscopy), electrical characterizations (using IV-characteristic, 4-point probe, and electrical impedance), and dielectric characterizations (dielectric impedance). Nowadays, I am working on my Ph.D. dissertation about sensitivity enhancement of wide-field surface plasmon resonance microscopy for individual nano-objects detection. Through my Ph.D. study, I derived a discrete particle model of SPR to describe the SPR sensor of discrete particle detection.

5.2. Original Paper II: (Al-Bataineh et al., 2022)

biosensors

MDPI

Article

Surface Plasmon Resonance Sensitivity Enhancement Based on Protonated Polyaniline Films Doped by Aluminum Nitrate

Qais M. Al-Bataineh [1,2,*], Victoria Shpacovitch [1], Diyar Sadiq [3], Ahmad Telfah [1,4] and Roland Hergenröder [1,*]

[1] Leibniz Institut für Analytische Wissenschaften-ISAS-e.V., Bunsen-Kirchhoff-Straße 11, 44139 Dortmund, Germany
[2] Experimental Physics, TU Dortmund University, 44227 Dortmund, Germany
[3] Centre for Material Science and Nanotechnology, Department of Physics, The University of Zakho, Zakho Box. 12, Iraq
[4] Nanotechnology Center, The University of Jordan, 11942 Amman, Jordan
* Correspondence: qais.al-bataineh@isas.de (Q.M.A.-B.); roland.hergenroeder@isas.de (R.H.)

Abstract: Complex composite films based on polyaniline (PANI) doped hydrochloric acid (HCl) incorporated with aluminum nitrate ($Al(NO_3)_3$) on Au-layer were designed and synthesized as a surface plasmon resonance (SPR) sensing device. The physicochemical properties of (PANI-HCl)/$Al(NO_3)_3$ complex composite films were studied for various $Al(NO_3)_3$ concentrations (0, 2, 4, 8, 16, and 32 wt.%). The refractive index of the (PANI-HCl)/$Al(NO_3)_3$ complex composite films increased continuously as $Al(NO_3)_3$ concentrations increased. The electrical conductivity values increased from 5.10 µS/cm to 10.00 µS/cm as $Al(NO_3)_3$ concentration increased to 32 wt.%. The sensitivity of the SPR sensing device was investigated using a theoretical approach and experimental measurements. The theoretical system of SPR measurement confirmed that increasing $Al(NO_3)_3$ in (PANI-HCl)/$Al(NO_3)_3$ complex composite films enhanced the sensitivity from about 114.5 [Deg/RIU] for Au-layer to 159.0 [Deg/RIU] for Au-((PANI-HCl)/$Al(NO_3)_3$ (32 wt.%)). In addition, the signal-to-noise ratio for Au-layer was 3.95, which increased after coating by (PANI-HCl)/$Al(NO_3)_3$ (32 wt.%) complex composite layer to 8.82. Finally, we conclude that coating Au-layer by (PANI-HCl)/$Al(NO_3)_3$ complex composite films enhances the sensitivity of the SPR sensing device.

Keywords: polyaniline (PANI); aluminum nitrate ($Al(NO_3)_3$); complex composite films; surface plasmon resonance (SPR); electrical conductivity

Citation: Al-Bataineh, Q.M.; Shpacovitch, V.; Sadiq, D.; Telfah, A.; Hergenröder, R. Surface Plasmon Resonance Sensitivity Enhancement Based on Protonated Polyaniline Films Doped by Aluminum Nitrate. *Biosensors* **2022**, *12*, 1122. https://doi.org/10.3390/bios12121122

Received: 12 October 2022
Accepted: 30 November 2022
Published: 3 December 2022

1. Introduction

Light photons interact with the conduction electrons at the metal/dielectric interface, which generates longitudinal surface waves called surface plasmons [1]. Recently, SPR (surface plasmon resonance)-based sensors have earned growing attention due to their high sensitivity and capability to perform real-time measurements [2,3]. The imaging wide-field SPR microscopy sensor is an optical device that enables the spatiotemporal detection of individual nano-particles in solutions and gas media [4–9]. The described wide-field SPR microscopy sensor is based on Kretschmann's scheme [10] of plasmon excitation. In this scheme, a thin (around 50 nm) planar gold film coats the base of a glass prism and is irradiated by a laser beam. In an attempt to enhance the sensitivity of SPR sensors, various design modifications have been employed, such as the incorporation of different nanostructures [11,12], bimetallic layers [13,14], and conducting and insulating polymer coating [15,16]. Conductive polymer films located on the gold layer have been used to improve the SPR sensitivity [17,18] due to their electrical, optical, and chemical properties [19,20]. F. Usman et al. [21] investigated the sensitivity of SPR-based sensors based on polyaniline/chitosan composite film for detecting low-concentration acetone

vapor. They found that polyaniline/chitosan composite film has good selectivity and sensitivity for detecting low-concentration acetone vapor.

Polyaniline (PANI) is an attractive conductive polymer because it exhibits thermal and electrochemical stability, can be relatively easily prepared, and possesses excellent biocompatibility, flexibility, conductivity, and optoelectrical characteristics [17]. PANI composite films are promising candidates for many applications, such as organic solar cells, photodetectors, and gas sensors [22–26]. The high optical response of PANI can be the foremost essential property for optical bio-detectors due to its simplicity, high stability, and cost-effectiveness [27–29]. Doping PANI with protonic acids containing different types of counterions enhances electrical conductivity and stability under ambient conditions [30]. Introducing metal ions into the polymer matrix enhances the ionic kinetics of the composite by inducing greater closeness through the metal/polymer blend [31]. In addition, incorporating polymer with aluminum (Al^{3+}) ions enhances the electrical conductivity and tuning of the optical properties [32]. Al^{3+} ions could be incorporated with the polymer as intense ions using aluminum nitrate ($Al(NO_3)_3$), aluminum chloride ($AlCl_3$), or other ionic forms. However, using aluminum nitrate as incorporation in a polymer matrix is favorable due to the hydrogen bonds between it and the polymer [33]. In addition, aluminum nitrate is an ionic compound composed of aluminum metal and a nitrogen oxoanion that is used for corrosion inhibitors, nitrating agents, and insulating papers [34].

In this research, the SPR microscopy sensor based on (PANI-HCl)/$Al(NO_3)_3$ complex composite layer on Au-layer was designed to enhance the sensitivity of the instrument. (PANI-HCl)/$Al(NO_3)_3$ complex composite films were chosen as a model of SPR application due to their high refractive index, which enhances the SPR signal sensitivity. The sensitivity of the SPR sensor was studied using a theoretical approach and experimental measurements based on imaging a wide-field SPR microscopy sensor. In addition, the structural, chemical, morphological, optical, and electrical properties of (PANI-HCl)/$Al(NO_3)_3$ complex composite films were investigated.

2. Materials and Methods

2.1. Synthesis Technique

Protonated PANI composite solution was synthesized by dissolving 0.5 g Polyaniline (PANI, emeraldine base, M_W = 50,000 g/mol, Sigma Aldrich, Darmstadt, Germany) with 0.07 mL hydrochloric acid (HCl, M_w = 36.458 g/mol, Sigma Aldrich) in 100 mL N-Methyl-2-Pyrrolidone (NMP, M_w = 99.133 g/mol, Sigma Aldrich) using a magnetic stirrer overnight at 55°C. The PANI-HCl composite solution was then transferred to a sonication bath for 3 h at 55°C to reach high homogeneity. The solution was filtered using a centrifuge system and filter paper according to a protocol in the literature [35]. (PANI-HCl)/$Al(NO_3)_3$ complex composite solutions were prepared by adding aluminum nitrate ($Al(NO_3)_3$, 212.996 g/mol, Sigma Aldrich) directly into the PANI-HCl composite solution by the desired amount to achieve the desirable concentrations (0, 2, 4, 8, 16, and 32 wt.%). (PANI-HCl)/$Al(NO_3)_3$ complex composite solutions were homogenized using continuous stirring overnight at room temperature. Next, the complex composite solutions were transferred to a sonication bath for 3 h at 55°C to reach high homogeneity. (PANI-HCl)/$Al(NO_3)_3$ complex composite films were synthesized by spin coating technique to achieve 250 nm film thickness. The complex composite films were dried at 40°C in a vacuum oven for 24 h to ensure the total solvent drying and avoid morphology changing. In addition, the (PANI-HCl)/$Al(NO_3)_3$ complex composite film on the gold layer was deposited using the spin coating technique at a higher speed to get a smooth layer with a 30 nm film thickness.

2.2. Characterization Techniques

All measurements were performed under ambient conditions. The chemical properties of the complex composite were investigated by studying the vibrational bands obtained from FTIR microscope measurement (HYPERION 3000 Bruker, Karlsruhe,

Germany). In addition, the crystal structure was studied using Powder XRD (Malvern Panalytical Ltd., Malvern, UK) using CuKα_1 ray (λ = 0.1540598 nm). Surface wettability was studied using water contact angle measurements for a water droplet (pH = 7) of size 10 µL taken on three occasions. The thermal stability was measured using thermogravimetric analysis (TGA) (NETZSCH Premier Technologies). Optical properties were investigated by analyzing transmittance, and reflectance spectra were measured using a UV–Vis spectrophotometer (Hitachi U-3900H) with a total internal sphere. The electrical conductivity was measured by a 4-point probe (Microworld Inc., New Jersey, USA) connected with a high-resolution multimeter (Keithley 2450 Sourcemeter) for various temperatures from 298–328 K.

2.3. Surface Plasmon Resonance (SPR) Measurements

The SPR experimental setup was built up as described previously [8,36]. Glass slides with the same refractive index as a prism (n = 1.725) and made from the same type of glass (SF10) were employed as sensing surface carrying slides (glass slides were produced by Hellma Optics, Jena, Germany). Glass slides (sizes 14 × 75 × 1 mm) were coated with 5 nm adhesion layer of Ti and approximately 41–45 nm layer of gold [8]. The deposition was performed using a magnetron-sputtering technique (Innolume, Dortmund, Germany). The gold layer was used as a seed layer on the prism for (PANI-HCl)/Al$(NO_3)_3$ complex composite film. A laser diode (HL6750MG, Thorlabs GmbH, Bergkirchen, Germany; λ = 685 nm) was used to irradiate the (Au-(PANI-HCl)/Al$(NO_3)_3$) layer through a glass prism. The (Au-(PANI-HCl)/Al$(NO_3)_3$) layer was imaged onto a video camera with a CMOS chip (MT9P031 CMOS image sensor chip with a resolution of 5 Mp (megapixel). This chip possesses a pixel size of 2.2 × 2.2 µm) employing macro-objective (Cannon Compact-Macro Lens EF 50 mm 1:2.5). The gold substrate was placed on the glass prism using RI matching immersion liquid (Cargille Laboratories via VWR (n = 1.725) to avoid the air gap between the Au layer and prism. The resonance angle represented the minimum reflectivity of the camera image. Polystyrene nanoparticles (PSNPs, refractive index n = 1.59 [37]) with an average size of 200 nm were used in SPR measurements.

3. Results and Discussion

3.1. Physicochemical Properties

The chemical and crystal structure of (PANI-HCl)/Al$(NO_3)_3$ complex composite films was characterized by analyzing the FTIR absorbance spectra (Figure 1, Table 1) and XRD patterns (Figure 2). For PANI-HCl film, the absorption band at 506 cm^{-1} represented the out-of-plane $C-H$ bending vibrations, while the absorption band at 660 cm^{-1} referred to $C=N$ iminoquinone [38,39]. The absorption band at 825 cm^{-1} referred to paradisubstituted aromatic rings indicating polymer formation [30]. Moreover, the absorption band at 1172 cm^{-1} represented the in-plane $C-H$ bending vibrations within the quinoid unit ($N=Q=N$). The absorption band at 1314 cm^{-1} represented the aromatic $C-N$ stretching vibrations within a secondary aromatic amine group, confirming the protonation of PANI with HCl [35]. In addition, $C-N$ stretching vibrations within benzenoid ($N-B-N$) and quinoid ($N=Q=N$) rings appeared at 1515 and 1615 cm^{-1}, respectively. The absorption bands between 1999 and 2155 cm^{-1} represented the aromatic $C-H$ stretching vibrations, while the absorption bands after 3000 cm^{-1} represented the $N-H$ stretching vibrations [30,38]. The appearance of an additional peak at 420 cm^{-1} ($Al-N$) in (PANI-HCl)/Al$(NO_3)_3$ complex composite films confirmed the existence of Al^{3+} ions inside the polymer matrix within Al^{3+} ions connected with the N atoms in the benzoin ring of the PANI or as Al$(NO_3)_3$ [40]. In conclusion, FTIR absorbance spectra confirmed the protonation of PANI by HCl in addition to their interactions with Al$(NO_3)_3$.

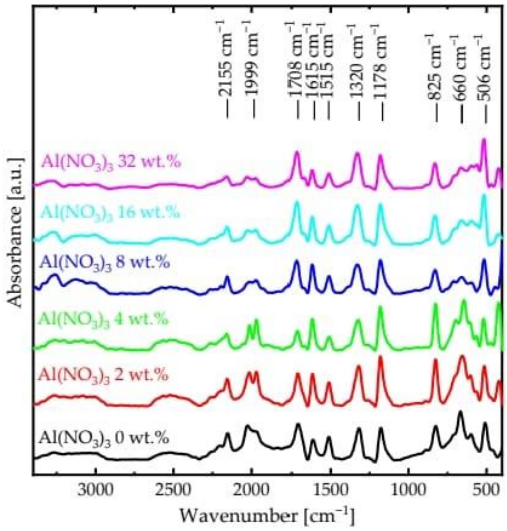

Figure 1. FTIR spectra of (PANI-HCl)/$Al(NO_3)_3$ complex composite films with various $Al(NO_3)_3$ concentrations.

Table 1. Vibrational bands of (PANI-HCl)/$Al(NO_3)_3$ complex composite film for different $Al(NO_3)_3$ concentrations.

Absorption Bands	$Al(NO_3)_3$ 0 wt.%	$Al(NO_3)_3$ 2 wt.%	$Al(NO_3)_3$ 4 wt.%	$Al(NO_3)_3$ 8 wt.%	$Al(NO_3)_3$ 16 wt.%	$Al(NO_3)_3$ 32 wt.%
out-of-plane C − H bending	506	510	515	517	519	521
C = N iminoquinone	660	658	656	652	650	646
paradisubstituted aromatic rings	825	827	828	829	832	835
in-plane C − H bending vibrations	1178	1178	1178	1184	1184	1184
aromatic C − N stretching	1320	1320	1320	1329	1334	1334
C − N stretching (N − B − N)	1515	1514	1511	1511	1511	1511
C − N stretching (N = Q = N)	1615	1615	1615	1615	1615	1615

The crystalline nature of the PANI is essential because the highly crystalline conductive polymer displays a conductive property [41]. However, PANI crystallinity depends on synthesis conditions in addition to acid dopants [42]. The XRD patterns for PANI-HCl film showed broad diffraction peaks at 2θ of 14.97°, 20.72°, and 25.38° associated with the crystallographic plane (200), (100), and (110), respectively, which indicated the low degree of crystallinity (Figure 2). All peaks were in good agreement with the literature [43]. Moreover, the broad peak between 10° and 35° and the three diffraction peaks confirmed that PANI-HCl film had a semi-crystalline nature. According to Bhadra and Khastgir [44], PANI has semi-crystalline nature with two phases; the crystal phase, in which the polymer chains are ordered in the close-packed array, and the amorphous phase, where the polymer chains do not order. Introducing $Al(NO_3)_3$ into PANI-HCl film led to an increase in the (200) and (110) plane intensities, which means that the Al^{3+} interacted with the PANI-HCl matrix at N atoms and consequently changed the crystal structure of the complex composite films by making it ordered in the close-packed array.

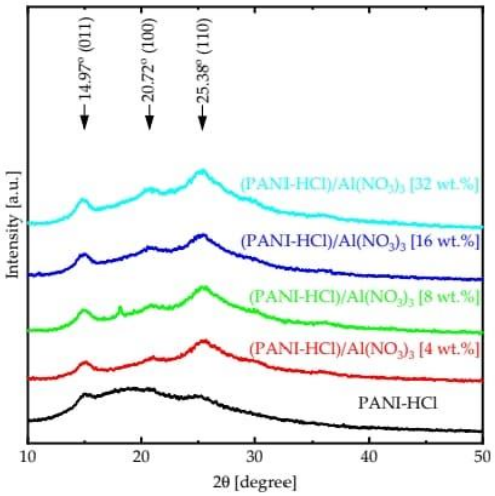

Figure 2. XRD patterns for (PANI-HCl)/$Al(NO_3)_3$ complex composite films for varying $Al(NO_3)_3$ concentrations (wt.%).

Figure 3 shows the SEM images for (PANI-HCl)/$Al(NO_3)_3$ complex composite films at $Al(NO_3)_3$ concentrations of 0, 8, and 32 wt.%. The PANI-HCl film showed a rod-like shape with an average diameter of 130 nm (Figure 3a). Adding $Al(NO_3)_3$ into the PANI-HCl films by 8% and 32% led to a decrease in the average diameter of rod-like shapes to 92 nm and 45 nm, respectively (Figure 3b,c). In addition, adding $Al(NO_3)_3$ to the PANI-HCl films also increased the film surface's smoothness.

The surface wettability, in addition to SEM micrographs of the (PANI-HCl)/$Al(NO_3)_3$ complex composite films with various $Al(NO_3)_3$ concentrations, was studied to understand the physicochemical interactions between polymer matrix and $Al(NO_3)_3$ (Figure 4). The WCA for PANI-HCl film was 38°, which means that the PANI-HCl film exhibited a hydrophilic nature [45]. Increasing $Al(NO_3)_3$ in (PANI-HCl)/$Al(NO_3)_3$ complex composite films reduced the WCA continuously until it reached 20° at $Al(NO_3)_3$ concentration of 32 wt.%, which means that increasing $Al(NO_3)_3$ concentration in (PANI-HCl)/$Al(NO_3)_3$ complex composite films enhanced the hydrophilicity nature of the film surface, which was attributed to a decrease in the average diameter of rod-like shapes and a reduction in the surface roughness.

The thermal stability of (PANI-HCl)/$Al(NO_3)_3$ complex composite films was investigated using Thermogravimetric Analysis (TGA) at temperatures up to 500°C (Figure 5). TGA curves of all composite films underwent two stages of weight loss. In the first stage, the PANI-HCl film lost around 13% of its weight when the temperature rose from 75°C to 300°C, which was attributed to solvent evaporation. In addition, the second stage showed a considerable weight loss (around 42%) as the temperature rose from 300°C to 500°C, which was attributed to the PANI chains decomposition [30]. The weight loss of all composite films shifted toward higher temperatures as increasing $Al(NO_3)_3$ concentrations increased, which was attributed to an increase in the strength of physicochemical bonding density in the (PANI-HCl)/$Al(NO_3)_3$ complex composite films [46]. To conclude, (PANI-HCl)/$Al(NO_3)_3$ complex composite films were thermally stable within the temperatures at the optical, electrical, and SPR applications.

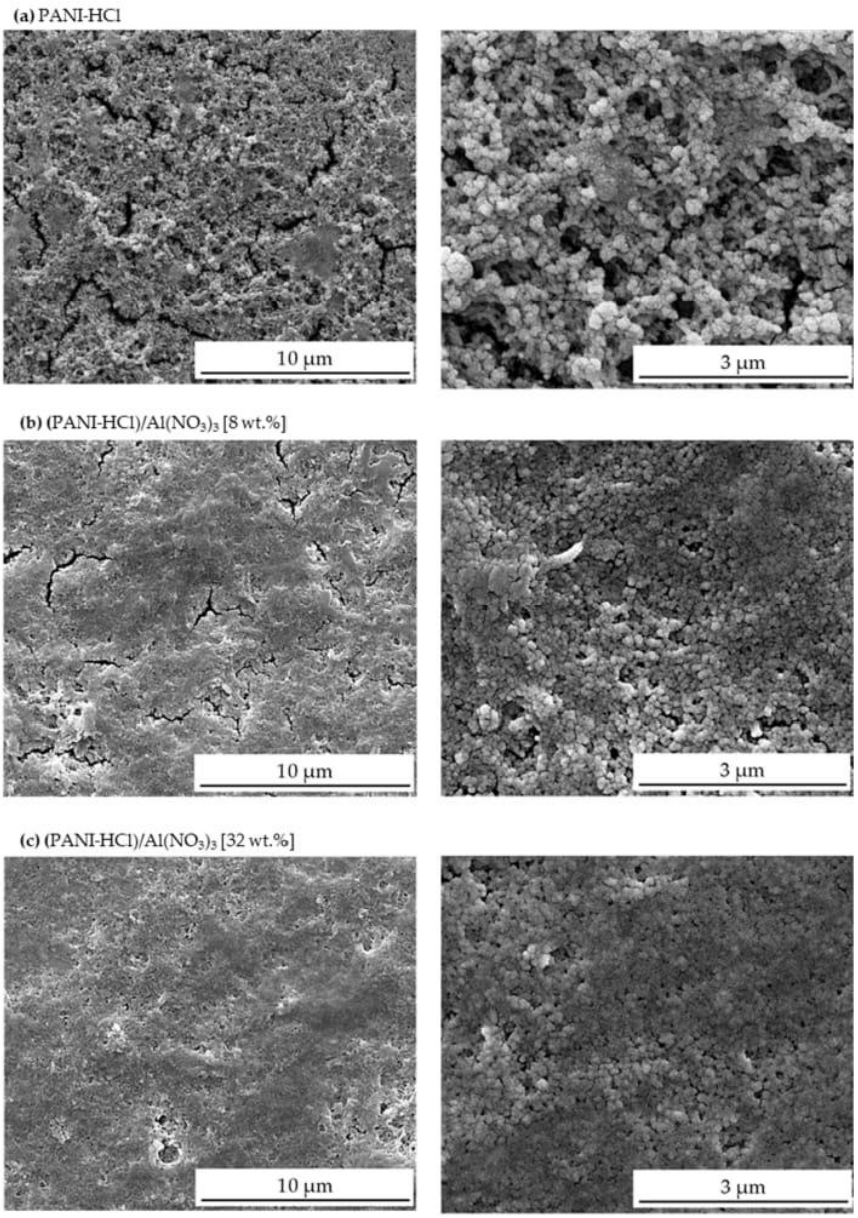

Figure 3. SEM micrographs from (PANI-HCl)/$Al(NO_3)_3$ complex composite films with $Al(NO_3)_3$ concentration (0, 8, and 32 wt.%).

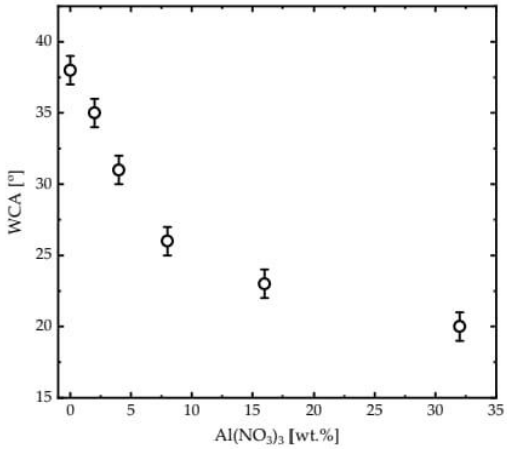

Figure 4. Water contact angles of (PANI-HCl)/$Al(NO_3)_3$ complex composite films as a function of $Al(NO_3)_3$ concentration.

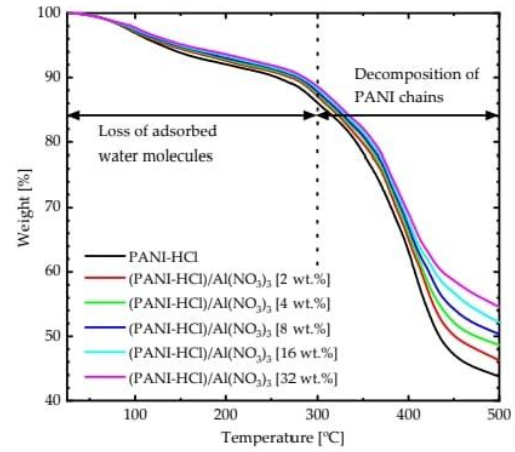

Figure 5. TGA curves of (PANI-HCl)/$Al(NO_3)_3$ complex composite films with various $Al(NO_3)_3$ concentrations.

3.2. Optical Characterizations

UV-Vis transmittance, reflectance spectra, and the corresponding optical properties of (PANI-HCl)/$Al(NO_3)_3$ complex composite films are illustrated in Figure 6. The transmittance spectra of the PANI-HCl film exhibited the first steep escalating values from around 0.0% up to 47.5% as the wavelength increased from 300 nm to 370 nm, and the second steep escalating values from 51.0% up to 63.0% as the wavelength increased from 440 nm to 490 nm. In addition, by increasing the wavelength from 490 nm to 700 nm, the transmittance decreased from 63.0% to 52.5% (Figure 6a). Introducing $Al(NO_3)_3$ into the PANI-HCl films reduced the transmittance values in the visible region with non-linear behavior. For instance, the transmittance value of PANI-HCl film at 550 nm was 60%, which decreased to 31% for (PANI-HCl)/$Al(NO_3)_3$ complex composite film with 32 wt.% of $Al(NO_3)_3$. Additionally, the sharp decrease in the transmittance of the PANI-HCl film in the UV region (300–370 nm) indicated strong electronic transitions within a high-absorption region. The inclusion of $Al(NO_3)_3$ into the PANI-HCl films led to a red shift in

the absorption edge, which means increased electron transitions between the PANI and Al^{+3} ions. The reflectance spectra of (PANI-HCl)/$Al(NO_3)_3$ complex composite films with different $Al(NO_3)_3$ concentrations are presented in Figure 6b. The reflectance continuously decreased as the wavelength increased from 250 nm to 700 nm. Incorporation of $Al(NO_3)_3$ into the PANI-HCl films increased reflectance. As expected, the reflectance spectrum showed the opposite trend to the transmittance spectrum.

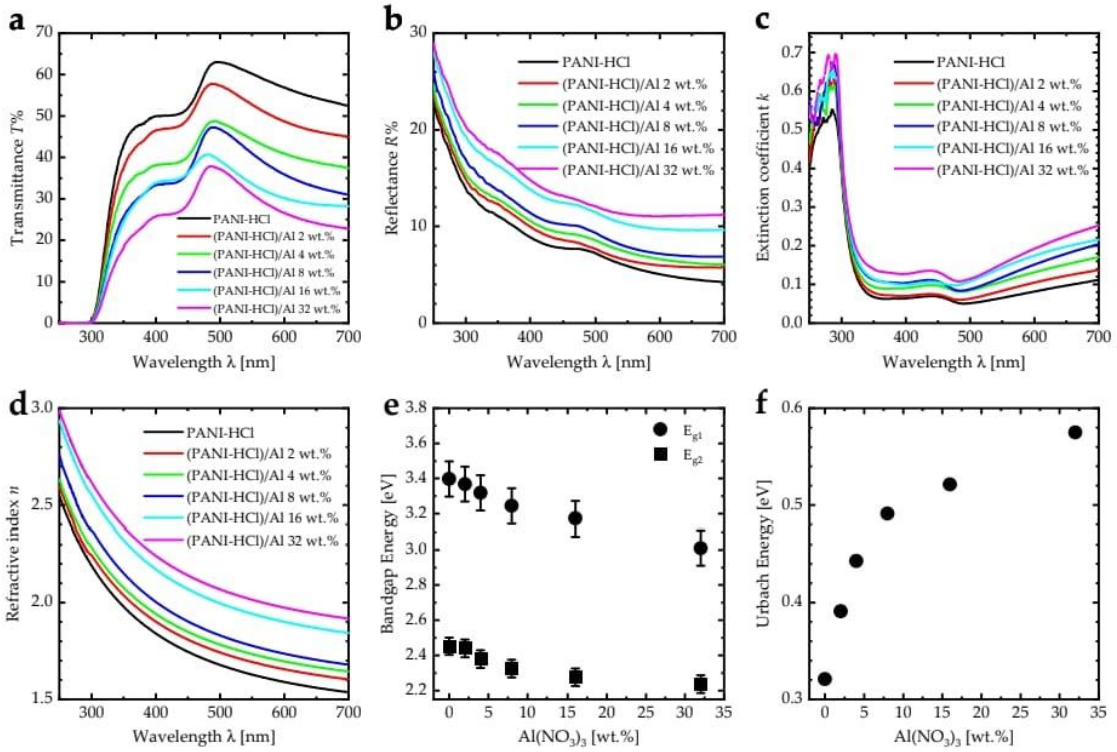

Figure 6. (**a**) Transmittance spectra, (**b**) reflectance spectra, (**c**) extinction coefficient spectra, (**d**) refractive index spectra, (**e**) bandgap energy, and (**f**) Urbach energy for (PANI-HCl)/$Al(NO_3)_3$ complex composite films with varying $Al(NO_3)_3$ concentration.

The extinction coefficient (k) can be calculated using $k = \alpha\lambda/4\pi$, where α is the absorption coefficient, given by $\alpha = (1/d)\ln((1\text{-}R)/T)$, where R is the reflectance, T is the transmittance, and d is the film thickness [47]. The extinction coefficient spectra had a noticeable drop in the wavelength range of 250–350 nm, indicating strong electronic transitions within a high-absorption region (Figure 6c). However, the increase in $Al(NO_3)_3$ concentration in (PANI-HCl)/$Al(NO_3)_3$ complex composite films increased the extinction coefficient values in the visible region, indicating that more photon energy was lost by absorption and scattering. Additionally, the extinction coefficient spectra of (PANI-HCl)/$Al(NO_3)_3$ complex composite films exhibited overlapping bands in the region of 360–500 nm, representing the π-π^* transition within the benzoin ring and localized polarons (polaron-π^*) transition [48]. The increase in the extinction coefficient values after 500 nm was attributed to the π-polaron transition, which occurred between 820–840 nm [49]. The extinction coefficient peak was de-convoluted by fitting the spectral envelope to four Gaussian peaks as a function of energy (Figure 7) [50]. The fitting was converged with an R^2 of about 0.99. De-convoluted was tested by fitting the extinction coefficient band to Lorentzian, bi-Gaussian, and Voigt functions, but the fitting converged more poorly than the Gaussian

fitting. Before fitting, the baseline correction was performed according to the algorithm described in [51]. For the PANI-HCl film, the first peak at 3.24 eV represented the π-π* transition. In addition, the other three peaks at 2.92 eV, 2.77 eV, and 2.67 eV represented the polaron-π* transition [48]. The broad distribution of the polaron-π* transition can be attributed to how the rod-like shape increased the interaction between polarons and consequently improved the interband transitions [52]. Adding $Al(NO_3)_3$ into the PANI-HCl led to a decrease in the π-π* transition band until it disappeared at 16 wt.% of $Al(NO_3)_3$, which can be attributed to the interaction between the nitrogen atom in the benzoin ring of PANI and the Al^{3+} ions (Figure 1).

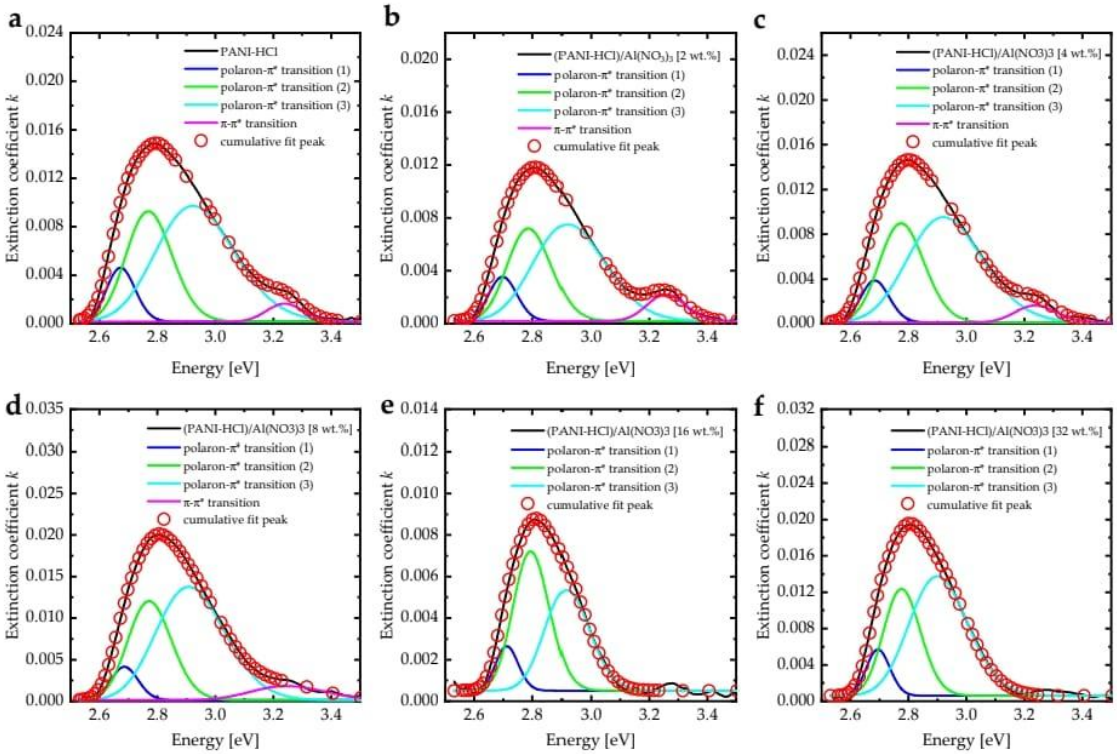

Figure 7. The extinction coefficient band de-convoluted by fitting the spectral envelope to four Gaussian peaks of (PANI-HCl)/$Al(NO_3)_3$ complex composite films with varying $Al(NO_3)_3$ concentrations: (**a**) 0, (**b**) 2, (**c**) 4, (**d**) 8, (**e**) 16, and (**f**) 32 wt.%.

The refractive index values (n) can be calculated using $n = (1 + R)/(1 - R) + \sqrt{(4R/(1 - R)^2) - k^2}$ and fitted to the Cauchy model, which is given by $n = A + B/\lambda^2$, where A and B are constants [53]. The refractive index for the PANI-HCl film decreased from 2.55 to 1.54 as the incident photon wavelength increased from 250 nm to 700 nm (Figure 6d). Moreover, increasing the $Al(NO_3)_3$ concentration in (PANI-HCl)/$Al(NO_3)_3$ complex composite films increased the refractive index due to the interaction between Al^{3+} ions and the PANI interaction that may increase the compositional density of the composite films [54].

Tauc plots were performed to investigate the bandgap energy of (PANI-HCl)/$Al(NO_3)_3$ complex composite films by plotting $(\alpha h\nu)^2$ versus $h\nu$, according to the equation $(\alpha h\nu)^2 = \beta(h\nu - E_g)$ for direct band-gap semiconductors. All the films exhibited two bandgap energies; the first band-gap energy (E_{g1}) decreased from 3.40 eV to 3.01 eV, representing the π-π* electron transition within the benzenoid (B) ring, while the second

bandgap energy (E_{g2}) decreased from 2.45 eV to 2.24 eV, representing localized polarons (polaron-π*) (quinoid, Q) electron transition (Figure 6e). The decrease in the bandgap energies as increasing $Al(NO_3)_3$ can be attributed to generating new energy levels between the HUMO and LOMO because of the disorder in the structure of the composite films [55]. Urbach energy, E_U is considered an essential method for studying the degree of disorder in films, which is calculated using $\alpha = \alpha_0 \exp(h\nu/E_U)$, where: α_0 is a constant [56,57]. The Urbach energy for the PANI-HCl film was 321 meV, which was consistent with the Urbach energy for PANI-CSA in the literature [58]. An increase of the concentration of $Al(NO_3)_3$ in the PANI-HCl matrix to 32 wt.% led to the growth of Urbach energy to 575 meV, suggesting the highest disorder at this concentration.

3.3. Electrical Conductivity

Figure 8a illustrates the electrical conductivity (σ) variations of the (PANI-HCl)/$Al(NO_3)_3$ complex composite films as a function of $Al(NO_3)_3$ concentration. The electrical conductivity of the PANI-HCl film was 5.10 μS/cm, which can be attributed to the polaron states in PANI and doping by HCl, which has an essential influence on polymer oxidation. However, the conductivity of the (PANI-HCl)/$Al(NO_3)_3$ complex composite films can be attributed to the superposition of polaron states in PANI and the effects of the Al^{3+} ions [59]. An increase of $Al(NO_3)_3$ concentration in the PANI-HCl films to 32% led to the growth of conductivity up to 10.00 μS/cm due to the increase of Al^{3+} ion density, which was determined through the conduction process formed by the incorporation $Al(NO_3)_3$ with PANI by ionic interactions [60]. The electrical conductivity of (PANI-HCl)/$Al(NO_3)_3$ complex composite films increased as the temperature increased (Figure 8b). This can be attributed to the thermal activation of ion mobility and electron hopping [61]. In addition, the electrical conductivity values as a function of 1000/T(K) for (PANI-HCl)/$Al(NO_3)_3$ complex composite films were fitted to the Arrhenius function ($\sigma = \sigma_0 \exp(-E_a/K_BT)$) [32]. The activation energy (E_a) of (PANI-HCl)/$Al(NO_3)_3$ complex composite films increased with increasing $Al(NO_3)_3$ concentration (Figure 8c).

The conductivity maps (1 cm × 1 cm) of (PANI-HCl)/$Al(NO_3)_3$ complex composite films are shown in Figure 9. The conductivity of the PANI-HCl film showed a slight alteration of electrical conductivity across the film (Figure 9a), which can be attributed to the surface morphology and growth process quality. Including $Al(NO_3)_3$ in the PANI-HCl film increased the electrical conductivity across the film. Moreover, the electrical conductivity of (PANI-HCl)/$Al(NO_3)_3$ complex composite films had a semi-homogeneous distribution (Figures 9b to 9f).

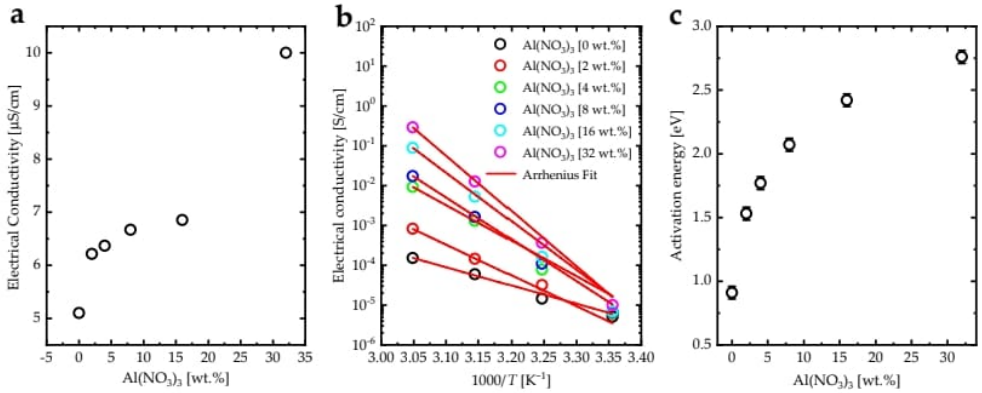

Figure 8. (**a**) Electrical conductivity vs. $Al(NO_3)_3$ concentration [wt.%], (**b**) electrical conductivity vs. 1000/T [K^{-1}], and (**c**) activation energy vs. $Al(NO_3)_3$ concentration [wt.%] for (PANI-HCl)/$Al(NO_3)_3$ complex composite films.

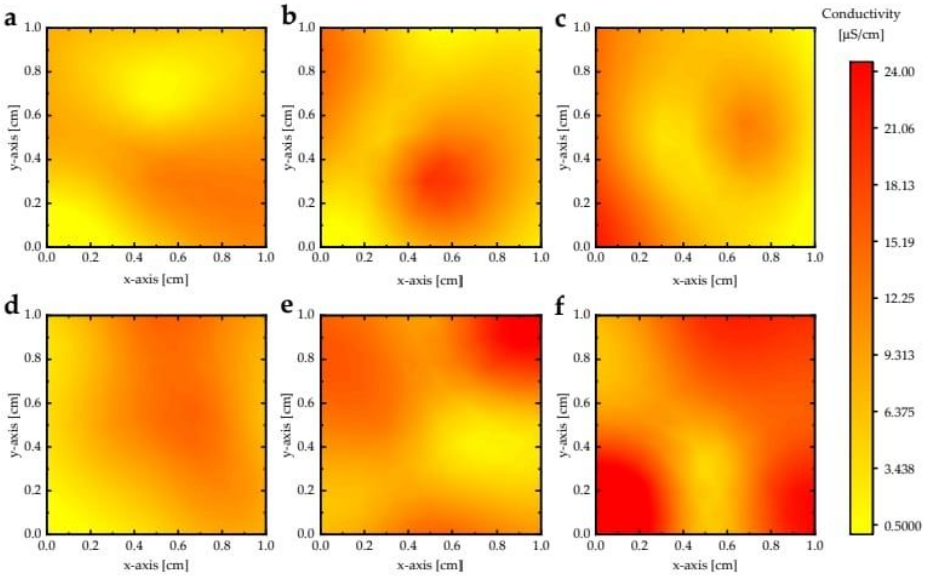

Figure 9. The conductivity maps (1 cm × 1 cm) of (PANI-HCl)/$Al(NO_3)_3$ complex composite films with $Al(NO_3)_3$ concentrations: (**a**) 0 wt.%, (**b**) 2 wt.%, (**c**) 4 wt.%, (**d**) 8 wt.%, (**e**) 16 wt.%, and (**f**) 32 wt.%.

3.4. Surface Plasmon Resonance (SPR) Measurements

This section describes a model built using real SPR microscopy sensor measurements. The (PANI-HCl)/$Al(NO_3)_3$ complex composite films were used to improve the SPR sensitivity [62]. The model was composed of a glass prism, a titanium adhesion layer (5 nm), a gold layer (41–45 nm), and a (**P**ANI-HCl)/$Al(NO_3)_3$ complex composite layer (30 nm) (Figure 10). Additionally, (PANI-HCl)/$Al(NO_3)_3$ complex composite films were connected with the analyte (water) for detecting polystyrene nanoparticles. The n of each complex composite layer was determined experimentally (Figure 6) at a wavelength of 685 nm in order to match the wavelength in the theoretical model to that used in the experimental SPR measurements (Table 1) since W. Mukhtar et al. [63] concluded that visible light in the range of 600–700 nm has **a** high sensitivity for SPR measurements.

Figure 11a shows the theoretical reflectivity values of the Au layers for selected concentrations of $Al(NO_3)_3$ as a function of beam angle using WINSPALL software [64]. The inclusion of $Al(NO_3)_3$ in (PANI-HCl)/$Al(NO_3)_3$ complex composite films increased the incident photon angle at minimum reflectivity (Table 2). The sensitivity of the SPR sensor based on Au-((PANI-HCl)/$Al(NO_3)_3$) layers was calculated by $S = \Delta\theta/\Delta n$, where: $\Delta\theta$ represented the SPR angle shift [degree] and Δn was refractive index change [refractive index unit: RIU]. The linear fit of the SPR angle shift as a function of refractive index changes represented the sensitivity of the SPR sensor (Figure 11b). Inclusion of $Al(NO_3)_3$ in the PANI-HCL films enhanced the SPR sensitivity from 114.5 [Deg/RIU] for pare Au-layer to 159.0 [Deg/RIU] for Au-((PANI-HCl)/$Al(NO_3)_3$) layers for 32 wt.% of $Al(NO_3)_3$ (Figure 11c). In addition, another measurement scale for getting a clear concept of the sensing efficiency is the figure of merit (FOM) of the sensor. This is determined as the ratio of the sensitivity to the sensor's linewidth (LW), which is given by FOM = S/LW [65]. According to the definition of FOM, increasing the sensitivity led to enhancing the FOM. However, the higher increases in the LW decreased the FOM values. Therefore, the FOM decreased as $Al(NO_3)_3$ concentrations decreased in the PANI-HCl.

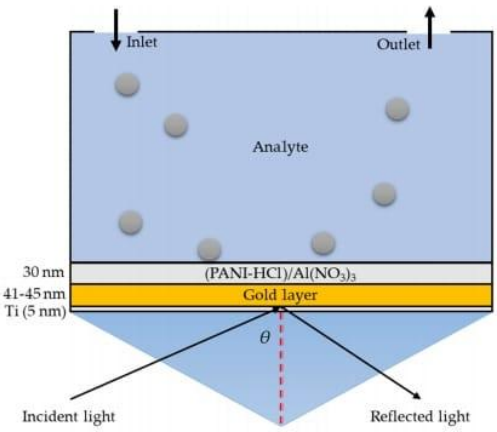

Figure 10. Kretschmann configuration employed in SPR-microscopy sensor: a glass prism, titanium adhesion layer (5 nm), gold layer (41–45 nm), and (PANI-HCl)/$Al(NO_3)_3$ complex composite layer (30 nm) with an analyte for sensing biomolecules.

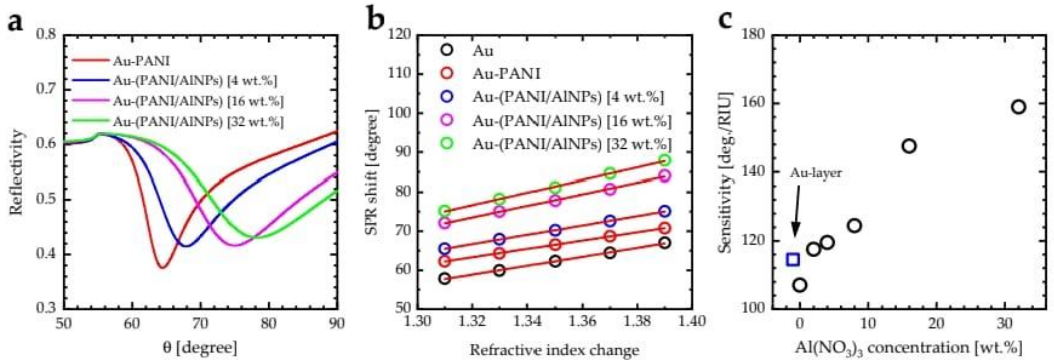

Figure 11. (**a**) SPR reflectivity curve for Kretschmann configuration of the prism-gold-(PANI-HCl)/$Al(NO_3)_3$ systems for selected $Al(NO_3)_3$ content [wt.%], (**b**) SPR angle shift versus the refractive index change of selected $Al(NO_3)_3$ content [wt.%], and (**c**) Sensitivity variation as a function of $Al(NO_3)_3$ concentration [wt.%] of prism-gold-(PANI-HCl)/$Al(NO_3)_3$ system.

Table 2. Optical constant values, SPR angle, and SPR sensitivity of the gold film, and (PANI-HCl)/$Al(NO_3)_3$ complex composite film for different $Al(NO_3)_3$ concentrations at a wavelength of 685 nm.

$Al(NO_3)_3$ Concentration [wt.]	Refractive Index *n*	Extinction Coefficient *k*	SPR Angle [°]	SPR Sensitivity [deg/RIU]	Figure of Merit (FOM) [RIU^{-1}]
Gold layer	0.15 [66]	4.91 [66]	59.9	114.5	79.51
0	1.51	0.11	64.3	107.0	8.99
2	1.61	0.13	67.0	117.5	8.64
4	1.63	0.17	67.9	119.5	6.91
8	1.67	0.19	69.1	124.5	6.66
16	1.87	0.21	75.0	147.5	7.45
32	1.96	0.24	78.2	159.0	7.23

The detection of spherical PSNPs (200 nm) by Au layer and Au-((PANI-HCl)/$Al(NO_3)_3$) layers with $Al(NO_3)_3$ concentration of 32 wt.% were studied

experimentally. After recording images using a CMOS camera, ImageJ software [67] was applied for image processing, including averaging and background subtraction. Figure 12a illustrates the relative intensity before the binding of PSNPs with the surface and the sudden increase of the local intensity level in a moment of a nano-particle binding. The signal intensity to the noise intensity of the Au-((PANI-HCl)/Al(NO_3)$_3$) layers was higher than the signal intensity to the noise intensity of the Au layer. The performance of the SPR measurement was investigated by calculating the signal-to-noise ratio (S/N) in addition to the linewidth in the line profile plot in the x-direction parallel to the surface plasmon propagation vector for three individual bound PSNPs to the surface presented in the inset [56] (Figure 12b,c). The average signal-to-noise ratio for Au-layer was 6.22, which increased after coating with (PANI-HCl)/Al(NO_3)$_3$ complex composite layer to 9.97. This means (PANI-HCl)/Al(NO_3)$_3$ that complex composite films enhance the sensitivity of SPR measurement for particle detection. In addition, it was clearly seen that the average linewidth (LW) of the recorded image decreased from 4.98 pixels to 3.62 pixels by using the Au-((PANI-HCl)/Al(NO_3)$_3$) layers, which means that not only were the sensitivity and SNR improved, but the spatial resolution of the recorded image was also enhanced.

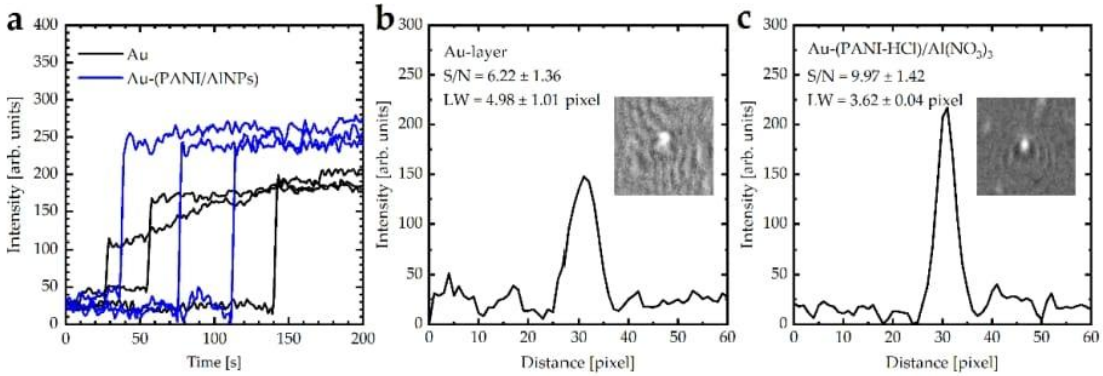

Figure 12. (**a**) Time dependence of the intensity in the middle of the three bright spots for PSNPs by Au-layer and Au-((PANI-HCl)/Al(NO_3)$_3$) layers with Al(NO_3)$_3$ concentration of 36 wt.%., (**b**) line profile plot of PSNPs detected by Au-layer, and (**c**) line profile plot of PSNPs detected by Au-((PANI-HCl)/Al(NO_3)$_3$) layers. The inset in (**b**) and (**c**) represents the typical processed image of bound polystyrene particles to the surface, which showed bright spots surrounded by a relatively low-intensity background. Three replicates were performed.

The sensor can also be used as a classical—not as a nano-particle imaging—SPR instrument. In this case, a critical parameter in classical SPR is the limit of detection (LOD), which is defined as the smallest concentration giving the output signal and given by LOD = 3σ/S, where: σ is the noise, and S is the sensitivity of the sensor [68]. The LOD value for the bare Au layer was 0.12 RIU, which decreased to 0.08 RIU after coating with (PANI-HCl)/Al(NO_3)$_3$ with a concentration of 32 wt.%. This means that coating the Au layer with (PANI-HCl)/Al(NO_3)$_3$ can detect fewer concentrations than the bare Au layer.

4. Conclusions

Synthesized (PANI-HCl)/Al(NO_3)$_3$ complex composite films were designed as a special coating for a wide-field SPR microscopy sensor chip. The structural, morphological, optical, and electrical properties of (PANI-HCl)/Al(NO_3)$_3$ complex composite films in various Al(NO_3)$_3$ concentrations were investigated and analyzed. FTIR spectra of (PANI-HCl)/Al(NO_3)$_3$ complex composite films confirmed the existence of Al^{3+} ions inside the polymer matrix within Al^{3+} ions connected with the N atoms in the benzoin ring of the PANI or existing as Al(NO_3)$_3$. In addition, the inclusion of Al(NO_3)$_3$ into the PANI-HCl

film increased the (011) and (110) plane intensities, indicating that Al^{3+} interacted with the PANI-HCl matrix at N atoms and consequently changed the crystal structure of the complex composite films. SEM images showed that the PANI-HCl film had a rod-like shape with an average diameter of 130 nm. Adding $Al(NO_3)_3$ into the PANI-HCl films by 8% and 32% decreased the average diameter of the rod-like shapes to 92 nm and 45 nm, respectively. Moreover, an increase of $Al(NO_3)_3$ concentration in (PANI-HCl)/$Al(NO_3)_3$ complex composite films enhanced the hydrophilicity of the film surface. Growing $Al(NO_3)_3$ concentration in (PANI-HCl)/$Al(NO_3)_3$ complex composite films leads to the rise of the refractive index of the complex composite film. Increasing the $Al(NO_3)_3$ concentration in the PANI-HCl films to 32% elevated the conductivity up to 10.00 μS/cm, which can be attributed to the growing Al^{3+} ion density. The sensitivity of the SPR wide-field microscopy sensor was investigated using a theoretical approach and experimental measurements. The modeling (simulation) of SPR measurements confirmed that the inclusion of growing concentrations of $Al(NO_3)_3$ in (PANI-HCl)/$Al(NO_3)_3$ complex composite films enhanced sensor sensitivity from around 114.5 [Deg/RIU] for Au-layer to 159.0 [Deg/RIU] for Au-((PANI-HCl)/$Al(NO_3)_3$ (32 wt.%)). In addition, the signal-to-noise ratio for Au-layer was 6.22, which reached 9.97 after coating by (PANI-HCl)/$Al(NO_3)_3$ (32 wt.%) complex composite layer. In addition, the FOM of the bare Au layer was 79.51 RIU^{-1}, which decreased as $Al(NO_3)_3$ concentrations increased in the PANI-HCl to 7.23 RIU^{-1}. The LOD value for the bare Au layer was 0.12 RIU, which decreased to 0.08 RIU after coating with (PANI-HCl)/$Al(NO_3)_3$ with a concentration of 32 wt.%. This means that coating the Au layer with (PANI-HCl)/$Al(NO_3)_3$ can detect fewer concentrations than the bare Au layer.

Author Contributions: Conceptualization, Q.M.A.-B. and A.T; methodology, Q.M.A.-B., D.S., and V.S.; software, Q.M.A.-B., D.S., and R.H.; validation, A.T. and R.H.; formal analysis, Q.M.A.-B. and V.S.; investigation, A.T. and D.S.; resources, A.T. and R.H.; data curation, Q.M.A.-B. and R.H.; writing—original draft preparation, Q.M.A.-B. and A.T.; writing—review and editing, D.S., V.S., and R.H.; visualization, Q.M.A.-B. and A.T.; supervision, A.T. and R.H.; project administration, A.T. and R.H. All authors have read and agreed to the published version of the manuscript.

Funding: This work was supported in part by Deutsche Forschungsgemeinschaft (DFG) within the Collaborative Research Center SFB 876 "Providing Information by Resource-Constrained Analysis", Project B2. This research was also funded by Deutscher Akademischer Austauschdienst (DAAD) within the "Hochschulpartnerschaften mit dem Irak 2021-2022 Programme" under Project 57567978.

Institutional Review Board Statement: Not applicable

Informed Consent Statement: Not applicable

Data Availability Statement: Not applicable.

Acknowledgments: The scientific support by the Ministerium für Innovation, Wissenschaft und Forschung des Landes Nordrhein-Westfalen, the Senatsverwaltung für Wirtschaft, Technologie und Forschung des Landes Berlin, and the Bundesministerium für Bildung und Forschung is gratefully acknowledged. Our thanks also to Ahmad A. Ahmad for helping our members to use the thin films laboratory at Jordan University of Science & Technology, Irbid, Jordan.

Conflicts of Interest: The authors declare no conflict of interest.

References

1. Santos, J.L.; Farahi, F. *Handbook of Optical Sensors;* CRC Press: Boca Raton, FL, USA, 2014.
2. Masson, J.-F. Surface plasmon resonance clinical biosensors for medical diagnostics. *ACS Sens.* **2017**, *2*, 16–30. https://doi.org/10.1021/acssensors.6b00763.
3. Shpacovitch, V.; Hergenröder, R. Surface plasmon resonance (SPR)-based biosensors as instruments with high versatility and sensitivity. *Sensors* **2020**, *20*, 3010.
4. Nizamov, S.; Sazdovska, S.D.; Mirsky, V.M. A review of optical methods for ultrasensitive detection and characterization of nanoparticles in liquid media with a focus on the wide field surface plasmon microscopy. *Anal. Chim. Acta* **2022**, *1204*, 339633

5. Sidorenko, I.; Nizamov, S.; Hergenröder, R.; Zybin, A.; Kuzmichev, A.; Kiwull, B.; Niessner, R.; Mirsky, V.M. Computer assisted detection and quantification of single adsorbing nanoparticles by differential surface plasmon microscopy. *Mikrochim. Acta* **2015**, *183*, 101–109. https://doi.org/10.1007/s00604-015-1599-0.
6. Nizamov, S.; Scherbahn, V.; Mirsky, V.M. Detection and quantification of single engineered nanoparticles in complex samples using template matching in wide-field surface plasmon microscopy. *Anal. Chem.* **2016**, *88*, 10206–10214. https://doi.org/10.1021/acs.analchem.6b02878.
7. Shpacovitch, V.; Sidorenko, I.; Lenssen, J.E.; Temchura, V.; Weichert, F.; Müller, H.; Überla, K.; Zybin, A.; Schramm, A.; Hergenröder, R. Application of the pamono-sensor for quantification of microvesicles and determination of nano-particle size distribution. *Sensors* **2017**, *17*, 244. https://doi.org/10.3390/s17020244.
8. Zybin, A.; Shpacovitch, V.; Skolnik, J.; Hergenröder, R. Optimal conditions for SPR-imaging of nano-objects. *Sensors Actuators B Chem.* **2017**, *239*, 338–342. https://doi.org/10.1016/j.snb.2016.07.124.
9. Rouf, H.K.; Haque, T. Performance enhancement of Ag-Au bimetallic surface plasmon resonance biosensor using INP. *Prog. Electromagn. Res. M* **2018**, *76*, 31–42. https://doi.org/10.2528/pierm18092503.
10. Kretschm, E. Determination of optical constants of metals by excitation of surface plasmons. *Z. Fur Phys.* **1971**, *241*, 313.
11. Li, Q.; Wang, Q.; Yang, X.; Wang, K.; Zhang, H.; Nie, W. High sensitivity surface plasmon resonance biosensor for detection of microRNA and small molecule based on graphene oxide-gold nanoparticles composites. *Talanta* **2017**, *174*, 521–526. https://doi.org/10.1016/j.talanta.2017.06.048.
12. Amendola, V.; Pilot, R.; Frasconi, M.; Maragò, O.M.; Iatì, M.A. Surface plasmon resonance in gold nanoparticles: A review. *J. Phys. Condens. Matter* **2017**, *29*, 203002. https://doi.org/10.1088/1361-648x/aa60f3.
13. Du, W.; Zhao, F. Silicon carbide based surface plasmon resonance waveguide sensor with a bimetallic layer for improved sensitivity. *Mater. Lett.* **2017**, *186*, 224–226.
14. Kim, S.H.; Kim, T.U.; Jung, H.Y.; Ki, H.C.; Kim, D.G.; Lee, B.-T. The effect of Au/Ag bimetallic thin-films on surface plasmon resonance properties comparing with those of Au and Ag single thin-films. *J. Nanosci. Nano-Technol.* **2018**, *18*, 1777–1781.
15. Menegazzo, N.; Herbert, B.; Banerji, S.; Booksh, K.S. Discourse on the utilization of polyaniline coatings for surface plasmon resonance sensing of ammonia vapor. *Talanta* **2011**, *85*, 1369–1375. https://doi.org/10.1016/j.talanta.2011.06.020.
16. Yılmaz, E.; Özgür, E.; Bereli, N.; Türkmen, D.; Denizli, A. Plastic antibody based surface plasmon resonance nanosensors for selective atrazine detection. *Mater. Sci. Eng. C* **2017**, *73*, 603–610.
17. Park, G.; Kim, H.-O.; Lim, J.-W.; Park, C.; Yeom, M.; Song, D.; Haam, S. Rapid detection of influenza A (H_1N_1) virus by conductive polymer-based nanoparticle via optical response to virus-specific binding. *Nano Res.* **2021**, *15*, 2254–2262. https://doi.org/10.1007/s12274-021-3772-6.
18. Omar, N.A.S.; Fen, Y.W.; Abdullah, J.; Kamil, Y.M.; Daniyal, W.M.E.M.M.; Sadrolhosseini, A.R.; Mahdi, M.A. Sensitive detection of dengue virus type 2 e-proteins signals using self-assembled monolayers/reduced graphene oxide-pamam dendrimer thin film-SPR optical sensor. *Sci. Rep.* **2020**, *10*, 1–15. https://doi.org/10.1038/s41598-020-59388-3.
19. Agarwal, A.; Vitiello, M.S.; Viti, L.; Cupolillo, A.; Politano, A. Plasmonics with two-dimensional semiconductors: From basic research to technological applications. *Nanoscale* **2018**, *10*, 8938–8946. https://doi.org/10.1039/c8nr01395k.
20. Politano, A.; Viti, L.; Vitiello, M.S. Optoelectronic devices, plasmonics, and photonics with topological insulators. *APL Mater.* **2017**, *5*, 35504.
21. Usman, F.; Dennis, J.O.; Seong, K.C.; Ahmed, A.Y.; Ferrell, T.L.; Fen, Y.W.; Sadrolhosseini, A.R.; Ayodele, O.B.; Meriaudeau, F.; Saidu, A. Enhanced sensitivity of surface plasmon resonance biosensor functionalized with doped polyaniline composites for the detection of low-concentration acetone vapour. *J. Sensors* **2019**, *2019*, 1–13. https://doi.org/10.1155/2019/5786105.
22. Ahmad, A.A.; Bani-Salameh, A.A.; Al-Bataineh, Q.M.; Jum'h, I.; Telfah, A.D. Optical, structural and morphological properties of synthesized PANI-CSA-PEO-based GaN nanocomposite films for optoelectronic applications. *Polym. Bull.* **2022**, 1–20. https://doi.org/10.1007/s00289-021-04033-w.
23. Aksimentyeva, O.I.; Savchyn, V.P.; Dyakonov, V.P.; Piechota, S.; Horbenko, Y.Y.; Opainych, I.Y.; Demchenko, P.Y.; Popov, A.; Szymczak, H. Modification of polymer-magnetic nanoparticles by luminescent and conducting substances. *Mol. Cryst. Liq. Cryst.* **2014**, *590*, 35–42. https://doi.org/10.1080/15421406.2013.873646.
24. Bayan, M.A.H.; Taromi, F.A.; Lanzi, M.; Pierini, F. Enhanced efficiency in hollow core electrospun nanofiber-based organic solar cells. *Sci. Rep.* **2021**, *11*, 1–11. https://doi.org/10.1038/s41598-021-00580-4.
25. Chen, Y.; Su, L.; Jiang, M.; Fang, X. Switch type PANI/ZnO core-shell microwire heterojunction for UV photodetection. *J. Mater. Sci. Technol.* **2021**, *105*, 259–265. https://doi.org/10.1016/j.jmst.2021.07.031.
26. Yang, M. Resistive room temperature DMA gas sensor based on the forest-like unusual n-type PANI/TiO_2 nano-composites. *Sens. Actuators B Chem.* **2021**, *342*, 130067.
27. Botewad, S.; Pahurkar, V.; Muley, G. Fabrication and evaluation of evanescent wave absorption based polyaniline-cladding modified fiber optic urea biosensor. *Opt. Fiber Technol.* **2018**, *40*, 8–12.
28. Ramos, K.C.; Nishiyama, K.; Maeki, M.; Ishida, A.; Tani, H.; Kasama, T.; Baba, Y.; Tokeshi, M. Rapid, sensitive, and selective detection of h5 hemagglutinin from avian influenza virus using an immunowall device. *ACS Omega* **2019**, *4*, 16683–16688. https://doi.org/10.1021/acsomega.9b02788.

29. Maddali, H.; Miles, C.E.; Kohn, J.; O'Carroll, D.M. Optical biosensors for virus detection: Prospects for SARS-CoV-2/COVID-19. *ChemBioChem* **2021**, *22*, 1176–1189.
30. Kulkarni, M.V.; Viswanath, A.K.; Marimuthu, R.; Seth, T. Spectroscopic, transport, and morphological studies of polyaniline doped with inorganic acids. *Polym. Eng. Sci.* **2004**, *44*, 1676–1681. https://doi.org/10.1002/pen.20167.
31. Işik, C.; Arabaci, G.; Doğaç, Y.I.; Deveci, İ.; Teke, M. Synthesis and characterization of electrospun PVA/Zn^{2+} metal composite nanofibers for lipase immobilization with effective thermal, pH stabilities and reusability. *Mater. Sci. Eng. C* **2019**, 99, 1226–1235.
32. Migdadi, A.B.; Ahmad, A.A.; Alsaad, A.M.; Al-Bataineh, Q.M.; Telfah, A. Electrical and thermal characterizations of synthesized composite films based on polyethylene oxide (PEO) doped by aluminium chloride ($AlCl_3$). *Polym. Bull.* **2022**, 1–14. https://doi.org/10.1007/s00289-022-04329-5.
33. Sarkar, R.; Kundu, T.K. Hydrogen bond interactions of hydrated aluminum nitrate with PVDF, PVDF-TrFE, and PVDF-HFP: A density functional theory-based illustration. *Int. J. Quantum Chem.* **2020**, *120*, e26328.
34. Patnaik, P. *Handbook of Inorganic Chemicals*; McGraw-Hill: New York, NY, USA, 2003.
35. Chamroukhi, H. Optical and structural properties enhancement of hybrid nanocomposites thin films based on polyaniline doped with Zinc Oxide embedded in bimodal mesoporous silica (ZnO@ SiOX) nanoparticles. *Opt. Mater.* **2018**, *84*, 703–713.
36. Gurevich, E.; Temchura, V.; Überla, K.; Zybin, A. Analytical features of particle counting sensor based on plasmon assisted microscopy of nano objects. *Sensors Actuators B Chem.* **2011**, *160*, 1210–1215. https://doi.org/10.1016/j.snb.2011.09.050.
37. Schnorrenberg, H.-J.; Hengstebeck, M.; Schlinkmeier, K. The attenuation of a coherent field by scattering. *Opt. Commun.* **1995**, *117*, 532–540. https://doi.org/10.1016/0030-4018(95)00240-9.
38. Li, J.; Tang, X.; Li, H.; Yan, Y.; Zhang, Q. Synthesis and thermoelectric properties of hydrochloric acid-doped polyaniline. *Synth. Met.* **2010**, *160*, 1153–1158.
39. Daikh, S.; Zeggai, F.; Bellil, A.; Benyoucef, A. Chemical polymerization, characterization and electrochemical studies of PANI/ZnO doped with hydrochloric acid and/or zinc chloride: Differences between the synthesized nanocomposites. *J. Phys. Chem. Solids* **2018**, *121*, 78–84. https://doi.org/10.1016/j.jpcs.2018.02.003.
40. Thapa, R.; Saha, B.; Goswami, S.; Chattopadhyay, K.K. Study of field emission and dielectric properties of AlN films prepared by DC sputtering technique at different substrate temperatures. *Indian J. Phys.* **2010**, *84*, 1347–1354. https://doi.org/10.1007/s12648-010-0125-9.
41. Vivekanandan, J.; Ponnusamy, V.; Mahudeswaran, A.; Vijayanand, P. Synthesis, characterization and conductivity study of polyaniline prepared by chemical oxidative and electrochemical methods. *Arch. Appl. Sci. Res.* **2011**, *3*, 147–153.
42. Mazzeu, M.A.C.; Faria, L.K.; Cardoso, A.D.M.; Gama, A.M.; Baldan, M.R.; Gonçalves, E.S. Structural and morphological characteristics of polyaniline synthesized in pilot scale. *J. Aerosp. Technol. Manag.* **2017**, *9*, 39–47. https://doi.org/10.5028/jatm.v9i1.726.
43. Diggikar, R.S.; Deshmukh, S.; Thopate, T.S.; Kshirsagar, S.R. Performance of polyaniline nanofibers (PANI NFs) as PANI NFs-silver (Ag) nanocomposites (NCs) for energy storage and antibacterial applications. *ACS Omega* **2019**, *4*, 5741–5749. https://doi.org/10.1021/acsomega.8b02834.
44. Bhadra, S.; Khastgir, D. Determination of crystal structure of polyaniline and substituted polyanilines through powder X-ray diffraction analysis. *Polym. Test.* **2008**, *27*, 851–857. https://doi.org/10.1016/j.polymertesting.2008.07.002.
45. Waikar, M.R.; Shaikh, A.A.; Sonkawade, R.G. Paninfs synthesized electrochemically as an electrode material for energy storage application. *Polym. Bull.* **2018**, *76*, 4703–4718. https://doi.org/10.1007/s00289-018-2634-1.
46. Jum'h, I.; Mousa, M.S.; Mhawish, M.; Sbeih, S.; Telfah, A. Optical and structural properties of (PANI-CSA-PMMA)/NiNPs nanocomposites thin films for organic optical filters. *J. Appl. Polym. Sci.* **2020**, *137*, 48643.
47. Alsaad, A.; Al-Bataineh, Q.M.; Ahmad, A.; Albataineh, Z.; Telfah, A. Optical band gap and refractive index dispersion parameters of boron-doped ZnO thin films: A novel derived mathematical model from the experimental transmission spectra. *Optik* **2020**, *211*, 164641. https://doi.org/10.1016/j.ijleo.2020.164641.
48. Gul, S.; Shah, A.-U.A.; Bilal, S. Synthesis and characterization of processable polyaniline salts. *J. Physics: Conf. Ser.* **2013**, *439*, 012002. https://doi.org/10.1088/1742-6596/439/1/012002.
49. Abdiryim, T.; Xiao-Gang, Z.; Jamal, R. Comparative studies of solid-state synthesized polyaniline doped with inorganic acids. *Mater. Chem. Phys.* **2005**, *90*, 367–372.
50. Brik, M.; Srivastava, A.; Popov, A. A few common misconceptions in the interpretation of experimental spectroscopic data. *Opt. Mater.* **2022**, *127*, 112276. https://doi.org/10.1016/j.optmat.2022.112276.
51. Liland, K.H.; Almøy, T.; Mevik, B.-H. Optimal choice of baseline correction for multivariate calibration of spectra. *Appl. Spectrosc.* **2010**, *64*, 1007–1016. https://doi.org/10.1366/000370210792434350.
52. Al-Gharram, M.; Jum'h, I.; Telfah, A.; Al-Hussein, M. Highly crystalline conductive electrodeposited films of PANI-CSA/$CoFe_2O_4$ nanocomposites. *Colloids Surf. A Physicochem. Eng. Asp.* **2021**, *628*, 127342.
53. Ahmad, A.A.; Khazaleh, M.H.; Alsaad, A.M.; Al-Bataineh, Q.M.; Telfah, A.D. Characterization of As-prepared PVA-PEO/ZnO-Al_2O_3-NPs hybrid nanocomposite thin films. *Polym. Bull.* **2022**, *79*, 9881–9905.
54. Atta, A.; Abdelhamied, M.M.; Abdelreheem, A.M.; Berber, M.R. Flexible methyl cellulose/polyaniline/silver composite films with enhanced linear and nonlinear optical properties. *Polymers*, **2021**, *13*, 1225.

55. Al-Bataineh, Q.M.; Aljarrah, I.A.; Ahmad, A.A.; Alsaad, A.M.; Telfah, A. Investigation of the doping mechanism and electron transition bands of PEO/$KMnO_4$ complex composite films. *J. Mater. Sci. Mater. Electron.* **2022**, *33*, 14051–14062. https://doi.org/10.1007/s10854-022-08336-0.
56. Urbach, F. The long-wavelength edge of photographic sensitivity and of the electronic absorption of solids. *Phys. Rev.* **1953**, *92*, 1324–1324. https://doi.org/10.1103/physrev.92.1324.
57. Parmar, R.; Kundu, R.; Punia, R.; Aghamkar, P.; Kishore, N. Iron modified structural and optical spectral properties of bismuth silicate glasses. *Phys. B Condens. Matter* **2014**, *450*, 39–44. https://doi.org/10.1016/j.physb.2014.05.056.
58. Al-Bataineh, Q.M.; Telfah, M.; Abu-Zurayk, R.; Benchaabane, A.; Tavares, C.J.; Telfah, A. Nano-SnO_2/polyaniline composite films for surface plasmon resonance. *Mater. Chem. Phys.* **2022**, *293*, 126816.
59. Asiri, A.M.; Lichtfouse, E. *Nanophotocatalysis and Environmental Applications: Detoxification and Disinfection*; Springer: Berlin/Heidelberg, Germany, 2019.
60. Al-Akhras, M.; Alzoubi, S.E.; Ahmad, A.A.; Ababneh, R.; Telfah, A. Studies of composite films of polyethylene oxide doped with potassium hexachloroplatinate. *J. Appl. Polym. Sci.* **2020**, *138*, 49757. https://doi.org/10.1002/app.49757.
61. Al-Bataineh, Q.M.; Ahmad, A.A.; Alsaad, A.M.; Migdadi, A.; Telfah, A. Correlation of electrical, thermal, and crystal parameters of complex composite films based on polyethylene oxide (PEO) doped by copper sulfate ($CuSO_4$). *Phys. B Condens. Matter* **2022**, *645*, 414224. https://doi.org/10.1016/j.physb.2022.414224.
62. Singh, S.; Singh, P.K.; Umar, A.; Lohia, P.; Albargi, H.; Castañeda, L.; Dwivedi, D.K. 2D nanomaterial-based surface plasmon resonance sensors for biosensing applications. *Micromachines* **2020**, *11*, 779. https://doi.org/10.3390/mi11080779.
63. Mukhtar, W.M.; Murat, N.F.; Samsuri, N.D.; Dasuki, K.A. Maximizing the response of SPR signal: A vital role of light excitation wavelength. **2018**, *2016*, 020104. https://doi.org/10.1063/1.5055506.
64. Available online: http://www.res-tec.de/ (accessed on 12 October 2022).
65. Rahman, M.; Abdulrazak, L.F.; Ahsan, M.; Based, A.; Rana, M.; Anower, S.; Rikta, K.A.; Haider, J.; Gurusamy, S. 2D nanomaterial-based hybrid structured (Au-WSe_2-$PtSe_2$-BP) surface plasmon resonance (SPR) sensor with improved performance. *IEEE Access* **2021**, *10*, 689–698. https://doi.org/10.1109/access.2021.3137420.
66. Yakubovsky, D.I.; Arsenin, A.V.; Stebunov, Y.; Fedyanin, D.; Volkov, V.S. Optical constants and structural properties of thin gold films. *Opt. Express* **2017**, *25*, 25574–25587. https://doi.org/10.1364/oe.25.025574.
67. Rasband, W.S. ImageJ. (1997–2018). Available online: https://imagej.nih.gov/ij/ (accessed on 12 October 2022).
68. Prabowo, B.A.; Purwidyantri, A.; Liu, K.-C. Surface plasmon resonance optical sensor: A review on light source technology. *Biosensors* **2018**, *8*, 80. https://doi.org/10.3390/bios8030080.

5.3. Original Paper III: (Al-Bataineh et al., 2023a)

sensors

MDPI

Article

Switchable Polyacrylic Acid Polyelectrolyte Brushes for Surface Plasmon Resonance Applications

Qais M. Al-Bataineh [1,2,*], Ahmad D. Telfah [1,3], Victoria Shpacovitch [1], Carlos J. Tavares [4] and Roland Hergenröder [1,*]

[1] Leibniz Institut für Analytische Wissenschaften-ISAS-e.V., Bunsen-Kirchhoff-Straße 11, 44139 Dortmund, Germany
[2] Experimental Physics, TU Dortmund University, 44227 Dortmund, Germany
[3] Nanotechnology Center, The University of Jordan, Amman 11942, Jordan
[4] Centre of Physics of Minho and Porto Universities, University of Minho, 4804-533 Guimarães, Portugal
* Correspondence: qais.al-bataineh@isas.de (Q.M.A.-B.); roland.hergenroeder@isas.de (R.H.)

Abstract: Imaging wide-field surface plasmon resonance (SPR) microscopy sensors based on polyacrylic acid polyelectrolyte brushes (PAA PEBs) were designed to enhance the sensitivity of nano-object detection. The switching behavior of the PAA PEBs against changes in the pH values was investigated by analyzing the chemical, morphological, optical, and electrical properties. At pH ~1, the brushes collapse on the surface with the dominance of carboxylic groups (COOH). Upon the increase in the pH to nine, the switching process completes, and the brushes swell from dissociating most of the COOH groups and converting them into COO^- groups. The domination of the negatively charged COO^- groups increases the electrostatic repulsion in the polymer chains and stretches the brushes. The sensitivity of the SPR sensing device was investigated using a theoretical approach, as well as experimental measurements. The signal-to-noise ratio for a Au layer increases from six to eighteen after coating with PAA PEBs. In addition, the linewidth of the recorded image decreases from six pixels to five pixels by using the Au-PAA layers, which results from the enhanced spatial resolution of the recorded images. Coating a Au-layer with PAA PEBs enhances the sensitivity of the SPR sensing device, and improves the spatial resolution of the recorded image.

Keywords: imaging wide-field SPR microscopy sensor; polyacrylic acid (PAA); polyelectrolyte brushes (PEBs)

Citation: Al-Bataineh, Q.M.; Telfah, A.D.; Shpacovitch, V.; Tavares, C.J.; Hergenröder, R. Switchable Polyacrylic Acid Polyelectrolyte Brushes for Surface Plasmon Resonance Applications. *Sensors* **2023**, *23*, 4283. https://doi.org/10.3390/s23094283

Academic Editors: Antonella Macagnano and Jingyun Huang

Received: 20 February 2023
Revised: 23 April 2023
Accepted: 24 April 2023
Published: 26 April 2023

1. Introduction

Polyelectrolyte brushes (PEBs) are charged poly acids or bases grafted to the substrate surface which undergo reversible protonation or deprotonation upon shifting the pH value across the acidity of the brush [1,2]. This shift allows for the binding of the PEBs with their target molecules [3], and consequently has various applications in biosensors and bioelectronic devices [4,5].

The physical binding between the polyelectrolyte brushes with the macromolecules remains an open question. For instance, several researchers have stated that the proteins bind to the PEBs even when they have the same net charge [6], which can be attributed to the interactions with the local patches on the protein surface that have the opposite charge to the PEBs [7,8], or that the local environment inside PEBs reverses the protein charge [9]. Using different chemical modifications, the PEBs can coat surfaces of different materials, such as metals, metal oxides, silicon, and silica [10].

Polyacrylic acid (PAA) has gained attention due to the existence of a carboxylic group on each repeating unit that changes its charges, structures, and hydrophilicity due to the variation in pH [11,12]. Increasing the pH value of the PAA PEBs leads to the deprotonation of COOH and converting it into the COO^- of the carboxylic group. The dominance of the negatively charged COO^- groups increases the electrostatic repulsion in the polymer chains, consequently stretching the brushes and converting the PAA into a hydrophilic

behavior. Moreover, the reduction in the value of the PAA PEBs leads to the re-protonation of COO^- groups, and the PEBs return to their initial state [13].

Recently, imaging wide-field SPR microscopy sensors (WF-SPRM) have gained substantial attention in the real-time detection of viruses and virus-like particles due to their capability to measure low particle concentrations with a high sensitivity [14–16]. In addition, the WF-SPRM of nano-objects is a spatio-temporal detector based on SPR phenomena for imaging the nano-objects in solution and gas media due to the interaction between nano-objects with the evanescent electrical field near the sensor surface [17–22].

Various studies have been conducted to enhance the sensitivity and selectivity of the SPR sensors [23]. G. del Castillo and colleagues [3] investigated the binding of enzymes to the polyelectrolyte brushes compared to self-assembled monolayers. They concluded that the application of polyelectrolyte brushes enhances enzyme binding. Y. Wang et al. [24] found that the polyacrylic acid polyelectrolyte brushes demonstrated a higher selectivity to protein loading than bare gold surfaces.

This work describes the design of the WF-SPRM based on PAA PEBs deposited on a Au layer, which improves the sensitivity of the SPR sensing device. Fourier transform infrared (FTIR) and nuclear magnetic resonance (NMR) spectroscopies were employed to investigate the transformation of the carboxylic acid (COOH) group into the carboxylate (COO^-) group of the PAA PEBs with increasing pH values due to added NaOH. Atomic force microscopy (AFM) was used to monitor the transformation of the carboxylic acid (COOH) group into the carboxylate (COO^-) group, which changes the PAA PEBs from a collapsed to a stretched form. The effect of switching the behavior on the optical constants and electrical conductivity was investigated. Finally, PAA PEBs were chosen for the SPR sensing device due to their high refractive index. Theoretical calculations, in addition to experimental measurements of WF-SPRM, were used to investigate the sensitivity of the SPR sensing device.

2. Materials and Methods

Polyacrylic acid ($(CH_2-CHCO_2H)_n$, 1800 g/mol), N-hydroxy succinimide ($C_4H_5NO_3$, 115.09 g/mol), cysteamine hydrochloride (C_2H_7NS, 113.61 g/mol), toluene ($C_6H_5CH_3$, 92.14 g/mol), hydrochloric acid (HCl, 36.458 g/mol), and sodium hydroxide (NaOH, 39.997 g/mol) were all purchased from Sigma-Aldrich, except for 1-ethyl-3-(3-(dimethylamino) propyl) carbodiimide) hydrochloride ($C_8H_{17}N_3$, 155.245 g/mol), which was purchased from ThermoFisher. The following sections describe the synthesis and characterization methods in detail.

2.1. Synthesis of Thiolated Polyacrylic Acid (PAA-SH)

PAA stock solution was prepared by dissolving 1.000 g polyacrylic acid in 100 mL distilled water using a magnetic stirrer for four hours under ambient conditions. As according to the literature [25], thiolated polyacrylic acid (PAA-SH) was synthesized via carbodiimide amide coupling, in which 0.320 g of N-hydroxy succinimide and 0.533 g of 1-ethyl-3-(3-(dimethylamino) propyl) carbodiimide) hydrochloride were added into 100 mL of PAA stock solution in a 6:1 molar ratio under continuous stirring for 30 min at room temperature. After that, 0.316 g of cysteamine hydrochloride in a 6:1 molar ratio (carboxyl to thiol) was added to the reaction, and stirred continuously for four hours at room temperature. Finally, the PAA-SH PEBs were purified by adding toluene to small amounts of the final solution (100 mL toluene to 10 mL PAA-SH solution). After that, PAA-SH powder was collected using a centrifuge system. Finally, 1 g of PAA-SH was suspended in 100 mL of absolute ethanol for further use. The pH value of the solution was 2.

The pH value of the preparation solvent varied from 1 to 9, which was controlled by adding hydrochloric acid (HCl) or sodium hydroxide (NaOH) to the final solution. Adding HCl leads to a reduction in pH through the delivery of Cl^- ions to the solvent preparation.

However, adding NaOH leads to an increase in pH via the delivery of Na^+ ions to the solvent preparation.

2.2. Surface Cleaning

Before surface functionalization, indium-tin-oxide (ITO) glass substrates (100 nm ITO on glass) and n-type silicon wafers (0.5 mm-thick) were cleaned by sonicating in acetone and isopropyl alcohol for 30 min under ambient conditions. In addition, the gold substrates were prepared by first coating a glass slide ($14 \times 75 \times 1$ mm^3, SF10 glass, $n = 1.72$) with a 5 nm titanium adhesion layer and, subsequently, with an approximately 41-45 nm gold layer via a magnetron sputtering technique (Innolume, Dortmund, Germany). These gold substrates were further cut and cleaned using piranha solution (H_2SO_4/H_2O_2, 3:1 v/v) for 10 min. Afterward, ITO, silicon, and the gold substrates were rinsed with water and dried at ambient conditions.

2.3. Brushes by the "Grafting to" Method

PAA PEBs were deposited on the gold, ITO, and silicon substrates as according to the "grafting to" method by modifying the PAA brushes using the thiol group. The PAA-SH PEBs were deposited via the spin coating technique. Afterward, the films dried at 70 °C to vaporize the solvent. ITO substrate was used for optical and electrical characterizations, an n-type silicon wafer was used for X-ray photoelectron spectroscopy experiments, and a gold substrate was used for SPR experiments.

2.4. Chemical Structure Characterizations

The chemical structure was investigated using ^{1}H NMR measurements (600.13 MHz, Bruker AVANCE III NMR spectrometer) and near-ambient-pressure X-ray photoelectron spectroscopy (NAP-XPS). ^{1}H NMR measurements were conducted at 600.13 MHz using a 5 mm high-resolution multi-channel and broadband (5 mm BBO model) equipped with Z-gradient.

2.5. The Swelling Behavior Characterizations

The swelling behavior and the dissociation degree were investigated using FTIR (Bruker VERTEX 80/80v Vacuum FTIR Spectrometers) and NMR (Bruker AVANCE III NMR spectrometer). In addition, surface morphology and wettability were studied using an atomic force microscope (SPM SmartSPM™-1000) and water contact angle measurements (WCA) for a water droplet (pH = 7) of size 10 µL taken on three occasions. These measurements were performed at room temperature for PAA-SH PEBs at different pH values (1, 4, 7, and 9, respectively).

2.6. Optical and Electrical Properties

The optical transmittance and reflectance spectra were measured using a double-beam UV–Vis spectrophotometer (Hitachi U-3900H) with a total integration sphere. After that, the optical constants (extinction coefficient (k) and refractive index (n)) were calculated using $k = \alpha\lambda/4\pi$ and $n = (1+R/1-R) + \sqrt{\left(4R/(1-R)^2\right) - k^2}$, respectively, where α is the absorption coefficient, given by $\alpha = (1/d)\ln((1-R)/T)$ [26,27], λ is the photon wavelength, and d is the thickness. The n-spectra were fitted to the Cauchy model [28]. A 4-point probe (Microworld Inc., Kuala Lumpur, Malaysia) was used to measure the electrical conductivity.

2.7. WF-SPRM Measurements

The SPR instrument employed for measurements with the (PAA PEBs–Au) layer is based on Kretschmann's scheme of plasmon excitation [29,30]. The PAA-SH PEBs with 20 nm thickness were deposited onto the gold substrate using the spin coating technique. The gold substrate was pressed onto a glass prism using RI matching immersion liquid

($n = 1.725$, Cargill Laboratories, Fort Collins, CO, USA) to avert the air gap. SPR measurements were performed by illuminating the (PAA PEBs–Au) layer through a prism using a laser diode (HL6750MG, Thorlabs GmbH, Bergkirchen, Germany) with a wavelength of $\lambda = 685$ nm. Images of the gold layer interface were taken using a CMOS video camera DMK 23UP031 (Imaging Source, Bremen, Germany, with a resolution of 5 Mp (megapixel) and a pixel size 2.2 × 2.2 µm) and using a macro-objective (Cannon Compact-Macro Lens EF 50 mm 1:2.5). Details of WF-SPRM are described elsewhere [20,31]. The resonance angle represents the minimum residual reflectivity. Finally, polystyrene nanoparticles (refractive index n = 1.59 [32]) with an average size of 200 nm were used to simulate the binding events of the biological nanoparticles.

3. Results and Discussion

The main challenge in using PAA PEBs as a coating on metal films or other substrates is the lack of a functional group that strongly binds to the surface. Therefore, a fraction of carboxylic groups of PAA were modified with thiol functional groups binding to a gold layer. PAA-SH was synthesized using carbodiimide amide coupling reactions between PAA and cysteamine with specific molar ratios to obtain a modified one in four carboxylic acid groups (Figure 1a) [25]. The ^{1}H-NMR spectrum of PAA PEBs shows signals at 1.1, 1.2–1.7, and 2.01 ppm ascribed to CH_3, CH_2, and CHCOOX protons, respectively. In addition, the multiplet peaks between 1.76 and 1.85 ppm represent the thiol (–SH) group in the PAA–SH PEBs, which thereby confirms the existence of the –SH group in the PAA matrix (Figure 1b) [33,34]. Performed XPS measurements also confirmed the presence of the thiol group in PAA-SH PEBs (Figure 1c–f). CasaXPS software was used to investigate the peak deconvolution, in addition to the baseline correction of the XPS peaks, as according to the literature [35]. XPS C1s core line peaks of PAA-SH PEBs appear at 284.8 eV (C−C, C−H), 285.4 eV (C−N), and 286.1 eV ($-COO^-$) (Figure 1c). XPS O 1s core line peaks appear at 531.9 eV (C=O), 534.6 eV (O−OH), 536.8 eV (C−O), and 539.0 eV (O=C−O^-) (Figure 1d). In addition, XPS N 1s core line peaks appear at 398.7 eV (N−H) and 400.7 eV (N−C) (Figure 1e). The XPS S 2p core line peak at 162.8 eV (C−SH) was also measured (Figure 1f). These results confirm the connecting of the thiol group and the PAA matrix, as shown in Figure 1a.

FTIR spectroscopy is one of the main techniques used to investigate the swelling behavior and the dissociation degree of the PAA PEBs due to differences in the IR vibrational bands of the carboxylic acid (COOH) and carboxylate (COO^-) groups [13]. The vibrational bands of the carboxylic acid (COOH) and carboxylate (COO^-) groups of the PAA PEBs for different pH values (one, four, seven, and nine) are in the wavenumber range of 1350–1800 cm^{-1} (Figure 2a). In addition, the dissociation degree is calculated using $\alpha = [COO^-]/([COO^-] + \epsilon(COO^-)/\epsilon(COOH)[COOH])$, where $[COO^-]$ and $[COOH]$ are the integrated areas of COO^- and COOH vibrational bands. The extinction coefficient ratio of the COO^- and COOH groups is $(\epsilon(COO^-)/\epsilon(COOH) = 1.8 \pm 0.3)$ [36]. At pH = 1, the COOH vibrational band at 1700 cm^{-1} dominates the PAA PEBs, with the ratio between the area under the COOH to COO^- vibrational bands being about 5.8. Increasing the pH value to 4 by adding NaOH to the PAA stock solution converts the COOH groups of the upper molecules into symmetric COO^- and asymmetric COO^- groups at vibrational bands of 1553 and 1430 cm^{-1} due to the dissociation of the COOH, with the ratio between the area under the COOH to COO^- vibrational bands being about 1.4. Additionally, increasing the pH value to seven leads to an additional conversion of the COOH groups into symmetric COO^- and asymmetric COO^- groups, with the ratio between the area under the COOH to COO^- vibrational bands being around 0.27. Increasing the pH value further to nine leads to a domination of the asymmetric COO^- groups at a vibrational band of 1430 cm^{-1}, with the ratio between the area under the COOH to COO^- vibrational bands decreasing to 0.01. The domination of the negatively charged COO^- groups increases the electrostatic repulsion in the polymer chains and stretch the brushes. The titration curve of PAA PEBs was performed by plotting the dissociation degree versus pH and then fitted to the sigmoid

function (Figure 2b) [36]. The pK_a value of the PAA PEBs is defined as the pH value at the midpoint of the titration curve. Therefore, the effective pK_a of the PAA PEBs is about 5.54, which is accepted by the literature [37,38].

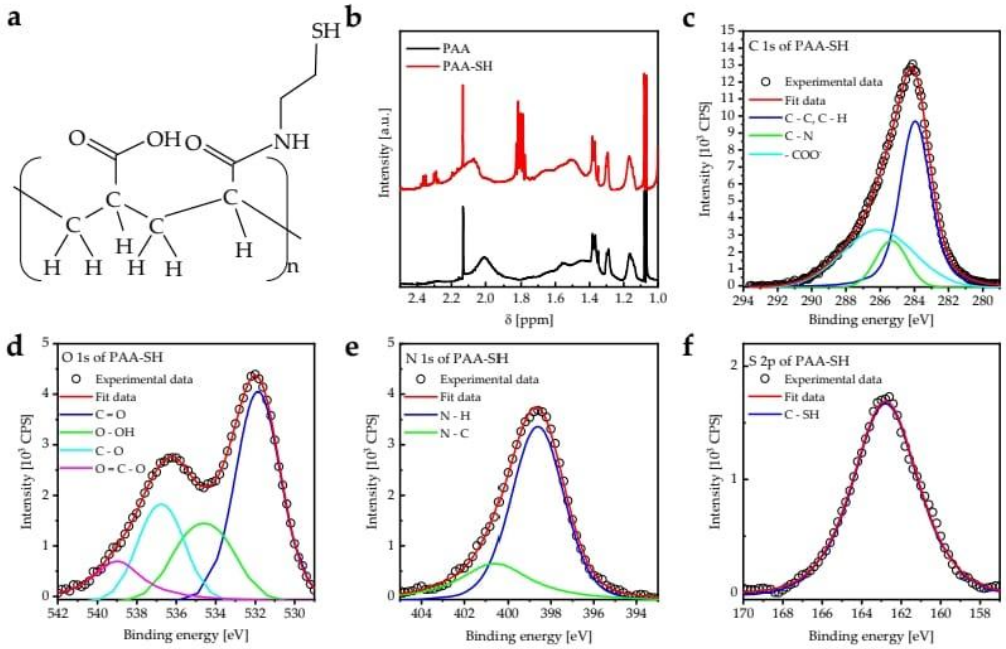

Figure 1. (**a**) Molecular structure of PAA-SH with a carboxyl-to-thiol ratio (1:4). (**b**) ^{1}H NMR spectra for PAA and PAA–SH PEBs at pH = 7 measured at room temperature. NMR spectrum of PAA-SH shows the chemical shift of PAA and the -SH group. (**c**) Deconvoluted XPS C 1s spectra of PAA-SH PEBs. (**d**) Deconvoluted XPS O 1s spectra of PAA-SH PEBs. (**e**) Deconvoluted XPS N 1s of PAA-SH PEBs. (**f**) Deconvoluted XPS S 2p spectra of PAA-SH PEBs.

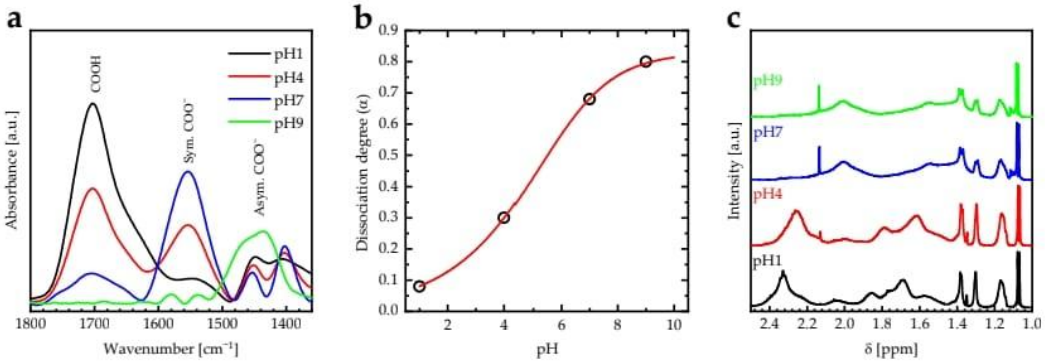

Figure 2. (**a**) FTIR absorbance spectra for carboxylic groups of PAA PEBs at pH 1, 4, 7, and 9 in the range of 1350–1800 cm^{-1} measured at room temperature. (**b**) The dissociation degree (α) calculated using $\alpha = [COO^-]/([COO^-] + \epsilon(COO^-)/\epsilon(COOH)[COOH])$ of PAA PEBs versus pH value. The red line describes the sigmoidal fitting function for the data (**c**) ^{1}H NMR spectra for PAA PEBs at the pH values of 1, 4, 7, and 9 measured at room temperature.

In addition, ^{1}H-NMR spectra of PAA PEBs for different pH values are shown in Figure 2c. The spectral signatures at ppm 1.10, 1.0–1.7, and 2.32 ppm taken at pH = 1

represent the CH_3, CH_2, and CHCOOH protons, respectively. Increasing the pH from one to nine leads to the shifting of the signal of the CHCOOH protons towards smaller chemical shifts, which results in the transformation of the CHCOOH into $CHCOO^-$, which thereby confirms the changes in the chemical structure of the PAA PEBs in the FTIR spectra.

To better understand the effects of the dissociation of the carboxylic acid groups of PAA PEBs on the structure following pH variation, schematic diagrams in addition to 2D AFM measurements of PAA PEBs at different pH values (one, seven, and nine) are shown in Figure 3. At pH ~1, the initial state represents the brushes collapsed to the surface (with 1.5 nm roughness), with the domination of the carboxylic groups (COOH) (Figure 3a). This state represents the hydrophobic behavior of the PEBs. The addition of sodium cations through adding NaOH into the preparation solvent until the pH reaches seven leads to dissociation in the COOH groups into COO^- groups of the upper molecules of the brushes. Consequently, the collapsed brushes transform into swollen brushes with 0.6 nm roughness (Figure 3b). The cations were unable to reach the deeper molecules of the brush film because of their high density. After pH = 9, the ion concentration is appropriate for reaching all molecules of the PEBs and consequently dissociates most of the COOH groups. This event results in the prevalence of the COO^- groups in the brushes (Figure 3c). The domination of the negatively charged COO^- groups increases the electrostatic repulsion in the polymer chains and stretches the brushes with 0.3 nm roughness. In this state, the switching process completes, and the brushes swell. Moreover, the PEBs transform from a hydrophobic to a hydrophilic state (Figure 4) [13]. The contact angle of the PAA PEBs at pH = 1 was initially ~42°, which then decreased to ~24° with an increased pH value of nine.

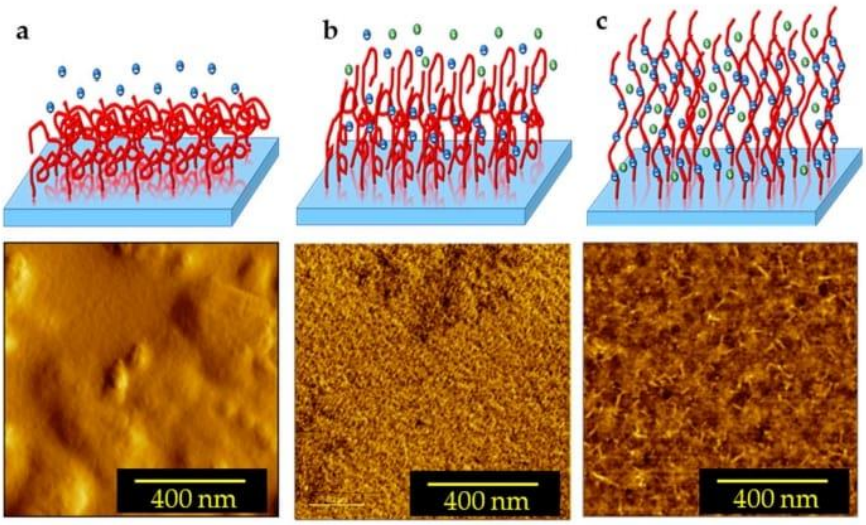

Figure 3. Schematic diagram in addition to 2D AFM images of the switching process of a polymer brush film: (**a**) collapsed brush at pH = 1; (**b**) swollen brush at pH = 7; and (**c**) stretched brush at pH = 9. The negative blue dots: Cl^-; the positive green dots: Na^+.

Increasing the solvent pH increases the electrical conductivity of the PAA PEBs, which can be attributed to the $COOH \rightarrow COO^-$ conversion, and from increasing the ion transfer inside the polymer brush layer [13]. In addition, an increase in temperature enhances the electrical conductivity due to a rise in the energy of the segment motion [39]. This results in a concomitant increase in the free volume around the polymer chains as well as the mobility of ions [40]. Figure 5a shows the variation in electrical conductivity (σ) as a function (1000/T(K)) of the PAA PEBs for different pH values. Arrhenius-like behavior for σ can be defined as $\sigma = \sigma_0 \exp(-E_a/K_BT)$, where σ_0 is the pre-exponential factor [41]. The activation energies deduced from σ for the PAA PEBs have an anomalous behavior

at pH = 5 (Figure 5b), which can be attributed to the fact that the effective pK_a of the PAA PEBs is about 5.54. The refractive index spectrum of the PAA PEBs at pH = 1 exhibits values between 3.15 and 2.08 in the range of 250–700 nm, with a value of 2.09 at a wavelength of 685 nm (Figure 5c). Upon the increase in the pH value to seven, which is the value of the analyte in the SPR measurement, the refractive index decreases to 1.92 at 685 nm. An additional increase in the pH value leads to a decrease in the refractive index to 1.74 at 685 nm. The decrease in the refractive index values upon increasing the pH can be attributed to the change in the PEBs from collapsed to stretched brushes. In addition, the increase in the charge density of the PAA PEBs upon increasing pH values leads to a decrease in the refractive index [42].

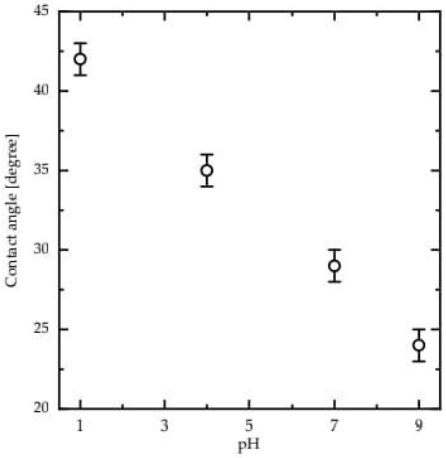

Figure 4. Water contact angle measurements (pH = 7) of PAA PEBs as a function of the pH value measured at room temperature.

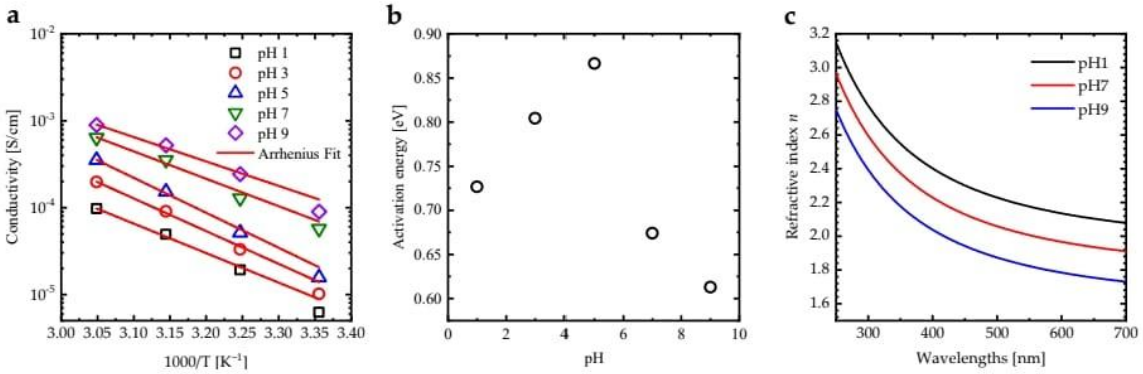

Figure 5. (**a**) Electrical conductivity of the PAA PEBs for different pH values as a function of 1000/T [K^{-1}] fitted by the Arrhenius function to calculate the activation energy of the systems, (**b**) activation energy of the PAA PEBs deduced from the Arrhenius function as a function of the pH value, and (**c**) the refractive index spectra of PAA PEBs for the different pH values of 1, 7, and 9.

WF-SPRM was employed to record a series of 2D images demonstrating local spatiotemporal changes in intensity, which helps to detect the binding of nano-particles. Thiolated PAA (PAA-SH) was deposited onto the gold sensor surface using the spin coating method (Figure 6a). Figure 6b illustrates the theoretical reflectivity curves of the Au layer and Au-PAA layers, which were modeled via employing WINSPALL software [43]. Coating

the Au layer with PAA PEBs increases the incident photon angle and the linewidth (LW). Figure 6c illustrates the shifting in the SPR angle for the Au layer and Au-PAA layers as a function of the refractive index values. The slope of the linear fit represents the sensitivity of the SPR sensor. The SPR sensitivity increases from 114 deg./RIU to 167 deg./RIU as the PAA PEBs appear on the surface of the gold sensing film. Additionally, the figure of merit (FOM) of the sensor, which is defined as the ratio of sensitivity to the LW, was calculated (Table 1) [44]. Coating the Au film with PAA PEBs increases the FOM from 80 to 89 [RIU^{-1}].

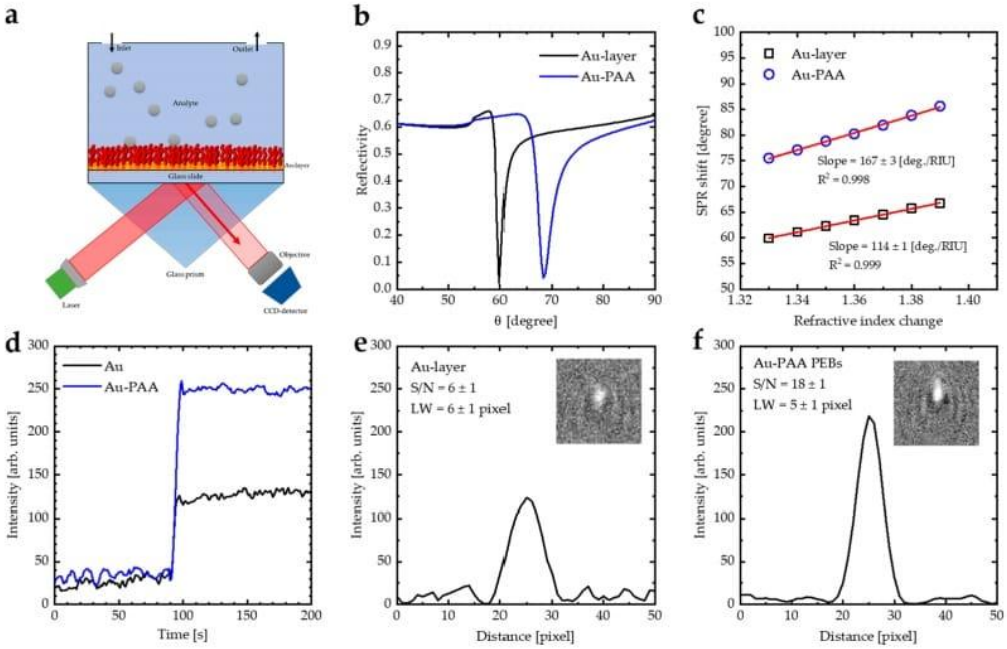

Figure 6. (**a**) Kretschmann's configuration: a model of a glass prism, a gold layer (41–45 nm), and a PAA layer (30 nm) with an analyte for sensing biomolecules. (**b**) SPR reflectivity curve for Kretschmann's configuration of the prism–Au-PAA system deduced from WINSPALL software. (**c**) Sensitivity calculations of bare Au and Au-(PAA PEBs) layers from the data calculated by WINSPALL software. (**d**) Time dependence of the detecting event of PSNPs by the Au layer and Au-PAA layers measured by WF-SPRM. (**e**) Line profile plot of PSNPs detected by the Au layer. (**f**) Line profile plot of PSNPs detected by the Au-PAA layers measured by WF-SPRM. Three replicates were performed.

Table 1. Essential parameters analysis of SPR for bare Au layer and Au-PAA layers.

Layers	R_{min}	θ_{SPR} **[deg.]**	**LW [deg.]**	S **[deg./RIU]**	**FOM [RIU^{-1}]**
Equation	–	–	–	$S = \Delta\theta/\Delta n$	FOM $= S/LW$
Au	0.02	59.8	3.8	114	80
Au-PAA	0.05	75.5	4.8	167	89

Figure 6d demonstrates a local intensity of PSNP detected by the Au layer and Au-PAA layers as a function of the measurement time measured by WF-SPRM. The signal-to-noise ratio (S/N) of the Au-PAA layer is higher than the S/N of the Au layer, which is calculated by studying the line profile plot in the x-direction of the images (Figure 6e,f). The S/N for the Au-layer is 6 ± 1, which increased after coating with the PAA layer to 18 ± 1, indicating that the PAA PEBs enhance the sensitivity of the SPR instrument. In addition, the line

width (LW) of the recorded image decreased from 6 ± 1 pixels to 5 ± 1 pixels through using the Au-PAA layers, which indicates that the spatial resolution of the recorded image is enhanced. In our previous work [15], we used (PANI-HCl)/$Al(NO_3)_3$ complex composite film as a coating for the Au layer to enhance the sensitivity of the WF-SPRM. We found that the S/N for Au-(PANI-HCl)/$Al(NO_3)_3$ with S/N of 10 ± 1. Therefore, we can conclude that coating the Au layer with PAA brushes is more efficient than our previous work. This can be attributed to the fact that the PAA brushes have a higher refractive index than the (PANI-HCl)/$Al(NO_3)_3$ complex composite film.

4. Conclusions

Our work aims to describe the influence of the coating gold sensing surface with the PAA-PEBs on the sensitivity of the WF-SPRM sensor, as well as to provide characteristics of the PAA-PEBs. For this, the pH-dependent switching properties of the PAA-PEBs and their effects on the optical and electrical characterizations were studied. It is demonstrated that, at pH ~1, the initial state of the PEBs corresponds to the brushes that collapse to the surface, with the dominance of the carboxylic groups (COOH). The prevalence of the negatively charged COO^- groups increases the electrostatic repulsion in the polymer chains and stretches the brushes. AFM confirms that the PAA PEBs at pH = 1 exhibit collapsed brushes. Increasing the pH to seven leads to the dissociation of the COOH groups of the upper molecules and conversion into the negatively charged COO^- groups, and consequently transforms the collapsed brushes into swollen brushes. At pH = 9, the ion concentration is sufficient to reach the deeper molecules of the PEBs that consequently dissociate most of the COOH groups, leading to the prevalence of the COO^- groups that, in turn, completes the switching process, leading to stretched brushes. Under increasing pH, the PAA PEBs transform from a hydrophobic to hydrophilic state. Increasing the solvent pH leads to an enhancement in the electrical conductivity of the PAA PEBs. This can be attributed to the COOH → COO^- conversion. PAA PEBs were deposited on a gold layer using a thiol group (PAA-SH), which was confirmed by XPS and NMR spectroscopy. The signal-to-noise ratio for the Au layer is six, increasing after coating by PAA PEBs to eighteen. In addition, the linewidth of the recorded image decreased from six pixels to five pixels through using the Au-PAA layers. Finally, it was demonstrated that coating the Au layer with PAA PEBs enhances the sensitivity of the SPR sensor and improves the spatial resolution of the recorded image.

Author Contributions: Conceptualization, Q.M.A.-B. and A.D.T.; methodology, Q.M.A.-B. and V.S; software, Q.M.A.-B. and R.H.; validation, A.D.T., C.J.T. and R.H.; formal analysis, Q.M.A.-B., C.J.T. and V.S.; investigation, A.D.T. and R.H.; resources, A.D.T. and R.H.; data curation, Q.M.A.-B. and R.H.; writing—original draft preparation, Q.M.A.-B. and A.D.T.; writing—review and editing, C.J.T., V.S. and R.H.; visualization, Q.M.A.-B., A.D.T. and C.J.T.; supervision, A.D.T. and R.H.; project administration, A.D.T. and R.H. All authors have read and agreed to the published version of the manuscript.

Funding: This research received no external funding.

Institutional Review Board Statement: Not applicable.

Informed Consent Statement: Not applicable.

Data Availability Statement: Not applicable.

Acknowledgments: The scientific support by the Ministerium für Innovation, Wissenschaft und Forschung des Landes Nordrhein-Westfalen, the Senatsverwaltung für Wirtschaft, Technologie und Forschung des Landes Berlin, and the Bundesministerium für Bildung und Forschung is gratefully acknowledged. We also thank Ahmad A. Ahmad for helping our members use the thin films laboratory at the Jordan University of Science and Technology. This work was also supported by the German Research Association (DFG) within the Collaborative Research Centre 876 SFB 876 "Providing Information by Resource-Constrained Data Analysis", project B2.

Conflicts of Interest: The authors declare no conflict of interest.

References

1. Yuan, J.; Antila, H.S.; Luijten, E. Dielectric effects on ion transport in polyelectrolyte brushes. *ACS Macro Lett.* **2019**, *8*, 183–187. [CrossRef]
2. Ferrand-Drake del Castillo, G.; Hailes, R.L.; Dahlin, A. Large changes in protonation of weak polyelectrolyte brushes with salt concentration—Implications for protein immobilization. *J. Phys. Chem. Lett.* **2020**, *11*, 5212–5218. [CrossRef]
3. Ferrand-Drake del Castillo, G.; Koenig, M.; Müller, M.; Eichhorn, K.-J.; Stamm, M.; Uhlmann, P.; Dahlin, A. Enzyme immobilization in polyelectrolyte brushes: High loading and enhanced activity compared to monolayers. *Langmuir* **2019**, *35*, 3479–3489. [CrossRef]
4. Yuan, J.; Antila, H.S.; Luijten, E. Structure of polyelectrolyte brushes on polarizable substrates. *Macromolecules* **2020**, *53*, 2983–2990. [CrossRef]
5. Das, S.; Banik, M.; Chen, G.; Sinha, S.; Mukherjee, R. Polyelectrolyte brushes: Theory, modelling, synthesis and applications. *Soft Matter* **2015**, *11*, 8550–8583. [CrossRef]
6. Ballauff, M.; Borisov, O. Polyelectrolyte brushes. *Curr. Opin. Colloid Interface Sci.* **2006**, *11*, 316–323. [CrossRef]
7. Yigit, C.; Kanduc, M.; Ballauff, M.; Dzubiella, J. Interaction of charged patchy protein models with like-charged polyelectrolyte brushes. *Langmuir* **2017**, *33*, 417–427. [CrossRef] [PubMed]
8. Koenig, M.; Bittrich, E.; König, U.; Rajeev, B.L.; Müller, M.; Eichhorn, K.-J.; Thomas, S.; Stamm, M.; Uhlmann, P. Adsorption of enzymes to stimuli-responsive polymer brushes: Influence of brush conformation on adsorbed amount and biocatalytic activity. *Colloids Surf. B Biointerfaces* **2016**, *146*, 737–745. [CrossRef]
9. De Vos, W.M.; Leermakers, F.A.; De Keizer, A.; Cohen Stuart, M.A.; Kleijn, J.M. Field theoretical analysis of driving forces for the uptake of proteins by like-charged polyelectrolyte brushes: Effects of charge regulation and patchiness. *Langmuir* **2010**, *26*, 249–259. [CrossRef]
10. Li, M.; Pester, C.W. Mixed polymer brushes for "smart" surfaces. *Polymers* **2020**, *12*, 1553. [CrossRef] [PubMed]
11. Mumtaz, F.; Chen, C.; Zhu, H.; Pan, C.; Wang, Y. Controlled protein adsorption on PMOXA/PAA based coatings by thermally induced immobilization. *Appl. Surf. Sci.* **2018**, *439*, 148–159. [CrossRef]
12. Currie, E.; Sieval, A.; Fleer, G.; Stuart, M.C. Polyacrylic acid brushes: Surface pressure and salt-induced swelling. *Langmuir* **2000**, *16*, 8324–8333. [CrossRef]
13. Aulich, D.; Hoy, O.; Luzinov, I.; Brücher, M.; Hergenröder, R.; Bittrich, E.; Eichhorn, K.-J.; Uhlmann, P.; Stamm, M.; Esser, N. In situ studies on the switching behavior of ultrathin poly (acrylic acid) polyelectrolyte brushes in different aqueous environments. *Langmuir* **2010**, *26*, 12926–12932. [CrossRef] [PubMed]
14. Masson, J.-F. Surface plasmon resonance clinical biosensors for medical diagnostics. *ACS Sens.* **2017**, *2*, 16–30. [CrossRef] [PubMed]
15. Al-Bataineh, Q.M.; Shpacovitch, V.; Sadiq, D.; Telfah, A.; Hergenröder, R. Surface Plasmon Resonance Sensitivity Enhancement Based on Protonated Polyaniline Films Doped by Aluminum Nitrate. *Biosensors* **2022**, *12*, 1122. [CrossRef]
16. Shpacovitch, V.; Hergenröder, R. Surface plasmon resonance (SPR)-based biosensors as instruments with high versatility and sensitivity. *Sensors* **2020**, *20*, 3010. [CrossRef] [PubMed]
17. Nizamov, S.; Sazdovska, S.D.; Mirsky, V.M. A review of optical methods for ultrasensitive detection and characterization of nanoparticles in liquid media with a focus on the wide field surface plasmon microscopy. *Anal. Chim. Acta* **2022**, *1204*, 339633. [CrossRef]
18. Sidorenko, I.; Nizamov, S.; Hergenröder, R.; Zybin, A.; Kuzmichev, A.; Kiwull, B.; Niessner, R.; Mirsky, V.M. Computer assisted detection and quantification of single adsorbing nanoparticles by differential surface plasmon microscopy. *Microchim. Acta* **2016**, *183*, 101–109. [CrossRef]
19. Nizamov, S.; Scherbahn, V.; Mirsky, V.M. Detection and quantification of single engineered nanoparticles in complex samples using template matching in wide-field surface plasmon microscopy. *Anal. Chem.* **2016**, *88*, 10206–10214. [CrossRef]
20. Shpacovitch, V.; Sidorenko, I.; Lenssen, J.E.; Temchura, V.; Weichert, F.; Müller, H.; Überla, K.; Zybin, A.; Schramm, A.; Hergenröder, R. Application of the PAMONO-sensor for quantification of microvesicles and determination of nano-particle size distribution. *Sensors* **2017**, *17*, 244. [CrossRef]
21. Zybin, A.; Shpacovitch, V.; Skolnik, J.; Hergenröder, R. Optimal conditions for SPR-imaging of nano-objects. *Sens. Actuators B Chem.* **2017**, *239*, 338–342. [CrossRef]
22. Rouf, H.K.; Haque, T. Performance enhancement of Ag-Au bimetallic surface plasmon resonance biosensor using InP. *Prog. Electromagn. Res. M* **2018**, *76*, 31–42. [CrossRef]
23. Shalabney, A.; Abdulhalim, I. Sensitivity-enhancement methods for surface plasmon sensors. *Laser Photonics Rev.* **2011**, *5*, 571–606. [CrossRef]
24. Wang, Y.-M.; Cui, Y.; Cheng, Z.-Q.; Song, L.-S.; Wang, Z.-Y.; Han, B.-H.; Zhu, J.-S. Poly (acrylic acid) brushes pattern as a 3D functional biosensor surface for microchips. *Appl. Surf. Sci.* **2013**, *266*, 313–318. [CrossRef]
25. Ansar, S.M.; Fellows, B.; Mispireta, P.; Mefford, O.T.; Kitchens, C.L. pH triggered recovery and reuse of thiolated poly (acrylic acid) functionalized gold nanoparticles with applications in colloidal catalysis. *Langmuir* **2017**, *33*, 7642–7648. [CrossRef] [PubMed]
26. Ahmad, A.; Migdadi, A.; Alsaad, A.; Al-Bataineh, Q.M.; Telfah, A. Optical, structural, and morphological characterizations of synthesized (Cd–Ni) co-doped ZnO thin films. *Appl. Phys. A* **2021**, *127*, 922. [CrossRef]

27. Alsaad, A.; Al-Bataineh, Q.M.; Ahmad, A.; Albataineh, Z.; Telfah, A. Optical band gap and refractive index dispersion parameters of boron-doped ZnO thin films: A novel derived mathematical model from the experimental transmission spectra. *Optik* **2020**, *211*, 164641. [CrossRef]
28. Ahmad, A.A.; Khazaleh, M.H.; Alsaad, A.M.; Al-Bataineh, Q.M.; Telfah, A.D. Characterization of As-prepared PVA-PEO/ZnO-Al2O3-NPs hybrid nanocomposite thin films. *Polym. Bull.* **2022**, *79*, 9881–9905. [CrossRef]
29. Rothenhäusler, B.; Knoll, W. Surface–plasmon microscopy. *Nature* **1988**, *332*, 615–617. [CrossRef]
30. Kretschmann, E. Determination of optical constants of metals by excitation of surface plasmons. *Z. Phys.* **1971**, *241*, 313–324. [CrossRef]
31. Shpacovitch, V.; Hergenroeder, R. Optical and surface plasmonic approaches to characterize extracellular vesicles. A review. *Anal. Chim. Acta* **2018**, *1005*, 1–15. [CrossRef] [PubMed]
32. Schnorrenberg, H.-J.; Hengstebeck, M.; Schlinkmeier, K. The attenuation of a coherent field by scattering. *Opt. Commun.* **1995**, *117*, 532–540. [CrossRef]
33. Zhang, Y.; Rossi, F.; Papa, S.; Violatto, M.B.; Bigini, P.; Sorbona, M.; Redaelli, F.; Veglianese, P.; Hilborn, J.; Ossipov, D.A. Non-invasive in vitro and in vivo monitoring of degradation of fluorescently labeled hyaluronan hydrogels for tissue engineering applications. *Acta Biomater.* **2016**, *30*, 188–198. [CrossRef] [PubMed]
34. Schuetze, B.; Mayer, C.; Loza, K.; Gocyla, M.; Heggen, M.; Epple, M. Conjugation of thiol-terminated molecules to ultrasmall 2 nm-gold nanoparticles leads to remarkably complex 1 H-NMR spectra. *J. Mater. Chem. B* **2016**, *4*, 2179–2189. [CrossRef]
35. Ahmad, M.J.A.; Telfah, A.; Al-Bataineh, Q.M.; Tavares, C.J.; Hergenröder, R. Nanoparticles positioning effect on properties of (PS-PANI/NiNPs) nanocomposite films. *Polym. Adv. Technol.* **2023**, *34*, 110–119. [CrossRef]
36. Dong, R.; Lindau, M.; Ober, C.K. Dissociation behavior of weak polyelectrolyte brushes on a planar surface. *Langmuir* **2009**, *25*, 4774–4779. [CrossRef]
37. Wiśniewska, M.; Urban, T.; Grządka, E.; Zarko, V.I.; Gun'ko, V.M. Comparison of adsorption affinity of polyacrylic acid for surfaces of mixed silica–alumina. *Colloid Polym. Sci.* **2014**, *292*, 699–705. [CrossRef]
38. Aureau, D.; Ozanam, F.; Allongue, P.; Chazalviel, J.-N. The titration of carboxyl-terminated monolayers revisited: In situ calibrated Fourier transform infrared study of well-defined monolayers on silicon. *Langmuir* **2008**, *24*, 9440–9448. [CrossRef]
39. Pillai, P.; Khurana, P.; Tripathi, A. Dielectric studies of poly (methyl methacrylate)/polystyrene double layer system. *J. Mater. Sci. Lett.* **1986**, *5*, 629–632. [CrossRef]
40. AL-Akhras, M.A.; Alzoubi, S.E.; Ahmad, A.A.; Ababneh, R.; Telfah, A. Studies of composite films of polyethylene oxide doped with potassium hexachloroplatinate. *J. Appl. Polym. Sci.* **2021**, *138*, 49757. [CrossRef]
41. Telfah, A.; Al-Akhras, M.-A.; Al-Izzy, K.A.; Ahmad, A.A.; Ababneh, R.; Ahmad, M.J.A.; Tavares, C.J.; Hergenröder, R. Dielectric relaxation, XPS and structural studies of polyethylene oxide/iodine complex composite films. *Polym. Bull.* **2022**, *79*, 3759–3778. [CrossRef]
42. Cho, J.; Hong, J.; Char, K.; Caruso, F. Nanoporous block copolymer micelle/micelle multilayer films with dual optical properties. *J. Am. Chem. Soc.* **2006**, *128*, 9935–9942. [CrossRef] [PubMed]
43. Available online: http://www.res-tec.de/ (accessed on 25 February 2023).
44. Rahman, M.M.; Abdulrazak, L.F.; Ahsan, M.; Based, M.A.; Rana, M.M.; Anower, M.S.; Rikta, K.A.; Haider, J.; Gurusamy, S. 2D Nanomaterial-Based Hybrid Structured (Au-WSe 2-PtSe 2-BP) Surface Plasmon Resonance (SPR) Sensor With Improved Performance. *IEEE Access* **2021**, *10*, 689–698. [CrossRef]

5.4. Original Paper IV: Al-Bataineh et al., 2024b)

Applied Surface Science 649 (2024) 159189

Contents lists available at ScienceDirect

Applied Surface Science

journal homepage: www.elsevier.com/locate/apsusc

Full Length Article

Wide-field surface plasmon resonance microscope based on polyethylene oxide/polyacrylic acid brushes

Qais M. Al-Bataineh [a,b,*], Ahmad D. Telfah [c,d], Carlos J. Tavares [e], Roland Hergenröder [a,*]

[a] Leibniz-Institut für Analytische Wissenschaften-ISAS-e.V., 44139 Dortmund, Germany
[b] Department of Physics, TU Dortmund University, 44227 Dortmund, Germany
[c] Nanotechnology Center, The University of Jordan, 11942 Amman, Jordan
[d] Department of Physics, University of Nebraska at Omaha, Omaha NE-68182, USA
[e] Physics Centre of Minho and Porto Universities (CF-UM-UP), University of Minho, 4804-533 Guimaraes, Portugal

ARTICLE INFO

Keywords:
Surface plasmon resonance (SPR)
Imaging wide-field SPR microscope (WF-SPRM)
Polyelectrolyte brushes (PEBs)
Polyacrylic acid (PAA)
Polyethylene oxide (PEO)

ABSTRACT

Wide-field surface plasmon resonance microscope (WF-SPRM) based on polyethylene oxide/polyacrylic acid (PEO/PAA) polyelectrolyte brushes (PEBs) is presented for particle detection application. PEO acts as an H-bond acceptor, while PAA serves as an H-bond donor, forming hydrogen-bonding complexes within the brushes. Morphological, chemical, and crystal structural analyses confirm that the PEO/PAA brushes undergo a transition from a collapsed to a stretched state as the solvent pH is increased from 1 to 10. This pH-dependent change also renders the PEO/PAA brushes more hydrophilic. Additionally, the electrical conductivity and refractive index of the PEO/PAA brushes increase concomitantly with the increase of solvent pH. Furthermore, theoretical and experimental approaches study the sensitivity of WF-SPRM utilizing Au-(PEO/PAA) polyelectrolyte layers. The theoretical sensitivity of WF-SPRM is enhanced from 118.5 deg./RIU for the Au-layer to 178.1 deg./RIU for Au-(PEO/PAA PEBs). Moreover, the signal-to-noise ratio for the Au-(PEO/PAA PEBs) layer is 20 ± 1, indicating improved sensing performance compared to the Au-layer (signal-to-noise ratio of 6 ± 1). A mathematical model to describe the discrete particle detection by WF-SPRM is presented, where results demonstrate a good agreement between the calculated intensity profile and experimental data.

1. Introduction

Polyelectrolyte brushes (PEBs) are a class of intelligent polymers with the remarkable ability to undergo reversible transformations between different shapes when exposed to external stimuli, such as changes in pH, light, temperature, or electric fields [1]. The versatility of PEBs makes them highly promising for various practical applications, including sensors, smart actuators, and biomedical devices [2–5]. The formation of polymer–polymer complexes arises from noncovalent interactions between the functional groups of the polymer chains [6]. These complexes can be further categorized based on the dominating interaction types, such as polyelectrolyte complexes driven by Coulombic forces, hydrogen-bonding complexes stabilized by hydrogen bonds, and charge-transfer complexes [7,8].

This study focuses on investigating the polymer–polymer complexes formed by polyethylene oxide (PEO) and polyacrylic acid (PAA), which are classified as hydrogen-bonding complexes. PEO possesses H-bond acceptor properties, enabling the formation of hydrogen-bonding complexes [9]. Moreover, PEO-based hydrogen-bonding complexes can be created with H-bond donor polymers like polyelectrolytes [10,11]. Among the polyelectrolytes, PAA is a weak polyelectrolyte brushes (PEBs) containing carboxylic acid, exhibiting variations in structures, charges, and hydrophilicity at different pH levels [12,13]. PAA PEBs have diverse applications, including protein refinement, enzyme immobilization, drug delivery, bioinspired nanoreactors, artificial joints, smart actuators, and bioelectronic devices [14–16].

Mixed PEBs, combining protein-adsorbing and protein-repellent properties, can be beneficial for protein adsorption and nano-particle detection [17]. Previous models based on PEO/PAA brushes in saline solutions suggested that PEO/PAA brushes efficiently adsorb and desorb proteins [18,19]. The physical interactions between PEBs and macromolecules remain a topic of investigation, with proposed mechanisms involving local patches on the macromolecule surface and the environment within the PEBs [20–23].

* Corresponding authors at: Leibniz Institut für Analytische Wissenschaften-ISAS-e.V., 44139 Dortmund, Germany (Q.M. Al-Bataineh).
E-mail addresses: qais.albataineh@tu-dortmund.de (Q.M. Al-Bataineh), a.telfah@ju.edu.jo (A.D. Telfah), roland.hergenroeder@isas.de (R. Hergenröder).

https://doi.org/10.1016/j.apsusc.2023.159189
Received 6 November 2023; Received in revised form 12 December 2023; Accepted 19 December 2023
Available online 21 December 2023

To enhance surface plasmon resonance (SPR) sensitivity, a wide-field surface plasmon resonance microscope (WF-SPRM) based on Au-(PEO/PAA PEBs) layers is designed. WF-SPRM is a spatiotemporal sensor capable of imaging nano-objects in solution through interactions with the sensor surface [24,25]. This sensor can detect individual nano-objects, such as viruses and virus-like particles [26,27].

The presented work investigates the chemical, crystal, and morphological properties of switchable PEO/PAA PEBs under varying pH conditions. An increase in pH value transforms the carboxylic acid (COOH) groups into carboxylate (COO^-) groups, leading to the transformation of collapsed PEBs into stretched PEBs. Additionally, the effect of pH variation on the optical refractive index, electrical conductivity, and hydrophobicity behavior of the PEO/PAA PEBs is explored.

2. Experimental sections

2.1. Synthesis technique

The "grafting to" method was employed for depositing PEO/PAA PEBs through thiol group modification. Initially, stock solutions of polyethylene oxide (PEO, 300,000 $g.mol^{-1}$, Sigma-Aldrich) and polyacrylic acid (PAA, 1800 $g.mol^{-1}$, Sigma-Aldrich) were prepared by dissolving 1.0 g of each polymer in 100 mL distilled water under continuous stirring at 45 °C for five hours. Subsequently, a PEO/PAA blend (50:50 wt%) stock solution was formed using the solution mixing method and subjected to sonication at 40 °C for five hours to produce PEO/PAA blends.

Thiolated PEO/PAA (PEO/PAA-SH) was then prepared by performing carbodiimide amide coupling reactions for one in four hydroxyls and/or carboxylic acid groups, following previous research [28]. In which 0.320 g of N-hydroxy succinimide (115.09 $g.mol^{-1}$, Sigma-Aldrich) and 0.533 g of 1-ethyl-3-(3-(dimethylamino) propyl) carbodiimide) hydrochloride (155.245 $g.mol^{-1}$, Sigma-Aldrich) were added into 100 mL of PEO/PAA stock solution under continuous stirring for 30 min at room temperature. After that, 0.316 g of cysteamine hydrochloride (113.61 $g.mol^{-1}$, Sigma-Aldrich) was added to the reaction under continuous stirring for four hours at room temperature. Finally, the PEO/PAA-SH PEBs were purified by adding toluene in small amounts to the final solution. The initial solution had a pH value of approximately 1, which was adjusted to 4, 7, and 10 by adding sodium hydroxide (NaOH, 39.997 g/mol, Sigma-Aldrich) to the PEO/PAA-SH solvent.

Before surface functionalization, n-type silicon wafers and ITO glass substrates were cleaned using acetone for 30 min in a sonication bath. Gold substrates, consisting of a 5 nm adhesion Ti-layer and approximately 41–45 nm Au-layer on glass, were cleaned using piranha solution for 10 min. All substrates were then rinsed with distilled water and dried using argon gas. The PEO/PAA-SH PEBs with about 20 nm were deposited onto the substrates using the spin coating method. Finally, the films were dried at 70 °C under ambient pressure to evaporate the solvents. The "grafting to" method is illustrated in Figure S1.

2.2. Characterization techniques

The chemical structure analysis of the polyelectrolyte brushes was carried out using three main spectroscopic techniques: Fourier-transform infrared spectroscopy (FTIR) (Bruker VERTEX 80/80v Vacuum FTIR Spectrometers), nuclear magnetic resonance (^1H NMR) (Bruker AVANCE III NMR spectrometer, 600.13 MHz, 600 μL D_2O: 200 μL PEO/PAA-SH solution), and near-ambient pressure X-ray photoelectron spectroscopy NAP-XPS (SPECS Surface Nano Analysis GmbH). In parallel, the crystal structure investigation of the PEBs was conducted using an X-ray diffractometer (Malvern Panalytical Ltd) with Cuk_α radiation. For assessing the morphological properties of the PEBs, atomic force microscopy (AFM) (SPM SmartSPM™-1000) and water contact angle experiments have recurred. The refractive index was determined based on the optical properties measured using a UV–Vis spectrophotometer (Hitachi U-3900H), following the procedures already outlined [28–30]. Electrical conductivity measurements were carried out using a 4-point probe (Microworld Inc.).

Additionally, WF-SPRM measurements were performed as previously described [28,31]. The PEO/PAA-SH PEBs at pH 7 were deposited on a gold substrate by spin-coating technique, resulting in a thickness of ~20 nm. Silica nanoparticles (refractive index n = 1.420 [32]) with an average size of 100 nm were employed to Simulate biological particles due to their refractive index similarity to biological particles.

3. Results and discussion

PEO/PAA blend PEBs with a weight ratio of 50:50 were synthesized using the solution mixing method. These blends form interpolymer hydrogen bonds, with the ether oxygen atoms in PEO acting as H-acceptors and the carboxylate group of PAA acting as H-donors (Supplementary S2) [1]. However, applying PEO/PAA PEBs as coatings on various substrates poses a challenge due to the absence of strongly functional group binding to the surfaces. To address this, thiol groups were introduced into the hydroxyl and carboxylic groups of PEO/PAA PEBs through carbodiimide amide coupling reactions (Supplementary S3).

3.1. Dissociation behavior of PEO/PAA PEBs

The dissociation behavior of PEO/PAA PEBs was investigated using FTIR spectroscopy, as the COOH and COO^- groups exhibit distinct vibrational bands at different IR wavelengths [33]. Fig. 1a presents the vibrational bands of COOH and COO^- groups in PEO/PAA PEBs at varying pH values (1, 4, 7, and 10). At pH equal to 1, the vibrational band of COOH groups (at approximately 1700 cm^{-1}) is about 7 times higher than the vibrational band of asymmetric COO^- groups (at around 1500 cm^{-1}), with no observable symmetric COO^- groups. As the pH value increases to 4, the vibrational band of COOH groups decreases, while the vibrational bands of symmetric and asymmetric COO^- groups increase due to the dissociation of COOH groups by OH^- ions. However, the vibrational band of COOH groups remains approximately 3 times more intense than the combined vibrational bands of symmetric and asymmetric COO^- groups. Further elevation of the pH value to 10 results in the dominance of symmetric and asymmetric COO^- groups, leading to increased electrostatic repulsion within the polymer chains and elongation of the brushes. The dissociation degree at each pH value was calculated using methods from the literature [34]. Plotting the dissociation degree against the solvent pH values yields the titration curve of the PEO/PAA PEBs (Fig. 1b), which was fitted to the sigmoid function [34]. The effective dissociation constant (pKa) of the PEO/PAA PEBs is 4.95.

Fig. 1c displays the ^1H NMR spectra of PEO/PAA PEBs at different pH values. The signals observed at 1.10, 1.0–1.7, and 2.32 ppm correspond to CH_3, CH_2, and CHCOOH protons, respectively, in the PAA segments. The broad peak at 3.62 ppm is attributed to $-OCH_2CH_2-$ in the PEO segments. With an increase in pH from 1 to 10, the CHCOOH signal shifts to lower chemical shifts, indicating a transformation to $CHCOO^-$, leading to electrostatic repulsion between the brushes. The surface morphology of the PEO/PAA PEBs is affected by the solvent pH values, as evidenced by AFM measurements at pH values of 1, 4, 7, and 10 (Fig. 2). At low pH values (1 and 4), the dominance of COOH groups results in collapsed brushes, indicating the absence of repulsion forces between the brushes, with surface roughness about 1 nm and 3 nm, and thickness about 17 nm and 19 nm, respectively (Fig. 2a and 2b). As the pH increases to 7, the COOH groups dissociate into negatively charged COO^- groups, inducing electrostatic repulsion between the brushes and transforming them into swollen brushes, with surface roughness of 5 nm and thickness of 20 nm (Fig. 2c). At pH 10, complete dissociation of COOH groups to COO^- groups intensify the electrostatic repulsion

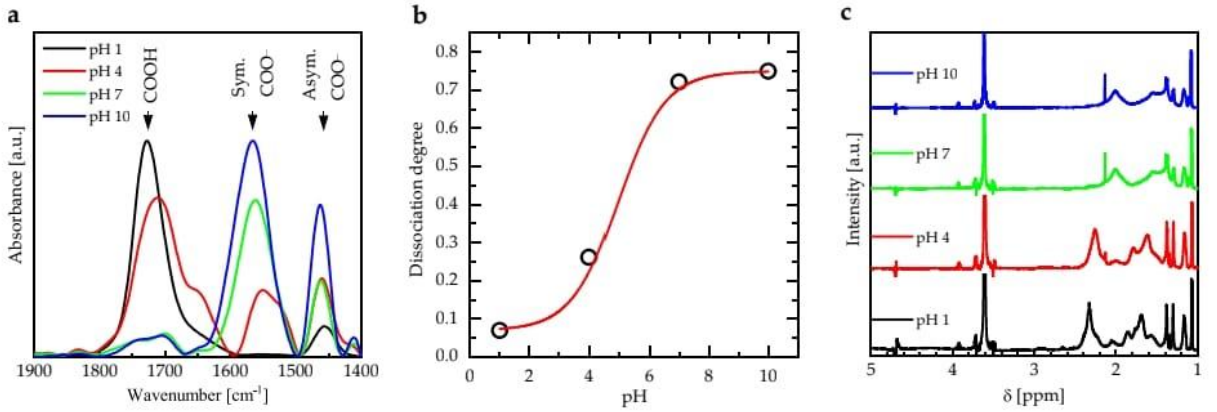

Fig. 1. **(a)** Fourier Transform Infrared (FTIR) spectra of PEO/PAA PEBs at pH values of 1, 4, 7, and 10 within the wavenumber range of 1400–1900 cm^{-1}. **(b)** Plot illustrating the dissociation degree of PEO/PAA PEBs as a function of pH value. **(c)** ^{1}H NMR) spectra of PEO/PAA PEBs recorded at pH values of 1, 4, 7, and 10.

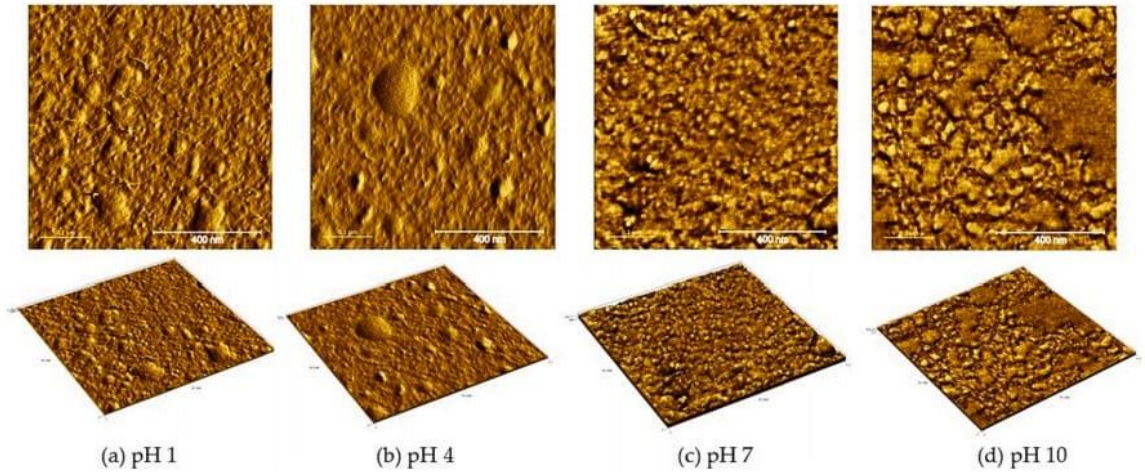

Fig. 2. 2D- and 3D-AFM micrographs of PEO/PAA PEBs at different pH values, namely **(a)** pH 1, (b) pH 4, **(c)** pH 7, and **(d)** pH 10.

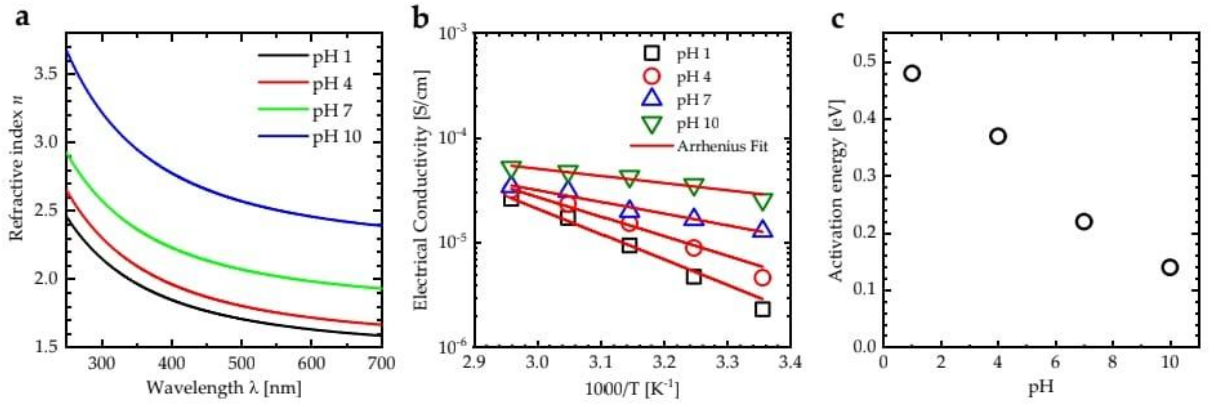

Fig. 3. **(a)** Refractive index spectra of PEO/PAA PEBs at various pH values. **(b)** Electrical conductivity of PEO/PAA PEBs at different pH values as a function of 1000/T $[K^{-1}]$. **(c)** The activation energy of the PEO/PAA PEBs as a function of pH value.

between the brushes, leading to stretched brushes with surface roughness of 7 nm and thickness of 23 nm (Fig. 2d). Moreover, higher pH values (pH 7 and 10) promote increased hydrophilicity of PEO/PAA PEBs, enhancing interacting surfaces between the PEBs and the surrounding medium (Supplementary S4). Additionally, as pH values increase to 10, the crystallinity degree of PEO/PAA PEBs changes due to the forming of new PEBs from a collapsed to a stretched state (Supplementary S5).

3.2. Optical and electrical properties

The sensitivity of SPR in the WF-SPRM relies on the refractive index (n) of the dielectric layer that coats the Au layer. Thus, the refractive index spectra of PEO/PAA PEBs for various solvent pH values are investigated (Fig. 3a). At pH 1, the refractive index of PEO/PAA PEBs decreases from 2.45 to 1.59 as the incident photon wavelength increases from 250 to 700 nm, being 1.59 at 685 nm. As the pH values increase to 10, n increases continuously, reaching 2.40 at 685 nm, which is attributed to the transformation of PEBs from collapsed brushes to stretched brushes. However, particle detection by WF-SPRM was performed at pH 7. At pH 7, *the* refractive index of PEO/PAA PEBs decreases from 2.93 to 1.93 in the range of 250 to 700 nm, being 1.94 at 685 nm.

Furthermore, the electrical conductivity (σ) of the PEO/PAA PEBs increases with increasing solvent pH, attributed to the dissociation of COOH groups into negatively charged COO^- groups, enhancing the ion transfer inside the polymer brush and consequently increasing electrical conductivity [33]. An increase in temperature also leads to increased electrical conductivity due to higher segment vibration energy, resulting in more segmental motion and enhanced ion mobility [35,36]. The electrical conductivity of PEO/PAA PEBs as a function of 1000/T [K^{-1}] for different pH values exhibits Arrhenius-like behavior $\sigma = \sigma_0 \exp(-E_a/k_BT)$ (Fig. 3b), where T is temperature and k_B the Boltzmann constant. The activation energy (E_a) determined from the Arrhenius function decreases from 0.48 eV to 0.14 eV as the solvent pH increases from 1 to 10 (Fig. 3c).

3.3. Wide-field SPR microscopy

A wide-field surface plasmon resonance microscope was employed to capture time series of 2D images. It created a spatiotemporal volume of intensities to detect the SPR effects of nano-objects and quantify their presence. The gold surface was functionalized under controlled flow conditions, and PEO/PAA-SH was deposited on the gold layer to establish connections with the analyte for detecting silica nanoparticles (Fig. 4a). The SPR sensitivity of the Au-layer and Au-(PEO/PAA-SH) layers were initially investigated through theoretical simulations using Winspall software [41]. Theoretical reflectivity curves of the Au-layer and Au-(PEO/PAA-SH) layers were plotted against the incident beam angles in Fig. 4b. The SPR angle for the Au-layer is 59.85°, which increases to 75.93° after coating with PEO/PAA PEBs. The SPR sensitivity is calculated as $S = \Delta\theta/\Delta n$, where $\Delta\theta$ represents the SPR angle shift, and Δn is the refractive index change. Consequently, a series of SPR angle values were generated by increasing the analyte's refractive index from 1.33 (refractive index of water) to 1.40, with an interval increase of 0.01 (Fig. 4c). The plot of SPR shift as a function of the analyte's refractive index displays a linear relationship, and the slope of this curve represents the SPR sensitivity. The SPR sensitivity increases from 119 deg./RIU to 178 deg./RIU when PEO/PAA PEBs are coated onto the gold layer.

Subsequently, experimental investigations are conducted using the Au-layer and Au-(PEO/PAA-SH) layers to explore the sensitivity of the wide-field surface plasmon resonance microscope (WF-SPRM) in detecting silica nanoparticles with a size of 100 nm. The study involves analyzing the signal-to-noise ratio and linewidth of the detected particles. ImageJ software is employed for image averaging and background subtraction [37]. Notably, the binding of particles to both the Au-layer and Au-PEO/PAA layers results in the sudden appearance of a distinct bright spot corresponding to the particle shape on the micrographs (as shown in the inset image of Fig. 5a).

Fig. 5a presents the time-dependent relative intensity that represents the binding event of silica nanoparticles to the sensor surface. The abrupt increase in relative intensity is indicative of a binding event. Notably, the relative intensity of the detected silica nanoparticles on the Au-(PEO/PAA-SH) layers surpasses that of the Au-layer. In Fig. 5b, the line profile in the x-direction showcases the bound silica nanoparticles on both Au- and Au-(PEO/PAA-SH) layers. The signal-to-noise ratio (S/N) for the Au-layer is 6 ± 1, which notably increases to 20 ± 1 for the Au-(PEO/PAA-SH) layers, indicating that the presence of PEO/PAA PEBs enhances the SPR sensitivity for particle detection. Moreover, the linewidth of the recorded spot decreases from 8 ± 1 pixels (Au-layer) to 5 ± 1 pixels (Au-(PEO/PAA-SH) layers), demonstrating the improved spatial resolution of the recorded images.

The second parameter that effects on detected particle intensity is the particle size, where the signal intensity of silica nanoparticle detected by the Au layer increases from about 90 a.u. to about 128 a.u. as silica nanoparticle size increases from 100 to 400 nm (Fig. 5c). On the other hand, the signal intensity of silica nanoparticle detected by the Au-(PEO/PAA-SH) layers increases from about 115 a.u. to about 165 a.u. as silica nanoparticle size increases from 100 to 400 nm (Fig. 5c). The signal intensity for silica nanoparticles detected by Au and Au-(PEO/PAA-SH) layers can be fitted by a straight line between 100 and 400 nm, indicating the fundamental difference between the Mie scattering and

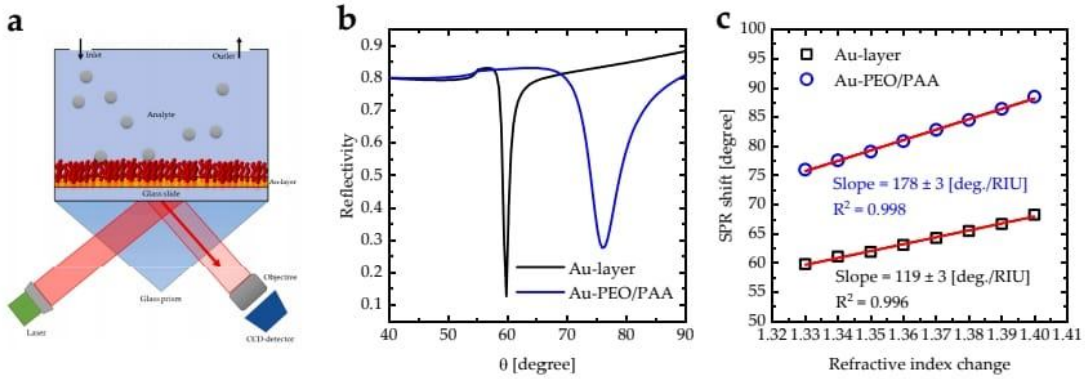

Fig. 4. **(a)** The Kretschmann configuration illustrating the prism-gold-PEO/PAA PEBs system, **(b)** Reflectivity versus incident angle for the Kretschmann configuration of the prism-gold-PEO/PAA PEBs system, and **(c)** SPR angle shift versus the refractive index change of bare Au-layer and Au-(PEO/PAA PEBs) layers.

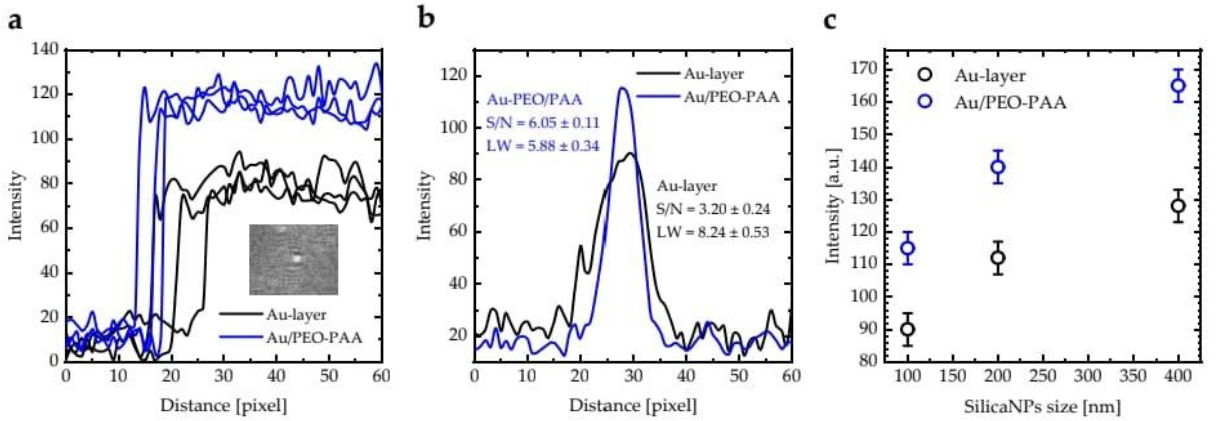

Fig. 5. **(a)** Time-dependent intensity variation in the center of the bright spot for detected silica nanoparticles using the Au-layer and Au-PEO/PAA PEBs. **(b)** Line profile plot representing the detected silica nanoparticles by the Au-layer and Au-PEO/PAA PEBs. Three independent replicates are conducted for each measurement. S/N is the signal-to-noise ratio, and LW is the linewidth. **(c)** Experimental intensity of detected silica nanoparticle by Au and Au-PEO/PAA PEBs as a function of silica nanoparticle size.

the signal-generating method. However, the dependence's regularity suggests that the images correspond to single particles rather than agglomerates.

3.4. Discrete particle detection model

The conventional mathematical model for SPR detection considers the molecules bound to the sensor surface as an effective medium with an effective refractive index and thickness [38]. The SPR image intensity of the detected silica nanoparticles is a result of the interference between the plasmons of the Au-layer and the bound molecules. This is achieved through the incident p-polarized light, which generates reflected light (E_r)) at the Au/prism interface and transmits light into the Au-layer as an evanescent wave, exciting the surface plasmons (E_{sp}) [39]. The total electric field (E) can be expressed as follows [40–42],

$$E = E_r \sin(\omega t) + E_{sp} \sin(\omega t + \varphi) \tag{1}$$

where φ is the phase shift between the background and the radiation generated by the particle. Additionally, the resulting intensity from the SPR detection process is given by [24],

$$I = c\varepsilon_0 n |E|^2 = c\varepsilon_0 n \left| E_r \sin(\omega t) + E_{sp} \sin(\omega t + \varphi) \right|^2 \tag{2}$$

or,

$$I = \frac{1}{2} c\varepsilon_0 n \left(E_r^2 + E_{sp}^2 + 2E_r E_{sp} \cos\varphi \right) \tag{3}$$

where ω is the frequency, t is time, c is the speed of light, ε_0 is the vacuum permittivity, and n is the refractive index. Moreover, the elastic scattering theory explains surface plasmon scattering by the particle, and when the surface plasmon wave is larger than the particle size, the scattered field can be expressed by a decaying cylindrical plasmonic wave [43–45],

$$E_s(r, r') = E_{sp}^0(r') e^{-\kappa|r-r'|} e^{-ik|r-r'|} \tag{4}$$

where r' is the particle location, $E_{sp}(r')$ is the SPR field in the absence of the particle, κ is the decaying constant of the SP, and k is the wave number of SPR. The total surface plasmon field (E_{sp}) based on the Born approximation is given by [44,46],

$$E_{sp}(r, r') = E_{sp}^0(r) + \alpha E_{sp}^0(r') e^{-\kappa|r-r'|} e^{-ik|r-r'|} = E_{sp}^0(r) + \alpha E_s(r, r') \tag{5}$$

where α is a scattering coefficient related to the particle's polarizability. $E_{sp}^0(r)$ is the SPR field in the absence of the particle. The SPR image contrast of the particle is described by:

$$I(r, r') = \frac{1}{2} c\varepsilon_0 n \left[\left(E_r^2 + \left(E_{sp}^0(r) + \alpha E_s(r, r') \right)^2 + 2E_r \left(E_{sp}^0(r) + \alpha E_s(r, r') \right) \cos\varphi \right) - \left(E_r^2 + E_{sp}^2 + 2E_r E_{sp} \cos\varphi \right) \right] \tag{6}$$

The system symmetry is disrupted when a molecule binds to the Au surface. A 100 nm silica nanoparticle located at 5 nm from the Au- and Au-(PEO/PAA-SH) layers is considered in the model, and the resulting electric field distribution across the structure at the resonance angle is plotted in Fig. 6a. The electric field intensity is enhanced at the metal/analyte interface at the resonance angle, breaking the symmetry of the electric field. The electric field profile at the resonance angle with the presence of silica nanoparticles was computed using COMSOL Multiphysics software. Utilizing equation (6), the intensity distribution of the binding event between the molecule and the Au- and Au-(PEO/PAA-SH) layers is calculated. Fig. 6b and 6c illustrate the intensity profile distribution for the experimentally detected silica nanoparticle bound to the Au- and Au-(PEO/PAA-SH) layers, compared with the calculated intensity profile. The agreement between the estimated intensity profile and the experimental data confirms the success of the derived model. According to the calculated and experimental results of the WF-SPRM measurements, it can be concluded that coated the Au layer by PEO/PAA-SH layer enhances the signal-to-noise ratio of the particle detection.

4. Conclusions

Polymer-polymer complexes involving polyacrylic acid (PAA) and polyethylene oxide (PEO) form hydrogen-bonding complexes, with PEO acting as the hydrogen-bond acceptor and PAA as the donor. The dissociation behavior of PEO/PAA polymer brushes is investigated under varying solvent pH conditions. At low pH values, the dominant presence of COOH groups in the PEO/PAA PEBs results in collapsed brushes due to the absence of repulsive forces between the brushes. As the pH increases to 7, the COOH groups in the top layer of the brushes dissociate into negatively charged COO^- groups, leading to the formation of swollen brushes due to electrostatic repulsion between the chains. At pH 10, all COOH groups in the PEO/PAA PEBs dissociate into negatively charged COO^- groups, further increasing electrostatic

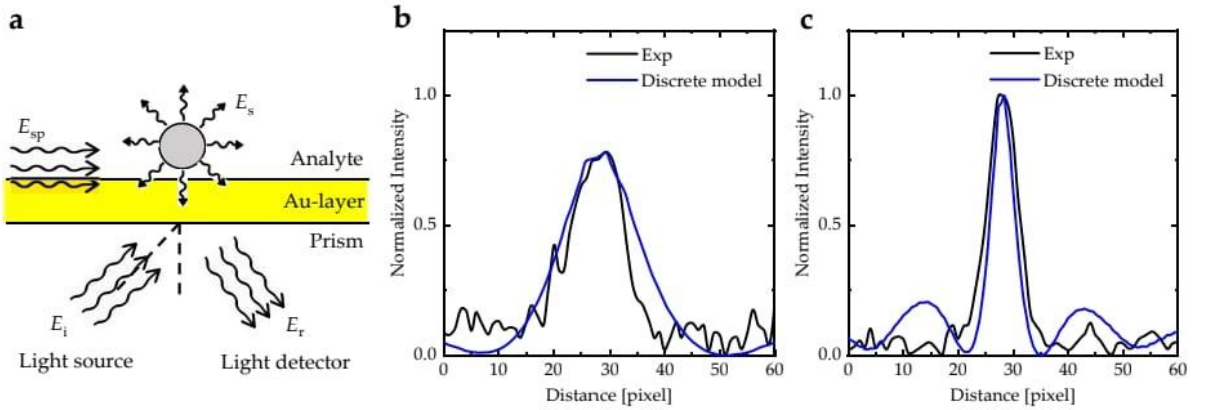

Fig. 6. Discrete Particle Model of Surface Plasmon Resonance Sensor. **(a)** Schematics illustrating the discrete particle model. Experimental and calculated intensities as a function of the distance of the silica nanoparticle from **(b)** the Au- and **(c)** the Au-(PEO/PAA-SH) layers.

repulsion and causing the brushes to stretch. With increasing pH towards 10, PEO/PAA PEBs exhibit a hydrophilic nature, promoting greater interaction with the surrounding medium. The refractive index of PEO/PAA PEBs also increases with increasing solvent pH, with the refractive index of 1.94 at 685 nm for a pH 7. The sensitivity of the wide-field surface plasmon resonance microscope (WF-SPRM) is explored through theoretical and experimental approaches using an Au-(PEO/PAA PEBs) layer. The theoretical sensitivity of the Au-(PEO/PAA PEBs) layer improves from 118.5 deg./RIU to 178.1 deg./RIU compared to the Au-layer. Moreover, the signal-to-noise ratio for the Au-(PEO/PAA PEBs) layer increases from 6 ± 1 to 20 ± 1 compared to the Au layer. Following this, a mathematical model to describe discrete particle detection by WF-SPRM is presented. The calculated intensity profile derived from the model matches well with the experimental data, confirming the validity of this approach.

Funding

This research received no external funding.

CRediT authorship contribution statement

Qais M. Al-Bataineh: Writing – original draft, Visualization, Software, Methodology, Formal analysis, Data curation, Conceptualization. **Ahmad D. Telfah:** Writing – original draft, Visualization, Validation, Supervision, Resources, Project administration, Methodology, Investigation, Conceptualization. **Carlos J. Tavares:** Writing – review & editing, Visualization, Validation, Formal analysis. **Roland Hergenröder:** Writing – review & editing, Validation, Supervision, Software, Resources, Project administration, Investigation, Data curation.

Declaration of competing interest

The authors declare that they have no known competing financial interests or personal relationships that could have appeared to influence the work reported in this paper.

Data availability

Data will be made available on request.

Acknowledgments

The scientific support by the Ministerium für Innovation, Wissenschaft und Forschung des Landes Nordrhein-Westfalen, the Senatsverwaltung für Wirtschaft, Technologie und Forschung des Landes Berlin, and the Bundesministerium für Bildung und Forschung is gratefully acknowledged. We also thank Prof. Ahmad A. Ahmad for helping our members use the thin films laboratory at Jordan University of Science and Technology.

Appendix A. Supplementary data

Supplementary data to this article can be found online at https://doi.org/10.1016/j.apsusc.2023.159189.

References

[1] S. Zou, R. Lv, Z. Tong, B. Na, K. Fu, H. Liu, In situ hydrogen-bonding complex mediated shape memory behavior of PAA/PEO blends, Polymer 183 (2019), 121878.
[2] A. Khaldi, J.A. Elliott, S.K. Smoukov, Electro-mechanical actuator with muscle memory, J. Mater. Chem. C 2 (38) (2014) 8029–8034.
[3] A. Ahmad, et al., Synthesis and characterization of ZnO NPs-doped PMMA-BDK-MR polymer-coated thin films with UV curing for optical data storage applications, Polym. Bull. 78 (3) (2021) 1189–1211.
[4] Q.M. Al-Bataineh, A.A. Ahmad, A.M. Alsaad, A. Telfah, New Insight on photoisomerization kinetics of photo-switchable thin films based on azobenzene/graphene hybrid additives in polyethylene oxide, Polymers 12 (12) (2020) 2954.
[5] J. Kunzelman, T. Chung, P.T. Mather, C. Weder, Shape memory polymers with built-in threshold temperature sensors, J. Mater. Chem. 18 (10) (2008) 1082–1086.
[6] J. Hao, G. Yuan, W. He, H. Cheng, C.C. Han, C. Wu, Interchain Hydrogen-Bonding-Induced Association of Poly (acrylic acid)-graft-poly (ethylene oxide) in Water, Macromolecules 43 (4) (2010) 2002–2008.
[7] Y. Wang, E.J. Goethals, F.E. Du Prez, Association Behavior between End-Functionalized Block Copolymers PEO-PPO-PEO and Poly (acrylic acid), Macromol. Chem. Phys. 205 (13) (2004) 1774–1781.
[8] H. Kaczmarek, A. Szalla, H. Chaberska, J. Kowalonek, Changes of surface morphology in UV-irradiated poly (acrylic acid)/poly (ethylene oxide) blends, Surf. Sci. 566 (2004) 560–565.
[9] R.-Y. Wang, et al., Closed-loop phase behavior of block copolymers in the presence of competitive hydrogen-bonding and Coulombic interaction, Macromolecules 51 (12) (2018) 4727–4734.
[10] G. Liu, X. Ding, Y. Cao, Z. Zheng, Y. Peng, Shape memory of hydrogen-bonded polymer network/poly (ethylene glycol) complexes, Macromolecules 37 (6) (2004) 2228–2232.
[11] T. Liu, J. Li, Y. Pan, Z. Zheng, X. Ding, Y. Peng, A new approach to shape memory polymer: design and preparation of poly (methyl methacrylate) composites in the presence of star poly (ethylene glycol), Soft Matter 7 (5) (2011) 1641–1643.
[12] J. Yuan, H.S. Antila, E. Luijten, Dielectric effects on ion transport in polyelectrolyte brushes, ACS Macro Lett. 8 (2) (2019) 183–187.
[13] E. Currie, A. Sieval, G. Fleer, M.C. Stuart, Polyacrylic acid brushes: surface pressure and salt-induced swelling, Langmuir 16 (22) (2000) 8324–8333.
[14] J. Yuan, H.S. Antila, E. Luijten, Structure of polyelectrolyte brushes on polarizable substrates, Macromolecules 53 (8) (2020) 2983–2990.
[15] S. Das, M. Banik, G. Chen, S. Sinha, R. Mukherjee, Polyelectrolyte brushes: theory, modelling, synthesis and applications, Soft Matter 11 (44) (2015) 8550–8583.

[16] G. Ferrand-Drake del Castillo, R.L. Hailes, A. Dahlin, Large Changes in Protonation of Weak Polyelectrolyte Brushes with Salt Concentration—Implications for Protein Immobilization, J. Phys. Chem. Lett. 11 (13) (2020) 5212–5218.
[17] M. Delcroix, et al., Design of mixed PEO/PAA brushes with switchable properties toward protein adsorption, Biomacromolecules 14 (1) (2013) 215–225.
[18] M. Delcroix, S. Demoustier-Champagne, C.C. Dupont-Gillain, Quartz crystal microbalance study of ionic strength and pH-dependent polymer conformation and protein adsorption/desorption on PAA, PEO, and mixed PEO/PAA brushes, Langmuir 30 (1) (2014) 268–277.
[19] A. Bratek-Skicki, P. Eloy, M. Morga, C. Dupont-Gillain, Reversible Protein adsorption on mixed PEO/PAA Polymer brushes: Role of Ionic strength and PEO content, Langmuir 34 (9) (2018) 3037–3048.
[20] M. Ballauff, O. Borisov, Polyelectrolyte brushes, Curr. Opin. Colloid Interface Sci. 11 (6) (2006) 316–323.
[21] C. Yigit, M. Kanduc, M. Ballauff, J. Dzubiella, Interaction of charged patchy protein models with like-charged polyelectrolyte brushes, Langmuir 33 (1) (2017) 417–427.
[22] M. Koenig, et al., Adsorption of enzymes to stimuli-responsive polymer brushes: Influence of brush conformation on adsorbed amount and biocatalytic activity, Colloids Surf. B Biointerfaces 146 (2016) 737–745.
[23] W.M. De Vos, F.A. Leermakers, A. De Keizer, M.A. Cohen Stuart, J.M. Kleijn, Field theoretical analysis of driving forces for the uptake of proteins by like-charged polyelectrolyte brushes: effects of charge regulation and patchiness, Langmuir 26 (1) (2010) 249–259.
[24] A. Zybin, V. Shpacovitch, J. Skolnik, R. Hergenröder, Optimal conditions for SPR-imaging of nano-objects, Sens. Actuators B 239 (2017) 338–342.
[25] H.K. Rouf, T. Haque, Performance enhancement of Ag-Au bimetallic surface plasmon resonance biosensor using InP, Progr. Electromagnetics Res. M 76 (2018) 31–42.
[26] V. Shpacovitch, et al., Application of the PAMONO-sensor for quantification of microvesicles and determination of nano-particle size distribution, Sensors 17 (2) (2017) 244.
[27] A. Shalabney, I. Abdulhalim, Sensitivity-enhancement methods for surface plasmon sensors, Laser Photonics Rev. 5 (4) (2011) 571–606.
[28] Q.M. Al-Bataineh, A.D. Telfah, V. Shpacovitch, C.J. Tavares, R. Hergenröder, Switchable Polyacrylic Acid Polyelectrolyte Brushes for Surface Plasmon Resonance Applications, Sensors 23 (9) (2023) 4283.
[29] A. Ahmad, A. Migdadi, A. Alsaad, Q.M. Al-Bataineh, A. Telfah, Optical, structural, and morphological characterizations of synthesized (Cd–Ni) co-doped ZnO thin films, Appl. Phys. A 127 (12) (2021) 1–12.
[30] A. Alsaad, Q.M. Al-Bataineh, A. Ahmad, Z. Albataineh, A. Telfah, Optical band gap and refractive index dispersion parameters of boron-doped ZnO thin films: A novel derived mathematical model from the experimental transmission spectra, Optik 211 (2020), 164641.
[31] Q.M. Al-Bataineh, V. Shpacovitch, D. Sadiq, A. Telfah, R. Hergenröder, Surface Plasmon Resonance Sensitivity Enhancement Based on Protonated Polyaniline Films Doped by Aluminum Nitrate, Biosensors 12 (12) (2022) 1122.
[32] A.W. Peterson, M. Halter, A. Tona, A.L. Plant, High resolution surface plasmon resonance imaging for single cells, BMC Cell Biol. 15 (1) (2014) 1–14.
[33] D. Aulich, et al., In situ studies on the switching behavior of ultrathin poly (acrylic acid) polyelectrolyte brushes in different aqueous environments, Langmuir 26 (15) (2010) 12926–12932.
[34] R. Dong, M. Lindau, C.K. Ober, Dissociation behavior of weak polyelectrolyte brushes on a planar surface, Langmuir 25 (8) (2009) 4774–4779.
[35] P. Pillai, P. Khurana, A. Tripathi, Dielectric studies of poly (methyl methacrylate)/polystyrene double layer system, J. Mater. Sci. Lett. 5 (6) (1986) 629–632.
[36] M.A. AL-Akhras, S.E. Alzoubi, A.A. Ahmad, R. Ababneh, A. Telfah, Studies of composite films of polyethylene oxide doped with potassium hexachloroplatinate, J. Appl. Polym. Sci. 138 (5) (2021) 49757.
[37] W.S. Rasband. "ImageJ." National Institutes of Health. https://imagej.nih.gov/ij/ (accessed).
[38] J. Maurya, Y. Prajapati, V. Singh, J. Saini, R. Tripathi, Performance of graphene–MoS 2 based surface plasmon resonance sensor using silicon layer, Opt. Quant. Electron. 47 (11) (2015) 3599–3611.
[39] H. Yu, X. Shan, S. Wang, H. Chen, N. Tao, Molecular scale origin of surface plasmon resonance biosensors, Anal. Chem. 86 (18) (2014) 8992–8997.
[40] H. Raether, Surface plasmons on gratings, Surface plasmons on smooth and rough surfaces and on gratings, 1988, pp. 91-116.
[41] T. Leskova, A. Maradudin, W. Zierau, Surface plasmon polariton propagation near an index step, Opt. Commun. 249 (1–3) (2005) 23–35.
[42] S.-H. Cao, W.-P. Cai, Q. Liu, Y.-Q. Li, Surface plasmon–coupled emission: what can directional fluorescence bring to the analytical sciences? Annu. Rev. Anal. Chem. 5 (2012) 317–336.
[43] B. Hecht, H. Bielefeldt, L. Novotny, Y. Inouye, D. Pohl, Local excitation, scattering, and interference of surface plasmons, Phys. Rev. Lett. 77 (9) (1996) 1889.
[44] S.I. Bozhevolnyi, V. Coello, Elastic scattering of surface plasmon polaritons: modeling and experiment, Phys. Rev. B 58 (16) (1998) 10899.
[45] A. Shchegrov, I. Novikov, A. Maradudin, Scattering of surface plasmon polaritons by a circularly symmetric surface defect, Phys. Rev. Lett. 78 (22) (1997) 4269.
[46] S.I. Bozhevolnyi, Localization phenomena in elastic surface-polariton scattering caused by surface roughness, Phys. Rev. B 54 (11) (1996) 8177.

5.5. Original Paper V: (Al-Bataineh et al., 2024c)

Qais M. Al-Bataineh, Gaith Rjoub, Ahmad D. Telfah, Ahmad A. Ahmad, Carlos J. Tavares, Roland Hergenröder, *Developing surface plasmon resonance imaging for discrete particle detection based on a silver layer coated with polyacrylic acid/iodine polyelectrolyte brushes*. Applied Surface Science 682 (2024): 161755. https://doi.org/10.1016/j.apsusc.2024.161755 (Al-Bataineh et al., 2024c)

5.6. Original Paper VI: (Al-Bataineh et al., 2023b)

scientific reports

OPEN

Surface plasmon coupling between wide-field SPR microscopy and gold nanoparticles

Qais M. Al-Bataineh[1,2,3]✉, Ahmad D. Telfah[1,4,5], Carlos J. Tavares[6] & Roland Hergenröder[1]✉

The coupling behavior of the wide field surface plasmon microscopy (WF-SPRM) with single-, two-, and multiple-gold nanoparticles (AuNPs) with different AuNPs sizes is investigated using theoretical, simulation, and experimental approaches. The signal intensity of a single AuNP increases from 208 a.u. to 583 a.u. as particle size increases from 40 to 80 nm, which evidences the signal-building mechanism of Rayleigh scattering theory. A discrete particle model of SPR is used to understand the interaction between an Au-layer and a single AuNP. The calculated intensity profile of the single AuNP from the discrete particle model is accepted with the experimental data. In addition, the superposition between 2-AuNPs surface plasmon waves is studied using the finite element method as well as experimental data from WF-SPRM. The surface plasmon waves around the two particles generate an interference pattern. Finally, it is demonstrated that plasmonic multiple particles scattering can be represented by an effective media, which is described by Maxwell-Garnet equations.

Detecting and characterizing nano-objects with low concentrations, such as biological particles (e.g., viruses and exosome particles), presents a significant challenge in analytical science[1]. Surface plasmon resonance (SPR) stands out as one of the most impressive biodetection techniques, thanks to its various advantages, including label-free detection, high sensitivity, excellent reproducibility, and real-time measurements[2,3]. Moreover, an SPR sensor can be considered as an optical refractometer that examines changes in refractive index near the sensing surface. Consequently, SPR sensors can measure a wide range of binding interactions, such as protein adsorption, ligand-receptor binding, hybridization of RNA and DNA, and nucleic acid detection[4–6].

Wide-field surface plasmon resonance microscopy (WF-SPRM) follows the principles of SPR based on the classical Kretschmann's scheme[7]. WF-SPRM can detect individual nano-objects in solutions and gases[8–12]. In WF-SPRM, a gold layer is illuminated by a polarized laser beam through a glass prism. The illuminated area is then imaged on a CCD camera to capture high-resolution images of the binding area. Subsequently, a bright spot representing the shape of the detected particle appears in the image, indicating the particle's binding on the surface[13]. The propagation of plasmons by light requires a nano-metal layer on the prism for attenuated total reflection. Several factors influence surface plasmons, including light wavelengths, metal layer thickness and properties, prism properties, and the properties of the surrounding dielectric medium[14]. For ultra-low concentration detection, signal amplification tags are utilized to enhance the sensitivity of SPR detection. Gold nanoparticles (AuNPs) are the most effective tags for enhancing detection due to their unique optical properties and high physical and chemical stability[15].

A traditional medium model describes the principle of the SPR sensor by treating molecules bound to the sensor surface as an effective medium with an effective refractive index and thickness. However, WF-SPRM can detect individual nano-objects in solutions and gases. Therefore, an SPR discrete particle model is introduced to describe the detection principle for discrete particles. The coupling behavior of WF-SPRM with single, two, and multiple gold nanoparticles (AuNPs) of different sizes (40, 60, and 80 nm) are investigated using theoretical, simulation, and experimental approaches. Furthermore, the finite element method, specifically COMSOL Multiphysics software, is used to examine the interactions between AuNPs of varying sizes and the Au-layer of the SPR sensor. Also, the superposition of surface plasmon waves between two AuNPs using the finite element method is studied, along with experimental data from WF-SPRM. Finally, multiple AuNPs near the gold-sensor

[1]Leibniz-Institut für Analytische Wissenschaften-ISAS-e.V., 44139 Dortmund, Germany. [2]Department of Physics, TU Dortmund University, 44227 Dortmund, Germany. [3]Department of Physics, Jordan University of Science and Technology, Irbid 22110, Jordan. [4]Nanotechnology Center, The University of Jordan, Amman 11942, Jordan. [5]Department of Physics, University of Nebraska at Omaha, Omaha, NE 68182, USA. [6]Physics Centre of Minho and Porto Universities (CF-UM-UP), University of Minho, 4804-533 Guimaraes, Portugal. ✉email: qais.albataineh@tu-dortmund.de; roland.hergenroeder@isas.de

surface can be represented through the effective media approximation, specifically the Maxwell-Garnet approximation. The effective dielectric constants are determines for all AuNP sizes to calculate the impact of AuNP size on the sensitivity of the SPR sensor.

Methods

Experiment design

The WF-SPRM experiments, based on Kretschmann's configuration[16], were conducted to detect gold nanoparticles (AuNPs) of different sizes (40, 60, and 80 nm) (Fig. S1)[17–19]. In this experiment, a red (685 nm) laser diode (HL6750MG, Thorlabs GmbH) illuminates the gold-sensor substrate through a glass prism (SF10, n = 1.725) at a fixed incidence angle. The scattered and reflected light is captured through an objective lens (Canon Compact-Macro Lens EF 50 mm 1 : 2.5) onto a CMOS video camera (MT9P031, with a resolution of 5 Mp and a pixel size of 2.2 × 2.2 µm). By varying the incident light angle, the reflected light intensity reaches a minimum, known as the resonance angle.

Preparation of Au sensor substrate

The gold-sensor substrate is prepared by coating glass slides (SF10, n = 1.725, Helma Optics, Germany) with a Ti adhesive layer (5 nm thickness) and, subsequently, an Au-layer (41–45 nm thickness) using a magnetron-sputtering technique (Innolume). The optical transmittance of the Au-sensor substrate at normal incidence at 685 nm is approximately 4%. Before using the gold-sensor substrate, it undergoes a cleaning process by immersion in a piranha solution (3:1 sulfuric acid (Sigma-Aldrich): hydrogen peroxide (VWR chemicals)) for 5 min, followed by rinsing with distilled water to eliminate traces of the piranha solution, and finally drying with argon gas. For the detection of AuNPs, the Au-sensor substrate is coated with aluminum hydroxide chloride by applying 150 µL of aluminum hydroxide chloride solution (10 wt.%) onto the gold-sensor substrate for 20 min under ambient conditions. Subsequently, the aluminum hydroxide chloride solution is removed, and the Au-sensor substrate is rinsed with distilled water and dried with argon gas.

Experimental procedures

The Au-sensor substrate is positioned on the base of the glass prism using RI-matching immersion liquid (2 µL, n = 1.725) to match the refractive indices between the glass prism and glass substrate. AuNPs with sizes of 40 nm and a concentration of 7.16×10^{10} particles/mL, 60 nm and a concentration of 1.96×10^{10} particles/mL, and 80 nm and a concentration of 7.82×10^{9} particles/mL were obtained from Sigma-Aldrich. Stock solutions of AuNPs with different sizes were prepared by dilution in water with 0.3% NaCl as follows: 40 nm AuNPs (1:50, 1.431×10^{8} particles/mL), 60 nm AuNPs (1:20, 9.80×10^{8} particles/mL), and 80 nm AuNPs (1:10, 7.82×10^{8} particles/mL). Initially, a sodium chloride buffer solution (NaCl, 0.3%) is pumped through the sensor cell for 1–2 min. After reaching equilibrium, the prism is rotated to the resonance angle (R_{min}). Starting from the reflectance minimum, the working point is set to $4R_{min}$ within the linear region of the reflectivity curve[20]. Subsequently, AuNPs are introduced into the sensor cell at an average flow rate of 300 µL/min. Within a few seconds, signals arising from the adsorption of AuNPs on the gold-sensor substrate become visible on the video camera, as WF-SPRM visualizes optical patterns generated from the scattering of SP waves on the gold-sensor substrate. Image J software is employed to determine the intensity step signal of the nanoparticle binding event[21]. Additionally, COMSOL Multiphysics is used to design and analyze the proposed model of the SPR sensor using a finite element method-based numerical simulation (Supplementary S2).

Theoretical analysis

p-polarized light reflectance model

The *p*-polarized light is essential for the sensing of the SPR sensors. The reflectivity (R_p) of the SPR sensor can be determined by[22]:

$$R_p = |r_p|^2 \tag{1}$$

$$r_p = \left[(M_{11} + M_{12}q_5)q_1 - \frac{(M_{21} + M_{22}q_5)}{(M_{11} + M_{12}q_5)q_1} + (M_{21} + M_{22}q_5) \right] \tag{2}$$

where r_p represents the reflection coefficient of $p-$ polarized light and M_{ij} are the components of the characteristic matrix, given by[22],

$$M_{ij} = \prod_{K=2}^{N-1} M_K = \begin{pmatrix} M_{11} & M_{12} \\ M_{21} & M_{22} \end{pmatrix} \tag{3}$$

where

$$M_K = \begin{pmatrix} \cos\beta_k & -\frac{i\sin\beta_k}{q_k} \\ -iq_k\sin\beta_k & \cos\beta_k \end{pmatrix} \tag{4}$$

$$q_k = \frac{\sqrt{\varepsilon_k - n_1^2 \sin\theta_1^2}}{\varepsilon_k} \tag{5}$$

$$\beta_k = \frac{2\pi d_k}{\lambda}\left(\sqrt{\varepsilon_k - n_1^2 \sin\theta_1^2}\right) \tag{6}$$

where q represents the wavenumber, β represents optical admittance, ε_k and d_k are the dielectric constant and layer thickness of the k_{th}-layer, θ_k and λ are the incident angle and wavelength of the incident light, and n is the refractive index.

Discrete particle model of SPR

Figure 1a shows the detected intensity of the SPR image of the particles arising from the interference between the reflected rays from the Au surface and the scattered plasmons. The incident p-polarized light is partly reflected (E_r) at the Au/prism interface and partly transmitted into the Au-layer as an evanescent wave, which excites surface plasmons (E_{sp})[23]. Initially, the total electric field resulting from the reflected rays and the scattered plasmons primary of the Au/prism systems can be expressed as[24–26],

$$E = E_r \sin(\omega t) + E_{sp} \sin(\omega t + \varphi) \tag{7}$$

where φ is the phase shift between the background and the radiation generated by the particle. The resulting intensity is given by[18],

$$I = c\varepsilon_0 n|E|^2 = c\varepsilon_0 n\left|E_r \sin(\omega t) + E_{sp} \sin(\omega t + \varphi)\right|^2 \tag{8}$$

or,

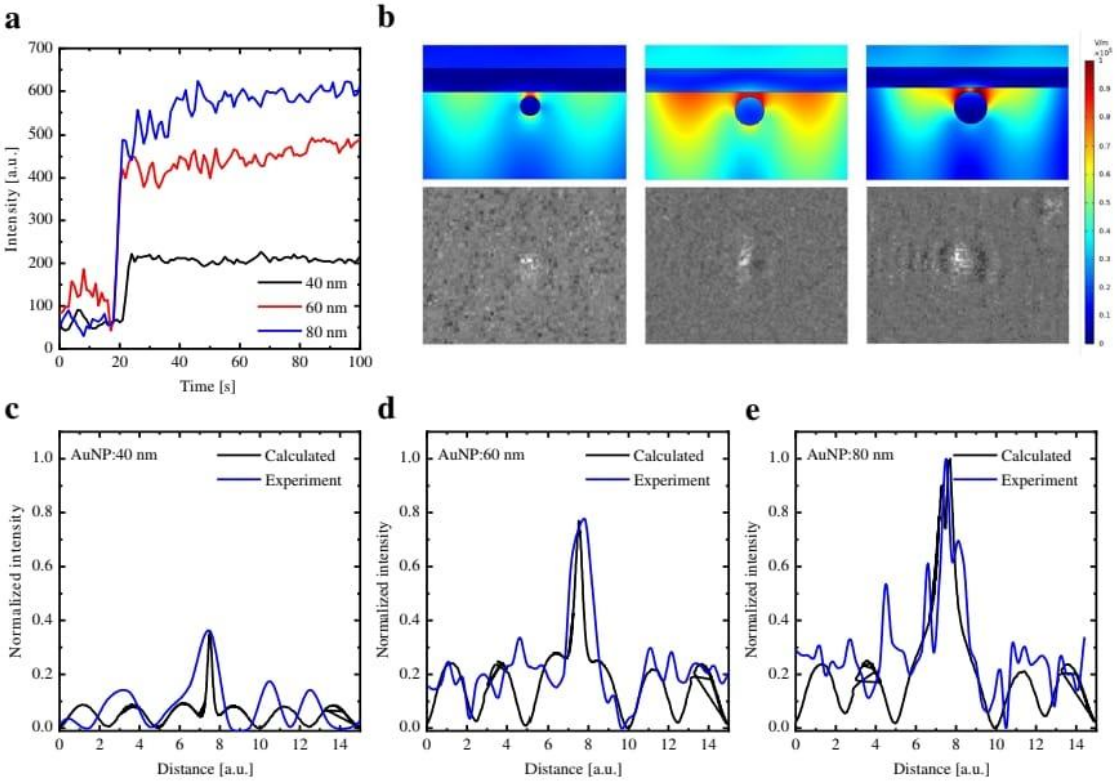

Figure 1. (**a**) Time dependence of the intensity in the middle of the bright spot for AuNPs bound to the Au-layer with different sizes (40, 60, and 80 nm). (**b**) Electric field distribution in the vicinity of AuNPs with different sizes (40, 60, and 80 nm) was simulated using COMSOL Multiphysics and compared to WF-SPRM images. The bright spots are caused by particles bound to the sensor surface. Experimental normalized intensity versus distance compared with the calculated intensity deduced from Eq. (12) for the AuNPs with different sizes: (**c**) 40 nm, (**d**) 60 nm, and (**e**) 80 nm.

$$I = \frac{1}{2} c\varepsilon_0 n\left(E_r^2 + E_{sp}^2 + 2E_r E_{sp}\cos\varphi\right) \tag{9}$$

Elastic scattering theory can be employed to study the scattering of surface plasmons by a particle. When the surface plasmon wave is larger than the particle size, the scattered field can be described by a decaying cylindrical plasmonic wave,

$$E_s(r, r\prime) = E_{sp}^0(r\prime)e^{-\kappa|r-r\prime|}e^{-ik|r-r\prime|} \tag{10}$$

where r is the measured location, $r\prime$ is the particle location. $E_{sp}(r\prime)$ is the surface plasmon field at the location of the particle, κ is the decaying constant of the SP, and k is the wave number of SP. Therefore, the total surface plasmon field (E_{sp}) based on the Born approximation is given by[27,28],

$$E_{sp}(r, r\prime) = E_{sp}^0(r) + \alpha E_{sp}^0(r\prime)e^{-\kappa|r-r\prime|}e^{-ik|r-r\prime|} = E_{sp}^0(r) + \alpha E_s(r, r\prime) \tag{11}$$

where α is a scattering coefficient related to the polarizability of the particle. $E_{sp}^0(r)$ is the SP field in the absence of the particle. The SPR image contrast of the particle is described by,

$$I(r, r\prime) = \frac{1}{2} c\varepsilon_0 n\left[\left(E_r^2 + \left(E_{sp}^0(r) + \alpha E_s(r, r\prime)\right)^2 + 2E_r\left(E_{sp}^0(r) + \alpha E_s(r, r\prime)\right)\cos\varphi\right) - \left(E_r^2 + E_{sp}^2 + 2E_r E_{sp}\cos\varphi\right)\right] \tag{12}$$

The values E_r and E_{sp} are derived from FEM simulation data. E_r corresponds to the electric field distribution on the surface of the Au layer in the absence of nanoparticles, while E_{sp} corresponds to the electric field distribution on the surface of the Au layer in the presence of nanoparticles. These electric field distributions on the surface of the Au layer represent the experimental data obtained through WF-SPRM measurements on the Au sensor surface.

Results and discussion

Single-particle modeling

When AuNPs are bound to an Au surface, the system's symmetry is disrupted. Additionally, plasmon coupling between the AuNPs and the Au surface occurs, resulting in an induced charge in the Au surface that interacts with the AuNPs. However, the polarities of these charges are opposite, leading to an increase in the local electric field between AuNPs and the Au surface due to near-field coupling[29]. An intriguing aspect of WF-SPRM is its ability to detect individual particles bound to the surface. Consequently, the time-dependent relative intensities of AuNPs (40, 60, and 80 nm) binding to the gold-sensor substrate represent three distinct stages: a relatively low, flat intensity before AuNPs binding, a sudden increase in local intensity at the moment of AuNPs binding, and a high, flat intensity after AuNPs binding (Fig. 1a). It is evident that the magnitude of the intensity step is proportional to the size of the AuNPs[30]. The signal intensity increases linearly from 208 a.u. for 40 nm AuNPs to 583 a.u. This clearly demonstrates that the signal generation mechanism fundamentally differs according to Rayleigh's theory[31]. Additionally, the signal noise of AuNPs increases as the size of the AuNPs increases from 40 to 80 nm, which can be attributed to the increasing surface plasmon polaritons produced by the coupling effect between the AuNPs and the Au surface. When the surface plasmon polaritons produced by the Au surface are coupled to the AuNPs, the surface charges between them are redistributed, increasing the local electric field. Figure 1b shows the plasmon coupling occurring between the AuNPs and the Au surface. This coupling results in the generation of a local electromagnetic field when exposed to a 685 nm wavelength laser at an incident angle of 59.8°.

The red regions represent the coupling enhancement regions between AuNPs and the Au surface. 80 nm AuNPs exhibit greater enhancement and confinement than 40 nm AuNPs, indicating that the electric field intensity between the AuNPs and the Au layer increases with increasing AuNPs size. A 40 nm diameter confines incident light between AuNPs and the Au layer in closer proximity to the particle surface than 80 nm AuNPs, indicating a lower efficiency of confined field between AuNPs and the Au layer. This results in efficient excitation of the gap-mode plasmon by 80 nm AuNPs, aligning with the experimental data (Fig. 1b). Furthermore, the presence of AuNPs near the sensor surface disrupts the electric field in the analyte region[32]. Utilizing Eq. 12, we can calculate the intensity distribution of the binding event between the AuNP and the Au surface. Figure 1c–e illustrate the intensity profile distribution for the experiment with AuNPs bound to the Au surface compared to the calculated intensity profile. It is evident that the calculated intensity profile matches the experimental data, indicating the success of our derived model. However, the above simulation assumes a perfect surface, whereas the gold surface has finite roughness. The variation between the calculated and experimental intensities can be attributed to the surface roughness, which is particularly essential for small particle detection compared to the grains[33].

Two-particle modeling

When two gold nanoparticles (2-AuNPs) are bound to the surface of the Au layer at a distance smaller than the surface plasmon propagation length, the surface plasmon waves around this pair are enhanced due to the constructive and destructive interferences of the surface plasmon waves from each particle (Fig. 2).

Figures 2a,b show the electric field intensity distribution obtained from COMSOL simulations and a WF-SPRM image for two AuNPs with a size of 80 nm. This occurs when they are irradiated with a 685 nm wavelength laser at an incident angle of 59.8°. The surface plasmon waves around the two particles result from the superposition of electric fields between these waves. Combining plasmon intensities of two AuNPs with an initial phase

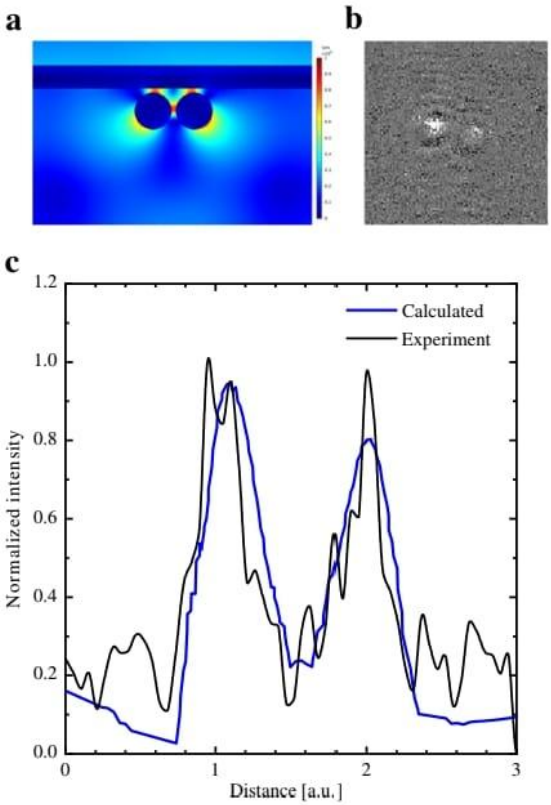

Figure 2. (**a**) Electric field distribution in the vicinity of 2-AuNPs (80 nm). (**b**) WF-SPRM images of 2-AuNPs (80 nm). The bright spots are caused by particles bound to the sensor surface. (**c**) Experimental normalized intensity versus distance compared with the calculated intensity deduced from Eq. (13) for the 2-AuNPs (80 nm).

difference (φ) as $|a + a|^2$ (or $|2a|^2$) produces complex and cumulative superposed plasmon intensities[34]. This can be inferred from Eq. (11), which can be reformulated for two particles:

$$I(r) = I_1 + I_2 + c\varepsilon_0 n|E_{s1}||E_{s2}|\cos(\varphi_1 - \varphi_2) \tag{13}$$

with,

$$E_{sj} = E^0_{sp}(r_j)e^{-\kappa|r-r_i\prime|}e^{-ik|r-r_i\prime|} \tag{14}$$

$$I_j(r, r\prime) = \frac{1}{2}c\varepsilon_0 n\left[\left(E_r^2 + \left(E^0_{sp}(r) + \alpha E_{sj}\right)^2 + 2E_r\left(E^0_{sp}(r) + \alpha E_{sj}\right)\cos\varphi\right) - \left(E_r^2 + E_{sp}^2 + 2E_r E_{sp}\cos\varphi\right)\right] \tag{15}$$

Hence, we can compute the intensity distribution of the binding event between the 2-AuNPs and the Au surface. Figure 2c presents the intensity profile distribution for the experiment with 2-AuNPs bound to the Au surface alongside the calculated intensity profile. It is evident that the calculated intensity profile aligns with the experimental data, affirming the success of our derived model. The intensity enhancement observed with the two AuNPs compared to a single AuNP is attributed to the increased local surface plasmon coupling between the AuNPs with the Au surface and each other[35].

Multiple-particle model

The multiple particles near the Au layer can be represented by effective media characterized by the effective dielectric constant. The effective dielectric constant of the AuNPs in the analyte, as per the Maxwell-Garnet equations, is provided by[36]:

$$\varepsilon_{eff}(\omega) = \varepsilon_{eff}\prime + i\varepsilon''_{eff} \tag{16}$$

with $\varepsilon_{eff}{}'$ and ε''_{eff} are the effective real and imaginary parts of effective dielectric constants, respectively, which are given by:

$$\varepsilon_{eff}{}' = \varepsilon_w + \frac{f(\varepsilon_{Au}{}' - \varepsilon_w) \times \{\varepsilon_w + \beta(\varepsilon_{Au}{}' - \varepsilon_w) - f(\gamma\varepsilon_{Au}{}' - \varepsilon_w)\} - f\varepsilon''_{Au} \times (\beta\varepsilon''_{Au} - f\gamma\varepsilon''_{Au})}{\{\varepsilon_w + \beta(\varepsilon_{Au}{}' - \varepsilon_w) - f(\gamma\varepsilon_{Au}{}' - \varepsilon_w)\}^2 + (\beta\varepsilon''_{Au} - f\gamma\varepsilon''_{Au})^2} \quad (17)$$

$$\varepsilon''_{eff} = \frac{f\varepsilon''_{Au} \times \{\varepsilon_w + \beta(\varepsilon'_{Au} - \varepsilon_w) - f(\gamma\varepsilon'_{Au} - \varepsilon_w)\} - f(\varepsilon'_{Au} - \varepsilon_w) \times (\beta\varepsilon''_{Au} - f\gamma\varepsilon''_{Au})}{\{\varepsilon_w + \beta(\varepsilon'_{Au} - \varepsilon_w) - f(\gamma\varepsilon'_{Au} - \varepsilon_w)\}^2 + (\beta\varepsilon''_{Au} - f\gamma\varepsilon''_{Au})^2} \quad (18)$$

where $\varepsilon_{Au}{}'$ and ε''_{Au} are components of the complex dielectric constant of AuNPs, ε_w is the dielectric constant of water, f is the filling factor, defined as the total volume of particles divided by the total volume of the composite analyte, β is the shape factor of the particle ($\beta = 1/3$ for sphere), and γ is a factor, which is given by:

$$\gamma = \frac{1}{3\varepsilon_w} + \frac{K}{4\pi\varepsilon_w} \quad (19)$$

Here, K represents the interaction parameter between the electric fields generated by adjacent particles. Since the AuNPs in the analyte are present at low concentrations and are sufficiently far apart, the dipolar interaction is negligible, and K equals 0[37]. The calculated values of $\varepsilon_{eff}{}'$ and ε''_{eff} for AuNPs in the analyte, as a function of the filling factor $f\,(0 < f < 1)$ are depicted in Fig. 3a,b. The ε''_{eff} values increase with an increasing filling factor up to approximately $f = 0.7$, and the transition between the positive and negative portions of $\varepsilon_{eff}{}'$ occurs at $f = 0.71$. Consequently, the effective dielectric constant of AuNPs in the analyte exhibits a nonlinear response with respect to the filling factor, consistent with the study by Tamada et al.[36].

Based on the preceding discussion, we have calculated the theoretical reflectivity curves of the Au layer with different sizes of AuNPs (40, 60, and 80 nm) and a constant filling factor of 0.02 using WINSPALL software (Fig. 3c)[38]. For all AuNP sizes, an increase in the filling factor results in an increase in the incident photon angle at minimum reflectivity (Supplementary S3). At a constant filling factor, the incident photon angle at minimum reflectivity also increases with an increase in the size of the AuNPs (Fig. 3c). The SPR sensitivity is determined as $S = \Delta\theta/\Delta n$, where $\Delta\theta$ represents the SPR angle shift [°], and Δn is the refractive index change [RIU]. The sensitivity for 40 nm AuNPs is 50.6 deg./RIU, and this sensitivity increases linearly to 93.5 deg./RIU for the detection of 80 nm AuNPs (Fig. 3d). Consequently, larger-sized AuNPs offer improved detection sensitivity. This observation aligns well with the experimental and simulation data presented in Fig. 1b.

Additionally, the WF-SPRM images for multiple 80 nm AuNPs before binding show a distinct dark image (Fig. 3e). After binding multiple 80 nm AuNPs, the image transforms into continuous bright spots, resulting in a brighter image (Fig. 3f). On the other hand, the electric field distribution, derived from COMSOL Multiphysics

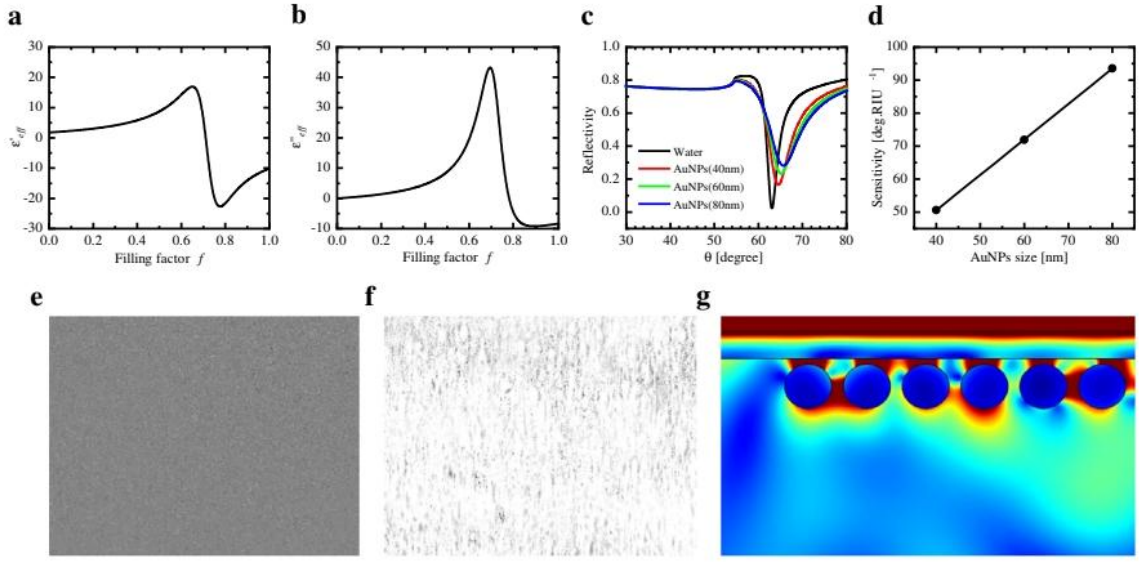

Figure 3. Calculated effective (**a**) real part ($\varepsilon_{eff}{}'$) and (**b**) imaginary part (ε''_{eff}) of the dielectric constant of AuNPs in the analyte as a function of the filling factor $f\,(0 < f < 1)$. (**c**) SPR reflectivity curve for Kretschmann's configuration with a constant filling factor ($f = 0.02$) for different AuNPs sizes (40, 60, and 80 nm). (**d**) Response of SPR sensitivity as a function of AuNPs size. WF-SPRM images for multiple 80 nm AuNPs (**e**) before binding, (**f**) after binding, and (**g**) Electric field distribution in the vicinity of multiple 80 nm AuNPs.

software, reveals a continuous electric field distribution at the Au surface resulting from the coupling of AuNPs with the Au layer (Fig. 3g).

Conclusions

The coupling behavior of WF-SPRM with single, double, and multiple gold nanoparticles (AuNPs) of varying sizes is investigated through a combination of theoretical, simulation, and experimental approaches. When AuNPs bind to the Au surface, it disrupts the system's symmetry. Furthermore, plasmon coupling occurs between the AuNPs and the Au surface, leading to the generation of an induced charge in the Au surface, which interacts with AuNPs. The signal intensity of a single AuNP increases from 208 a.u. to 583 a.u. as the particle size increases from 40 to 80 nm, indicating that the signal-building mechanism is based on Rayleigh scattering theory. A discrete particle model of SPR is used to understand the interaction between the Au-layer and a single AuNP. The calculated intensity profile of the single AuNP from the discrete particle model aligns with the experimental data. Additionally, the superposition of surface plasmon waves between two AuNPs is studied using the finite element method and experimental data from WF-SPRM. The surface plasmon waves around the two particles result from the superposition of electric fields between these waves. Combining plasmon intensities of two AuNPs with an initial phase difference (φ) as $|a + a|^2$ (or $|2a|^2$) yields a quantum superposition of $|2a|^2 = |a|^2 + |a|^2 + 2|a|^2\cos\varphi$, resulting in complex and cumulative superposed plasmon intensities. Finally, the multiple particles near the Au layer are represented as effective media, described by Maxwell–Garnet equations. The sensitivity of 40 nm AuNPs is 50.6 deg./RIU, and this sensitivity increases linearly to 93.5 deg./RIU for the detection of 80 nm AuNPs.

Data availability

The datasets used and/or analysed during the current study available from the corresponding author on reasonable request.

Received: 4 July 2023; Accepted: 9 December 2023
Published online: 16 December 2023

References

1. Scherbahn, V., Nizamov, S. & Mirsky, V. M. Plasmonic detection and visualization of directed adsorption of charged single nanoparticles to patterned surfaces. *Microchim. Acta* **183**(11), 2837–2845 (2016).
2. Masson, J.-F. Surface plasmon resonance clinical biosensors for medical diagnostics. *ACS Sensors* **2**(1), 16–30 (2017).
3. Xue, T. *et al.* Ultrasensitive detection of miRNA with an antimonene-based surface plasmon resonance sensor. *Nat. Commun.* **10**(1), 1–9 (2019).
4. Singh, S. *et al.* 2D nanomaterial-based surface plasmon resonance sensors for biosensing applications. *Micromachines* **11**(8), 779 (2020).
5. Wu, B. *et al.* Detection of C-reactive protein using nanoparticle-enhanced surface plasmon resonance using an aptamer-antibody sandwich assay. *Chem. Commun.* **52**(17), 3568–3571 (2016).
6. Šípová, H. & Homola, J. Surface plasmon resonance sensing of nucleic acids: A review. *Anal. Chim. Acta* **773**, 9–23 (2013).
7. K. E, Determination of optical constants of metals by excitation of surface plasmons. *Zeitschrift Fur Physik 241*(4), 313 (1971).
8. Nizamov, S., Sazdovska, S. D. & Mirsky, V. M. A review of optical methods for ultrasensitive detection and characterization of nanoparticles in liquid media with a focus on the wide field surface plasmon microscopy. *Anal. Chim. Acta* **33**, 9633 (2022).
9. Sidorenko, I. *et al.* Computer assisted detection and quantification of single adsorbing nanoparticles by differential surface plasmon microscopy. *Microchim. Acta* **183**(1), 101–109 (2016).
10. Nizamov, S., Scherbahn, V. & Mirsky, V. M. Detection and quantification of single engineered nanoparticles in complex samples using template matching in wide-field surface plasmon microscopy. *Anal. Chem.* **88**(20), 10206–10214. https://doi.org/10.1021/acs.analchem.6b02878 (2016).
11. Shpacovitch, V. *et al.* Application of the PAMONO-sensor for quantification of microvesicles and determination of nano-particle size distribution. *Sensors* **17**(2), 244 (2017).
12. Rouf, H. K. & Haque, T. Performance enhancement of Ag-Au bimetallic surface plasmon resonance biosensor using InP. *Prog. Electromagn. Res. M* **76**, 31–42 (2018).
13. Shpacovitch, V. & Hergenroeder, R. Optical and surface plasmonic approaches to characterize extracellular vesicles. A review. *Anal. Chim. Acta* **1005**, 1–15 (2018).
14. Steiner, G. Surface plasmon resonance imaging. *Anal. Bioanal. Chem.* **379**(3), 328–331 (2004).
15. Yang, C.-T. *et al.* Surface plasmon enhanced light scattering biosensing: size dependence on the gold nanoparticle tag. *Sensors* **19**(2), 323 (2019).
16. Kretschmann, E. The determination of optical constants of metals by excitation of surface plasmons (Die Bestimmung optischer Konstanten von Metallen durch Anregung von Oberflächenplasmaschwingungen). *Z. Phys.* **241**, 313–324 (1971).
17. Al-Bataineh, Q. M., Shpacovitch, V., Sadiq, D., Telfah, A. & Hergenröder, R. Surface plasmon resonance sensitivity enhancement based on protonated polyaniline films doped by aluminum nitrate. *Biosensors* **12**(12), 1122 (2022).
18. Zybin, A., Shpacovitch, V., Skolnik, J. & Hergenröder, R. Optimal conditions for SPR-imaging of nano-objects. *Sens. Actuators B Chem.* **239**, 338–342 (2017).
19. Gurevich, E., Temchura, V., Überla, K. & Zybin, A. Analytical features of particle counting sensor based on plasmon assisted microscopy of nano objects. *Sens. Actuators B Chem.* **160**(1), 1210–1215 (2011).
20. Zybin, A. *et al.* Double-wavelength technique for surface plasmon resonance measurements: Basic concept and applications for single sensors and two-dimensional sensor arrays. *Anal. Chem.* **77**(8), 2393–2399 (2005).
21. Rasband, W. S. "ImageJ." National Institutes of Health. https://imagej.nih.gov/ij/ (accessed).
22. Maurya, J., Prajapati, Y., Singh, V., Saini, J. & Tripathi, R. Performance of graphene–MoS 2 based surface plasmon resonance sensor using silicon layer. *Opt. Quant. Electron.* **47**(11), 3599–3611 (2015).
23. Yu, H., Shan, X., Wang, S., Chen, H. & Tao, N. Molecular scale origin of surface plasmon resonance biosensors. *Anal. Chem.* **86**(18), 8992–8997 (2014).
24. Raether, H. Surface plasmons on gratings. In *Surface plasmons on smooth and rough surfaces and on gratings*, pp. 91–116 (1988).
25. Leskova, T., Maradudin, A. & Zierau, W. Surface plasmon polariton propagation near an index step. *Opt. Commun.* **249**(1–3), 23–35 (2005).
26. Cao, S.-H., Cai, W.-P., Liu, Q. & Li, Y.-Q. Surface plasmon–coupled emission: What can directional fluorescence bring to the analytical sciences?. *Annu. Rev. Anal. Chem.* **5**, 317–336 (2012).

27. Bozhevolnyi, S. I. Localization phenomena in elastic surface-polariton scattering caused by surface roughness. *Phys. Rev. B* **54**(11), 8177 (1996).
28. Bozhevolnyi, S. I. & Coello, V. Elastic scattering of surface plasmon polaritons: Modeling and experiment. *Phys. Rev. B* **58**(16), 10899 (1998).
29. Niu, L.-Y., Wang, Q., Jing, J.-Y. & Zhao, W.-M. Sensitivity enhanced D-type large-core fiber SPR sensor based on Gold nanoparticle/Au film co-modification. *Opt. Commun.* **450**, 287–295 (2019).
30. Shpacovitch, V. *et al.* Application of surface plasmon resonance imaging technique for the detection of single spherical biological submicrometer particles. *Anal. Biochem.* **486**, 62–69 (2015).
31. Zybin, A. *et al.* Real-time detection of single immobilized nanoparticles by surface plasmon resonance imaging. *Plasmonics* **5**(1), 31–35 (2010).
32. Zhang, P. *et al.* A high-sensitivity SPR sensor with bimetal/silicon/two-dimensional material structure: A theoretical analysis. *Photonics* **8**(7), 270 (2021).
33. Ma, G. *et al.* Optical imaging of single-protein size, charge, mobility, and binding. *Nat. Commun.* **11**(1), 4768 (2020).
34. Li, P. *et al.* Peak splitting and locking behavior arising from Fano interference between localized surface plasmons and cavity modes. *Phys. Rev. B* **99**(12), 125420 (2019).
35. Xia, F. *et al.* Ultra-high sensitivity SPR fiber sensor based on multilayer nanoparticle and Au film coupling enhancement. *Measurement* **164**, 108083 (2020).
36. Tamada, K., Nakamura, F., Ito, M., Li, X. & Baba, A. SPR-based DNA detection with metal nanoparticles. *Plasmonics* **2**(4), 185–191 (2007).
37. Lazarides, A. A. & Schatz, G. C. DNA-linked metal nanosphere materials: Structural basis for the optical properties. *J. Phys. Chem. B* **104**(3), 460–467 (2000).
38. Resonant Technologies GmbH. http://www.res-tec.de/ (accessed).

Acknowledgements
The scientific support by the Ministerium für Innovation, Wissenschaft und Forschung des Landes Nordrhein-Westfalen, the Senatsverwaltung für Wirtschaft, Technologie und Forschung des Landes Berlin, and the Bundesministerium für Bildung und Forschung is gratefully acknowledged. C.T. acknowledges the funding by FCT (Portugal) / PIDDAC through the Strategic Funds project reference UIDB/04650/2020-2023.

Author contributions
Conceptualization, Q.B. and A.T; methodology, Q.B. and A.T.; software, Q.B. and R.H.; validation, A.T., C.T. and R.H.; formal analysis, Q.B., and C.T.; investigation, A.T. and R.H.; resources, A.T. and R.H.; data curation, Q.B. and R.H.; writing—original draft preparation, Q.B. and A.T.; writing—review and editing, C.T., and R.H.; visualization, Q.B., A.T., C.T.; supervision, A.T. and R.H.; project administration, A.T. and R.H. All authors have read and agreed to the published version of the manuscript.

Funding
Open Access funding enabled and organized by Projekt DEAL.

Competing interests
The authors declare no competing interests.

Additional information
Supplementary Information The online version contains supplementary material available at https://doi.org/10.1038/s41598-023-49583-3.

Correspondence and requests for materials should be addressed to Q.M.A.-B. or R.H.

5.7. Original Paper VII: (Al-Bataineh et al., 2024d)

Qais M. Al-Bataineh, Ihsan Aljarrah, Ahmad A. Ahmad, Gaith Rjoub, Ahmad D. Telfah, Roland Hergenröder, *Surface Plasmon Coupling Between Different Shapes of Silver Nanostructures and Wide Field SPR Microscopy*. Submitted to Journal of Materials Science. (Al-Bataineh et al., 2024d)

CHAPTER 6

6. APPENDIX II: SUPPLEMENTARY MATERIALS

6.1. Supplementary Materials: Original Paper I: (Al-Bataineh et al., 2024a)

S1. Optimization of laser wavelength for Au-layer

The ability of electromagnetic waves at different wavelengths from 200 nm (UV region) to 1500 nm (IR region) to excite the surface plasmon polaritons is investigated. A Kretschmann's configuration is proposed based on glass prism ($n = 1.725$)/gold layer ($n = 0.15 + i4.91$)/ water ($n = 1.33$). The minimum reflectivity ($R_{\min}$) and SPR angle as a function of incident light wavelength, deduced from Figure S1, are plotted in Figure S2. As $R_{\min}$ decreases, the amount of surface plasmon polaritons excitation increases due to the absorption of a large amount of incident light by the gold layer, resulting in the generation of an evanescent field (Mukhtar et al., 2014). At incident light of wavelengths in the range of 200-300 nm, there is no observed SPR signal. When increasing the wavelength to 400 nm (blue light), a small drop with $R_{\min} \approx 0.78$ is registered, indicating the generation of a weak evanescent field due to the small surface plasmon polaritons excitation. Therefore, the light in the UV region is unsuitable for generating SPR signals.

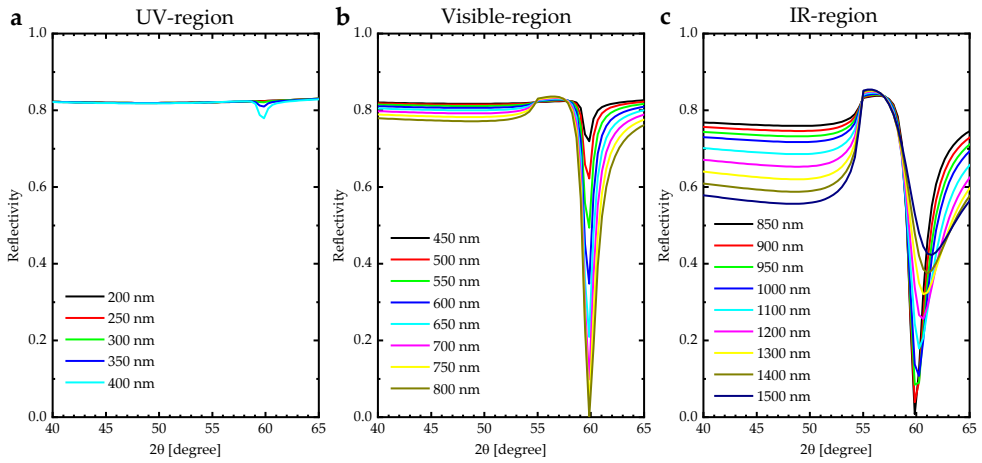

Figure S1: SPR curves of p-polarized light with various wavelengths incident through the 50 nm thickness of Au-coated triangular prism (a) UV-region (200-400 nm) (b) visible region (450-800 nm) (c) IR-region (λ=850-1500 nm).

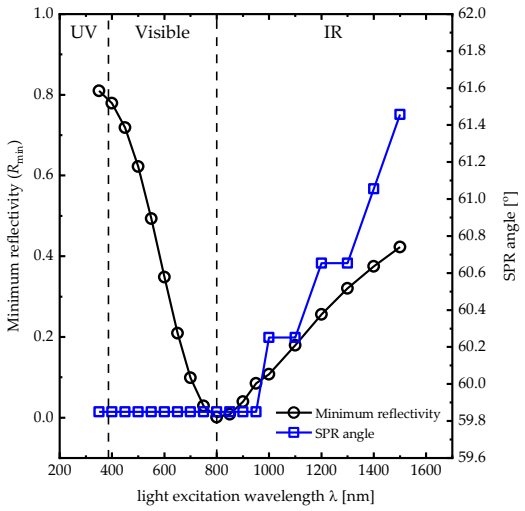

Figure S2: Response of R_{min} and SPR angle as a function of light excitation wavelength.

An increase in the wavelength to 550 nm (green light) increases the SPR signal with $R_{\min} \approx 0.49$. In addition, a strong SPR signal is generated in the wavelength range of 600-800 nm (red to near-IR light), validating the use the red light to excite maximum surface plasmon polaritons. This is attributed to the strong coupling between the photon and the surface electron in this wavelength range, leading to a pull of these electrons along the gold surface (Novotny et al., 2012). However, increasing the wavelength above 800 nm (infrared light) decreases the SPR signal again.

S2. Optimization of gold layer thickness

Kretschmann's configuration of the prism-Ti(5 nm)-Au(various thicknesses from 20 to 60 nm) system is simulated to optimize the thickness for high SPP excitation (Figure S3a). In this section, two main factors are considered to optimize the gold layer thickness, which are $R_{\min}$ and detection accuracy ($\mathrm{DA} = 1/\mathrm{FWHM}$) (Akib et al., 2021). The minimum values of $R_{\min}$ and a higher detection accuracy was generated in the thickness range of 40-45 nm, which is accepted with A. Zybin et al. study (Zybin et al., 2017) (Figure S3b, c).

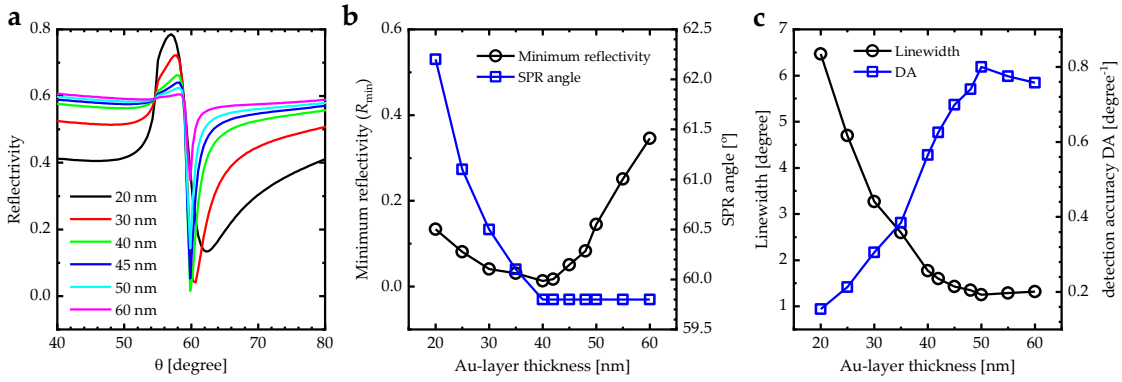

Figure S3: (a) SPR reflectivity curve for Kretschmann configuration of the prism-Ti(5 nm)-gold system for different gold layer thicknesses, (b) Response of R_{min} and SPR angle as an Au-layer thickness, and (c) Response of LW and DA as an Au-layer thickness.

S3. WFSPR instruments

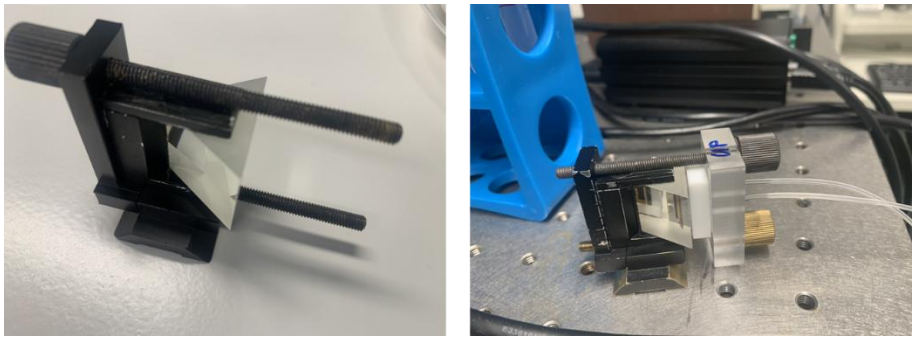

Figure S4: Response of R_{min} and SPR angle as a function of light excitation wavelength.

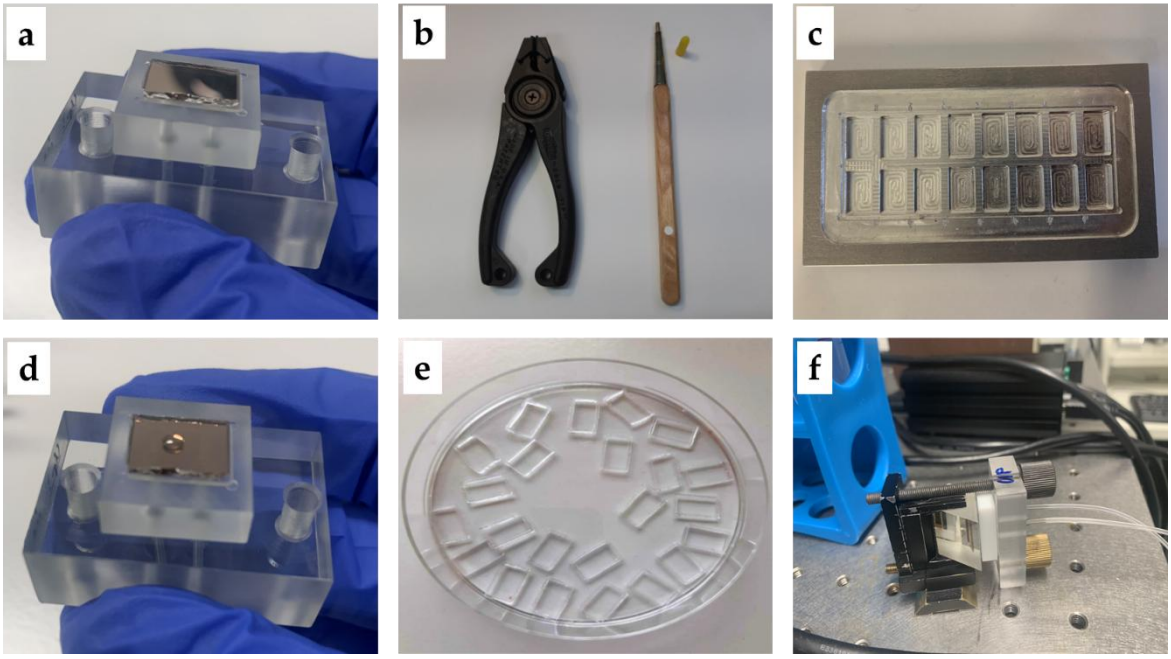

Figure S5: Gold-sensor substrate preparation (a) fitted gold-sensor substrate to the sizes of the flow cell, (b) diamond cutter, (c) wafer cleaving pliers, (d) using RI matching immersion liquid, (e) PDMS gaskets, and (f) the final gold-sensors substrate connected to glass prism and flow cell.

S4. Coating gold layer with a dielectric layer

As shown in Figure S6a, increasing the refractive index value of the dielectric layer increases the SPR angle. The linear fit of the SPR angle shifts as a function of refractive index changes represents the sensitivity of the SPR sensor (Figure S6b). The sensitivity and detection accuracy (DA = 1/LW) of the SPR sensor of the prism-Ti-gold system is 119.5 deg.RIU-1 and 0.70 deg.-1, respectively. Coating the gold layer with a dielectric layer with a refractive index lower than 1.8 decreases the sensitivity and DA. However, increasing the refractive index above 1.8 significantly increases the SPR sensor sensitivity (Figure S6c). In contrast, the detection accuracy decreases continuously with increasing refractive index of the dielectric layer due to the concomitant increase in the line width of the SPR signal.

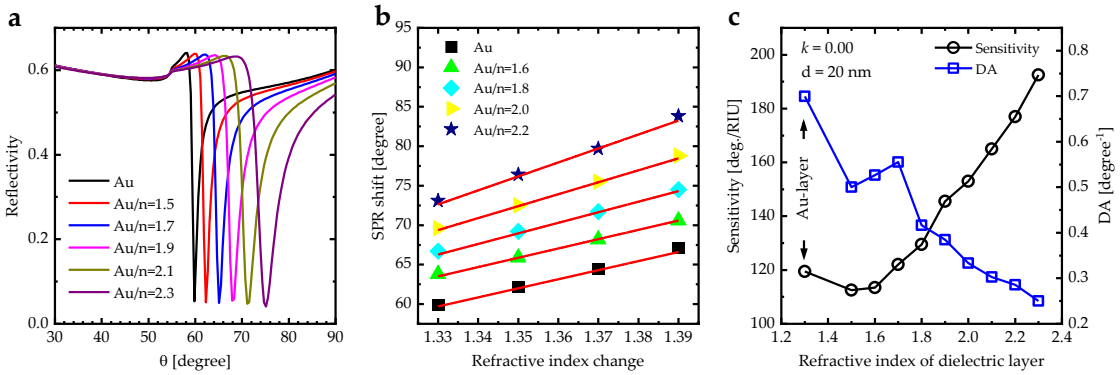

Figure S6: (a) SPR reflectivity curve for Kretschmann's configuration of the prism-Ti-gold-dielectric system for selected refractive indices of a dielectric layer, (b) SPR angle shift versus the refractive index change of selected refractive indices of a dielectric layer, and (c) Sensitivity and DA variation as a function of refractive indices of a dielectric layer of prism-Ti-gold- dielectric system.

The effect of extinction coefficient and thickness variation is also studied to optimize the dielectric layer coated the Au-layer to get higher sensitivity with accepted detection accuracy (Figure S7). The sensitivity does not depend on the extinction coefficient value. However, an increase in the extinction coefficient value of the dielectric layer decreases the detection accuracy (Figure S7a). Therefore, it is concluded that the lower extinction coefficient with a higher refractive index of the dielectric layer is considered a target for coating the Au-layer to get higher sensitivity with an acceptable detection accuracy of SPR sensors. In addition, to get high sensitivity with an acceptable detection accuracy of SPR sensors, the thickness of the dielectric layer should be in the range of 15-20 nm (Figure S7b).

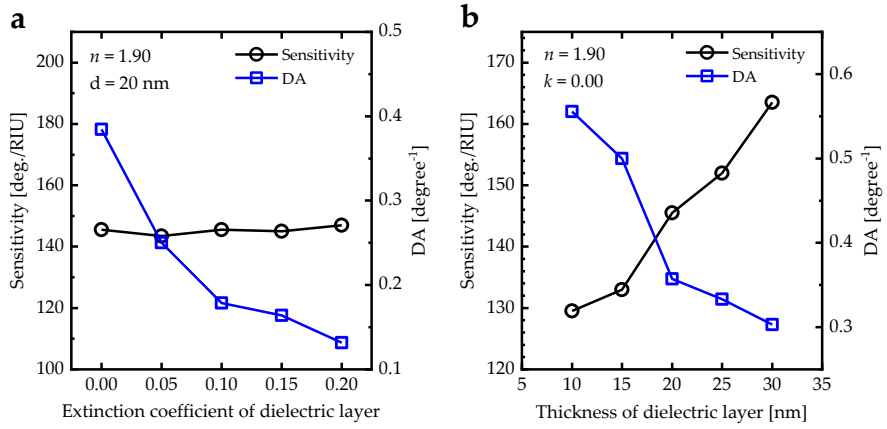

Figure S7: Sensitivity and DA variation as a function of (a) extinction coefficient and (b) thickness of a dielectric layer of prism-Ti-gold- dielectric system.

References

- W. M. Mukhtar, S. Shaari, A. A. Ehsan, and P. S. Menon, "Electro-optics interaction imaging in active plasmonic devices," Optical Materials Express, vol. 4, no. 3, pp. 424-433, 2014.
- L. Novotny and B. Hecht, Principles of nano-optics. Cambridge university press, 2012.
- T. B. A. Akib et al., "Design and numerical analysis of a graphene-coated SPR biosensor for rapid detection of the novel coronavirus," Sensors, vol. 21, no. 10, p. 3491, 2021.
- Zybin, V. Shpacovitch, J. Skolnik, and R. Hergenröder, "Optimal conditions for SPR-imaging of nano-objects," Sensors and Actuators B: Chemical, vol. 239, pp. 338-342, 2017.

6.2. Supplementary materials: Original Paper IV: (Al-Bataineh et al., 2024b)

S1. The "grafting to" method

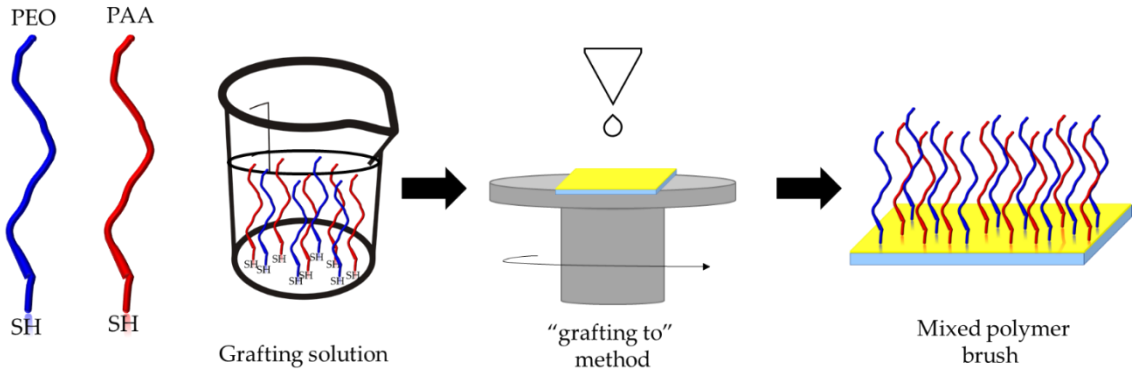

Figure S1: Illustration of the method used for simultaneous grafting of PEO/PAA on a gold substrate.

S2. Chemical structure of PEO/PAA PEBs

The interaction between PEO/PAA blends at pH 7 is investigated using FTIR (Figure S2). The absorption band at 1558 cm^{-1} corresponds to the symmetric COO^- bonds of PAA (Aulich et al., 2010), and the absorption band at 1091 cm-1 corresponds to the ether bond ($C-O-C$) of PEO. Both absorption bands are observed in all PEO/PAA films, which confirms that the blend films are composed of PEO and PAA. Upon the formation of interpolymer hydrogen bonds among PAA chains, the absorption bands of symmetric COO^- bonds of this polymer are shifted to a lower wavenumber (Figure S2a) (Zou et al., 2019). In addition, the absorption bands at 2866 cm-1 corresponding to the hydroxyls have different wavenumber in the PEO/PAA compared to PEO and PAA, which confirms the formation of interpolymer hydrogen bonds between PEO and PAA (Figure S2b). The formation of interpolymer hydrogen bonds is ascribed to the interactions between the ether oxygen atoms in PEO and carboxylic acid groups in PAA (Figure S2c).

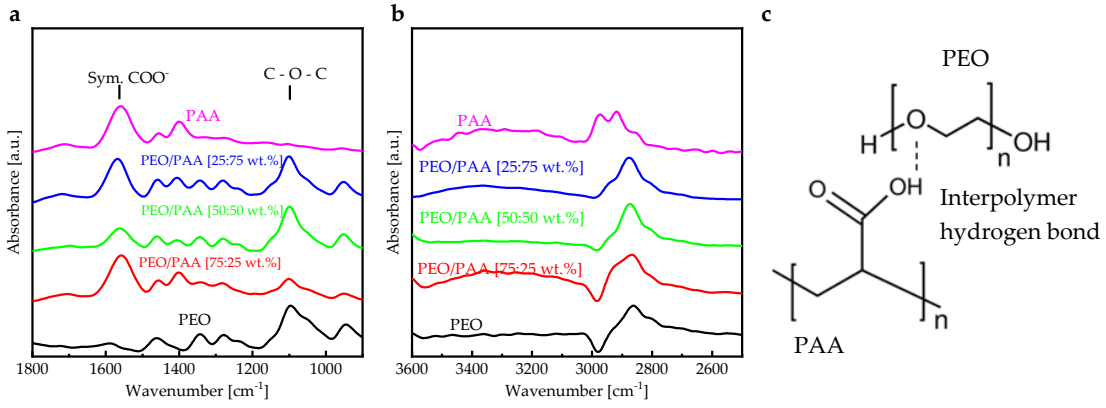

Figure S2: FTIR spectra of the PEO/PAA blend films in the wavenumber region of (a) 1800-1000 cm^{-1} and (b) 3600-2500 cm^{-1}. (c) The structure schematic drawing of interpolymer hydrogen bonds formed between PEO and PAA.

S3. NAP-XPS experiments

The measured C1s, O1s, S2p, and S2s core-level XPS peaks of PEO/PAA–SH PEBs at pH 7 are used to investigate the thiol group bindings. XPS C1s peaks of PAA–SH PEBs correspond to $C-C, C-H$ bonds at 284.6 eV, and $-COO^-$ at 285.9 eV (Figure S3a). The O1s photoelectron peaks appear at 532.9 eV ($C=O$), 534.4 eV ($O-OH$), and 536.9 eV ($C-O$) ($O=C-O^-$) (Figure S3b). Finally, S2p and S2s photoelectron peaks confirm the existence of the –SH group on the PAA matrix through two peaks at 161.8 eV and 228.8 eV. The first peak can be convoluted into two sub-peaks of $C-SH$ and $C-S-R$, whereas the second peak can be convoluted into two sub-peaks of $S-H$ and unbound sulfur atoms (Figures S3c, d).

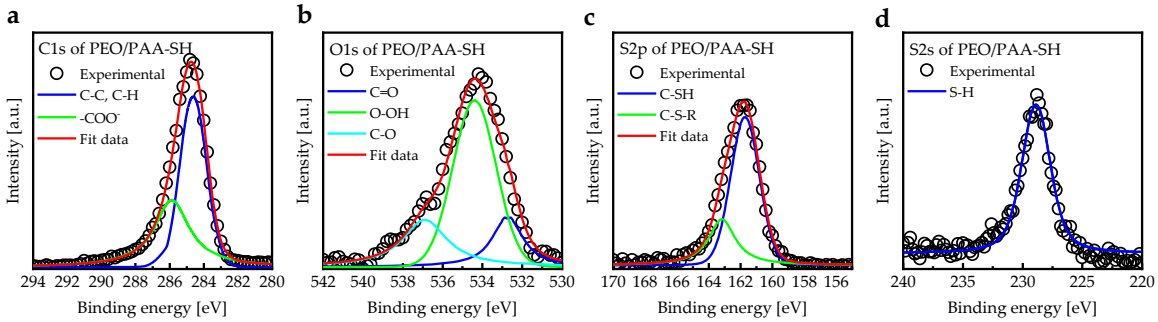

Figure S3: Deconvoluted XPS (a) C1s, (b) O1s, (c) S2p, and (d) S2s core-level spectra of PEO/PAA-SH PEBs.

S4. Surface wettability

The surface wettability was investigated using water contact angle measurements for a water droplet (pH = 7) of size 10 µL. Measurements were taken on both sides of the droplet to ensure the results' consistency. Figure S4 shows the water contact angle for PEO/PAA PEBs as a function of pH value.

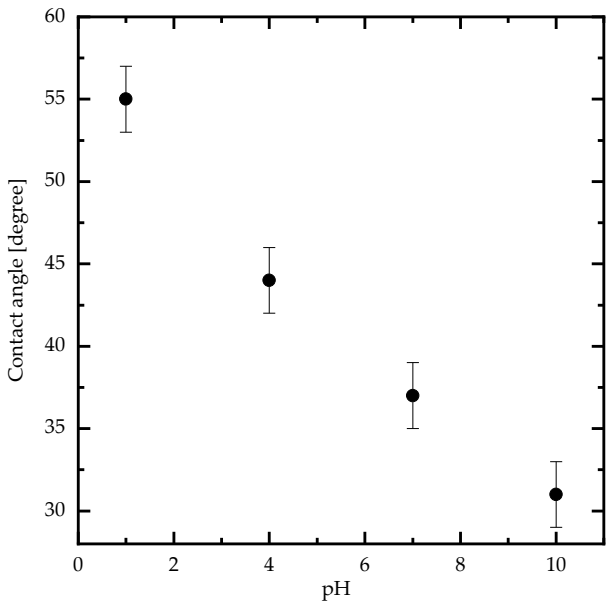

Figure S4: Contact angle measurements of PEO/PAA PEBs as a function of pH value.

S5. Crystal structure of PEO/PAA PEBs

The crystallinity of PEO/PAA PEBs with different pH values was investigated using XRD measurements with CuKα X-ray radiation with a wavelength of 0.1540598 nm (Figure S5). At a pH of 1, the PEO/PAA PEBs show an amorphous structure. Increasing pH from 1 to 10 increases the crystal

to the amorphous ratio of the PEO/PAA PEBs, which means that the PEO/PAA PEBs at pH higher than 4 have a semi-crystalline structure (Figure S5). The two main peaks of PEO/PAA PEBs at pH of 4 are observed at Bragg angles of 19.72° and 23.78°, corresponding to (120) and (112) atomic planes, respectively (Azli et al., 2015; Polu et al., 2016). Increasing pH to 10 shifts the diffraction peaks to lower angles. The crystallinity degree of PEO/PAA PEBs at pH 4 is 45.4%, increasing to 58.8% as pH increases to 10 due to the new formation of PEBs from collapsed to stretching. In addition, the crystallite size (D) and the microstrain (ε) of the PEO/PAA PEBs at pH of 4 are 7.7 nm and 0.0049. Increasing the pH to 7 decreases the crystallite size to 6.2 nm and increases the microstrain to 0.0059. Additional increase in the pH to 10 leads to increases in the crystallite size to 9.0 nm and increases in the microstrain to 0.0041.

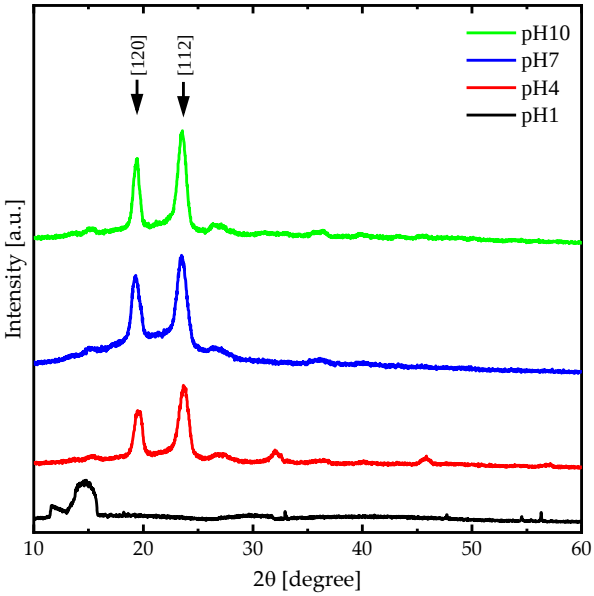

Figure 7: XRD pattern for PEO/PAA PEBs for different pH values.

References:

- D. Aulich et al., "In situ studies on the switching behavior of ultrathin poly (acrylic acid) polyelectrolyte brushes in different aqueous environments," Langmuir, vol. 26, no. 15, pp. 12926-12932, 2010.
- Q. M. Al-Bataineh, A. A. Ahmad, A. M. Alsaad, A. Migdadi, and A. Telfah, "Correlation of electrical, thermal, and crystal parameters of complex composite films based on polyethylene oxide (PEO) doped by copper sulfate (CuSO4)," Physica B: Condensed Matter, vol. 645, p. 414224, 2022.
- S. Zou, R. Lv, Z. Tong, B. Na, K. Fu, and H. Liu, "In situ hydrogen-bonding complex mediated shape memory behavior of PAA/PEO blends," Polymer, vol. 183, p. 121878, 2019.
- R. Polu and H.-W. Rhee, "The effects of LiTDI salt and POSS-PEG (n= 4) hybrid nanoparticles on crystallinity and ionic conductivity of PEO based solid polymer electrolytes," Science of Advanced Materials, vol. 8, no. 5, pp. 931-940, 2016.
- [A. Azli, N. Manan, and M. Kadir, "Conductivity and dielectric studies of lithium trifluoromethanesulfonate doped polyethylene oxide-graphene oxide blend based electrolytes," Advances in Materials Science and Engineering, vol. 2015, 2015.

6.3. Supplementary materials: Original Paper V: (Al-Bataineh et al., 2024c)

S1. Methods

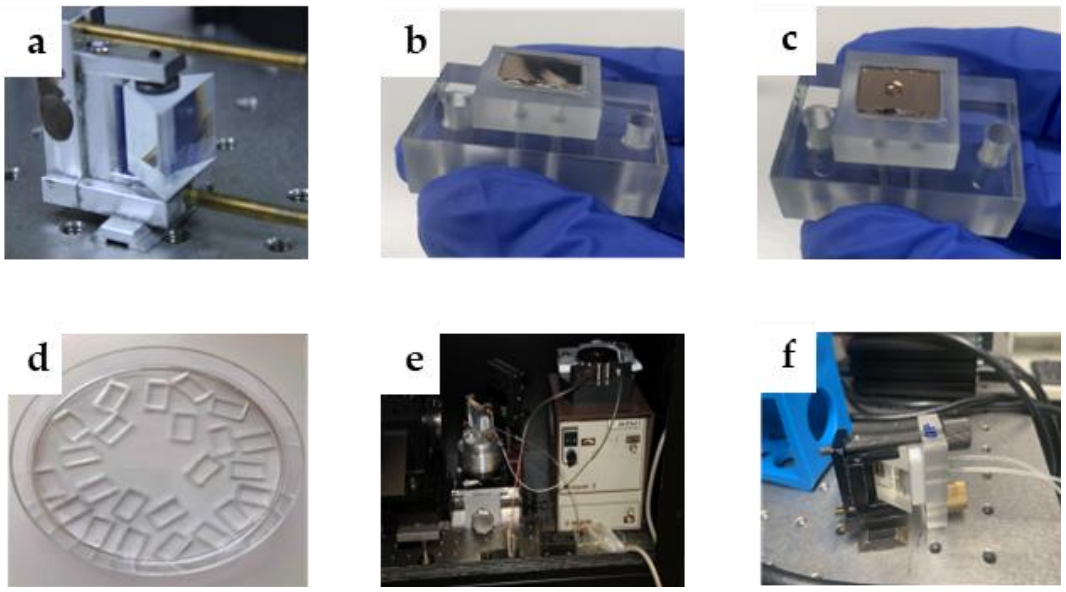

Supplementary Figure 1: Sensor substrate preparation. **(a)** Glass prism, **(b)** fitted gold-sensor substrate to the sizes of the flow cell, **(c)** using RI matching immersion liquid, **(d)** PDMS gaskets, **(e)** flow cell, and **(f)** the final gold-sensors substrate connected to glass prism and flow cell.

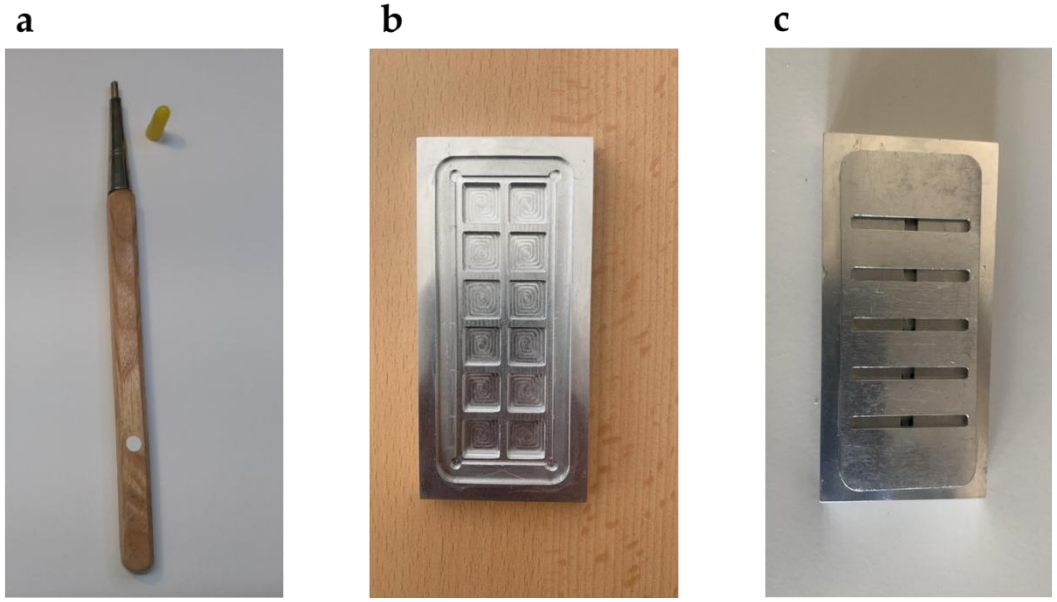

Supplementary Figure 2: (a) Diamond cutter and **(b, c)** designed steel plate to cut gold slides in smaller pieces, which can be placed into the flow cell.

S2. Optimization Of Laser Wavelength

The ability of electromagnetic waves in the wavelength range of 200-1500 nm to excite the surface plasmon polaritons is investigated using Winspall software (RES-TEC). The ability of electromagnetic waves in the wavelength range of 200-1500 nm to excite the surface plasmon polaritons is investigated. A Kretschmann's configuration is proposed based on glass prism ($n = 1.725$)/gold layer ($n = 0.15 + i4.91$)/ water ($n = 1.33$) and glass prism ($n = 1.725$)/silver layer ($n = 0.1726 + i3.421$)/ water ($n = 1.33$). The minimum reflectivity ($R_{\min}$) and SPR angle for Au-layer as a function of incident light wavelength, deduced from Supplementary Figure 3, are plotted in Supplementary Figure 4. On the other hand, the minimum reflectivity ($R_{\min}$) and SPR angle for the Ag-layer as a function of incident light wavelength, deduced from Supplementary Figure 5, are plotted in Supplementary Fig. 6. As $R_{\min}$ decreases, the amount of surface plasmon polaritons excitation increases due to the absorption of a large amount of incident light by the Au- and Ag-layer, resulting in the generation of an evanescent field (Mukhtar et al., 2014). A strong SPR signal is generated by Au- and Ag-layer in the wavelength range of 600-800 nm and 600-700 nm, respectively, validating the use of red light to excite maximum surface plasmon polaritons. This is attributed to the strong coupling between the photon and the surface electron in this wavelength range, leading to a pull of these electrons along the gold surface (Novotny et al., 2012).

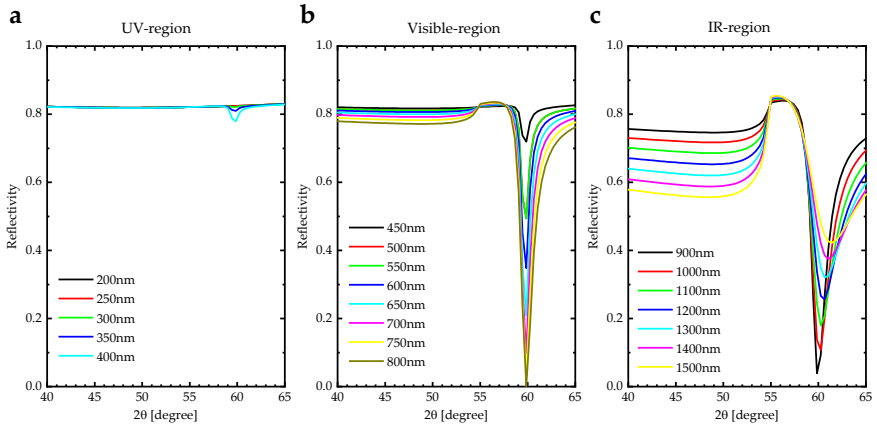

Supplementary Figure 3: SPR curves of p-polarized light with various wavelengths incident through the 50 nm thickness of Au-coated triangular prism **(a)** UV-region (200-400 nm) **(b)** visible region (450-800 nm) **(c)** IR-region (λ=900-1500 nm).

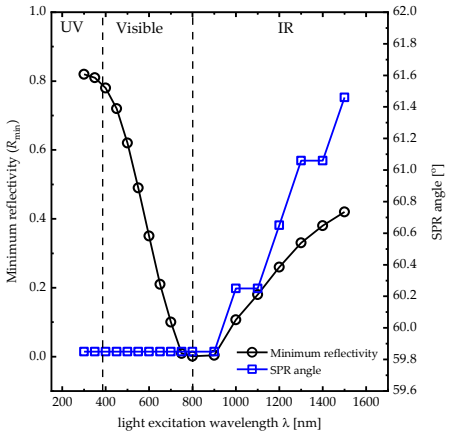

Supplementary Figure 4: Response of R_{min} and SPR angle for Au-layer as a function of light excitation wavelength.

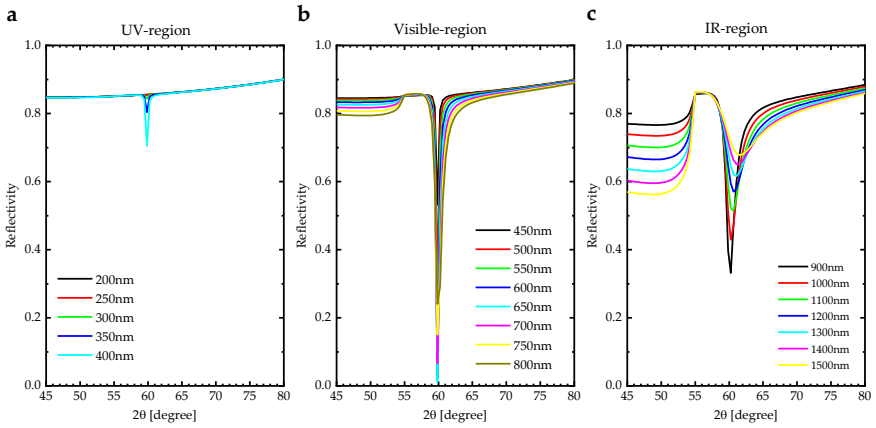

Supplementary Figure 5: SPR curves of p-polarized light with various wavelengths incident through the 50 nm thickness of Ag-coated triangular prism **(a)** UV-region (200-400 nm) **(b)** visible region (450-800 nm) **(c)** IR-region (λ=900-1500 nm).

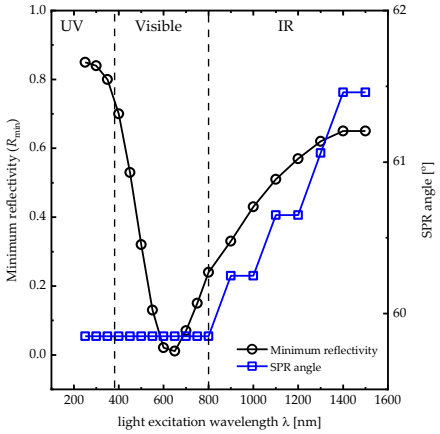

Supplementary Figure 6: Response of R_{min} and SPR angle for Ag-layer as a function of light excitation wavelength.

S3. Optimization of Au- and Ag-layer thickness

Kretschmann's configuration of the prism-Ti(5 nm)-Au/Ag(various thicknesses from 20 to 60 nm) system is simulated to optimize the thickness for high SPP excitation (Supplementary Figure 7). In this section, the minimum reflectivity ($R_{\min}$) are considered to optimize the gold layer thickness. The minimum values of $R_{\min}$ is generated in the thickness of 45 nm, which is accepted with A. Zybin et al. study (Zybin et al., 2017).

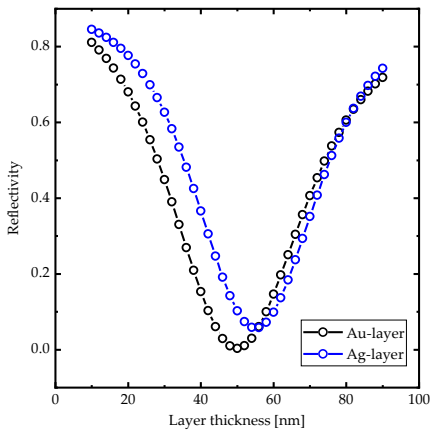

Supplementary Figure 7: Response of R_{min} of the SPR curves as an Au- and Ag-layers thickness.

S4. Particle Transfer Model

The particle transfer model was derived using Navier-Stokes equations with laminar flow conditions (Kuzmichev et al., 2018). The Poiseuille flow velocity ($u(\vec{r},t) = (u_x, u_y, u_z)$) is given by:

$$u_x = 4u_{max}\left(\frac{z}{h} - \frac{z^2}{h^2}\right), u_y = u_z = 0 \quad \text{(S1)}$$

where the x-axis is a flow direction, and the z-axis is perpendicular to the sensor surface. h is the height of the flow cell (Supplementary Figure 8). The velocity reaches a maximum in the middle of the channel ($u_{max} = u_x h/2$) and approaches zero at boundaries ($u_x(0) = u_x(h) = 0$). Additionally, a concentration gradient is large only within a thin boundary diffusion layer ($\delta \ll h$) at the sensor interface; therefore, z^2/h^2 can be neglected because $z^2/h^2 \ll z/h$.

Now, the linear approximation $u_x \approx \frac{6\bar{u}}{h} z$ in the diffusion layer ($z \ll h$) is applied, where $\bar{u} = \left(\frac{2}{3}\right) u_{max}$, which is used because it can be related directly to the volumetric flow rate V, where: $\bar{u} = V/hw$, where w is the width of the flow cell. The continuity equation is given by:

$$\frac{\partial C}{\partial t} = -\nabla\left(\vec{J}_{diff} + \vec{J}_{adv}\right) \quad \text{(S2)}$$

where:

$$\vec{J}_{diff} = -D\nabla C(\vec{r},t) \quad \text{(S3)}$$

$$\vec{J}_{adv} = C(\vec{r},t)\vec{u} \quad \text{(S4)}$$

The governing equation, omitting y-dependence ($C(\vec{r},t) = C(x,z)$) could be derived. Assuming the stationary state $\partial C/\partial t = 0$. The boundary conditions were re-established from (Levich et al., 1963):

$$\begin{cases} C(x, z \gg \delta) = C_0 \\ C(x,0) = 0 \end{cases} \quad \text{(S5)}$$

The equation is the bulk concentration out of the diffusion layer, whereas the second equation represents the zero concentration at the sensor, corresponding to the consideration of the sensor as an infinite sink. Defining a new variable:

$$\eta(x,z) = \left(\frac{3\bar{u}}{hDx}\right)^{1/2} z \quad \text{(S6)}$$

We obtain the following concentration profile:

$$C(\eta) = P\left(\frac{1}{3}, \frac{2}{9}\eta^3\right) C_0 \quad \text{(S7)}$$

where: $P\left(\frac{1}{3}, \frac{2}{9}\eta^3\right)$ regularized incomplete gamma function. For given boundary conditions, we obtain,

$$j(x) = D\left.\frac{\partial C}{\partial z}\right|_{z=0} = \frac{18^{\frac{1}{3}}}{\Gamma\left(\frac{1}{3}\right)}\left(\frac{\bar{u}D^2}{hx}\right)^{\frac{1}{3}} C_0 \quad \text{(S8)}$$

With numerical coefficient $\frac{18^{\frac{1}{3}}}{\Gamma\left(\frac{1}{3}\right)} \approx 0.98$. Under optimal ionic strength conditions, experiments at flow rates in the range 60−673 μL/min for silicaNPs were performed.

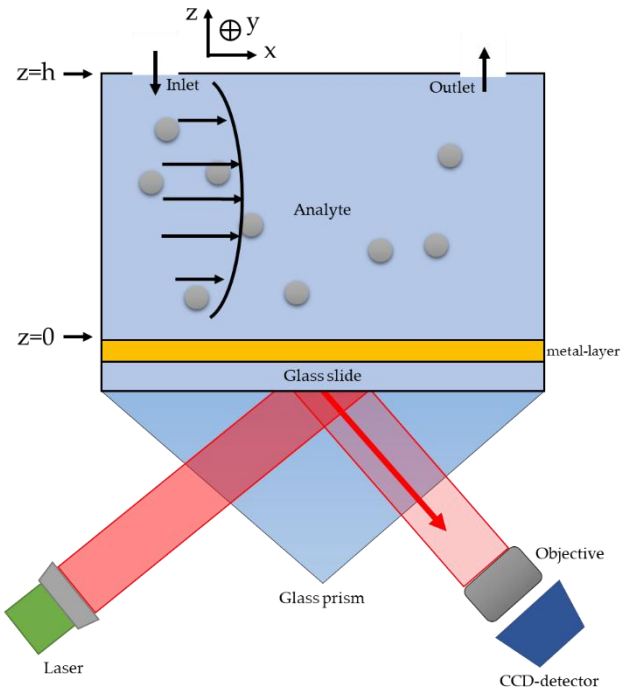

Supplementary Figure 8: Wide-field surface plasmon resonance microscope setup with flow rate conditions.

S5. Signal-To-Noise Optimization

The enhancement of the detection measurements, a result of signal-to-noise optimization, is demonstrated by applying different parameters for SPR detection. The SPR signal is generated from the refractive index variation (Δn) and can be given by (Zybin et al., 2007):

$$S = \eta \left(\frac{d(I_0 R)}{dn}\right) \Delta n = \eta I_0 \frac{dR}{dn} \Delta n \tag{S9}$$

where: η is the quantum efficiency of the photodetector and I_0 is the illumination intensity. There are different sources of noise sources, depending on the experimental parameters. The shot noise can be given by,

$$N = \sqrt{\eta I_0 R} \tag{S10}$$

Comparing equations (S9) and (S10), the signal-to-noise ratio (S/N) is given by,

$$S/N = \sqrt{\frac{\eta I_0}{R}} \frac{dR}{dn} \Delta n \tag{S11}$$

On the other hand, the CCD detector's illumination intensity must be fitted to the SPR reflectivity. Assume that the optimum illumination intensity is,

$$I_0^{opt} = I_{CCD}/R \tag{S12}$$

Therefore, the optimum signal-to-noise ratio becomes,

$$S/N = \sqrt{\eta I_{CCD}} \frac{dR/dn}{R} \Delta n \tag{S13}$$

To minimize the signal-to-noise ratio, the SPR angle is set to be four times the intensity of the resonance angle ($4R_{min}$). Therefore, the measuring point is adjusted to $4R_{min}$ into the linear region of the reflectivity curve by rotating the angle of incidence counter-clockwise (Zybin et al., 2005).

S6. Image J with plugin code

```
// "SubtractMeasuredBackground"
 // For each image in a stack, this macro subtracts the
 // background level calculated from the current selection.
 // Note that the selection may be a composite (discontinuous)
 // selection that was created by holding down the shift key.
 macro "Subtract Measured Background 1" {
    if (selectionType==-1)
      exit("This macro requires an area selection");
 getBoundingRect(x, y, width1, height1);
    for (i=1; i<=nSlices; i++) {
       setSlice(i);
       value=0;
       width = getWidth;
       height = getHeight;
       av=0;
       k=0;
          for (y=0; y<height1; y++) {
            for (x=0; x<width1; x++) {
//                value = getPixel(x,y)+value;
                k++;
                av=av+(getPixel(x,y)-av)/k;
             }

          }
//           av = value/height/width;


            for (y=0; y<height; y++) {
              for (x=0; x<width; x++) {
                value = getPixel(x,y)/av*6000;
                setPixel(x, y, value);
             }
            }
   showProgress(i, nSlices);

    }
 }

//  // This macro subtracts the mean gray level calculated
//  // from user-defined selections that have been added to the
//  //  ROI Manager. It works with both single images and a stacks.
//  macro "Subtract Measured Background 2" {
//     n = roiManager("count");
//     if (n==0)
//        exit("This macro requires at least one ROI Manager entry");
//     sum = 0;
//     for (i=0; i<n; i++) {
//        roiManager("select", i);
```

```
//        getStatistics(area, mean);
//        sum += mean;
//    }
//    average = sum/n;
//    run("Select None");
//    run("Subtract...", "stack value="+average);
// }
```

S7. Iodine complexation with PAA

The ^{1}H-NMR spectra of PAA and PAA/I_2 PEBs with I_2 concentration of 8 wt.% are shown in Supplementary Figure 9a. The signals in the PAA PEBs at 1.10, 1.0-1.7, and 2.01 ppm represent CH_3, CH_2, and CHCOOH protons, respectively. Adding I_2 into PAA PEBs leads to shifting the signal of CHCOOH protons into high chemical shifts, which indicates that the protons in PAA have higher electron density, and consequently, the interaction between the iodine and PAA is charge transfer, forming charge transfer complexes (Danyluk et al., 1962).

Supplementary Figures 9b and 9c show the FTIR spectrum for PAA/I_2 PEBs for different I_2 concentrations in the range of 1000-2000 cm^{-1} and 2500-4000 cm^{-1}, respectively. The bending C–H vibrational band in the PAA is at 1284 cm^{-1}. The vibrational bands at 1408 and 1560 cm^{-1} are attributed to the symmetric and asymmetric COO^- of carboxylate, respectively, while COOH of carboxylate is located at 1718 cm^{-1}. Finally, the CH_x and OH bonds appeared at 2930 and 3340 cm^{-1}, respectively (Yi et al., 2017). Increasing I_2 concentrations into PAA/I_2 PEBs leads to variations in linewidths, intensities, and vibrational bands position of all absorption bands due to the high electronegativity of iodine atoms that substantially influence the frequencies of the neighboring group in the PAA PEBs (Bazaka et al., 2017). In addition, the vanishing of CH_x vibrational band means that the iodide (I^-) and triiodide (I_3^-) are connecting with the carbon atoms in the carboxylate.

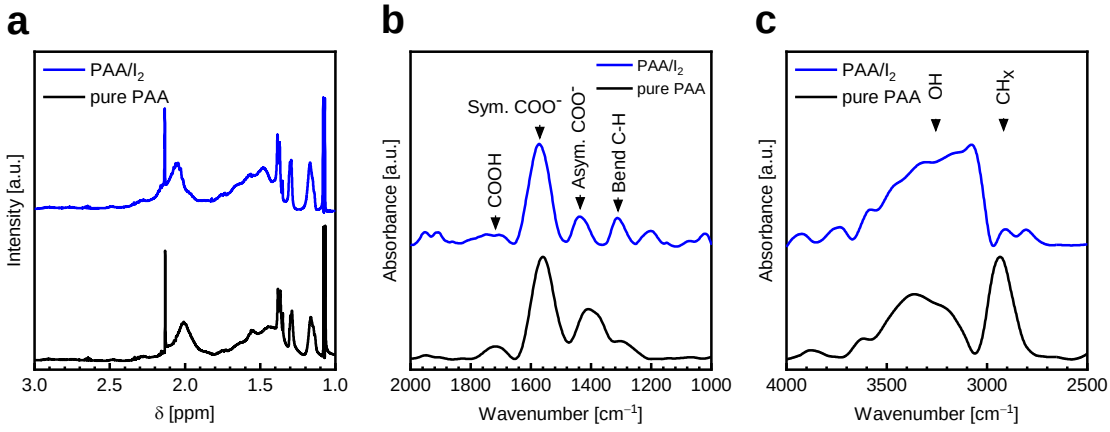

Supplementary Figure 9: Iodine complexation with PAA. (a) 1H NMR spectra for pure PAA and PAA/I_2 PEBs. FTIR absorbance spectra pure PAA and PAA/I_2 PEBs in the range of **(b)** 1000-2000 cm^{-1} and **(c)** 2500-4000 cm^{-1}.

S8. WF-SPRM results: silver versus gold

The time dependence of the local intensity of silicaNP with different sizes, 100, 200, and 300 nm, detected by Au and Ag layers, was measured three times, and the average value is illustrated in Supplementary Fig. 10a. The intensity step magnitude is proportional to the size of the detected

particles. Additionally, the intensity step magnitude of silicaNP detected by the Ag layer is higher than the silicaNP detected by the Au layer.

The WF-SPRM experimental results show that two parameters affect the signal intensity, the first being the metal sensor surface type. The signal intensity of the 100 silicaNP detected by the Au layer is about 79 a.u., whereas the signal intensity of 100 silicaNP detected by the Ag layer is about 226 a.u. (Supplementary Fig 10b). This can be attributed to the resultant evanescent field generated by the Ag sensor surface into the detection medium, which is stronger and penetrates deeper than the Au sensor surface. In addition, the second parameter is the particle size, where the signal intensity of silicaNP detected by the Au layer increases from about 79 a.u. to about 204 a.u. as silicaNP size increases from 100 to 300 nm. On the other hand, the signal intensity of silicaNP detected by the Ag layer increases from about 226 a.u. to about 373 a.u. as silicaNP size increases from 100 to 300 nm. The signal intensity for silicaNP detected by Au and Ag layers can be fitted by a straight line between 100 and 300 nm, indicating the fundamental difference between the Mie scattering and the signal-generating method. However, the dependence's regularity suggests that the images correspond to single particles rather than agglomerates.

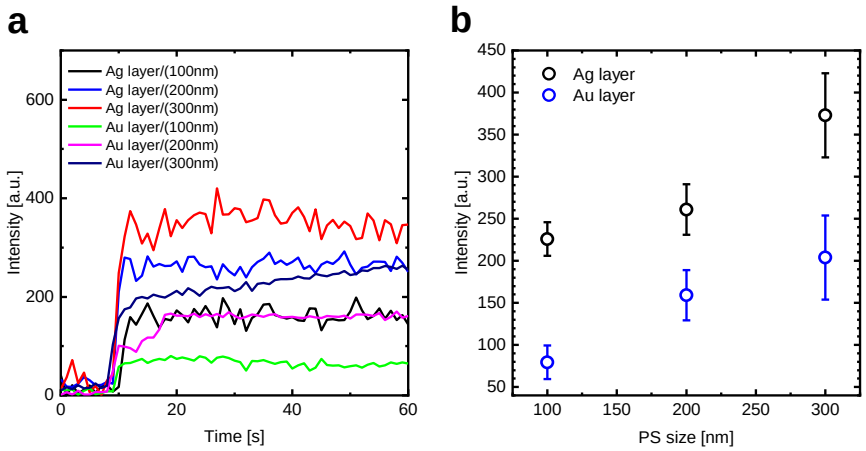

Supplementary Figure 10: WF-SPRM results: silver versus gold. (a) The time dependence of the local intensity of silicaNP with different sizes, 100, 200, and 300 nm, detected by Au and Ag layers. **(b)** Experimental intensity of detected silicaNP by Au and Ag layer as a function of silicaNP size.

S9. Coating metal layer with a dielectric layer

Coating the metal layer with a dielectric layer is a highly effective modification to enhance the sensitivity of the SPR sensor (Menegazzo et al., 2011; Yılmaz et al., 2017). In this section, the sensitivity enhancement resulting from the coating of a dielectric layer on the metal layer is explained (Mudgal et al., 2020). The propagation constant (β_{ev}) can characterize the propagation of evanescent waves and given by (Anower et al., 2021),

$$\beta_{ev} = \frac{2\pi}{\lambda_{light}} n_{prism} \sin\theta \tag{S14}$$

Here, n_{prism} and θ represent the refractive index of the prism and the incident light angle at the metal surface, respectively, and λ_{light} is the light wavelength. Additionally, the propagating constant of the surface plasmon wave for the SPR sensor with a single metal layer and sensing medium is given by (Anower et al., 2021),

$$\beta_{SPW} = \frac{2\pi}{\lambda_{light}} \sqrt{\frac{n_{metal}^2 n_{sm}^2}{n_{metal}^2 + n_{sm}^2}} \quad \text{(S15)}$$

Here, n_{metal} and n_{sm} represent the refractive indices for metal and sensing medium, respectively. Equations S14 and S15 at resonance can be connected to get the resonance SPR angle as,

$$\theta_{SPR} = \sin^{-1}\left(\frac{1}{n_{prism}} \sqrt{\frac{n_{metal}^2 n_{sm}^2}{n_{metal}^2 + n_{sm}^2}}\right) \quad \text{(S16)}$$

In addition, by coating the metal surface with a dielectric layer of refractive index ($n_{dielectric}$) in the SPR sensor changes the SPR angle equation to (Akib et al., 2021),

$$\theta_{SPR} = \sin^{-1}\left(\frac{1}{n_{prism}} \sqrt{\frac{n_{metal}^2 n_{dielectric}^2 n_{sm}^2}{n_{metal}^2 + n_{dielectric}^2 + n_{sm}^2}}\right) \quad \text{(S17)}$$

The sensitivity of SPR sensors (S) is calculated by $S = \Delta\theta/\Delta n$, where: $\Delta\theta$ is the SPR angle shift, and Δn is the refractive index change. As seen in Equation (S17), the SPR angle shift increases with an increase in the effective refractive index of the system.

S10. Binding investigations between PAA/I₂ and silicaNPs

FTIR spectra of silicaNPs, PAA/I₂, and PAA/I₂/silicaNPs were used to investigate the binding between PAA/I₂ and silicaNPs (Supplementary Figure 11). SilicaNPs have three main vibrational bands at 450, 910, and 1060 cm^{-1} corresponding to Si – O, Si – OH, Si – O – Si bonds, respectively. On the other hand, PAA/I₂ has four main vibrational bands at 670, 1400, 1556, and 1710 cm^{-1}, corresponding to bending C – H, asymmetric COO^-, symmetric COO^-, and COOH, respectively. There are no additional peaks for PAA/I₂/silicaNPs, indicating that the binding force between the silicaNPs and the PAA/I₂ PEBs is not a chemical bond.

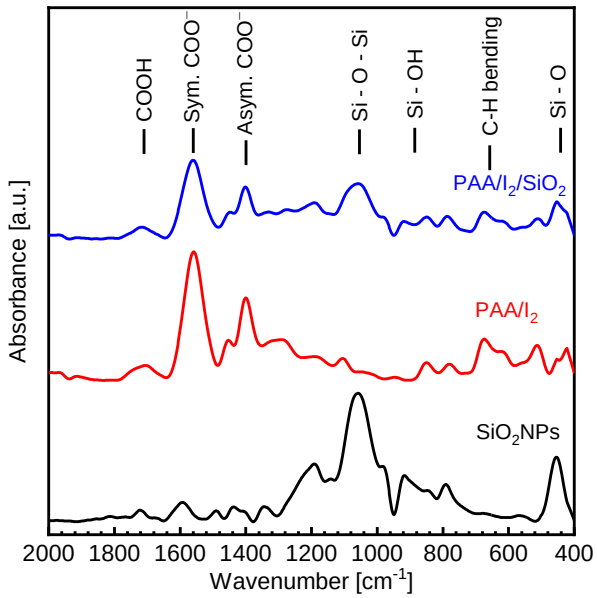

Supplementary Figure 11: Binding investigations between PAA/I₂ and silicaNPs. FTIR spectra of silicaNPs, PAA/I₂, and PAA/I₂/silicaNPs in the wavenumber range of 400 – 2000 cm^{-1}.

S11. Confirmation of single silica nanoparticles with SEM.

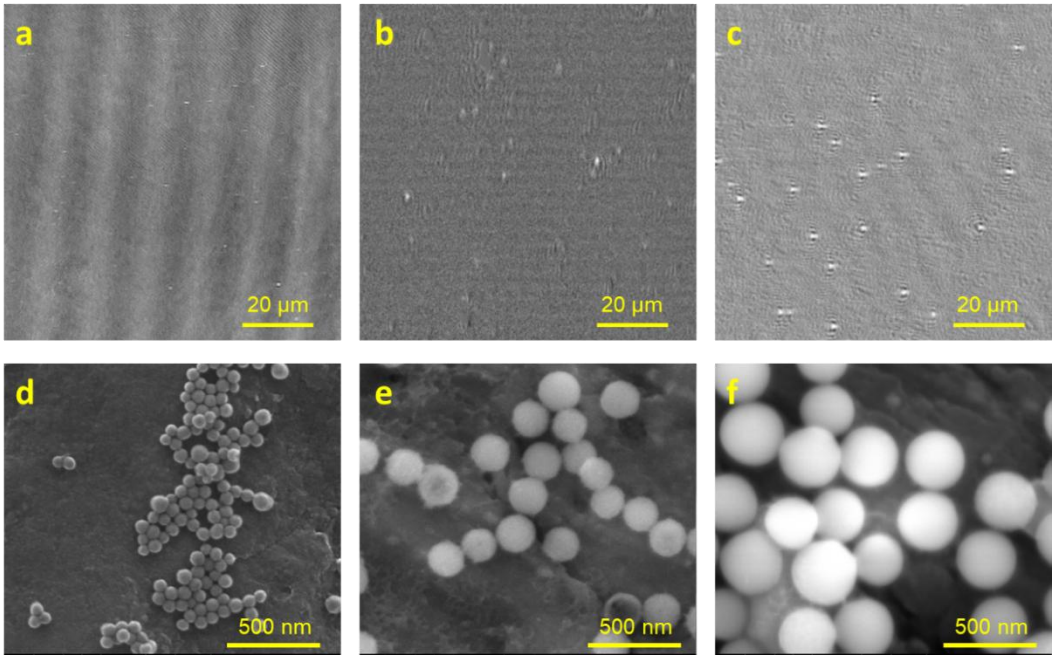

Supplementary Figure 12: Confirmation of single silica nanoparticles with SEM. (**a-c)** WFSPRM and **(d-f)** SEM images of nanoparticles of different sizes (100 nm, 200 nm, and 300 nm, respectively).

S12. Effective Mathematical Model

The effective medium model of the SPR sensor treated the detected molecules near the sensor surface as an effective medium with an effective refractive index and thickness (Supplementary Figure 13a). When light transmits the Ag layer, *p*-polarized SPR waves are generated at the metal/dielectric media interface. When the polarized light illuminates the Ag layer through the glass prism, the light reflection varies by changing the incident angle until it reaches the minimum at the resonance angle (θ_R), indicating surface plasmon excitation that induces surface plasmon resonance, where the *p*-polarized light interacts with the free electron of a metal film, resulting in free electron oscillations (Peterson et al., 2014). The reflectivity curve of the SPR phenomenon is calculated using the transfer matrix method. The SPR phenomenon is described using Maxwell's equations in (x, 0, z) as follows:

$$E_i(\vec{r},t) = (E_{ix}, 0, E_{iz})\left[e^{-|Z|k_{iz}}e^{i(xk_{ix}-\omega t)}\right] \quad \text{(S18)}$$

$$H_i(\vec{r},t) = (0, H_{iy}, 0)\left[e^{-|Z|k_{iz}}e^{i(xk_{ix}-\omega t)}\right] \quad \text{(S19)}$$

where: ω is the frequency, E is the electric field vector, H is the magnetic field vector, k_{iz} and k_{ix} are the z and x wave vector components. Applying the continuity conditions,

$$k_{iz} = \sqrt{\varepsilon_i\left(\frac{\omega}{c}\right)^2 - k_{ix}^2} \quad \text{(S20)}$$

and,

$$\frac{k_{z1}}{\varepsilon_m}H_{1y} + \frac{k_{z2}}{\varepsilon_d}H_{2y} = 0 \quad \text{(S21)}$$

$$H_{1y} - H_{2y} = 0 \quad \text{(S22)}$$

When the determinant is equal to zero,

$$k_{z1}\varepsilon_d + k_{z2}\varepsilon_m = 0 \quad \text{(S23)}$$

At $K_{x1} = K_{x2} = K_x$, the expression becomes:

$$K_x = \frac{\omega}{c}\sqrt{\frac{\varepsilon_m \varepsilon_d}{\varepsilon_m + \varepsilon_d}} \quad \text{(S24)}$$

Equation (S24) represents the SPW vector $K_x = K_{sp}$, illustrating the surface plasmon generation. ε_m and ε_d are the dielectric constants of the metal and dielectric layers. The transfer matrix method is used to investigate the reflectivity curve of the N-layer Kretschmann configuration model as follows (Maurya et al., 2015),

$$\begin{pmatrix} U_1 \\ V_1 \end{pmatrix} = M \begin{pmatrix} U_{N-1} \\ V_{N-1} \end{pmatrix} \quad \text{(S25)}$$

where: (U_1, V_1) and (U_{N-1}, V_{N-1}) are the borderline terms of the 1st and Nth layers of electromagnetic fields. Equation S26 represents the characteristic matrix (Maurya et al., 2015),

$$\prod_{K=2}^{N-1} M_K = \begin{pmatrix} M_{11} & M_{12} \\ M_{21} & M_{22} \end{pmatrix} \quad \text{(S26)}$$

where:

$$M_K = \begin{pmatrix} \cos\beta_k & -\frac{i\sin\beta_k}{q_k} \\ -iq_k \sin\beta_k & \cos\beta_k \end{pmatrix} \quad \text{(S27)}$$

$$q_k = \frac{\sqrt{\varepsilon_k - n_1^2 \sin\theta_1^2}}{\varepsilon_k} \quad \text{(S28)}$$

$$\beta_k = \frac{2\pi d_k}{\lambda}\left(\sqrt{\varepsilon_k - n_1^2 \sin\theta_1^2}\right) \quad \text{(S29)}$$

Where: d_k is the thickness of the k_{th}-layer, θ_k and λ are the incident angle and wavelength of the incident light. Subsequently, the complex reflection coefficient (r_p) is given by,

$$r_p = \left[(M_{11} + M_{12}q_5)q_1 - \frac{(M_{21} + M_{22}q_5)}{(M_{11} + M_{12}q_5)q_1} + (M_{21} + M_{22}q_5)\right] \quad \text{(S30)}$$

The reflectivity (R_p) is obtained by,

$$R_p = |r_p|^2 \quad \text{(S31)}$$

The sensitivity and the detection accuracy of the SPR sensor is given by:

$$S = \frac{\Delta\theta_R}{\Delta n}\,[\text{deg.RIU}^{-1}] \quad \text{(S32)}$$

$$DA = \frac{\Delta\theta_R}{\Delta LW} \quad \text{(S33)}$$

The resonance angle for the Ag layer is 60.01° with linewidth of 0.64° (Supplementary Figure 13b, black line), which shifted to 61.78° with linewidth of 0.81° as presented silica layer of 10 nm thickness due to a variation in the refractive index of the media above the Ag layer (Supplementary Figure 13b, blue line). On the other hand, the resonance angle of Ag-PAA/I_2 layers is 72.69° with linewidth of 2.91° (Supplementary Figure 13c, black line), which shifted to 77.20° with linewidth of 3.65° as presented silica layer of 10 nm thickness due to a variation in the refractive index of the media above the Ag layer (Supplementary Figure 13c, blue line).

The sensitivity of the SPR-based Ag-PAA/I_2 layers is higher than the SPR-based Ag layer due to the higher change in the resonance angle at presence of silica layer of Ag-PAA/I_2 layers is 4.51°, whereas the resonance angle at presence of silica layer of Ag layer is 1.77°, making it easier to detect small changes in the refractive index. Additionally, the evanescent field generated by the Ag-PAA/I_2 sensor into the detection medium is stronger and penetrates deeper into the detection medium compared to

Ag sensor, leading to higher sensitivity to refractive index changes to the sensor surface. The widely used method to detect the resonant angle shift in the SPR reflectivity curve at a fixed incident angle near the resonance angle. The reflectivity change (ΔR) is given by:

$$\Delta R(\theta) = -\frac{dR(\theta)}{d\theta}\Delta\theta \tag{S34}$$

To understand the generated evanescent field during SPR measurements at resonance angle, Kretschmann's configuration of our systems is simulated using COMSOL Multiphysics software. At the resonance angle, the electric field is enhanced at the metal/water interface because of the maximum surface plasmon excitations. However, the resultant evanescent field generated by the Ag-PAA/I_2 sensor surface into the detection medium is stronger and penetrates deeper than the Ag sensor surface. The presence of the silica layer above the Ag or Ag-PAA/I_2 layer increases the resultant evanescent field at the metal/silica interface (Supplementary Figure 13e, f). A significant rise in the electric field is generated at the metal/medium interface, and the electric field intensity decreases exponentially in the analyte-containing detected biomolecules. The resultant electric field of plasmons excited on the metal layer can be described in an exponential function as follows,

$$|E(h)| = E_{max}\exp(-h/L_{bd}) \tag{S35}$$

with,

$$L_{bd} = \lambda/Re\left\{2\pi i\frac{n_m^2}{\sqrt{n_m^2+n_b^2}}\right\} \tag{S36}$$

where: L_{bd} is the penetration depth, h is the distance from the metal surface, n_m is the metal refractive index, n_b is the dielectric refractive index, λ is the illumination wavelength. From Equation (S35), the generated electric field is maximal at the metal/dielectric interface and decays exponentially into the dielectric medium. The decaying rate depends on the penetration depth L_{bd}, which relates only to the optical refractive indices of the metal and the medium at a given illuminated wavelength.

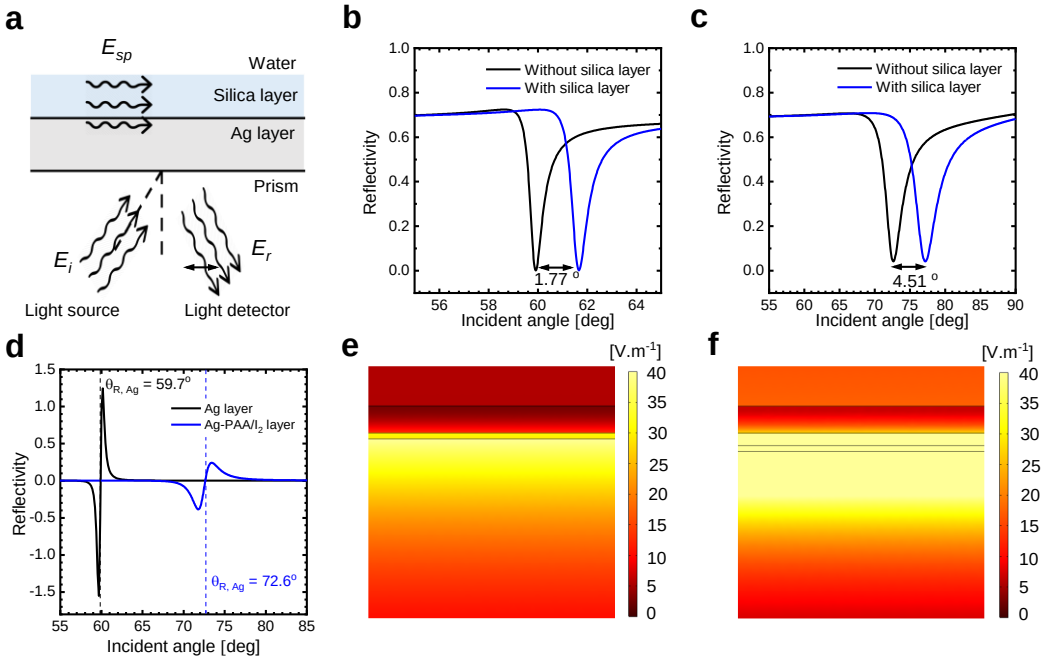

Supplementary Figure 13: The effective medium model of the SPR sensor. (a) Schematic diagram of the effective medium model. **(b)** SPR reflectivity curves of the SPR sensor based on the Ag layer, with the black line representing the curve without a 10 nm thick silica layer and the blue line representing the curve with this layer, were calculated using Fresnel's equations. **(b)** SPR reflectivity curves of the SPR sensor based on the Ag-PAA/I_2 layers, with the black line representing the curve without a 10 nm thick silica layer and the blue line representing the curve with this layer, were calculated using Fresnel's equations. **(d)** The slope of the reflectivity curve. Electric field distributions along the Kretschmann's configuration of the structures based on **(e)** Ag layer and **(f)** Ag-PAA/I_2 layers at resonance angles.

S13. Discrete Particle Model of The SPR Sensor

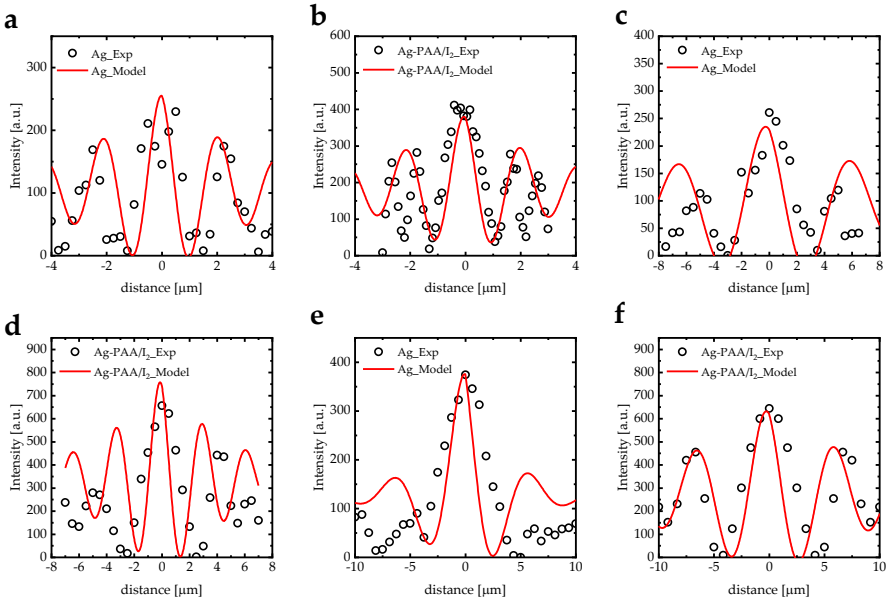

Supplementary Figure 14: Discrete particle model of the SPR sensor. Experimental and calculated intensities vs. distance of silicaNP with **(a)** 100 nm by Ag layer, **(b)** 100 nm by Ag-PAA/I_2 layers, **(c)** 200 nm by Ag layer, **(d)** 200 nm by Ag-PAA/I_2 layers, **(e)** 300 nm by Ag layer, and **(f)** 300 nm by Ag-PAA/I_2 layers.

References

- "RES-TEC." http://www.res-tec.de/ (accessed 07.09.2023.
- Kuzmichev, J. Skolnik, A. Zybin, and R. Hergenröder, "Absolute analysis of nanoparticle suspension with surface plasmon microscopy," Analytical chemistry, vol. 90, no. 18, pp. 10732-10737, 2018.
- W. Peterson, M. Halter, A. Tona, and A. L. Plant, "High resolution surface plasmon resonance imaging for single cells," BMC cell biology, vol. 15, no. 1, pp. 1-14, 2014.
- Zybin, C. Grunwald, V. M. Mirsky, J. Kuhlmann, O. S. Wolfbeis, and K. Niemax, "Double-wavelength technique for surface plasmon resonance measurements: basic concept and applications for single sensors and two-dimensional sensor arrays," Analytical chemistry, vol. 77, no. 8, pp. 2393-2399, 2005.
- Zybin, D. Boecker, V. M. Mirsky, and K. Niemax, "Enhancement of the detection power of surface plasmon resonance measurements by optimization of the reflection angle," Analytical chemistry, vol. 79, no. 11, pp. 4233-4236, 2007.
- Zybin, V. Shpacovitch, J. Skolnik, and R. Hergenröder, "Optimal conditions for SPR-imaging of nano-objects," Sensors and Actuators B: Chemical, vol. 239, pp. 338-342, 2017.

- E. Yılmaz, E. Özgür, N. Bereli, D. Türkmen, and A. Denizli, "Plastic antibody based surface plasmon resonance nanosensors for selective atrazine detection," Materials Science and Engineering: C, vol. 73, pp. 603-610, 2017.
- J. Maurya, Y. Prajapati, V. Singh, J. Saini, and R. Tripathi, "Performance of graphene–MoS 2 based surface plasmon resonance sensor using silicon layer," Optical and Quantum Electronics, vol. 47, no. 11, pp. 3599-3611, 2015.
- K. Bazaka and M. V. Jacob, "Effects of iodine doping on optoelectronic and chemical properties of polyterpenol thin films," Nanomaterials, vol. 7, no. 1, p. 11, 2017.
- L. Novotny and B. Hecht, Principles of nano-optics. Cambridge university press, 2012.
- M. S. Anower, M. M. Rahman, and M. S. Rahman, "Hybrid heterostructures for SPR biosensor," Biosensors-Current and Novel Strategies for Biosensing, p. 8, 2021.
- N. Menegazzo, B. Herbert, S. Banerji, and K. S. Booksh, "Discourse on the utilization of polyaniline coatings for surface plasmon resonance sensing of ammonia vapor," Talanta, vol. 85, no. 3, pp. 1369-1375, 2011.
- N. Mudgal, M. K. Falaswal, T. Ismail, I. Fahim, M. Tiwari, and G. Singh, "Study of approaches to implement the prism-based surface plasmon resonance sensors," in Optical and Wireless Technologies: Springer, 2020, pp. 353-362.
- S. Danyluk and W. Schneider, "THE ELECTRON SPIN RESONANCE OF NON-ALTERNANT AROMATIC HYDROCARBON–IODINE COMPLEXES," Canadian Journal of Chemistry, vol. 40, no. 9, pp. 1884-1885, 1962.
- T. B. A. Akib et al., "Design and numerical analysis of a graphene-coated SPR biosensor for rapid detection of the novel coronavirus," Sensors, vol. 21, no. 10, p. 3491, 2021.
- V. G. Levich and C. W. Tobias, "Physicochemical hydrodynamics," Journal of The Electrochemical Society, vol. 110, no. 11, p. 251C, 1963.
- W. M. Mukhtar, S. Shaari, A. A. Ehsan, and P. S. Menon, "Electro-optics interaction imaging in active plasmonic devices," Optical Materials Express, vol. 4, no. 3, pp. 424-433, 2014.
- X. Yi, Z. Xu, Y. Liu, X. Guo, M. Ou, and X. Xu, "Highly efficient removal of uranium (VI) from wastewater by polyacrylic acid hydrogels," RSC advances, vol. 7, no. 11, pp. 6278-6287, 2017.

LIST OF FIGURES

LIST OF ACRONYMS

SPR	Surface plasmon resonance
SPP	Surface plasmon polariton
LSPs	Localized surface plasmons
PSPs	Propagating surface plasmons
WF-SPRM	Wide-field surface plasmon resonance microscopy
Au	Gold
Ag	Silver
AuNPs	Gold Nanoparticles
AgNSs	Silver nanostructures
PEBs	Polyelectrolyte brushes
PAA	Polyacrylic acid
PAA-SH	Thiolated polyacrylic acid
PEO	Polyethylene oxide
I_2	Iodine
PSNPs	Polystyrene nanoparticles
SilicaNPs	Silica nanoparticles
UV	Ultraviolet
Vis	Visible
IR	Infrared
FTIR	Fourier transform infrared spectroscopy
XRD	X-ray diffraction
TGA	Thermogravimetric analysis
SEM	Scanning electron microscope
WCA	Water contact angle
LOD	Limit of detection
NMR	Nuclear magnetic resonance
AFM	Atomic force microscope
$COOH$	Carboxylic acid group
COO^-	Carboxylate group
ITO	Indium tin oxide
SMPs	Shape memory polymers
NAP-XPS	Near ambient pressure X-ray photoelectron spectroscopy

LIST OF SYMBOLS

ω_p	Plasma frequency
θ_c	Edge of total internal reflection
n	Refractive index
k	Extinction coefficient
$R_{\min}$	Minimum reflectance
DA	Detection accuracy
FWHM	Full width half maximum
λ	Wavelength
ω	Frequency
E	Electric field vector
H	Magnetic field vector
k_{iz}	z wave vector components
k_{ix}	x wave vector components
c	Light speed
ε_k	Dielectric constant
d_k	Layer thickness
R_p	Reflectivity
θ_R	Resonance angle
$u(\vec{r}, t)$	Poiseuille flow velocity
V	Volumetric flow rate
η	Quantum efficiency of the photodetector
I_0	Illumination intensity
I_{CCD}	CCD detector's illumination intensity
S/N	Signal-to-noise-ratio
E_r	Reflected electric field

E_s	A particle's scattered fields
E_{sp}	The electric field excites surface plasmons
k	The wavenumber ($k = 2\pi/\lambda$)
κ	The decays constant
φ	Phase shift
α	The polarizability
I	Intensity
β_{ev}	Propagation constant
ε_{eff}	Effective dielectric constant
E_g	Bandgap energy
E_U	Urbach energy
σ	Electrical conductivity
E_a	Activation energy
S/N	Signal-to-noise ratio
α	Absorption coefficient
X_{cryst}	Crystallinity degree
D	Crystalline size
$\langle\varepsilon\rangle$	Micro-strain
δ	Density of dislocations
N	Crystalline density
σ	Total internal stress
E_d	Strain energy density

BIBLIOGRAPHY

Agarwal, A., Vitiello, M. S., Viti, L., Cupolillo, A., & Politano, A. (2018). Plasmonics with two-dimensional semiconductors: from basic research to technological applications. *Nanoscale*, *10*(19), 8938-8946.

Akib, T. B. A., Mou, S. F., Rahman, M. M., Rana, M. M., Islam, M. R., Mehedi, I. M., Mahmud, M. P., & Kouzani, A. Z. (2021). Design and numerical analysis of a graphene-coated SPR biosensor for rapid detection of the novel coronavirus. *Sensors*, *21*(10), 3491.

Al-Bataineh, Q. M., Shpacovitch, V., Sadiq, D., Telfah, A., & Hergenröder, R. (2022). Surface plasmon resonance sensitivity enhancement based on protonated polyaniline films doped by aluminum nitrate. *Biosensors*, *12*(12), 1122.

Al-Bataineh, Q. M., Telfah, A. D., Shpacovitch, V., Tavares, C. J., & Hergenröder, R. (2023a). Switchable polyacrylic acid polyelectrolyte brushes for surface plasmon resonance applications. *Sensors*, *23*(9), 4283.

Al-Bataineh, Q. M., Telfah, A. D., Tavares, C. J., & Hergenröder, R. (2023b). Surface plasmon coupling between wide-field SPR microscopy and gold nanoparticles. *Scientific reports*, *13*(1), 22405.

Al-Bataineh, Q. M., Telfah, A. D., Tavares, C. J., & Hergenröder, R. (2024a). Modeling and analysis of discrete particle detection in wide-field surface plasmon resonance microscopy. *Sensors and Actuators A: Physical*, *370*, 115266.

Al-Bataineh, Q. M., Telfah, A. D., Tavares, C. J., & Hergenröder, R. (2024b). Wide-field surface plasmon resonance microscope based on polyethylene oxide/polyacrylic acid brushes. *Applied surface science*, *649*, 159189.

Al-Bataineh, Q. M., Telfah, M., Abu-Zurayk, R., Benchaabane, A., Tavares, C. J., & Telfah, A. (2023c). Nano-SnO2/polyaniline composite films for surface plasmon resonance. *Materials Chemistry and Physics*, *293*, 126816.

Alzoubi, F., Ahmad, A. A., Aljarrah, I. A., Migdadi, A., & Al-Bataineh, Q. M. (2023). Localize surface plasmon resonance of silver nanoparticles using Mie theory. *Journal of Materials Science: Materials in Electronics*, *34*(32), 2128.

Anower, M. S., Rahman, M. M., & Rahman, M. S. (2021). Hybrid heterostructures for SPR biosensor. *Biosensors-Current and Novel Strategies for Biosensing*, 8.

Aulich, D., Hoy, O., Luzinov, I., Brücher, M., Hergenröder, R., Bittrich, E., Eichhorn, K.-J., Uhlmann, P., Stamm, M., & Esser, N. (2010). In situ studies on the switching behavior of ultrathin poly (acrylic acid) polyelectrolyte brushes in different aqueous environments. *Langmuir*, *26*(15), 12926-12932.

Azli, A., Manan, N., & Kadir, M. (2015). Conductivity and dielectric studies of lithium trifluoromethanesulfonate doped polyethylene oxide-graphene oxide blend based electrolytes. *Advances in Materials Science and Engineering*, *2015*.

Ballauff, M., & Borisov, O. (2006). Polyelectrolyte brushes. *Current Opinion in Colloid & Interface Science*, *11*(6), 316-323.

Barnes, W. L., Dereux, A., & Ebbesen, T. W. (2003). Surface plasmon subwavelength optics. *Nature*, *424*(6950), 824-830.

Bazaka, K., & Jacob, M. V. (2017). Effects of iodine doping on optoelectronic and chemical properties of polyterpenol thin films. *Nanomaterials*, *7*(1), 11.

Bellassai, N., D'Agata, R., Jungbluth, V., & Spoto, G. (2019). Surface plasmon resonance for biomarker detection: advances in non-invasive cancer diagnosis. *Frontiers in chemistry*, *7*, 570.

Boecker, D., Zybin, A., Niemax, K., Grunwald, C., & Mirsky, V. M. (2008). Noise reduction by multiple referencing in surface plasmon resonance imaging. *Review of Scientific Instruments, 79*(2).

Burinaru, T. A., Adiaconiţă, B., Avram, M., Preda, P., Enciu, A.-M., Chiriac, E., Mărculescu, C., Constantin, T., & Militaru, M. (2022). Electrochemical impedance spectroscopy based microfluidic biosensor for the detection of circulating tumor cells. *Materials Today Communications, 32*, 104016.

Cisneros, J. S., Chain, C. Y., Millone, M. D., Labriola, C., Scollo, K., Ruiz, A., Estrela, P., & Vela, M. E. (2022). Electrochemical impedance biosensor for Chagas Disease diagnosis in clinical samples. *Biosensors and Bioelectronics: X, 12*, 100261.

Cui, F., Zhou, Z., & Zhou, H. S. (2019). Measurement and analysis of cancer biomarkers based on electrochemical biosensors. *Journal of The Electrochemical Society, 167*(3), 037525.

Dai, S., Yu, T., Zhang, J., Lu, H., Dou, J., Zhang, M., Dong, C., Di, J., & Zhao, J. (2021). Real-time and wide-field mapping of cell-substrate adhesion gap and its evolution via surface plasmon resonance holographic microscopy. *Biosensors and Bioelectronics, 174*, 112826.

Danyluk, S., & Schneider, W. (1962). THE ELECTRON SPIN RESONANCE OF NON-ALTERNANT AROMATIC HYDROCARBON–IODINE COMPLEXES. *Canadian Journal of Chemistry, 40*(9), 1884-1885.

Debye, P., & Scherrer, P. (1916). Interferenzen an regellos orientierten Teilchen im Röntgenlicht. I. *Nachrichten von der Gesellschaft der Wissenschaften zu Göttingen, Mathematisch-Physikalische Klasse, 1916*, 1-15.

Evlyukhin, A., & Bozhevolnyi, S. (2005). Point-dipole approximation for surface plasmon polariton scattering: Implications and limitations. *Physical Review B—Condensed Matter and Materials Physics, 71*(13), 134304.

Evlyukhin, A. B., & Bozhevolnyi, S. I. (2015). Resonant unidirectional and elastic scattering of surface plasmon polaritons by high refractive index dielectric nanoparticles. *Physical Review B, 92*(24), 245419.

Fan, X., White, I. M., Shopova, S. I., Zhu, H., Suter, J. D., & Sun, Y. (2008). Sensitive optical biosensors for unlabeled targets: A review. *Analytica Chimica Acta, 620*(1-2), 8-26.

Ferrand-Drake del Castillo, G., Koenig, M., Müller, M., Eichhorn, K.-J., Stamm, M., Uhlmann, P., & Dahlin, A. (2019). Enzyme immobilization in polyelectrolyte brushes: High loading and enhanced activity compared to monolayers. *Langmuir, 35*(9), 3479-3489.

Gaur, R., Manikandan, P., Manikandan, D., Umapathy, S., Padhy, H. M., Maaza, M., & Elayaperumal, M. (2021). Noble metal ion embedded nanocomposite glass materials for optical functionality of UV–visible surface plasmon resonance (SPR) surface-enhanced raman scattering (SERS) X-ray and electron microscopic studies: An overview. *Plasmonics, 16*, 1461-1493.

Gurevich, E., Temchura, V., Überla, K., & Zybin, A. (2011). Analytical features of particle counting sensor based on plasmon assisted microscopy of nano objects. *Sensors and Actuators B: Chemical, 160*(1), 1210-1215.

Halpern, A. R., Wood, J. B., Wang, Y., & Corn, R. M. (2014). Single-nanoparticle near-infrared surface plasmon resonance microscopy for real-time measurements of DNA hybridization adsorption. *ACS nano, 8*(1), 1022-1030.

Huang, B., Yu, F., & Zare, R. N. (2007). Surface plasmon resonance imaging using a high numerical aperture microscope objective. *Analytical chemistry, 79*(7), 2979-2983.

Johnson, P., & Christy, R. (1974). Optical constants of transition metals: Ti, v, cr, mn, fe, co, ni, and pd. *Physical Review B, 9*(12), 5056.

Jung, L. S., Campbell, C. T., Chinowsky, T. M., Mar, M. N., & Yee, S. S. (1998). Quantitative interpretation of the response of surface plasmon resonance sensors to adsorbed films. *Langmuir*, *14*(19), 5636-5648.

Karki, B., Pal, A., Singh, Y., & Sharma, S. (2022). Sensitivity enhancement of surface plasmon resonance sensor using 2D material barium titanate and black phosphorus over the bimetallic layer of Au, Ag, and Cu. *Optics Communications*, *508*, 127616.

Khan, S., & Sharma, I. (2023). Revolutionary Future Using the Ultimate Potential of Nanophotonics. *Photonic Materials: Recent Advances and Emerging Applications*, 141.

Kretschmann, E. (1971). The determination of optical constants of metals by excitation of surface plasmons (Die Bestimmung optischer Konstanten von Metallen durch Anregung von Oberflächenplasmaschwingungen). *Z. Phys.*, *241*, 313-324.

Kretschmann, E. (1996). Determination of optical constants of metals by excitation of surface plasmon sensing. *Sens. Actuators B Chem*, *35*, 212.

Kuzmichev, A., Skolnik, J., Zybin, A., & Hergenröder, R. (2018). Absolute analysis of nanoparticle suspension with surface plasmon microscopy. *Analytical chemistry*, *90*(18), 10732-10737.

Lenssen, J. E., Toma, A., Seebold, A., Shpacovitch, V., Libuschewski, P., Weichert, F., Chen, J.-J., & Hergenröder, R. (2018). Real-time Low SNR Signal Processing for Nanoparticle Analysis with Deep Neural Networks. BIOSIGNALS,

Levich, V. G., & Tobias, C. W. (1963). Physicochemical hydrodynamics. *Journal of the Electrochemical Society*, *110*(11), 251C.

Libuschewski, P. (2017). *Exploration of cyber-physical systems for GPGPU computer vision-based detection of biological viruses* Dissertation, Dortmund, Technische Universität, 2017].

Ly, N., Foley, K., & Tao, N. (2007). Integrated label-free protein detection and separation in real time using confined surface plasmon resonance imaging. *Analytical chemistry*, *79*(6), 2546-2551.

Ma, G., Liang, R., Wan, Z., & Wang, S. (2021). Critical angle reflection imaging for quantification of molecular interactions on glass surface. *Nature communications*, *12*(1), 3365.

Ma, G., Wan, Z., Yang, Y., Zhang, P., Wang, S., & Tao, N. (2020). Optical imaging of single-protein size, charge, mobility, and binding. *Nature communications*, *11*(1), 4768.

Masson, J.-F. (2017). Surface plasmon resonance clinical biosensors for medical diagnostics. *ACS sensors*, *2*(1), 16-30.

Maurya, J., Prajapati, Y., Singh, V., Saini, J., & Tripathi, R. (2015). Performance of graphene–MoS 2 based surface plasmon resonance sensor using silicon layer. *Optical and Quantum Electronics*, *47*(11), 3599-3611.

McDonnell, J. M. (2001). Surface plasmon resonance: towards an understanding of the mechanisms of biological molecular recognition. *Current opinion in chemical biology*, *5*(5), 572-577.

Mehrotra, P. (2016). Biosensors and their applications–A review. *Journal of oral biology and craniofacial research*, *6*(2), 153-159.

Menegazzo, N., Herbert, B., Banerji, S., & Booksh, K. S. (2011). Discourse on the utilization of polyaniline coatings for surface plasmon resonance sensing of ammonia vapor. *Talanta*, *85*(3), 1369-1375.

Meradi, K. A., Tayeboun, F., Guerinik, A., Zaky, Z. A., & Aly, A. H. (2022). Optical biosensor based on enhanced surface plasmon resonance: theoretical optimization. *Optical and Quantum Electronics*, *54*(2), 124.

Mudgal, N., Falaswal, M. K., Ismail, T., Fahim, I., Tiwari, M., & Singh, G. (2020). Study of approaches to implement the prism-based surface plasmon resonance sensors. In *Optical and Wireless Technologies* (pp. 353-362). Springer.

Mukhtar, W. M., Shaari, S., Ehsan, A. A., & Menon, P. S. (2014). Electro-optics interaction imaging in active plasmonic devices. *Optical Materials Express*, *4*(3), 424-433.

Nagata, K., & Handa, H. (2000). Real-time analysis of biomolecular interactions. *Applications of Biacore*, 13-22.

Nguyen, H. H., Park, J., Kang, S., & Kim, M. (2015). Surface plasmon resonance: a versatile technique for biosensor applications. *Sensors*, *15*(5), 10481-10510.

Nizamov, S., Sazdovska, S. D., & Mirsky, V. M. (2022). A review of optical methods for ultrasensitive detection and characterization of nanoparticles in liquid media with a focus on the wide field surface plasmon microscopy. *Analytica Chimica Acta*, 339633.

Novotny, L., & Hecht, B. (2012). *Principles of nano-optics*. Cambridge university press.

Novotny, L., Hecht, B., & Pohl, D. (1997). Interference of locally excited surface plasmons. *Journal of Applied Physics*, *81*(4), 1798-1806.

Oliveira, L. C., Lima, A. M. N., Thirstrup, C., & Neff, H. F. (2015). *Surface plasmon resonance sensors: a materials guide to design and optimization*. Springer.

Omar, N. A. S., Fen, Y. W., Abdullah, J., Kamil, Y. M., Daniyal, W. M. E. M. M., Sadrolhosseini, A. R., & Mahdi, M. A. (2020). Sensitive detection of dengue virus type 2 E-proteins signals using self-assembled monolayers/reduced graphene oxide-PAMAM dendrimer thin film-SPR optical sensor. *Scientific reports*, *10*(1), 1-15.

Otto, A. (1968). Excitation of nonradiative surface plasma waves in silver by the method of frustrated total reflection. *Zeitschrift für Physik A Hadrons and nuclei*, *216*(4), 398-410.

Park, G., Kim, H.-O., Lim, J.-W., Park, C., Yeom, M., Song, D., & Haam, S. (2021). Rapid detection of influenza A (H1N1) virus by conductive polymer-based nanoparticle via optical response to virus-specific binding. *Nano research*, 1-9.

Peterson, A. W., Halter, M., Tona, A., Bhadriraju, K., & Plant, A. L. (2009). Surface plasmon resonance imaging of cells and surface-associated fibronectin. *BMC cell biology*, *10*, 1-17.

Peterson, A. W., Halter, M., Tona, A., & Plant, A. L. (2014). High resolution surface plasmon resonance imaging for single cells. *BMC cell biology*, *15*(1), 1-14.

Politano, A., Cupolillo, A., Di Profio, G., Arafat, H., Chiarello, G., & Curcio, E. (2016). When plasmonics meets membrane technology. *Journal of Physics: Condensed Matter*, *28*(36), 363003.

Politano, A., Viti, L., & Vitiello, M. S. (2017). Optoelectronic devices, plasmonics, and photonics with topological insulators. *APL Materials*, *5*(3), 035504.

Polu, A. R., & Rhee, H.-W. (2016). The effects of LiTDI salt and POSS-PEG (n= 4) hybrid nanoparticles on crystallinity and ionic conductivity of PEO based solid polymer electrolytes. *Science of Advanced Materials*, *8*(5), 931-940.

Raether, H. (2006). Surface plasmons on smooth surfaces. *Surface plasmons on smooth and rough surfaces and on gratings*, 4-39.

Rasband, W. S. (1997-2018). *ImageJ*. National Institutes of Health. https://imagej.nih.gov/ij/

Reitz, J. R. (2009). *Foundations of electromagnetic theory*. Pearson Education India.

RES-TEC. Retrieved 07.09.2023 from http://www.res-tec.de/

Rich, R. L., & Myszka, D. G. (2003). A survey of the year 2002 commercial optical biosensor literature. *Journal of Molecular Recognition*, *16*(6), 351-382.

Rothenhäusler, B., & Knoll, W. (1988). Surface–plasmon microscopy. *Nature*, *332*(6165), 615-617.

Rycenga, M., Cobley, C. M., Zeng, J., Li, W., Moran, C. H., Zhang, Q., Qin, D., & Xia, Y. (2011). Controlling the synthesis and assembly of silver nanostructures for plasmonic applications. *Chemical reviews*, *111*(6), 3669-3712.

Schasfoort, R. (2017). History and Physics of Surface Plasmon Resonance.

Scherbahn, V., Nizamov, S., & Mirsky, V. M. (2016). Plasmonic detection and visualization of directed adsorption of charged single nanoparticles to patterned surfaces. *Microchimica Acta*, *183*(11), 2837-2845.

Shalabney, A., & Abdulhalim, I. (2011). Sensitivity-enhancement methods for surface plasmon sensors. *Laser & Photonics Reviews*, *5*(4), 571-606.

Shpacovitch, V., & Hergenroeder, R. (2018). Optical and surface plasmonic approaches to characterize extracellular vesicles. A review. *Analytica Chimica Acta*, *1005*, 1-15.

Shpacovitch, V., Sidorenko, I., Lenssen, J. E., Temchura, V., Weichert, F., Müller, H., Überla, K., Zybin, A., Schramm, A., & Hergenröder, R. (2017). Application of the PAMONO-sensor for quantification of microvesicles and determination of nano-particle size distribution. *Sensors*, *17*(2), 244.

Shpacovitch, V., Temchura, V., Matrosovich, M., Hamacher, J., Skolnik, J., Libuschewski, P., Siedhoff, D., Weichert, F., Marwedel, P., & Müller, H. (2015). Application of surface plasmon resonance imaging technique for the detection of single spherical biological submicrometer particles. *Analytical biochemistry*, *486*, 62-69.

Shumaker-Parry, J. S., & Campbell, C. T. (2004). Quantitative methods for spatially resolved adsorption/desorption measurements in real time by surface plasmon resonance microscopy. *Analytical chemistry*, *76*(4), 907-917.

Siedhoff, D. (2016). *A parameter-optimizing model-based approach to the analysis of low-SNR image sequences for biological virus detection* Dissertation, Dortmund, Technische Universität, 2016].

Singh, S., Singh, P. K., Umar, A., Lohia, P., Albargi, H., Castañeda, L., & Dwivedi, D. (2020). 2D nanomaterial-based surface plasmon resonance sensors for biosensing applications. *Micromachines*, *11*(8), 779.

Srivastava, A., Das, R., & Prajapati, Y. K. (2020). Effect of Perovskite material on performance of surface plasmon resonance biosensor. *IET Optoelectronics*, *14*(5), 256-265.

Steiner, G. (2004). Surface plasmon resonance imaging. *Analytical and bioanalytical chemistry*, *379*(3), 328-331.

Usman, F., Dennis, J. O., Seong, K. C., Ahmed, A. Y., Ferrell, T. L., Fen, Y. W., Sadrolhosseini, A. R., Ayodele, O. B., Meriaudeau, F., & Saidu, A. (2019a). Enhanced sensitivity of surface plasmon resonance biosensor functionalized with doped polyaniline composites for the detection of low-concentration acetone vapour. *Journal of Sensors*, *2019*.

Usman, F., Dennis, J. O., Seong, K. C., Ahmed, A. Y., Ferrell, T. L., Fen, Y. W., Sadrolhosseini, A. R., Ayodele, O. B., Meriaudeau, F., & Saidu, A. (2019b). Enhanced sensitivity of surface plasmon resonance biosensor functionalized with doped polyaniline composites for the detection of low-concentration acetone vapour. *Journal of Sensors*, *2019*, 1-13.

Usman, F., Dennis, J. O., Seong, K. C., Ahmed, A. Y., Ferrell, T. L., Fen, Y. W., Sadrolhosseini, A. R., Ayodele, O. B., Meriaudeau, F., & Saidu, A. (2019c). Enhanced Sensitivity of Surface Plasmon Resonance Biosensor Functionalized with Doped Polyaniline Composites for the Detection of Low-Concentration Acetone Vapour. *Journal of Sensors*, *2019*(1), 5786105.

Valle, P., Ortiz, E., & Saiz, J. (1997). Near field by subwavelength particles on metallic substrates with cylindrical surface plasmon excitation. *Optics communications*, *137*(4-6), 334-342.

Viti, L., Politano, A., & Vitiello, M. S. (2017). Black phosphorus nanodevices at terahertz frequencies: Photodetectors and future challenges. *APL Materials*, *5*(3), 035602.

Wang, D., Loo, J. F. C., Chen, J., Yam, Y., Chen, S.-C., He, H., Kong, S. K., & Ho, H. P. (2019). Recent advances in surface plasmon resonance imaging sensors. *Sensors*, *19*(6), 1266.

Wang, M., Yang, Y., Min, J., Song, Y., Tu, J., Mukasa, D., Ye, C., Xu, C., Heflin, N., & McCune, J. S. (2022). A wearable electrochemical biosensor for the monitoring of metabolites and nutrients. *Nature Biomedical Engineering*, *6*(11), 1225-1235.

Wang, Q., Ren, Z.-H., Zhao, W.-M., Wang, L., Yan, X., Zhu, A.-s., Qiu, F.-m., & Zhang, K.-K. (2022). Research advances on surface plasmon resonance biosensors. *Nanoscale*.

Wang, S., Shan, X., Patel, U., Huang, X., Lu, J., Li, J., & Tao, N. (2010). Label-free imaging, detection, and mass measurement of single viruses by surface plasmon resonance. *Proceedings of the National Academy of Sciences*, *107*(37), 16028-16032.

Xue, T., Liang, W., Li, Y., Sun, Y., Xiang, Y., Zhang, Y., Dai, Z., Duo, Y., Wu, L., & Qi, K. (2019a). Ultrasensitive detection of miRNA with an antimonene-based surface plasmon resonance sensor. *Nature communications*, *10*(1), 1-9.

Xue, T., Liang, W., Li, Y., Sun, Y., Xiang, Y., Zhang, Y., Dai, Z., Duo, Y., Wu, L., & Qi, K. (2019b). Ultrasensitive detection of miRNA with an antimonene-based surface plasmon resonance sensor. *Nature communications*, *10*(1), 28.

Yang, C.-T., Xu, Y., Pourhassan-Moghaddam, M., Tran, D. P., Wu, L., Zhou, X., & Thierry, B. (2019). Surface plasmon enhanced light scattering biosensing: size dependence on the gold nanoparticle tag. *Sensors*, *19*(2), 323.

Yang, Y., Matsubara, S., Xiong, L., Hayakawa, T., & Nogami, M. (2007). Solvothermal synthesis of multiple shapes of silver nanoparticles and their SERS properties. *The Journal of Physical Chemistry C*, *111*(26), 9095-9104.

Yano, T.-a., Kajisa, T., Ono, M., Miyasaka, Y., Hasegawa, Y., Saito, A., Otsuka, K., Sakane, A., Sasaki, T., & Yasutomo, K. (2022). Ultrasensitive detection of SARS-CoV-2 nucleocapsid protein using large gold nanoparticle-enhanced surface plasmon resonance. *Scientific Reports*, *12*(1), 1060.

Yi, X., Xu, Z., Liu, Y., Guo, X., Ou, M., & Xu, X. (2017). Highly efficient removal of uranium (VI) from wastewater by polyacrylic acid hydrogels. *Rsc Advances*, *7*(11), 6278-6287.

Yılmaz, E., Özgür, E., Bereli, N., Türkmen, D., & Denizli, A. (2017). Plastic antibody based surface plasmon resonance nanosensors for selective atrazine detection. *Materials Science and Engineering: C*, *73*, 603-610.

Yu, H., Shan, X., Wang, S., Chen, H., & Tao, N. (2014). Molecular scale origin of surface plasmon resonance biosensors. *Analytical chemistry*, *86*(18), 8992-8997.

Yu, H., Shan, X., Wang, S., & Tao, N. (2017). Achieving high spatial resolution surface plasmon resonance microscopy with image reconstruction. *Analytical chemistry*, *89*(5), 2704-2707.

Zhang, P., Ma, G., Dong, W., Wan, Z., Wang, S., & Tao, N. (2020). Plasmonic scattering imaging of single proteins and binding kinetics. *Nature Methods*, *17*(10), 1010-1017.

Zou, S., Lv, R., Tong, Z., Na, B., Fu, K., & Liu, H. (2019). In situ hydrogen-bonding complex mediated shape memory behavior of PAA/PEO blends. *Polymer*, *183*, 121878.

Zybin, A. (2010). Verfahren zur hochaufgelösten erfassung von nanopartikeln auf zweidimensionalen messflächen. In: Google Patents.

Zybin, A., Boecker, D., Mirsky, V. M., & Niemax, K. (2007). Enhancement of the detection power of surface plasmon resonance measurements by optimization of the reflection angle. *Analytical chemistry*, *79*(11), 4233-4236.

Zybin, A., Grunwald, C., Mirsky, V. M., Kuhlmann, J., Wolfbeis, O. S., & Niemax, K. (2005). Double-wavelength technique for surface plasmon resonance measurements: basic

concept and applications for single sensors and two-dimensional sensor arrays. *Analytical chemistry*, *77*(8), 2393-2399.

Zybin, A., Kuritsyn, Y. A., Gurevich, E. L., Temchura, V. V., Überla, K., & Niemax, K. (2010). Real-time detection of single immobilized nanoparticles by surface plasmon resonance imaging. *Plasmonics*, *5*(1), 31-35.

Zybin, A., Shpacovitch, V., Skolnik, J., & Hergenröder, R. (2017). Optimal conditions for SPR-imaging of nano-objects. *Sensors and Actuators B: Chemical*, *239*, 338-342.